Measurement of the Decays $B \rightarrow D\ell\nu$

DISSERTATION
zur Erlangung des akademischen Grades
Doctor rerum naturalium
(Dr. rer. nat.)

vorgelegt von
Enrico Feltresi

Lehrstuhl für Experimentelle Physik 5
Fakultät Physik
der Technischen Universität Dortmund

2010

Vom Fachbereich Physik der Technischen Universität Dortmund zur Erlangung des akademischen Grades eines Doktors der Naturwissenschaften genehmigte Dissertation.

1. Gutachter : Prof. Dr. Bernhard Spaan

2. Gutachter : Dr. Jochen Dingfelder

All work presented in this document is the author's own work, unless stated otherwise. This work is supported by the Bundesministerium für Bildung und the Forschung and Deutsche Forschungsgemeinschaft (Germany).

Abstract

One of the main goals of the BABAR Experiment at the SLAC National Accelerator Laboratory's e^+e^- storage ring PEP-II is the precise measurement of the CKM-Matrix elements. Semileptonic B-decays allow the extraction of both $|V_{cb}|$ and $|V_{ub}|$. This analysis presents an exclusive untagged measurement of the semileptonic decay $B \to D\ell\nu$ to extract $|V_{cb}|$ and the form factor slope $\hat{\rho}^2$. Results are presented based on a data sample of approximately 390 fb^{-1}, which corresponds to $(383.6 \pm 4.2) \times 10^6$ $\Upsilon(4\mathrm{S}) \to B\overline{B}$ decays. The results are:

$$\mathcal{G}(1)|V_{cb}| = (43.5 \pm 1.1 \pm 1.8) \times 10^{-3}, \tag{0.1}$$

$$\hat{\rho}^2 = 1.11 \pm 0.05 \pm 0.04, \tag{0.2}$$

where the first uncertainties are statistical and the second systematic, $\mathcal{G}(1)$ is the hadronic form factor at the point of zero recoil. Integrating the differential decay rate $d\Gamma/dw$ over the allowed values of w, and using the previous results, the branching fraction $\mathcal{B}(B \to D\ell\nu)$ has been determined:

$$\mathcal{B}(B \to D\ell\nu) = (2.38 \pm 0.03 \pm 0.10)\%. \tag{0.3}$$

Contents

Introduction

The Standard Model (SM) of Particle Physics successfully explains the fundamental interactions (strong, electromagnetic and weak) of particles in a unified theoretical framework. This theory gives an excellent description of all the phenomena observed in Particle Physics up to energies explored at today's accelerator experiments. However the Standard Model leaves too many unanswered questions such as non-zero neutrino masses, the presence of dark matter, the fermion mass hierarchy and the quantitative asymmetry between matter and antimatter in the universe. Nevertheless to find effects that go beyond the Standard Model theory and to explain these shortcomings it is very important to measure the many Standard Model parameters as precisely as possible.

The quark mixing formalism is a fundamental part of the Standard Model, describing the weak interactions among quarks through the CKM Matrix, named after N. Cabibbo, M. Kobayashi and T. Maskawa. The CKM matrix is a complex unitary matrix, it can be parameterized by three mixing angles and a phase, which are four of the free parameters of the Standard Model. One of them, the phase, is complex and alone accounts for the violation of the combination of particle-antiparticle (charge conjugation: C) and mirror (parity: P) symmetry, known as CP violation. CP violation may help explaining the matter-antimatter asymmetry observed in the universe. Precise experimental measurements of the CKM matrix elements allow to test the unitarity of the quark mixing matrix. Besides the elements $|V_{cb}|$ and $|V_{ub}|$ are important to understand the phenomenology of weak interaction, the physics of quark flavour and mass, and have interesting implication for the breakdown of the CP symmetry.

At the end of the nineties, two experimental facilities started to study B physics and to test Standard Model parameters in the fermion sector. One is *BABAR* at the SLAC national accelerator laboratory in California, USA, the other is BELLE at the KEK High Energy Accelerator Research Organization in Japan. The B-factory experiments have collected an huge amount of data for almost ten years, determining the CP-violation and fundamental Standard Model parameters (e.g. $|V_{cb}|$ and $|V_{ub}|$) with high precision. Experimentally $|V_{cb}|$ can be measured studying the exclusive $B \to D^{(*)}\ell\nu$ decay or the inclusive process $b \to c\ell\nu$. Exclusive determinations of $|V_{cb}|$ are based on a study of semileptonic B decays into charmed mesons (D or D^*), and both lepton and meson are identified. On the other hand inclusive determinations are based on a measurement of the total semileptonic decay rate $\Gamma(B \to X\ell\nu)$, where the final state consists of a lepton-neutrino pair accompanied by any number of hadrons, but only the lepton is identify. Both inclusive and exclusive determinations of $|V_{cb}|$ rely on theoretical calculations of the hadronic matrix element expressed in terms of form factors. The framework to calculate the form factors is provided by the Heavy Quark Effective Theory (HQET), an exact theory in the limit of infinite quark masses.

The differential decay rate for $B \to D\ell\nu$ is proportional to $|V_{cb}|^2$, and it can be expressed as:

$$\frac{d\Gamma(B \to D\ell\nu)}{dw} = \frac{G_F^2|V_{cb}|^2}{48\pi^3}\mathcal{K}(w)\mathcal{G}^2(w) \tag{0.4}$$

where w is the inner product of the B and D meson velocity 4-vectors, $w = v_B \cdot v_D$, corresponding to the energy of the final state hadron in the rest frame of the decay. $\mathcal{K}(w)$ is the phase space. Hadron kinematics and non-perturbative QCD involved in these decays is rigorously parametrized in terms of a hadronic form factor $\mathcal{G}(w)$. It is usually expressed as the product of a normalization factor, $\mathcal{G}(1)$, and a function, $g(w)$, constrained by dispersion relation.

Figure 0.1: The summary, made by the HFAG group, of the existing results for the $BR(B \to D\ell\nu)$ on the left plot, $\mathcal{G}(1) \times |V_{cb}|^2$ in the right plot. The measurements shown are from ALEPH[7], CLEO[8] and BELLE[9], *BABAR* and *BABAR* Tagged [10], and *BABAR* Global Fit [11].

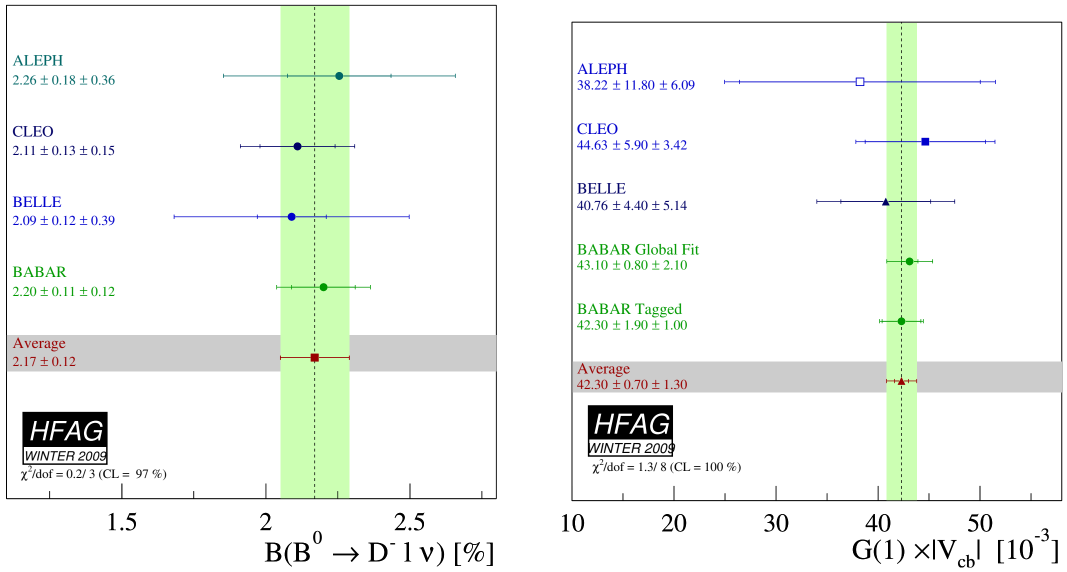

This thesis focuses on the extraction of the quark mixing parameter $|V_{cb}|$ by reconstructing the $B \to D\ell\nu$ decay in the data collected with the *BABAR* detector. Exclusive $B \to D\ell\nu$ events are selected implementing a technique based on the neutrino reconstruction method, which exploits the hermicity of the detector and the near zero mass of the neutrino.

The study of the decay $B \to D\ell\nu$, from a theoretical standpoint, is very interesting. In fact under particular assumptions (BPS[1] framework) the $|V_{cb}|$ extraction is more precise in the $B \to D\ell\nu$ process than in its antagonist, the decay $B \to D^*\ell\nu$, due to a better prediction of the form factor normalization ($\mathcal{G}_{B\to D}(1)$) based on unquenched Lattice QCD calculations[2][3]. Experimentally the $B \to D\ell\nu$ decay process has some advantages compared to the $B \to D^*\ell\nu$ too: it is not hampered by the detection efficiency of the π_{soft}, the slow pion ($\vec{p}_\pi < 200\,\mathrm{MeV}/c$) produced in the $D^* \to D\pi_{soft}$ decay, which is one of the biggest systematic uncertainties in the $B \to D^*\ell\nu$. The results of the $|V_{cb}|$ measurement obtained using the decay $B \to D\ell\nu$ are in a good agreement among different experiments and with inclusive measurements, whereas in $B \to D^*\ell\nu$ not all the measurements are in agreement[4]. From the experimental point of view it is hard to isolate this channel from the dominant $B \to D^*\ell\nu$ background, and the decay rate is heavily suppressed near the point of maximum momentum transfer to the leptons $w = 1$, the point of zero-recoil, due to the helicity mismatch between the initial and final state. But again new quenched lattice calculation results[5, 6] allow the extraction of $|V_{cb}|$ for $w > 1$.

The study of the decay process $B \to D\ell\nu$ have been already performed in the past by ALEPH[7], CLEO[8] and BELLE[9], more recently also *BABAR* published two independent measurements, based on tagged events [10], where one B meson from an $\Upsilon(4S)$ decay is fully reconstructed and on its recoil is studied the semileptonic B decay, or on a semi-inclusive reconstruction of $B \to DX\ell\nu$ decays [11], where the D and lepton are identified and a global fit to them allows to measure simultaneously both the $B \to D\ell\nu$ and $B \to D^*\ell\nu$ decays. The summary of the existing measurements for the $BR(B \to D\ell\nu)$ and $\mathcal{G}(1) \times |V_{cb}|$ can be found in figure 0.1[4].

This work is organized as followed:

Chapter 1: The theory of semileptonic $B \to D\ell\nu$ decays is reviewed together with a brief reminder of the electroweak sector of the standard model and the CKM mechanism.

Chapter 2: The *BABAR* detector is presented, where characteristics and specific performances of each *BABAR* sub-detector are outlined and briefly discussed.

Chapter 3 and 4: The analysis strategy is briefly introduced, then the event samples used in this analysis, consisting of data collected with the *BABAR* detector and simulated Monte Carlo events are summarized.

Chapter 5: The experimental techniques used to reconstruct events, identify particles and resonances are discussed. The criteria applied to select the signal sample are shown.

Chapters 6 and 7: Fit technique for the measurement of signal yields and the extraction of the CKM matrix element $|V_{cb}|$ are reported.

Chapter 8: Systematics uncertainties associated with this measurement are discussed.

1 Theory of Semileptonic B-Meson Decays

After a short introduction into the framework of the Standard Model, the CP-violation and the Cabibbo-Kobayashi-Maskawa quark mixing matrix this chapter will focus on special interest concepts for the theoretical description of the exclusive semileptonic B-Meson decays, and elementary aspects of the Heavy Quark Effective Theory, the theoretical framework used to describe the hadronic matrix element in the $B \to D$ process.

1.1 The Standard Model and the CP violation

The Standard Model (SM) is a theoretical framework which describes the interaction between fundamental particles. In this framework strong, weak and electromagnetic interactions of the basic constituent of matters are modeled using a gauge field theory. The SM is based on the symmetry group $SU(3) \otimes SU(2) \otimes U(1)$. The basic constituents of matter are a dozen of spin- $1/2$ particles (fermions) along with their antiparticles. These are the three pairs of leptons and three pairs of quarks which are organized in a three family structure:

$$\begin{bmatrix} \nu_e & u \\ e & d \end{bmatrix}, \begin{bmatrix} \nu_\mu & c \\ \mu & s \end{bmatrix}, \begin{bmatrix} \nu_\tau & t \\ \tau & b \end{bmatrix},$$

where

$$\begin{bmatrix} \nu_\ell & q_u \\ \ell & q_d \end{bmatrix} \equiv \begin{pmatrix} \nu_\ell \\ \ell \end{pmatrix}_L, \begin{pmatrix} q_u \\ q_d \end{pmatrix}_L, \ell_R, q_{uR}, q_{dR}.$$

The indices “L” and “R” denote the left-handed and right-handed components of the particle fields. The left-handed fields are weak isospin doublets, while all others are singlets with respect to the weak interaction. The interaction between the fermions is mediated by the exchange of integer-spin particles (bosons). Bosons are divided into *vector* and *scalar* bosons, according to the value of their spin being 1 or 0 respectively. The gauge (vector) bosons are:

- the photon, mediator of the electromagnetic interaction;
- the $W^\pm$ and the Z^0, gauge bosons of weak interactions;
- 8 gluons, mediators of the strong interactions.

The Higgs boson, a scalar field whose coupling with the other fields generates their masses while preserving the gauge-invariance of the theory, has not been experimentally observed yet. In the Standard Model, interactions are generated by a Lagrangian density that is invariant under transformations of the group $SU(3)_C \otimes SU(2)_L \otimes U(1)_Y$, which is made up by the strong interaction symmetry group (or *color* symmetry) $SU(3)_C$ and the electro-weak interaction group $SU(2)_L \otimes U(1)_Y$, product of the *weak isospin* and *hypercharge* symmetries. This Lagrangian density can be expressed as a sum of four contributions:

$$\mathcal{L}_{SM} = \mathcal{L}_{fermions} + \mathcal{L}_{Yang-Mills} + \mathcal{L}_{Higgs} + \mathcal{L}_{Yukawa} \,, \tag{1.1}$$

describing respectively:

- the dynamics of fermions in terms of their kinetic energy and their couplings to the gauge bosons ($\mathcal{L}_{fermions}$);
- the dynamics of gauge bosons in terms of their kinetic energy and their self-couplings, associated to local (non-Abelian) symmetry groups ($\mathcal{L}_{Yang-Mills}$);
- the spontaneous symmetry breaking term, derived from the Higgs mechanism, by which bosons acquire a finite mass ($\mathcal{L}_{Higgs}$);
- the fermion mass terms, derived from the same symmetry breaking mechanism and the Yukawa couplings of the fermions with the Higgs scalar ($\mathcal{L}_{Yukawa}$).

The last two terms, that would not appear in a massless particle theory, stem from the spontaneous breaking of the invariance of the SM Lagrangian in the group $SU(3)_C \otimes U(1)_Q$, where $U(1)_Q$ is the symmetry associated to electric charge conservation. This is due to the introduction of a scalar Higgs field with a non-zero vacuum expectation value. The Lagrangian 1.1 not only accounts for massive fermions and gauge bosons, but also allows the violation of the fundamental symmetry (*CP symmetry*) that is given by the composition of two discrete symmetries, namely the parity inversion and the charge conjugation.

1.2 The CKM matrix

The terms in the SM Lagrangian which describe the coupling between quarks and the $W^{\pm}$ bosons are of the (maximally parity violating) form:

$$\mathcal{L}_{fermions} = -\frac{g}{\sqrt{2}}(\mathcal{J}^{\mu} W^{+}_{\mu} + \mathcal{J}^{\mu\dagger} W^{-}_{\mu}) \,, \tag{1.2}$$

where the W^{+}_{μ} operator annihilates a W^{+} or creates a W^{-} (vice-versa for the W^{-}_{μ}) and the *current operator* $\mathcal{J}^{\mu}$ can be explicitly written as:

$$\mathcal{J}^{\mu} = \sum_{i} \bar{u}_i \gamma^{\mu} \frac{1}{2}(1-\gamma^5) V_{ij} d_i \,, \tag{1.3}$$

for quarks. The field operators $\bar{u}_i$ annihilate u, c and t or create their antiparticles, while the d_i operators annihilate d, s and b or create their antiparticles. In the quark case, transitions between different generations are determined by the quantities V_{ij}, (with the indices i, j running through the three quark generations) that are the elements of a 3×3 unitary matrix, the Cabibbo-Kobayashi-Maskawa (CKM) matrix [12]. From a physical point of view, the CKM matrix can be regarded as a rotation matrix between the mass eigenstates basis (d, s, b) and a set of new states (d', s', b') with diagonal couplings to (u, c, t). Feynman amplitudes of processes where a W^{-} is emitted ($d_j \to W^{-} u_i$, $\bar{u}_i \to W^{-} \bar{d}_j$) are then proportional to V_{ij}, while when a W^{+} is emitted ($u_i \to W^{+} d_j$, $\bar{d}_j \to W^{+} \bar{u}_i$) they are proportional to V^{*}_{ij}. The standard notation for the CKM matrix [13] is:

$$\begin{pmatrix} d' \\ s' \\ b' \end{pmatrix} = \begin{pmatrix} V_{ud} & V_{us} & V_{ub} \\ V_{cd} & V_{cs} & V_{cb} \\ V_{td} & V_{ts} & V_{tb} \end{pmatrix} \begin{pmatrix} d \\ s \\ b \end{pmatrix} . \tag{1.4}$$

The dominant terms in the CKM matrix are the diagonal ones, thus transitions between two different quark generations are suppressed with respect to $u \to d$, $c \to s$ and $t \to b$ transitions. The key feature of the CKM matrix is that its elements can be non-trivially complex, allowing for CP-violation phenomena in charged-current transitions. Like fermion masses, the CKM elements are free parameters in the Standard Model and their values are not predicted by the theory. Many parametrizations exist in literature, the most used are the *standard parametrization* [14], and a generalization of the *Wolfenstein parametrization* [15] as presented in [16]. In the Wolfenstein parametrization, the matrix elements are the result of an expansion in terms of a small parameter $\lambda = |V_{us}| \sim 0.22$. The four independent parameters are in this case:

$$\lambda \ , \ A \ , \ \rho \ , \ \eta .$$

where η is the CP violating phase and the matrix is written:

$$V_{CKM} = \begin{pmatrix} 1-\frac{\lambda^2}{2} & \lambda & A\lambda^3(\rho - i\eta) \\ -\lambda & 1-\frac{\lambda^2}{2} & A\lambda^2 \\ A\lambda^3(1-\rho-i\eta) & -A\lambda^2 & 1 \end{pmatrix} + O(\lambda^4) \qquad (1.5)$$

With respect to the Wolfenstein parametrization, given in 1.5, the corrections to the diagonal elements and to V_{ts} are of order $O(\lambda^4)$, corrections to V_{cd} and V_{td} are of order $O(\lambda^5)$, while additional terms to V_{us} and V_{cb} only appear at the orders $O(\lambda^7)$ and $O(\lambda^8)$ and the expression for V_{ub} stay unchanged. The main corrections to the imaginary parts are $\Delta V_{cd} = -iA^2\lambda^5\eta$ and $\Delta V_{ts} = -iA\lambda^4\eta$.

Thanks to the use of the variables:

$$\bar{\rho} = \rho(1-\frac{\lambda^2}{2}) \ , \ \bar{\eta} = \eta(1-\frac{\lambda^2}{2})$$

the orders $O(\lambda^5)$ can be included in the expression of V_{td}

$$V_{td} = A\lambda^3(1-\bar{\rho}-i\bar{\eta})$$

and the CKM matrix can be expressed as, omitting $O(\lambda^6)$ terms:

$$V_{CKM} = \begin{pmatrix} 1-\frac{\lambda^2}{2}-\frac{\lambda^4}{8} & \lambda & A\lambda^3(\bar{\rho}-i\bar{\eta}) \\ -\lambda+\frac{A^2\lambda^5}{2}(1-2(\bar{\rho}+i\bar{\eta})) & 1-\frac{\lambda^2}{2}-\lambda^4(1/8+A^2/2) & A\lambda^2 \\ A\lambda^3(1-\bar{\rho}-i\bar{\eta}) & -A\lambda^2+\frac{1}{2}A\lambda^4+A\lambda^4(\bar{\rho}+i\bar{\eta}) & 1-\frac{A^2\lambda^4}{2} \end{pmatrix}$$

The unitarity of the V_{CKM} matrix,

$$V_{CKM}V^{\dagger}_{CKM} = V^{\dagger}_{CKM}V_{CKM} = \mathbf{1},$$

implies several relations between its elements:

$$\sum_{i=1}^{3} V_{ij}V^*_{ik} = \delta_{jk} \text{ and } \sum_{j=1}^{3} V_{ij}V^*_{kj} = \delta_{ik}.$$

The six independent relations can be represented as a triangle in the $(\bar{\rho},\bar{\eta})$ plane, where the ones obtained by product of neighboring rows or columns are nearly degenerate.

The areas of all these triangles are equal to half of the Jarlskog invariant J, which is a phase-convention-independent measure of CP violation, defined by:

$$Im\{V_{ij}V_{kl}V^*_{il}V^*_{kj}\} = J\sum_{m,n=1}^{3}\epsilon_{ikm}\epsilon_{jln}$$

where ϵ_{abc} is the antisymmetric tensor.

The presence of a non-zero CKM phase, and hence of CP violation, requires $J \neq 0$. The elements of the relations: $V^*_{ub}V_{ud}+V^*_{cb}V_{cd}+V^*_{tb}V_{td} = 0$, can be determined by B physics measurements. This triangle is particularly attractive from the experimental point of view, since it has all the sides of order λ^3. Dividing all the terms of the relation by $|V^*_{cb}V_{cd}|$, one obtains:

$$\frac{V^*_{ub}V_{ud}}{V^*_{cb}V_{cd}} + 1 + \frac{V^*_{tb}V_{td}}{V^*_{cb}V_{cd}} = 0$$

Figure 1.1: Unitarity Triangle, represented in the $(\bar{\rho}, \bar{\eta})$ plane.

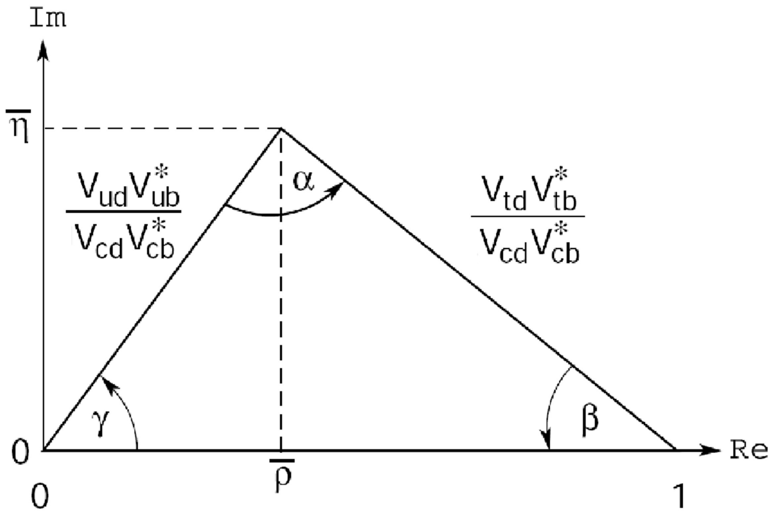

which is represented by the triangle in fig. 1.1. The imaginary coordinate of the apex is $\bar{\eta}$, the *CP* violating phase and, as already stated, the presence of *CP* violation, i.e. $\bar{\eta} \neq 0$, is described by a non-zero area of the triangle. The sides of the triangle can be expressed in terms of $\bar{\rho}$ and $\bar{\eta}$:

$$
\begin{aligned}
\frac{|V_{ub}^* V_{ud}|}{|V_{cb}^* V_{cd}|} &= \sqrt{\bar{\rho}^2 + \bar{\eta}^2} \\
\frac{|V_{tb}^* V_{td}|}{|V_{cb}^* V_{cd}|} &= \sqrt{(1-\bar{\rho})^2 + \bar{\eta}^2},
\end{aligned}
$$

and each angle is the relative phase between two adjacent sides:

$$
\begin{aligned}
\alpha &= \arg\left[\frac{V_{ub}^* V_{ud}}{V_{tb}^* V_{td}}\right] \\
\beta &= \arg\left[\frac{V_{tb}^* V_{td}}{V_{cb}^* V_{cd}}\right] \\
\gamma &= \arg\left[\frac{V_{ub}^* V_{ud}}{V_{cb}^* V_{cd}}\right].
\end{aligned}
$$

1.3 Exclusive Semileptonic B-Meson decay to charmed Mesons

Semileptonic B-meson decays to charmed mesons (figure 1.2) are useful processes used to measure the coupling of quarks to the W-boson: $|V_{cb}|$. These decays are interesting because the matrix element of a semileptonic decay can be written as the product of a leptonic current and a hadronic current. The leptonic current is well known, and the hadronic current, where all the non-perturbative QCD interactions are confined, can be parametrized in terms of Lorentz-invariant functions, form factors, expressed in terms of the square of the mass of the W-boson. One key variable used to describe this decay is: q^2, the squared momentum transfer, given the four-vectors momenta for the particles involved in the $B \to D\ell\nu$ decay, p_B, p_D, p_ℓ and p_ν, q^2 can be defined as

$$
q^2 \equiv (p_B - p_D)^2 \equiv (p_\ell + p_\nu)^2 \ , \tag{1.6}
$$

which is also equal to the squared mass of the virtual W^-. The momentum transfer q^2 is linearly related to another frequently-used variable, w, defined as the product of four-velocities

$$w \equiv v_B \cdot v_D = \frac{m_B^2 + m_D^2 - q^2}{2m_B m_D} \ . \tag{1.7}$$

This variable is particularly useful in HQET expressions for the form factors (see Section 1.3.2) due to the fact that it is more natural to work with velocities than momenta in HQET. This section will focus on the theoretical description of the $B \to D\ell\nu$ decay, where $\ell = e, \mu$, and the Caprini-Lellouch-Neubert model, which is used in this thesis to determine $|V_{cb}|$.

Figure 1.2: The Feynman diagram of a semileptonic $B \to D^{(*)}\ell\nu$ decay. The figure illustrates the complexity of the non-perturbative strong interaction through the great amount of gluon exchange.

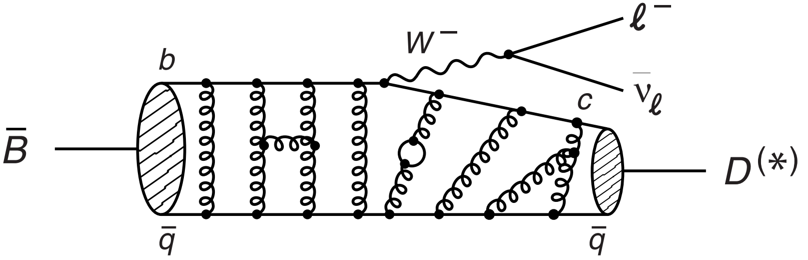

1.3.1 Matrix element

The matrix element for the semileptonic decay $M_{b\bar{q}} \to X_{c\bar{q}}\ell^-\overline{\nu}_\ell$ is the product of a hadronic and a leptonic current:

$$\begin{aligned}\mathcal{M}(M_{b\bar{q}} \to X_{c\bar{q}}\ell^-\overline{\nu}_\ell) = {} & \langle X_{c\bar{q}}|\bar{\mathbf{c}}\frac{-ig}{2\sqrt{2}}V_{cb}\gamma_\mu(1-\gamma_5)\mathbf{b}|M_{b\bar{q}}\rangle \\ & \times P^{\mu\nu}(q)\bar{u}_\ell\frac{-ig}{2\sqrt{2}}\gamma_\nu(1-\gamma_5)v_{\nu_\ell}\end{aligned} \tag{1.8}$$

where the operator $\mathbf{b}$ annihilates the quark b (or creates $\bar{b}$) and the W propagator is given by

$$P^{\mu\nu}(q) = \frac{i(-g^{\mu\nu} + q^\mu q^\nu/M_W^2)}{q^2 - M_W^2} \simeq i\frac{g^{\mu\nu}}{M_W^2}. \tag{1.9}$$

The last expression for the propagator is appropriate when the energies are much less than M_W. The phenomenological form for the matrix element is

$$\mathcal{M}(M_{b\bar{q}} \to X_{c\bar{q}}\ell^-\overline{\nu}_\ell) = -i\frac{G_F}{\sqrt{2}}V_{cb}L^\mu H_\mu, \tag{1.10}$$

where $G_F/\sqrt{2} = g^2/8M_W^2$. The leptonic current is exactly known

$$L^\mu = \bar{u}_\ell\gamma^\mu(1-\gamma_5)v_{\nu_\ell}, \tag{1.11}$$

and the hadronic current is given by

$$H_\mu = \langle X_{c\bar{q}}|\bar{\mathbf{c}}\gamma_\mu(1-\gamma_5)\mathbf{b}|M_{b\bar{q}}\rangle. \tag{1.12}$$

The hadronic current is reconstructed from the available four-vectors using the Lorentz invariance, which are momenta and spin-polarization vectors. The Lorentz vector or axial-vector quantities thus formed have Lorentz-invariant coefficients (form factors) that are functions of q^2. Classes of exclusive semileptonic decays considered are: $P \to P'\ell\nu$, where both P and P' are pseudoscalar mesons. In the case of a $P(b\overline{q}) \to P'(c\overline{q})\ell\nu$ decay, in parenthesis the quark contents of the mesons is described, there are only two independent four vectors, which could be $p+p'$ and $q = p-p'$. For these quantum numbers, the hadronic current H^μ has no contribution from the matrix element of the axial-vector current and can be written [17] as

$$\langle P'(p')|V^\mu|P(p)\rangle = f_+(q^2)(p+p')^\mu + f_-(q^2)(p-p')^\mu, \tag{1.13}$$

where $V^\mu = \overline{c}\gamma^\mu b$ and where $f_+(q^2)$ and $f_-(q^2)$ are the form factors describing the $P \to P'$ transition. For the cases $\ell = e$ and $\ell = \mu$, this expression for the hadronic current simplifies, because the terms proportional to q^μ are negligible. The reason is that, in the limit $m_\ell \to 0$, $q^\mu L_\mu = 0$, where L_μ is the lepton current. This means that the decays $B \to De^-\overline{\nu}_e$ and $B \to D\mu^-\overline{\nu}_\mu$ can be described by a single form factor:

$$\langle P'(p')|V^\mu|P(p)\rangle = f_+(q^2)(p+p')^\mu. \tag{1.14}$$

The differential decay rates for the processes $B \to D\ell^-\overline{\nu}_\ell$ can be calculated

$$\frac{d\Gamma}{dq^2} = \frac{G_F^2|V_{cb}|^2 p_{P'}^3}{24\pi^3}|f_+(q^2)|^2. \tag{1.15}$$

1.3.2 Form Factor Predictions

The decomposition of the hadronic currents in equation 1.13 is model-independent, and the differential decay rates in equation 1.15 follow immediately from this decomposition and the Dirac nature of the fermions. Within the Standard Model, the only unknown quantities are therefore $|V_{cb}|$ and the form factor; $|V_{cb}|$ sets the overall normalization, while the form factors describe the dynamics of the decay process. Because the form factors parameterize the hadronization of quarks into mesons, a non-perturbative QCD process, calculating them is a difficult problem which has been approached theoretically in a number of different ways. Calculations of the form factors typically break the problem into two pieces: calculation of the form factors at a fixed value of q^2, typically $q^2 = q^2_{\text{max}}$, and calculation of the q^2 dependence of the form factors. At $q^2 = q^2_{\text{max}}$, the hadronic system is least disturbed, which makes calculations at this point relatively easy. The variation of the form factors as functions of q^2 is typically assumed to have a very simple form. One older approach, used in the ISGW model [18], is to assume an exponential distribution for the form factors:

$$f_i(q^2) = Ce^{-a(q^2_{\text{max}} - q^2)}\ , \tag{1.16}$$

where C is a normalization constant and a is a parameter related to the meson size. Another approach, used in the WSB [19] and KS [20] models is the “nearest-pole dominance” model, in which the form factors are assumed to depend on q^2 like

$$f_i(q^2) = f_i(0) \cdot \left(\frac{m^2_{\text{pole}}}{m^2_{\text{pole}} - q^2}\right)^n\ , \tag{1.17}$$

where n is either 1 or 2, depending on the form factor involved, and m_{pole} is the mass of a $Q\overline{q}'$ meson with the quark content and quantum numbers determined by the underlying transition; for the $b \to c$ transition in $B \to D$, it would be the mass of the B_c meson, approximately 6.3 GeV/c^2.

Heavy Quark Effective Theory

The development of Heavy Quark Symmetry and Heavy Quark Effective Theory [17] (HQET) has led to improvements in the precision of form factor predictions. HQET is an effective field theory which allows us to calculate deviations from the heavy-quark limit as an expansion in powers of

$\Lambda_{\mathrm{QCD}}/m_b$ and $\Lambda_{\mathrm{QCD}}/m_c$, where Λ_{QCD} is an energy scale typical of QCD processes, and is of the order of 200 MeV. In the heavy-quark limit $m_b \to \infty$ and $m_c \to \infty$, the form factors are easy to calculate. The HQET parameterization of the form factors is written in terms of four-velocities ($w \equiv v \cdot v'$) rather than momenta ($q \equiv p - p'$). As before, the structure of the currents is completely determined by Lorentz invariance; in fact:

$$\langle P'(v')|V^{\mu}|P(v)\rangle = \sqrt{m_B m_D}\left[h_+(w)(v+v')^{\mu} + h_-(w)(v-v')^{\mu}\right] , \tag{1.18}$$

The HQET form factors h_+ and h_- are related to the traditional form factors (f_+ and f_-) by [21]:

$$\begin{aligned} Rf_+(q^2) &= h_+(w) - \Big(\frac{m_B - m_D}{m_B + m_D}\Big) h_-(w) & (1.19)\\ R^{-1}f_-(q^2) &= \Bigg[\Big(\frac{w+1}{2} - R^{-2}\Big)h_+(w) + \\ &\quad \Big(\frac{w-1}{2}\cdot\frac{m_B + m_D}{m_B - m_D}\Big)h_-(w)\Bigg]\frac{m_B^2 - m_D^2}{q^2} \ , & (1.20)\end{aligned}$$

with R given by

$$R = \frac{2\sqrt{m_B m_D}}{m_B + m_D}. \tag{1.21}$$

In the heavy-quark limit these form factors satisfy the following relations :

$$h_-(w) = 0 \tag{1.22}$$

and, at the zero-recoil point $w = 1$ ($q^2 = q^2_{\mathrm{max}}$),

$$h_+(1) = 1 \ . \tag{1.23}$$

This can easily be understood by considering the situation in the rest frame of the decaying B meson. The b quark is infinitely massive and so is at rest in this frame; it decays to an infinitely-massive c quark which, for $w = 1$, is also at rest in the B rest frame. The light degrees of freedom, the $\overline{q}$ and the gluons, see no change in the color field after the $b \to c$ transition, and their wavefunction remains undisturbed. In the heavy-quark limit, the w dependence of these form factors is identical, such that these four form factors are all equal

$$h_+(w) = \xi(w) \ , \tag{1.24}$$

where $\xi(w)$ is called the Isgur-Wise function [22, 23]. The Isgure-Wise function represents the elastic form factor of a heavy meson, at zero momentum transfer (zero-recoil: $v \cdot v' = 1$) it is normalized to one ($\xi(1) = 1$). A naïve interpretation of this normalization is the following: if the velocity remains unchanged the probability for an elastic transition is equal to one. When the b and c quark masses become finite, these form factors are no longer equal to $\xi(w)$ or to each other. The Isgur-Wise function is sometimes expanded as a Taylor series about the zero-recoil point; a linear form which has been used extensively is

$$\frac{\xi(w)}{\xi(1)} = 1 - \hat{\rho}^2(w-1) + \mathcal{O}[(w-1)^2] \ . \tag{1.25}$$

The differential decay rate is then:

$$\frac{d\Gamma}{dw} = \frac{G_F^2|V_{cb}|^2}{48\pi^3}\cdot(m_B + m_D)^2\cdot m_D^3\cdot(w^2-1)^{3/2}\cdot|\xi(w)|^2 \tag{1.26}$$

The Caprini, Lellouch and Neubert Form Factor Model

The CLN model gives the form factors [24] describing $B \to D^{(*)}$ transitions using dispersion relations. In this work the results of these calculations concerning only $B \to D\ell^-\overline{\nu}_\ell$ processes have been used to parametrize the form factor. This model of the form factors makes use of heavy-quark symmetry and HQET, and claims to describe the semileptonic form factors with an accuracy better than 2%. The CLN model introduces another variable related to q^2 and w: z, defined as

$$z \equiv \frac{\sqrt{w+1}-\sqrt{2}}{\sqrt{w+1}+\sqrt{2}} \; . \tag{1.27}$$

The authors of the CLN model express the form factors as functions of z rather than of w. Because the allowed range of z is much smaller than that of w (z varies from zero to ≈ 0.07 for $B \to D\ell^-\overline{\nu}_\ell$ decays, while w varies from 1 to ≈ 1.6), the Taylor-series expansion of the form factors is more efficient when performed as a function of z compared to w. For $B \to D\ell\nu$ decay the CLN model calculates one reference form factor, $h_+(z)$, as a Taylor series expansion in z, where the terms in the expansion take into account all heavy-quark-symmetry-breaking effects. The expansion has the form

$$\frac{h_+(w)}{h_+(1)} = 1 - 8\hat{\rho}_+^2 z + (51\hat{\rho}_+^2 - 10)z^2 - (252\hat{\rho}_+^2 - 84)z^3 + \cdots \; , \tag{1.28}$$

where $\hat{\rho}_+^2$ is an externally-determined slope parameter describing the form factor.

The CLN model with lepton mass

In the HQET and CLN model the lepton mass is neglected, this may lead to a bias in the determination of $|V_{cb}|$ of a few percent level in the muon case [25]. The re-introduction of the lepton-mass term in the partial branching ratio (eq. 1.26) is straight-forward.

$$\frac{d\Gamma(B \to D\ell\nu)}{dw} = \frac{G_F^2|V_{cb}|^2}{48\pi^3}\mathcal{K}(w)\mathcal{G}^2(w) \tag{1.29}$$

A lepton term is multiply to the phase space $\mathcal{K}(w)$:

$$f_{ps}^{lep} = \left(1 - \frac{m_l^2}{q^2}\right)^2 = \left(1 - \frac{1}{1+r^2-2rw}\frac{m_l^2}{m_B^2}\right)^2 \tag{1.30}$$

The form factor term $\mathcal{G}^2(w)$ will be changed in

$$\mathcal{G}^2(w) \propto |f_+(w)|^2 + \frac{m_\ell^2}{2q^2}\left(|f_+(w)|^2 + 3\frac{|(m_B^2 - m_D^2)f_+(w) + q^2 f_-(w)|^2}{4m_B^2 m_D^2(w^2-1)}\right) \tag{1.31}$$

given

$$Rf_+ = h_+ - \frac{1-r}{1+r}h_- \tag{1.32}$$

and

$$R^{-1}f_- = \left[\left(\frac{w+1}{2} - \frac{1}{R}\right)h_+ + \left(\frac{w-1}{2}\frac{1+r}{1-r}\right)h_-\right]\frac{m_B^2 - m_D^2}{q^2} \tag{1.33}$$

The heavy quark limit is still valid: $h_-(w) = 0$, and thus

$$\mathcal{G}^2(w) = (1+r)^2|h_+(w)|^2\left(1 + \mathcal{J}_D(w)\frac{m_\ell^2}{m_B^2}\right) \tag{1.34}$$

where

$$\mathcal{J}_D(w) = \left[1 + 3\left(\frac{1-r}{1+r}\right)^2\left(\frac{w+1}{w-1}\right)\right]\frac{1}{2(1+r^2-2wr)}. \tag{1.35}$$

2 The *BABAR* Experiment

BABAR is a high energy physics experiment located at the SLAC National Accelerator Laboratory, California (USA). The experiment consists of a high performance detector (*BABAR* [26]) built around the interaction region of a high luminosity e^+e^- asymmetric collider (PEP-II [27]), it was designed and built by a large international team of scientists and engineers in the 90s. It has been optimized for the systematic measurement of CP violation in the B meson system, but it has also a comprehensive physics program consisting in precision measurements of decays of heavy mesons and of the τ lepton, and search for rare processes. In this chapter the main features and the performances of PEP-II and the *BABAR* detector are described.

2.1 The PEP-II B-Factory

The PEP-II B-Factory is an asymmetric e^+e^- collider designed to operate at a center of mass energy of $E_{CM} = 10.58\,\text{GeV}$, corresponding to the mass of the $\Upsilon(4S)$ meson resonance. The $\Upsilon(4S)$ has a mass slightly above the $B\bar{B}$ threshold, and thus it decays almost exclusively into $B^0\bar{B}^0$ or B^+B^- pairs.

Electrons and positrons are accelerated from the 3.2 km long SLAC linac and accumulated into two 2.2 km long storage rings: the high-energy ring (HER), in which a 9.0 GeV electrons beam circulated and the low-energy ring (LER), in which a 3.1 GeV positrons beam circulated, the two beams collides head-on. The Lorentz boost of the $\Upsilon(4S)$ is $\beta\gamma = \frac{E_{e^-}-E_{e^+}}{E_{CM}} \sim 0.56$. An overview of the accelerator is shown in Figure 2.1.

Figure 2.1: Overview of the PEP-II 2 B-Factory.

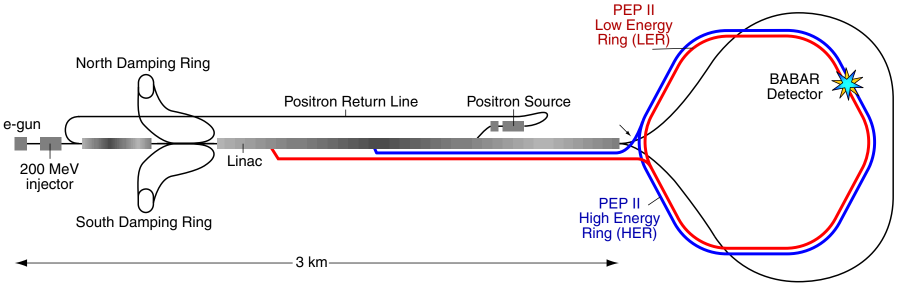

The cross sections of the main physics processes in PEP-II are listed in Tab. 2.1 [28]. At the peak of the $\Upsilon(4S)$ there is a non-negligible amount of continuum $e^+e^- \to q\bar{q}$ ($q = u, d, s, c$) and $e^+e^- \to \ell\ell$ ($\ell = e, \mu, \tau$) events. To study the background events due to these processes, part of the data was collected at a center of mass energy 40 MeV below the $\Upsilon(4S)$ peak, where $B\bar{B}$ production is not allowed. This data sample corresponds to about 1/10 of the sample taken at the $\Upsilon(4S)$ peak.

Table 2.1: Cross sections of the main physics processes at the $\Upsilon(4S)$. The cross section for e^+e^- is referred to the volume of the *BABAR* electromagnetic calorimeter, which is used to trigger these events.

Event	**Cross section (nb)**
$b\overline{b}$	1.05
$c\overline{c}$	1.30
$s\overline{s}$	0.35
$u\overline{u}$	1.39
$d\overline{d}$	0.35
e^+e^-	~53
$\mu^+\mu^-$	1.16
$\tau^+\tau^-$	0.94

2.1.1 PEP-II performances

The *BABAR* data taking, started with the first collisions in PEP-II at the end of 1999, and it has terminated in the first days of April 2008. *BABAR* has recorded an integrated luminosity[1] of about 531 fb^{-1}, including about 54 fb^{-1} of off-peak luminosity, 433 fb^{-1} recorded at the $\Upsilon(4S)$ and 44 fb^{-1} at other Υ resonances. The *BABAR* recorded luminosity until the end of data taking is shown in Figure 2.2.

Figure 2.2: PEP-II delivered and *BABAR* recorded integrated luminosity in Run 1 to Run 7 (from October 1999 to April 2008).

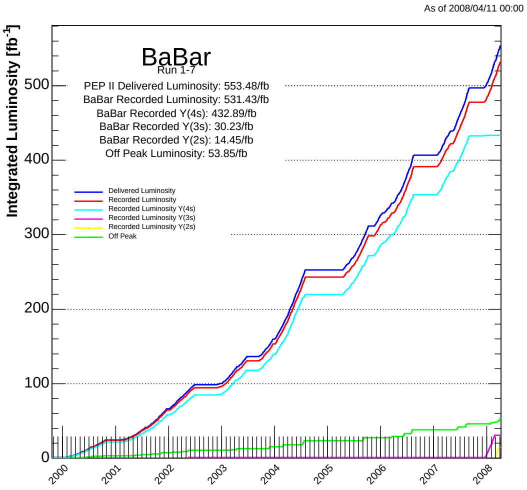

---

[1] The luminosity ($\mathcal{L}$) relates the expected event rate to the process cross-section (event rate $= \mathcal{L}\cdot\sigma$). The integrated (over time) luminosity: $L = \int \mathcal{L}dt$.

Table 2.2: PEP beam parameters. Values are given both for the design and for the records achieved during the last years.

Parameters	Design	Records
Energy HER/LER (GeV)	9.0/3.1	9.0/3.1
Current HER/LER (A)	0.75/2.15	2.1/3.2
# of bunches	1658	1722
Bunch length (mm)	15	11-12
Luminosity ($10^{33}\,\mathrm{cm}^{-2}\mathrm{s}^{-1}$)	3	12
Integrated luminosity (pb^{-1}/day)	135	911

2.2 Overview of the *BABAR* detector

Figure 2.3: *BABAR* detector front view on the left-hand side, side view on the right-hand

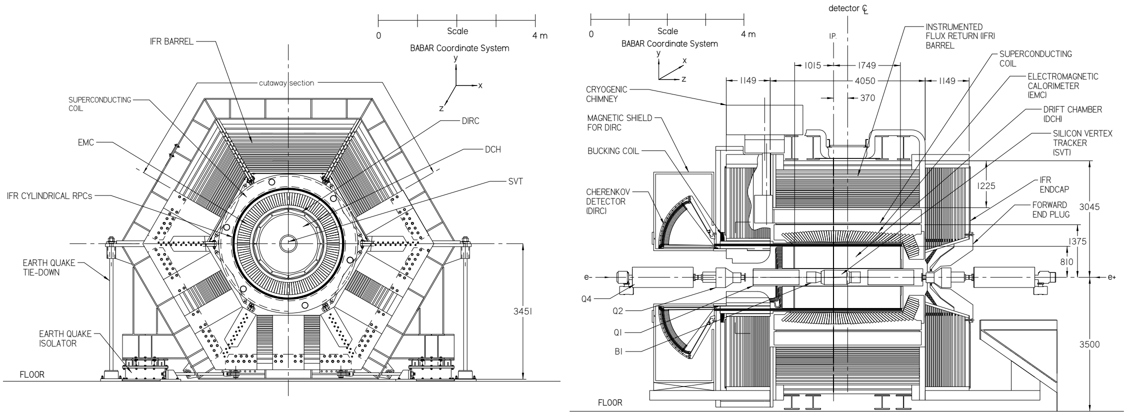

The design of the *BaBar* detector was optimized for *CP* violation studies, but it was also well suited for searches of rare B decays. To achieve the goal of performing accurate measurements many requirements are needed:

- a large and uniform acceptance, in particular down to small polar angles relative to the boost direction, to avoid particle losses;
- excellent detection efficiency for charged particles down to $60\,\mathrm{MeV}/c$ and for photons down to $25\,\mathrm{MeV}$;
- high momentum resolution to separate small signals from background;
- excellent energy and angular resolution for the detection of photons from π^0 and radiative B decays in the range from $25\,\mathrm{MeV}$ to $4\,\mathrm{GeV}$;
- very good vertex resolution, both transverse and parallel to the beam;
- identification of electrons and muons over a large range of momentum, primarily for the detection of semi-leptonic decays used to tag the B flavor and for the study of semi-leptonic and rare decays;
- identification of hadrons over a wide range of momentum for B flavor tagging as well as for the separation of pions from kaons in decay modes like $B^0 \to K^\pm\pi^\mp$ and $B^0 \to \pi^+\pi^-$ as well as in charm meson and τ decays;
- a highly efficient, selective trigger system with redundancy so as to avoid significant signal losses and systematic uncertainties.

The *BaBar* detector (Fig. 2.3), designed and fabricated by a collaboration of 600 physicists of 75 institutions from 9 countries, met all these requirements, as will be shown in the next sections of this chapter. The BABAR superconducting solenoid, which produces a 1.5 T axial magnetic field, contains a set of nested detectors, which are – going from inside to outside – a five layers Silicon Vertex Tracker (SVT), a central Drift Chamber (DCH) for charged particles detection and momentum measurement, a fused-silica Cherenkov radiation detector (DIRC) for particle identification, and a CsI(Tl) crystal electromagnetic calorimeter for detection of photons and electrons. The calorimeter has a barrel and an end-cap which extends it asymmetrically into the forward direction (e^- beam direction), where many of the collision products emerge. All the detectors located inside the magnet have full acceptance in azimuth (ϕ). The flux return outside the cryostat is composed of 18 layers of steel, which increase in thickness outwards, and are instrumented (IFR) with 19 layers of planar resistive plate chambers (RPCs) or limited streamer tubes (LSTs) in the barrel and 18 in the end-caps. The IFR allows the separation of muons and charged hadrons, and also detect penetrating neutral hadrons. As indicated in Fig.2.3, the right-handed coordinate system is anchored to the main tracking system, the drift chamber, with the z-axis coinciding with its principal axis. This axis is offset relative to the beam axis by about 20 mrad in the horizontal plane. The positive y-axis points upward and the positive x-axis points away from the center of the PEP-II storage rings.

2.2.1 The Silicon Vertex Tracker

The Silicon Vertex Tracker (SVT) provides a precise measurement of the decay vertices and of the charged particle trajectories near the interaction region. The SVT also provides stand alone tracking for particles with transverse momentum too low to reach the drift chamber, like soft pions from D^* decays and many charged particles produced in multi-body B meson decays. Finally, the SVT supplies particle identification (PID) information both for low and high momentum tracks. For low momentum tracks the SVT dE/dx measurement is the only PID information available, for high momentum tracks the SVT provides the best measurement of the track angles, required to achieve the design resolution on the Cherenkov angle measured by the DIRC. The design of the SVT adopted is a five-layer device with 340 double-sided silicon wafers mounted on a carbon-fiber frame (see fig. 2.4). On the inner (outer) face of each wafer, strip sensors are located running orthogonal (parallel) to the beam direction, measuring the z (ϕ) coordinate of the tracks. The wafers are organized in modules split into forward and backward sections: they are read out on their respective ends and the charge deposited by a particle is determined by the time over threshold of the signal on each strip. In total, 150,000 read-out channels are present. The spatial resolution of SVT hits is generally better than 40 μm in all layers for all track angles, allowing a precise determination of decay vertices to better than 70 μm.

Figure 2.4: Schematic view of the SVT longitudinal section.

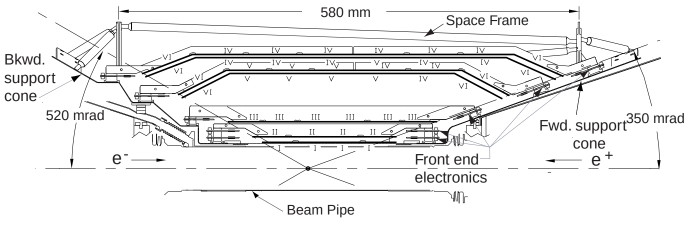

2.2.2 The Drift Chamber

The Drift Chamber (DCH) is the main tracking device for charged particles with transverse momenta p_T above $\sim 120\,\mathrm{MeV}/c$. The chamber is able to measure not only the transverse coordinate, but also the longitudinal (z) position of tracks with good resolution (about 1 mm). Good z resolution aids in matching DCH and SVT tracks, and in projecting tracks to the DIRC and the calorimeter. For low momentum particles the DCH provides particle identification by measurement of ionization loss (dE/dx), thus allowing for K/π separation up to $\approx 600\,\mathrm{MeV}/c$. This capability is complementary to that of the DIRC in the barrel region, while it is the only mean to discriminate between different particle hypotheses in the extreme backward and forward directions which fall outside of the geometric acceptance of the DIRC. Finally, the DCH provides real-time information used in the first level trigger system. The DCH is a 2.80 m long cylinder with an inner radius of 23.6 cm and an outer radius of 80.9 cm (Figure 2.5). Given the asymmetry of the beam energies, the DCH center is displaced by about 37 cm with respect to the interaction point in the forward direction. The active volume provides charged particle tracking over the polar angle range $-0.92 < \cos\theta < 0.96$. The drift system consists of 7104 hexagonal cells, approximately 1.8 cm wide by 1.2 cm high, arranged in 10 superlayers of 4 layers each, for a total of 40 concentric layers (Fig. 2.5). Each cell consists of one sense wire surrounded by six field wires. The sense wires are 20 μm Rh-W gold-plated wires operating nominally in the range 1900-1960 V, the field wires are 120 μm Al wires operating at 340 V. The layers are housed between a 1 mm beryllium inner wall and a 9 mm carbonfiber outer wall (corresponding to 0.28% and 1.5% radiation lengths, respectively) both to facilitate the matching between the SVT and DCH tracks and to minimize the amount of material in front of the DIRC and the calorimeter. The counting gas is a 80:20 mixture of helium: isobutane, which again satisfies the requirement of keeping the multiple scattering at minimum. Overall, the multiple scattering inside the DCH is limited by less than 0.2% radiation lengths of material. The p_T resolution is measured as a function of p_T in cosmic ray studies:

Figure 2.5: Schematic view of the DCH (longitudinal section on the left-hand side). On the right-hand side the schematic layout of the drift cells for the four innermost superlayers. The numbers on the top side give the stereo angles (mrad) of sense wires in each layer.

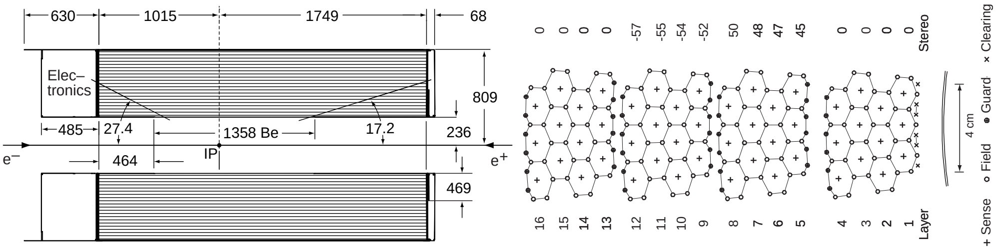

$$\frac{\sigma_{p_T}}{p_T} = (0.13 \pm 0.01)\% \cdot p_T + (0.45 \pm 0.03)\%, \tag{2.1}$$

where p_T is expressed in GeV/c. The first contribution, dominating at high p_T, comes from the curvature error due to finite spatial measurement resolution; the second contribution, dominating at low momenta, is due to multiple Coulomb scattering. The specific ionization loss dE/dx for charged particles traversing the drift chamber is derived from the total charge deposited in each drift cell. The resolution achieved to date is typically about 7.5%. A 3σ separation between kaons and pions can be achieved up to momenta of about 700 MeV/c [29].

2.2.3 The Cherenkov detector

The particle identification (PID) at low momenta exploits primarily the dE/dx measurements in the DCH and SVT. However, for momenta above the threshold of 700 MeV/c, the dE/dx information does not allow to separate pions and kaons. The Detector of Internally Reflected Cherenkov radiation (DIRC) (see fig. 2.6) is employed primarily for the separation of pions and kaons from about 500 MeV/c to the kinematic limit of 4 GeV/c. The principle of the DIRC is based on the detection of Cherenkov light generated by a charged particle in a medium of refractive index n, when its velocity v is greater than c/n. The photons are emitted on a cone of half-angle θ_c with respect to the particle direction, where $cos\theta_c = 1/\beta n$, with $\beta = v/c$. Knowing the particle momentum from the SVT and the DCH, the measurement of θ_c allows the mass determination. The radiator material of the DIRC is synthetic fused silica (refraction index $n = 1.473$) in the form of 144 long, thin bars with regular rectangular cross section. The bars, which are 17 mm thick, 35 mm wide and 4.9 m long, are arranged in a 12-sided polygonal barrel, each side being composed of 12 adjacent bars placed into sealed containers called bar boxes. Dry nitrogen gas flows through each bar box, and humidity levels are measured to monitor that the bar box to water interface remains sealed. The solid angle subtended by the radiator bars corresponds to 94% of the azimuth and 83% of the cosine of the polar angle in the center-of-mass system. The bars serve both as radiators and as light pipes for the portion of the light trapped in the radiator by total internal reflection. Once photons arrive at the instrumented end, most of them emerge into an expansion region filled with 6000 liters of purified water ($n = 1.346$), called the stand-off box (see Figure 2.6). A fused silica wedge at the exit of the bar reflects photons at large angles and thereby reduces the size of the required detection surface. The photons are detected by an array of densely packed photo-multiplier tubes (PMTs), each surrounded by reflecting "light catcher" cones to capture light which would otherwise miss the PMT active area. The PMTs, arranged in 12 sectors of 896 phototubes each, have a diameter of 29 mm and are placed at a distance of about 1.2 m from the bar end. The expected Cherenkov light pattern at this surface is essentially a conic section, whose cone opening-angle is the Cherenkov production angle modified by refraction at the exit from the fused silica window. The pion-kaon separation power is defined as the difference of the mean Cherenkov angles for pions and kaons assuming a Gaussian-like distribution, divided by the measured track Cherenkov angle resolution. The separation between kaons and pions at 3 GeV/c is about 4.3 σ.

Figure 2.6: Schematic view of the DIRC.

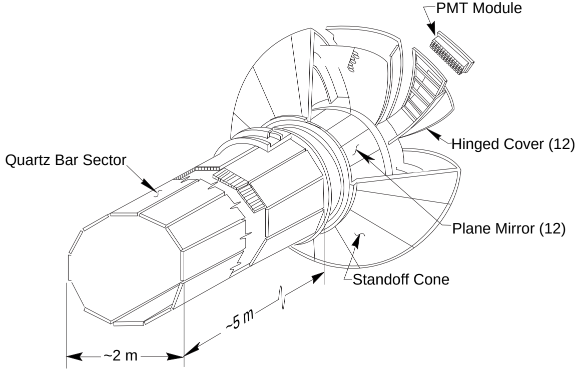

2.2.4 The Electromagnetic Calorimeter

The *BaBar* electromagnetic calorimeter (EMC) is designed to detect and measure electromagnetic showers with high efficiency and very good energy and angular resolution over a wide energy range between 20 MeV and 9 GeV. This allows the reconstruction of $\pi^0 \to \gamma\gamma$ and $\eta \to \gamma\gamma$ decays where the photons can have very low energy, as well as the reconstruction of Bhabha events and processes like $e^+e^- \to \gamma\gamma$, important for luminosity monitoring and calibration, where the electron and photon energies can be as large as 9 GeV. The EMC also provides the primary information for electron identification and electron-hadron separation. Energy deposit clusters in the EMC with lateral shape consistent with the expected pattern from an electromagnetic shower are identified as photons when they are not associated to any charged tracks extrapolated from the SVT and the drift chamber, and as electrons if they are matched to a charged track and if the ratio between the energy E measured in the EMC and the momentum p measured by the tracking system is $E/p \approx 1$. The EMC contains 6580 CsI crystals doped with Tl (Figure 2.7). CsI(Tl) has a high light yield (50,000 photons/ MeV) and a small Molière radius (3.8 cm), which provide the required energy and angular resolution; its radiation length of 1.86 cm guarantees complete shower containment at the *BABAR* energies. The crystals are read out by two independent 1 cm^2 PIN photodiodes, glued to their rear faces, which are connected to low-noise preamplifiers that shape the signal with a short shaping time (400 ns) to reduce low energetic beam-related photons backgrounds. The efficiency of the EMC exceeds 96% for the detection of photons with energy above 20 MeV. The energy resolution is usually parameterized by

Figure 2.7: Longitudinal section of the top half of the EMC. Dimensions are in mm.

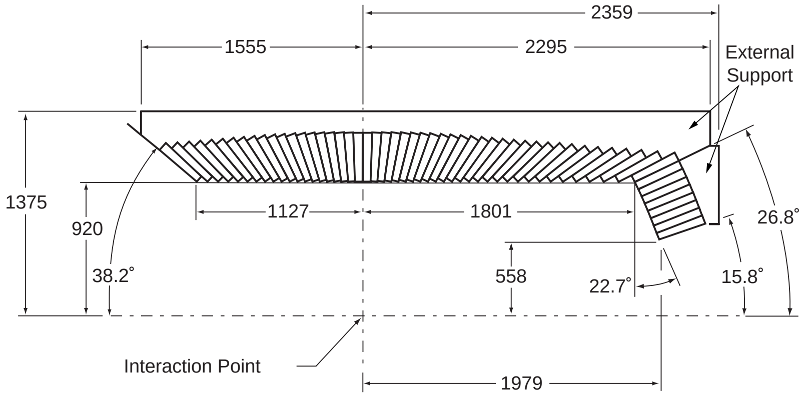

$$\frac{\sigma_E}{E} = \frac{\sigma_1}{E^{1/4}(\text{GeV})} \oplus \sigma_2, \tag{2.2}$$

where $\sigma_1 = 2.32 \pm 0.30\%$ and $\sigma_2 = 1.85 \pm 0.12\%$, as determined using the above mentioned sources. The first term in Eq. 2.2 arises from fluctuations in photon statistics and is dominant for energies below about 2.5 GeV, while the constant term takes into account several effects, such as fluctuations in shower containment, non-uniformities, calibration uncertainties and electronic noise.

2.2.5 The Instrumented Flux Return

The Instrumented Flux Return (IFR) is designed to identify muons and neutral hadrons (primarily K_L and neutrons). The principal requirements for IFR are large solid angle coverage, good efficiency and high background rejection for muons down to momenta below 1 GeV/c. For neutral hadrons, high efficiency and good angular resolution are most important. The IFR uses the steel flux return of the magnet as muon filter and hadron absorber, limiting pion contamination in the muon identification. Originally single gap resistive plate chambers (RPC) with two-coordinate readout, operated in limited streamer mode constituted the active part of the detector [30], with 19 layers in the barrel and 18 in each endcap. The RPC were installed in the gaps of the finely segmented steel of the six barrel sectors and the two end-doors of the flux return, as illustrated in Fig. 2.8. In addition, two layers of cylindrical RPCs were installed between the EMC and the magnet cryostat to detect particles exiting the EMC. RPCs contain a 2 mm Bakelite gap with $\sim$ 8 kV across it. Ionizing particles which cross the gap create streamers of ions and electrons in the gas mixture (Argon, freon and isobutane), which in turn creates signals via capacitive coupling on the strips mounted on each side of the RPC. Unfortunately the efficiency of a significant fraction of the chambers (initially greater then 90%) has started to deteriorate at a rate of 0.5-1%/month. In order to solve some of the inefficiency problems, an extensive improvement program has been developed. The forward endcap was retrofitted with new improved RPCs in 2002, their efficiency has not significantly decreased since then. In the barrel, the RPCs have been replaced in 2004 and 2006 by 12 layers of limited streamer tube (LST) detectors and 6 layers of brass have been added to improve hadron absorption. The tubes have performed well since their installation with an efficiency of all layers at the geometrically expected level of 90%.

Figure 2.8: Overview of the IFR Barrel sectors and forward and backward end-doors; the shape of the RPC modules and the way they are stratified is shown.

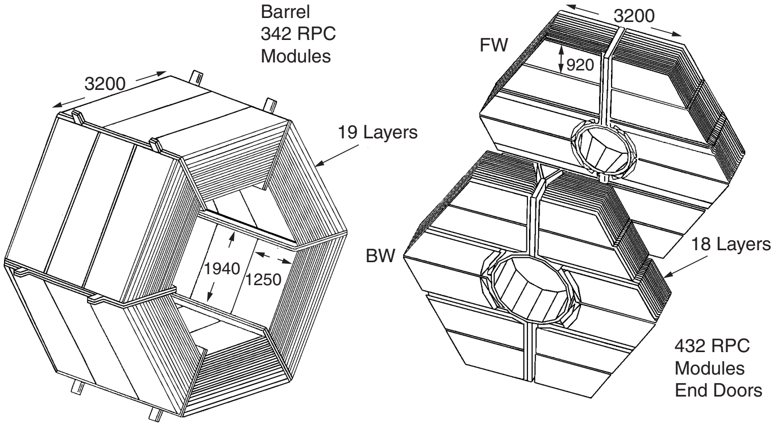

2.2.6 Trigger

The *BABAR* trigger is designed to select a large variety of physics processes (efficiency greater than 99% for $B\bar{B}$ events) while keeping the output rate below 400 Hz to satisfy computing limitations of the offline processing farms (beam induced background rates with at least one track with $p_t >$ 120 MeV/c or at least one EMC cluster with $E >$ 100 MeV are typically 20 kHz). The trigger accepts also 95 % of continuum hadronic events and more than 90 % of $\tau^+\tau^-$ events. It is implemented as a two level hierarchy, the hardware Level 1 (L1) followed by the software Level 3 (L3). The L1 trigger has an output rate of the order of 1 kHz to 3 kHz, depending on the luminosity and background conditions. It is based on charged tracks in the DCH above a preset transverse momentum, showers in the EMC, and track detected in the IFR. L3 operates by refining and augmenting the selection methods used in L1. Based on both the complete event and L1 trigger information, the L3 software algorithm selects events of interest allowing them to be transferred to mass storage data for further analysis. It uses an algorithm based on the drift chamber tracking, which rejects beam-induced charged particle background produced in the material close to the IP, and a second algorithm based on the calorimeter clustering.

3 Analysis Strategy

The present analysis reconstructs the $B \to D\ell\nu$ decay to determine its partial branching ratio, the element of the CKM matrix $|V_{cb}|$ and the form factor parameter ρ^2. All participating particles are identified and measured or computed, i.e. the B-Meson is reconstructed in the decay chain, as $B^- \to D^0\ell^-\bar{\nu}$ or $B^0 \to D^-\ell^+\nu$ [1]. From its decay products, which entails observing the lepton (electron or muon) and all decay products of the D-Meson, the presence of the neutrino is inferred from the missing momentum and energy in the whole event. The D-Meson is reconstructed as $D^0 \to K^-\pi^+$ or $D^+ \to K^-\pi^+\pi^+$ only. In this work an "untagged" analysis is performed, where the second B in the event is not fully reconstructed. This has the benefits of enhancing the signal efficiency and lowering the statistical uncertainties in comparison to a tagged analysis, where the other B is completely reconstructed through its decay products. Criteria to select signal events and to suppress backgrounds are applied to ensure an efficient selection, as described in detail in chapter 5. Selected events are divided in ten equally spaced bins of w ($w \equiv v_B \cdot v_D$) in its physical range $1.0 \leq w < 1.6$. In each of these bins a $2D$ distribution, as described in the chapter 6, the Monte Carlo simulation is fitted to the data for the signal yields with an extended binned Maximum Likelihood. The outcoming $B \to D\ell\nu$ yields are, then, fitted to the CLN model using a χ^2 function for extraction of $\mathcal{G}(1)|V_{cb}|$ and ρ^2 in chapter 7.

3.1 Signal and Background Sources

Events are grouped according to the following scheme:

- Events with a correctly reconstructed D candidate
  - Events originating from $\Upsilon(4S) \to B\bar{B}$ decays:
    - Signal: $B \to D\ell\nu$ decays.
    - $B \to D^*\ell\nu$ Background: $B \to D^*\ell\nu$ (both D^{*0} and D^{*+}) decays, where the slow bachelor in the decay chain $D^* \to D\pi_{soft}$ or $D^* \to D\gamma_{soft}$ is missed.
    - Peaking Background: $B \to D^{**}\ell\nu$ [2]; $B \to D^{(*)}X\ell\nu$; $B \to D_sD$, $D_s \to X\ell\nu$; $B \to D\tau\nu$, $\tau \to \ell\nu_\ell\nu_\tau$; all $B \to DX$ not belonging to signal or D^*-background event and $c\bar{c} \to DX$. Events with a well reconstructed D meson that mimic the signal in the m_D distribution.
- Combinatoric Background: background stemming from mis-reconstructed D-mesons due to random combinations of kaons and pions.

---

[1] Charge conjugation is always implied in the document if not otherwise stated.

[2] D^{**} means narrow and broad resonances namely D_1^* , D_2^* and D_0^*, $D_1^{*\prime}$

4 Data and Monte Carlo Samples

4.1 Data Samples

This analysis is based on data collected between the years 1999 and 2006 (Run-1 to Run-5) with the BABAR detector. The amount of *On-Peak* data, recorded at the energy of the $\Upsilon(4S)$ resonance, corresponds to a total integrated luminosity of $347.5\,fb^{-1}$, or $(383.6 \pm 4.2) \times 10^6$ [31] events where $\Upsilon(4S) \rightarrow B\overline{B}$. Moreover the analysis uses $36.6\,fb^{-1}$ recorded 40 MeV below the $\Upsilon(4S)$ resonance, *Off-Peak* data. Table 4.1 summarizes the data available splitted according to the different run-cycles.

Table 4.1: Integrated luminosity of data samples for each run-cycle

Run-Cycle		pb^{-1}	$N_{B\overline{B}}(\times 10^5)$
Run 1	On-Peak	20433	224 ± 2
	Off-Peak	2615	–
Run 2	On-Peak	61145	673 ± 7
	Off-Peak	6922	–
Run 3	On-Peak	32312	357 ± 4
	Off-Peak	2468	–
Run 4	On-Peak	100314	1107 ± 12
	Off-Peak	10121	–
Run 5	On-Peak	133265	1475 ± 16
	Off-Peak	14468	–

4.2 Monte Carlo Samples

A Monte Carlo (MC) simulation is used to study signal and background behavior, to determine efficiencies and to optimize analysis procedures. The BABAR simulation production uses a database tuned on the most recent measurements of B-decays, and most up-to-date models to represent the decay-kinematics, `EvtGen` [32] for the simulation of the B meson decays, whereas non $B\bar{B}$ events are generated by `Jetset7.4` [33]. A full model of the BABAR detector is realized using the `GEANT4` toolkit [34], which simulates the passage of particles through matter. The `PHOTOS` [35] Monte Carlo algorithm is also used to implement Final State Radiation (FSR) including QED interference and multiple-photon radiation. Besides randomly triggered background events recorded during the data taking, such as events stemming from sub-detectors noise or beam background, have been mixed to MC events to make the simulation of the underlying background processes as realistic as possible.

Various Monte Carlo samples are used in this analysis (MC available is summarize on table 4.2):

- The *generic $B\bar{B}$ MC* is a dataset of simulated MC events where the decay $\Upsilon(4S) \rightarrow B\bar{B}$ is simulated letting both B-mesons decay into most known final states measured so far [36]. The full detector response is simulated and reconstructed variables are available. This sample is generated at approximately three times the luminosity of the data. $B\overline{B}$ events are simulated to study the expected background shapes.

- The *continuum $q\bar{q}$ MC* is a dataset of simulated MC events where the process $\Upsilon(4S) \to q\bar{q}$ ($q = c, u, d, s$) is simulated without any constraint on the final states. The quark level QED *uds* processes are generated at approximately the same luminosity as the data. The $c\bar{c}$ events are generated at two times the luminosity expected in the data. Continuum events are simulated to study random combinatoric backgrounds.
- The *signal MC* is a particular dataset, where one B-meson decays generically (as in generic $B\overline{B}$ MC), the other is forced to decay in the signal mode $B \to D\ell\nu$. This sample is used to study reconstruction efficiencies and expected signal shapes.
- The pure *generator level signal MC*, it is a set of simulated events produced without including the response of the detector, the simulation is performed only for signal decay processes using `EvtGen`. It is used to verify and optimize a few analysis procedures, such as to test the fit method used to extract $|V_{cb}|$, and to estimate the systematic uncertainty stemming from the simulation of QED interference and multiple-photon radiation.

Table 4.2: Overview of the number of Events and the equivalent luminosity for Monte Carlo samples used

	Modes	Events$\times10^6$	fb^{-1}
Run 1	Generic $B^0\bar{B}^0$	69.2	65.8
	Generic B^+B^-	69.6	66.2
	Generic $c\bar{c}$	55.7	42.6
	Generic *uds*	46.5	22.3
Run 2	Generic $B^0\bar{B}^0$	104.5	98.4
	Generic B^+B^-	102.9	97.9
	Generic $c\bar{c}$	169.0	129.2
	Generic *uds*	130.8	62.6
Run 3	Generic $B^0\bar{B}^0$	50.6	48.1
	Generic B^+B^-	47.1	44.8
	Generic $c\bar{c}$	73.5	56.2
	Generic *uds*	66.9	32.0
Run 4	Generic $B^0\bar{B}^0$	167.1	158.9
	Generic B^+B^-	167.3	159.1
	Generic $c\bar{c}$	204.1	156.0
	Generic *uds*	213.4	102.1
Run 5	Generic $B^0\bar{B}^0$	162.4	154.5
	Generic B^+B^-	168.8	160.5
	Generic $c\bar{c}$	276.2	211.2
	Generic *uds*	314.2	150.4
Signal MC	$B^0 \to D^-e^+\nu_e$	0.1	
	$B^0 \to D^-\mu^+\nu_\mu$	0.1	
	$B^+ \to \bar{D}^0e^+\nu_e$	0.1	
	$B^+ \to \bar{D}^0\mu^+\nu_e$	0.1	

4.2.1 Monte Carlo Tuning

Further in this analysis corrections are applied to the BABAR Monte Carlo simulation. These correction factors are implemented to tune the simulation to data, making the MC more suitable for the description of the data. The corrections are designed for both physical processes ($B \to D^{(*)}\ell\nu$ modeling, etc.) and detector efficiency (K^0_L production).

- K^0_L energy, efficiency and production rate corrections. K^0_L efficiency and energy deposition in the EMC need to be tuned in MC to match data. The method to correct for this mismatch is explained in reference [37]. The energy of positively identified K^0_L in the MC is multiplied by given scaling factors, which vary between 1.014 and 1.223. The efficiency is corrected by randomly removing positively identified K^0_L according to a probability between 2% and 25% in order to match the actual efficiency. Both corrections are function of K^0_L kinematic properties: momentum and polar angle in the detector reference frame. A correction due to the differences between the data and the simulation for the K^0_L *production rate* is also applied, based on studies detailed in [38]. Given that such a correction can not be accomplished by rejecting K^0_L, a different approach has been employed. K^0_L positively identified are randomly transformed into "pseudo-photons" and in this way the energy and momentum balance in the event is restored. This is achieved by rescaling the measured energy and momentum of the K^0_L cluster to the true K^0_L momentum, assuming zero mass. The probability of the correction depends on the K^0_L momentum: 22% for momenta between 0 and 0.4 GeV/c, 1% for momenta between 0.4 and 1.4 GeV/c, 9% for momenta larger than 1.4 GeV/c.
- $D^{(*,**)}\ell\nu$ form factor re-weighting: the decay channels $B \to D^{(*,**)}\ell\nu$ are simulated using not up-to-date parametrizations and models. The event distributions are re-weighted according to the calculations by Caprini, Lellouch and Neubert [24] for $B \to D^{(*)}\ell\nu$ events, and according to the model by Leibovich-Ligeti-Stewart-Wise (LLSW) [39] based on the HQET for $B \to D^{**}\ell\nu$ events using the package described in [40]. The input parametes, as taken from the latest measurements [41] and [4], are reported in table 4.3.
- $D^{(*)}X\ell\nu$ and D $\mathcal{BR}$ Re-weighting [42]: the not up-to-date $\mathcal{BR}$, used to produce the MC, are scaled to their measured values, shown in table 4.4.

Table 4.3: Input parameters used to rescale the MC events according to up-to-date FF model.

Input parameters FF re-weighting	
$B \to D\ell\nu$	$\hat{\rho}^2 = 1.17$
$B \to D^*\ell\nu$	$R_1 = 1.429, R_2 = 0.827, \rho^2 = 1.191$
$B \to D^{**}\ell\nu$	approximation $B1$, FF slope $\hat{\tau}' = -1.5$.

Table 4.4: The $\mathcal{BR}$ of semileptonic B decays as used in the Simulation Production and the up-to-date central values with their uncertainties. NR means "Non Resonant". The last two rows show MC and up-to-date values for the $\mathcal{BR}$ of D-meson decays used in this work.

	MC ($B^{\pm}$)%	Value used ($B^{\pm}$)%	MC (B^0)%	Value used (B^0)%
$B \to D\ell\nu$	2.24	2.32 ± 0.08	2.07	2.17 ± 0.09
$B \to D^*\ell\nu$	6.17	5.48 ± 0.27	5.7	5.11 ± 0.19
$B \to D_1^*\ell\nu$	0.56	0.77 ± 0.15	0.52	0.69 ± 0.14
$B \to D_2^*\ell\nu$	0.3	0.59 ± 0.12	0.23	0.56 ± 0.11
$B \to D_0^*\ell\nu$	0.49	0.88 ± 0.22	0.45	0.81 ± 0.24
$B \to D_1'\ell\nu$	0.9	0.82 ± 0.25	0.83	0.76 ± 0.22
$B \to$ NR $D^{*+}\pi^-\ell\nu$	0.06	0.00 ± 0.3	-	-
$B \to$ NR $D^{*0}\pi^0\ell\nu$	0.03	0.00 ± 0.3	-	-
$B \to$ NR $D^+\pi^-\ell\nu$	0.19	0.00 ± 0.3	-	-
$B \to$ NR $D^0\pi^0\ell\nu$	0.10	0.00 ± 0.3	-	-
$B \to$ NR $D^{*+}\pi^0\ell\nu$	-	-	0.03	0.00 ± 0.3
$B \to$ NR $D^{*0}\pi^+\ell\nu$	-	-	0.07	0.00 ± 0.3
$B \to$ NR $D^+\pi^0\ell\nu$	-	-	0.10	0.00 ± 0.3
$B \to$ NR $D^0\pi^+\ell\nu$	-	-	0.20	0.00 ± 0.3
$\mathcal{BR}(B \to X_c\ell\nu)$	11.04	10.89 ± 0.16	10.2	10.15 ± 0.16
	MC ($D^{\pm}$)%	Value used ($D^{\pm}$)%	MC (D^0)%	Value used (D^0)%
$\mathcal{BR}(D^0 \to K\pi)$	-	-	3.83	3.91 ± 0.05
$\mathcal{BR}(D^{\pm} \to K\pi\pi)$	9.20	9.29 ± 0.25	-	-

5 Event Reconstruction and Selection

The following chapter introduces briefly the standard BABAR particle reconstruction, identification methods, and the preselection criteria. Finally the reconstruction and the suitable criteria used to select $B \to D\ell\nu$ candidates, as specifically developed in the framework of this analysis, will be described.

5.1 Charged Tracks and Neutral Clusters

All relevant particles of the analysis are reconstructed from charged tracks and calorimetric clusters representing the information provided by the BABAR detector.

5.1.1 Charged Particle Reconstruction

The charged particle tracks are reconstructed by processing the information from both tracking systems, the SVT and the DCH. Charged tracks are defined by five parameters ($d_0, z_0, \phi_0, \omega, \tan\lambda$) and their associated error matrix, measured at the point of closest approach (POCA) to the primary vertex:

- d_0 is the distance between the POCA and the origin of the coordinate system in the x-y plane;
- z_0 is the distance of the POCA along the z-axis;
- ϕ_0 is the azimuth of the POCA;
- ω is the curvature of the track, $\omega_t \propto 1/p_t$;
- λ is the dip angle of the track with respect to the transverse (xy) plane. It is complementary to the cylindrical polar angle θ: $\theta = \frac{\pi}{2} - \lambda$.

Variables d_0 and ω are signed and their sign is chosen to be equal to the charge of the track. The track finding and the fitting procedures use the *Kalman filter algorithm* [43] that selects tracks by performing helix fits to the hits found and takes into account the interaction of the particle with the material in the detector, and the full magnetic field map. For what this analysis is concerned, charged tracks fulfilling the BABAR *Good Tracks Very Loose* (GTVL) criteria are employed, described in the app. C.1.

5.1.2 Charged particles for the Neutrino Reconstruction

Specific restrictions [44] are applied to ensure high quality and efficiency of the track reconstruction, for the neutrino reconstruction:

- the candidate charged particle has to fulfill the *Charged Track* (CT) selection criteria described in the app. C.1.

- *Minimum transverse momentum* ($p_t > 60\,\mathrm{MeV}/c$): a minimum for the component of the momentum vector transverse to the beam-axis is required for a reliable track measurement.
- *Maximum transverse momentum for SVT-only tracks* ($p_t < 0.2\,\mathrm{GeV}/c$): this restriction is applied to the tracks, which have been measured only in the SVT, i.e., with no DCH hits. This requirement is applied to keep low momentum tracks, for instance tracks that may arise in the $D^* \to D^0\pi$ decay, which, due to magnetic bending, do not reach the DCH.
- *Polar angle acceptance*: the polar angle, in the laboratory frame, is required to be $(0.41 < \theta_{lab} < 2.54)$ *rad* in order to match the acceptance of the detector. This ensures a well-understood tracking efficiency, minimizing systematic uncertainty.
- *loopers rejection*: tracks with a transverse momentum $p_t < 0.36\,\mathrm{GeV}/c$ don't reach the EMC and therefore spiral inside the DCH ("loopers"). The tracking algorithms of BABAR usually reconstruct a looped track as a number of smaller segments, each one describing one half-turn of the helix. Therefore dedicated cuts (see table 5.1) have been developed to reject track fragments compatible with originating from loopers based on their distance from the beam spot. Looper candidates are identified as two tracks with a small difference in p_t, ϕ and θ. Only the track fragment with the smallest distance $|z_0|$ to the beam interaction point is retained. These cuts remove roughly 13% of all low-momentum tracks in the central part of the detector. On average, the mean observed charged multiplicity per B meson is reduced by less than 1%.

Table 5.1: When multiple turns of a loop are reconstructed, half of the turns will be reconstructed as positively-charged tracks with a polar coordinate θ_0, and half as negatively-charged tracks at $\theta_0 \pm \pi$. Because of this, pair of loopers are categorized as either "same-sign" or "opposite-sign" and they are treated separately. The pairs of tracks satisfying this criteria are added to the loopers set. The two tracks are labeled as 1 and 2. $\Delta\phi_{\mathrm{lab}}$ and $\Delta\theta_{\mathrm{lab}}$ are the difference polar angles (θ, ϕ) in the laboratory frame between track 1 and 2.

Loopers selection criteria	
$p^1_{t,\mathrm{lab}}, p^2_{t,\mathrm{lab}}$	$< 250\,\mathrm{MeV}/c$
$\cos\theta^i_{\mathrm{lab}}$	< 0.2
$\lvert p^2_{t,\mathrm{lab}} - p^1_{t,\mathrm{lab}}\rvert \equiv \lvert\Delta p_{t,\mathrm{lab}}\rvert$	$< 120\,\mathrm{MeV}/c$
$\Delta\phi_{\mathrm{lab,same-sign}}$	< 0.1
$\lvert\pi - \Delta\phi_{\mathrm{lab,opposite-sign}}\rvert$	< 0.1
$\lvert\Delta\theta_{\mathrm{lab}}\rvert_{\mathrm{same-sign}}$	< 0.1
$\lvert\pi - \Delta\theta_{\mathrm{lab}}\rvert_{\mathrm{opposite-sign}}$	< 0.1

- *ghost tracks rejection*: If the tracking algorithm reconstructs two tracks very closely aligned to each other from a single physical particle we call one of them a "ghosts" track(see table 5.2). These cases arise when the tracking algorithms splits the DCH hits belonging to a single physical particle track into two track fragments. If two tracks are very close in phase space only the track with the largest number of DCH hits is retained. This ensures that the fragment with the better momentum measurement is kept in the analysis.

5.1.3 Neutral particles reconstruction

Neutral particles (photons and neutral hadrons) are detected in the EMC and IFR by examining the deposited energy by means of electromagnetic and hadronic showers. Energy deposits in adjacent calorimeter crystals are combined to clusters. They are required not to be matched to any charged track extrapolated from the tracking volume to the inner surface of the EMC. Particles that are close together, e. g., photons from high-energetic π^0 mesons, may deposit their energy in contiguous crystals and produce one single cluster with two local maxima. These maxima are

Table 5.2: The pairs of tracks satisfying this criteria are added to the ghost-track set. The two tracks are labeled as 1 and 2. The track labeled as 1 has the greater number of DCH-hits. $|\Delta p_{t,\mathrm{lab}}|$, $\Delta\phi_{\mathrm{lab}}$ and $\Delta\theta_{\mathrm{lab}}$ are the difference transverse momentum (p_t), and polar angles (θ,ϕ) in the laboratory frame between track 1 and 2.

Ghosts selection criteria	
$p^1_{t,\mathrm{lab}}$, $p^2_{t,\mathrm{lab}}$	$< 350\,\mathrm{MeV}/c$
$\lvert\Delta p_{t,\mathrm{lab}}\rvert$	$< 150\,\mathrm{MeV}/c$
$\Delta\phi_{\mathrm{lab}}$	< 0.1
$\Delta\theta_{\mathrm{lab}}$	< 0.1
N^1_{DCH}	$< 45 - N^2_{\mathrm{DCH}}$

used to split the cluster into two bumps. Each bump corresponds to one particle. These clusters and bumps originate mostly from photons, thus momenta and angles are assigned to be consistent with photons originating from the interaction region. The requested requirement is to have photon candidate fulfilling the *BABAR* *Calor Neutral* selection criteria described in the app.C.2.

5.1.4 Neutral particles for the neutrino reconstruction

Specific restrictions [44] are employed to ensure a cluster reconstruction with high quality and efficiency to aid the reconstruction of the neutrino via missing energy. The requirements for photon candidates are:

- the photon candidate must fulfill the *Calor Neutral* selection criteria.
- *Energy*: $E_\gamma > 50\,\mathrm{MeV}$ in order to reduce the impact of the sizable beam-related background of low energy photons.
- *Cluster shape*: Some additional backgrounds, due to hadronic interactions, either by K^0_L or neutrons, can be reduced by applying requests on the shape of the calorimeter clusters. The lateral distribution of energy within a cluster depends on the incident particle: particles interacting electromagnetically deposit most of their energy in two to three crystals, however hadronic showers are less concentrated and exhibit larger energy deposits at larger distances from the bump center. A quantitative measure for the shower width is the lateral moment (LAT) defined as described in the app.C.2.

  $$LAT = \frac{\sum\limits_{i=3}^{N} E_i r_i^2}{\sum_{i=3}^{N} E_i r_i^2 + E_1 r_0^2 + E_2 r_0^2}, \tag{5.1}$$

  where N is the number of crystals associated with the electromagnetic shower, r_0 is the average distance between two crystals, which is approximately 5cm for the *BABAR* calorimeter, E_i is the energy deposited in the i^{th} crystal, ordered as $E_1 > E_2 > \ldots > E_N$ and r_i, ϕ_i are the polar coordinates in the plane perpendicular to the line pointing from the interaction point to the shower center centered in the cluster centroid. Considering that the summations start from $i = 3$, the two crystals containing the highest amounts of energy are omitted. Multiplying the energies by the squared distances enhances the effect for hadronic showers, compared with electromagnetic ones. The LAT is used to discriminate between electromagnetic and hadronic showers in the EMC, electrons and photons deposit most of their energy in two or three crystals, and thus the value of LAT is small. The requirement is LAT < 0.6
- *Number of crystals*: the minimal number of crystals with energy deposition is $N_{\mathrm{crys}} > 2$. Clusters consisting of one or two crystals are most likely background.

- *Angular range*: the requirement for the cluster's centroid is $(0.32 < \theta_{\rm clus} < 2.44) rad$, where $\theta_{\rm clus}$ is the polar angle. Since 99% of the energy of an electromagnetic shower are contained inside a cylinder with a radius of ≈ 3.5 Molière radii [36], the above requirement ensures full containment of all clusters considered in this analysis.
- *Rejection of unmatched clusters*: clusters not matched to any charged track, due to inefficiencies in the matching algorithms, fake the presence of an additional particle leading to double counting of their energies. This usually happens when the interaction of charged hadrons with the EMC is separated from the track's point of impact in the EMC. For every photon candidate in the event, the nearest charged track (taken from the tracks fulfilling the Charged Track selection criteria, but not identified as an electron) is selected by calculating the expected intersection between the track and the EMC face. If the nearest track satisfies the requirement:
  - $\Delta\alpha \equiv \arccos[\cos\theta_{\rm clus}\cos\theta_{\rm trk} + \sin\theta_{\rm clus}\sin\theta_{\rm trk}\cos(\phi_{\rm clus} - \phi_{\rm trk})] < 0.08 rad$, $\Delta\alpha$ is the angle difference between the position of the cluster and the impact point on the EMC surface of the nearest charged track, where $\theta_{\rm clus}$, $\theta_{\rm trk}$, $\phi_{\rm clus}$, $\phi_{\rm trk}$ are the polar coordinates for clusters and tracks respectively,
  - The track is not already matched to an EMC cluster,

  then the photon candidate is considered to be an unmatched cluster and it is rejected.

5.2 Particle identification

5.2.1 Electron identification

The criteria established to identify the electrons are a combination of information coming from the DCH, EMC and DIRC in a likelihood based selector [45]. Electrons are primarily separated from charged hadrons by taking into account the ratio of the energy E deposited in the EMC to the track momentum p ($\frac{E}{p}$). This quantity should be compatible with unity for electrons, since all their energy is deposited in the calorimeter. The other charged tracks should appear as minimal ionizing particles, unless they have hadronic interactions in the calorimeter crystals. To further reject hadrons the shape of the energy deposition in the EMC (LAT) is used. In addition, the dE/dx energy loss in the DCH, the DIRC Čerenkov angle and the number of Čerenkov photons associated to the track are required to be consistent with the values expected for an electron. This offers a good e/π separation in a wide range of momentum and angle. described in the app.C.2. The performance of the likelihood-based electron identification algorithm is summarized in Fig. 5.1, in terms of the electron identification efficiency and the per track probability that an hadron is misidentified as an electron. This electron selector is characterized by a selection efficiency larger than 90%, while the misidentification rates for pions, kaons, and protons are below 0.2%, 0.5%, and 0.2%, respectively. However, these numbers are only valid for momenta above 0.8 GeV/c, measured in the laboratory frame, and a minimal momentum in the laboratory frame of 0.3 GeV/c is required for reasonable results of the PID algorithm. In this analysis are selected electrons with momentum in the B meson rest-frame greater than 0.8 GeV/c, so the high quality of the selector is achieved in any case.

Bremsstrahlung Recovery

Photons coming from the interaction of electrons ($e^{\pm}$) in the detector material (radiation of bremsstrahlung), which is up to 20% of radiation length in front of the EMC, or internal bremsstrahlung processes have the effect of reducing the efficiency of the event selection of decay

Figure 5.1: Electron identification and hadron misidentification probability for the likelihood-based electron selector as a function of momentum (left) and polar angle (right). Note the different scales for identification and misidentification on the left and right ordinates, respectively.

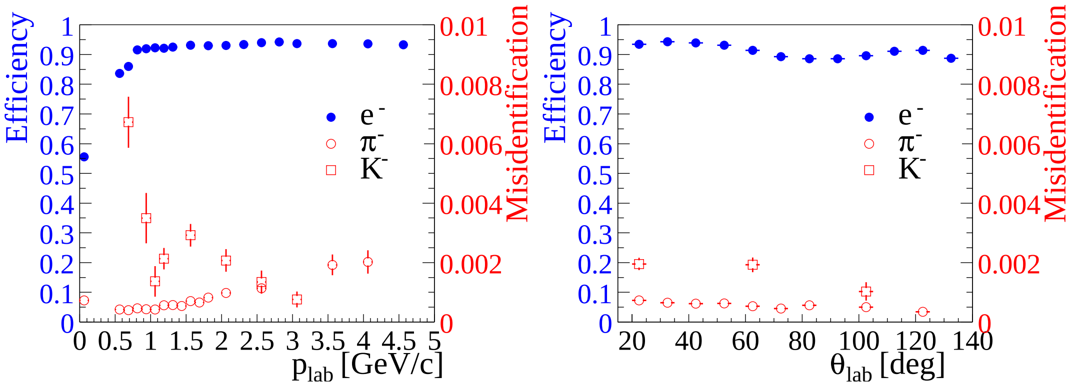

processes containing an electron ($B \to De\nu_e$) in the final state compared to the one with a muon ($B \to D\mu\nu_\mu$). Moreover, when a radiation of a photon occurs, the electron momentum is measured by the tracking system at a smaller value. Therefore the detection of the radiative photons and the measurement of their energy is useful to correct the momentum of the electrons. The standard *BABAR* algorithm [46] is applied to recover photons coming from Bremsstrahlung processes. The method uses the properties of these processes, since the direction of the photons emitted is very close to the direction of the parent electron. The emission angle ($\propto \frac{m_e c^2}{E_e}$) is in average less than 5mrad for electrons above 1 GeV/c. The algorithm combines photons, fulfilling the *Good Photon Loose* selection criteria described in the app.C.2, with an electron only if they satisfy requirements based on the initial direction of the $e^\pm$ (ϕ^e_o, θ^e_o) and its centroid position of the associated calorimeter shower ($\phi^e_{cent.}, \theta^e_{cent.}$):

- $\phi_0^{\mathrm{e}^-} - 0.05\,\mathrm{rad} < \phi_\gamma < \phi_{\mathrm{cent.}}^{\mathrm{e}^-}$ for electrons
- $\phi_{\mathrm{cent.}}^{\mathrm{e}^+} < \phi_\gamma < \phi_0^{\mathrm{e}^+} + 0.05\,\mathrm{rad}$ for positrons
- $|\theta_e - \theta_\gamma| < 0.035\,\mathrm{rad}$

All photons satisfying these requirements are combined with the electron, the corrected electron is then used in the analysis.

5.2.2 Muon identification

Muons are identified by a neural-network based selector [47], which combines IFR and EMC information: the number of traversed interaction lengths in the entire detector and comparing it with the number of expected interaction lengths predicted for a muon of the same momentum, the energy deposited in the EMC is required to be consistent with the minimum ionizing particle hypothesis, the average number and the r.m.s. of the distribution of the RPC and LST hits per layer and other variables exploiting clusters distribution shapes. The muon identification efficiency has been measured using $\mu^+\mu^-(\gamma)$ events and two-photon production of $\mu^+\mu^-$ pairs. The misidentification rates for pions, kaons, and protons are extracted from data control samples. The performance of the muon identification algorithm is summarized in Fig. 5.2, in terms of the muon identification efficiency. The errors shown are statistical only, the systematic error is dominated by variations in the performance of the IFR as a function of position and time.

Figure 5.2: *Muon identification efficiency for the muon selector as a function of momentum (top) and polar angle (bottom).*

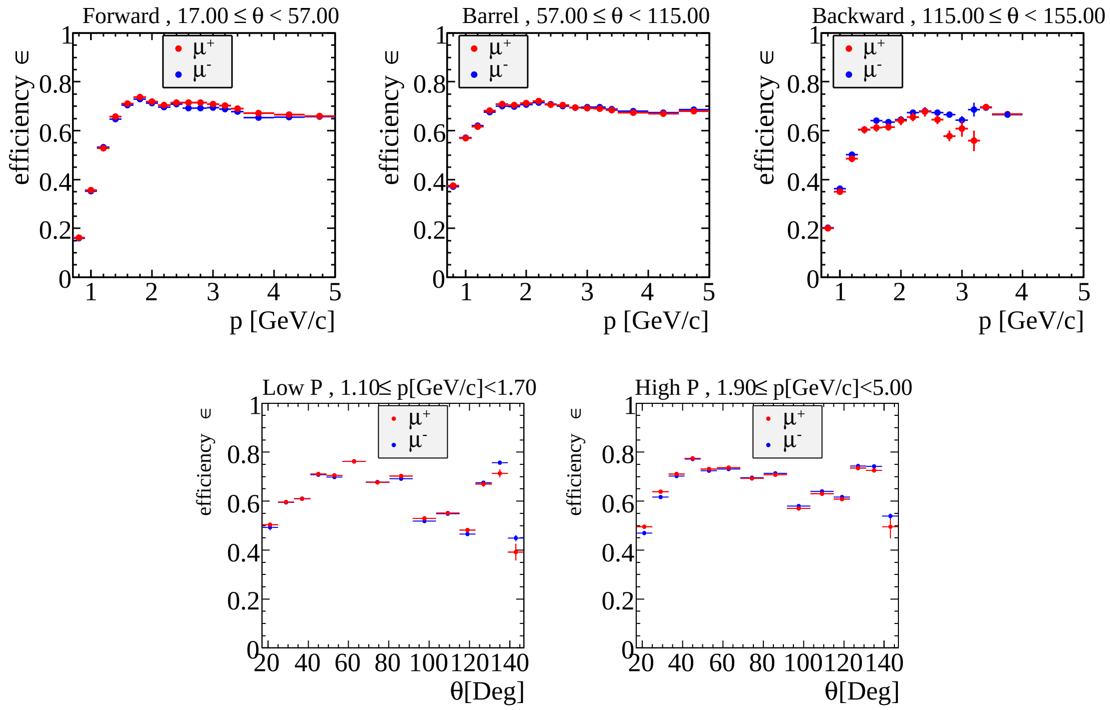

5.2.3 Charged kaon identification

A standard likelihood selector (called *Likelihood Kaon Not a Pion*), based on tracks with an associated momentum above 300 MeV/c and exploiting variables based on information from the DRC, the DCH and the SVT, is used to identify charged kaons. Likelihood functions are computed separately for charged particles, as products of three terms, one for each detector subsystem and then combined, similarly to the electron algorithm. The detector quantities considered in the likelihood are: the difference between the $\mathrm{d}E/\mathrm{d}x$ measured in the DCH and SVT, and the expected $\mathrm{d}E/\mathrm{d}x$ under the kaon hypothesis , the Cerenkov angle θ_c measured in the DIRC, the number of observed photons in the DIRC, the quality of the track prior to reaching the DIRC. Kaon efficiency is evaluated using a sample of kaons from the decay $D \to K\pi$ where the D is selected from the decay of a D^*. Kaons are most often misidentified as pions. The pion mis-identification rate is evaluated using pions from the same source. The efficiency of the kaon selection is more than 90% for most of the momentum spectrum with a misidentification from pions of $2-3\%$. Fig. 5.3 shows a comparison of the charged kaon efficiency in data and MC.

5.3 Reconstruction of Composite Particles

In this section the reconstruction of composite particles is described.

Figure 5.3: *Charged kaon identification efficiency for the kaon selector as a function of momentum, the plots on the right-hand and in the middle compare the efficiency on data with MC for K^+ (left-hand) and for K^- (middle), in the right-hand plot a comparison of the data identification efficiency between K^+ with K^- is shown.*

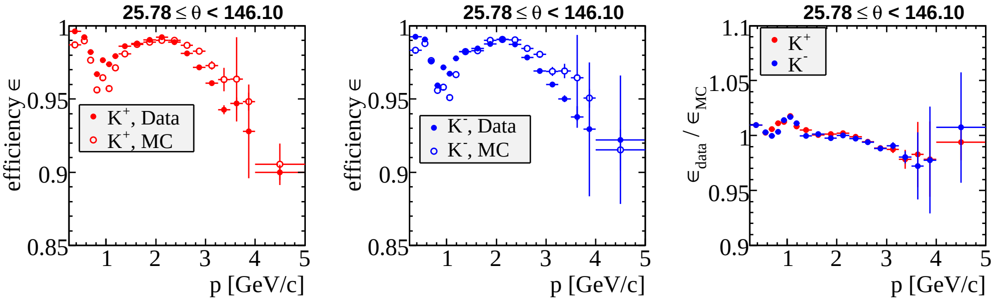

5.3.1 π^0 reconstruction

The process $\pi^0 \to \gamma\gamma$ is reconstructed using EMC clusters fulfilling the BABAR *Good Photon Loose* described in the app. C.2. The photons invariant mass has to be $0.115 < m_{\gamma\gamma} < 0.150\,\mathrm{GeV}/c^2$ to reject misreconstructed π^0 candidates, and the momentum vector must fulfill the following requirement $|\vec{p_{\gamma\gamma}}| < 0.450\,\mathrm{GeV}/c$, since the π^0 is needed for the reconstruction of D^* mesons, as explained later.

5.3.2 D meson reconstruction

D meson candidates are reconstructed in the following decay: $D^0 \to K^-\pi^+$ and $D^+ \to K^-\pi^+\pi^+$. The tracks identified as a charged kaon are taken from the charged tracks fulfilling the BABAR selection criteria *Likelihood Kaon Not a Pion*, whereas charged pions are from the tracks accepted by the BABAR *Good Tracks Very Loose* selection criteria. The kaon and pions daughters of a candidate D-meson are fitted together to a common vertex using the `Cascade` [48] algorithm. The D candidate is accepted if these requirements to suppress misreconstructed D-candidate are met: $|m_D^{Rec} - m_D^{PDG}| < 0.06\ \mathrm{GeV}/c^2$ and if the χ^2 probability of the vertex fitter is $\chi^2 > 0.1\%$.

5.3.3 D^* reconstruction

D^* meson candidates are reconstructed for veto purposes combining a D meson candidate with a pion or a photon, in the following decay final states:

- $D^{*0} \to D^0\ \pi^0$
- $D^{*0} \to D^0\ \gamma$
- $D^{*+} \to D^0\ \pi^+$
- $D^{*+} \to D^+\pi^0$.

The charged pion is reconstructed as a track satisfying the BABAR *Good Track Very Loose*, the π^0 belongs to the BABAR criteria *Pi0 Soft Default Mass* (described in 5.3.1) and photons satisfying the *Good Photon Default BABAR* selection criteria. For all the D^* reconstructed decay it is also required

- $|m_{D^*}^{Rec} - m_{D^*}^{PDG}| < 0.5\ \mathrm{GeV}/c^2$
- For D^{*+} $(0.130 < m_{D^*} - m_D < 0.175)\ \mathrm{GeV}/c^2$

- For D^{*0} $(0.135 < m_{D^*} - m_D < 0.175)$ GeV/c^2

to remove fake D^* composite candidates.

5.3.4 $D\ell$ reconstruction

D and lepton are combined to form the $D\ell$ candidate, hereafter referred also as to Y candidate. To reconstruct the Y candidate, it is required that the lepton momentum $p_e > 0.8\,\text{GeV}/c$, $p_\mu > 1.0\,\text{GeV}/c$ in the $\Upsilon(4S)$ rest frame. The D and the lepton are fitted to a common vertex using the `Cascade` [48] algorithm with a geometrical constraint: the χ^2 fit probability is asked to be $> 0.1\%$ in order to suppress misreconstructed Y-candidates.

5.4 Neutrino reconstruction

The kinematic properties of the neutrino stemming from the $B \to D\ell\nu$ decay can be inferred from the visible 4-momentum of the event. This technique is based on several hypotheses: the charged tracks and showers are produced exclusively in the e^+e^- interaction, energy and momentum associated to a particle is counted only once and the only undetected energy and momentum in an event is due to the neutrino. However, beam background can produce additional particles and thus additional reconstructed tracks and clusters, errors in the reconstruction algorithm may add energy to the event (for example, when clusters are not matched to a charged track) the finite acceptance of the BABAR detector lets particles go undetected, the presence of other neutral undetected particles such as other neutrinos, or badly measured neutrons or K^0_L can reduce the accuracy of this technique. The selection of tracks and clusters used for the neutrino reconstruction is defined as described in sections 5.1.2 and 5.1.4, and then they are used to compute the missing 4-momentum:

$$(E_{miss}, \vec{p}_{miss}) = (E_{beams}, \vec{p}_{beams}) - \left(\sum_i E_i, \sum_i \vec{p}_i\right)$$

where the index i runs over all the selected charged tracks and EMC clusters measured in the laboratory system, E_{beams} and $\vec{p}_{beams}$ refer to the sum of the energy and three-momenta of the two colliding beams respectively. The missing 4-momentum has been calculated in the lab-frame to confine the uncertainties due to the PID assignment to the missing energy. Moreover, since the neutrinos are virtually massless, $|\vec{p}_{miss}| \approx E_{miss}$ and the E_{miss} resolution is worse than $|\vec{p}_{miss}|$ (see figure 5.4), (because of undetected particles such as neutrinos, K^0_L) to get a more precise neutrino 4-vector P_ν, it is chosen: $P_\nu = (|\vec{p}_{miss}|, \vec{p}_{miss})$.

5.5 Preselection

The first stage of the event selection starts from the specific dataset [49], which reconstructs $B \to D^{(*)}\ell\nu(X)$-events with loose requirements. The selection efficiency of this dataset concerning all the charm semileptonic decays is pretty high, around 25%.

Since most of the decay reconstructed in the dataset are not used in this analysis and to remove mainly combinatoric background the selection criteria are tightened as followed:

- $N_{GTVL} \geq 4$: an event is held back if the number of tracks fulfilling the GTVL selection criteria is greater than four.

Figure 5.4: The plots show the resolution of E_{miss}(on the left) and $\vec{p}_{miss}$ (on the right) distribution for simulated signal events, after applying all the selection criteria. The distribution is broken down according to the event properties: events with only one neutrino (blue), more then one (red) and with other neutral missing particles (green): K_L^0, n, and the three categories are stacked together. The presence of undetected particles causes the tail for positive values of the resolution.

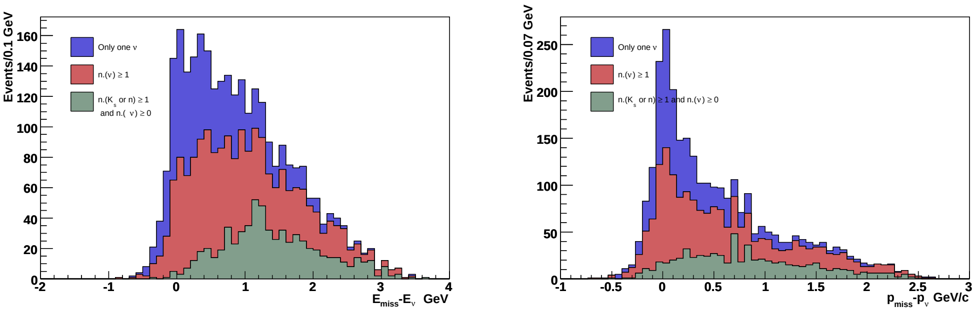

- $N_\ell \geq 1$: at least one lepton (electron or muon) identified with loose selection criteria is required.
- $R_2 < 0.5$: the normalized second Fox Wolfram [50] momentum R_2 defined as

  $$R_2 = \frac{H_2}{H_0}, \tag{5.2}$$

  where

  $$H_l = \sum_{i\,j} \frac{|p_i|\ |p_j|}{E_{\text{vis}}^2} P_l\left(\cos\theta_{ij}\right). \tag{5.3}$$

  The double sum runs over all particles i and j of the event, where p_i is the momentum of particle i, θ_{ij} is the opening angle between the momenta of particles i and j, and P_l is the l^{th} Legendre polynomial, $P_0(x) = 1$ and $P_2(x) = \frac{1}{2}\left(3x^2 - 1\right)$. E_{vis} is the total visible energy of the event. R_2 is calculated from charged tracks and neutral clusters passing loose quality requirements. By definition, the value of R_2 ranges from zero to one. R_2 is a variable characterizing the event's momentum distribution. For events with jet structure R_2 gives higher values (due to higher $|\cos\theta_{ij}|$ and higher P_2 values) than for events with spherical structure. Accordingly, the R_2 distribution of $e^+e^- \to B\overline{B}$ events is shifted to lower values compared to the R_2 distribution of $e^+e^- \to q\overline{q}$ events ($q = u, d, s, c$). The R_2 distributions in $B\overline{B}$ and $q\overline{q}$ events are shown in figure 5.5.
- an event is selected only if at least one reconstructed $D\ell$ (as described in 5.3.4) candidate is found.

5.6 The four-velocity product w

The variable w, defined as the product of the B and D four-velocities ($w = v_B \cdot v_D$), plays a key role in this analysis: its distribution for signal events allows the measurement of $G(1)|V_{cb}|$ and ρ^2. The following equations are used to find different algorithms to reconstruct w:

$$w = \frac{m_B^2 + m_D^2 - q^2}{m_B \cdot m_D} \tag{5.4}$$

where

$$q^2 = (P_B - P_D)^2 = (P_\ell + P_\nu)^2, \tag{5.5}$$

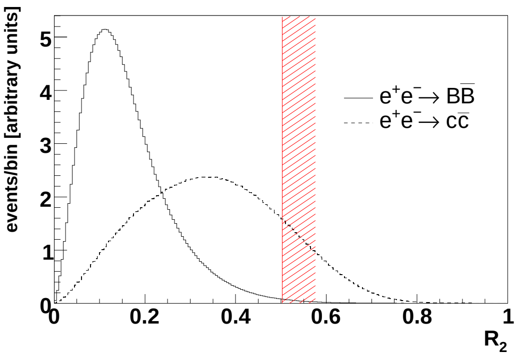

Figure 5.5: The second normalized Fox Wolfram Moment R_2 is plotted for MC events of type $e^+e^- \to B\bar{B}$ (solid) and $e^+e^- \to c\bar{c}$ (dashed). The two graphs are scaled to the same number of events.

and P_B, P_D, P_ℓ and P_ν, are the B, D, ℓ, and ν four-vector momenta. If φ defines the angle between the momenta of the B and the D meson, one can write

$$w = v_B v_D = \frac{p_B p_D}{m_B m_D} = \frac{(E_B^* E_D^* - |\vec{p}_B^{\,*}|\,|\vec{p}_D^{\,*}|\cos\varphi)}{m_B m_D}. \tag{5.6}$$

Due to the presence of a neutrino, the angle φ cannot be precisely determined. Several different approaches, listed below, have been compared. These approximations are justified by the small value of B momentum in the $\Upsilon(4S)$ rest-frame $|\vec{p}_B^{\,*}| \approx 300\,\mathrm{MeV}/c$.

Rough determination (w_{rough})

A first order approximation of equation (5.6) leads to

$$w_{rough} = \frac{E_B E_D}{m_B m_D}., \tag{5.7}$$

where E_B is half the total energy of the two beams in the CMS frame.

Y-average frame

Instead of neglecting the term with the B momentum, it's possible to get an estimation w_Y using the information from θ_{BY} and α, (see figure 5.6) where θ_{BY} is the angle between the B vector momentum and the Y candidate, and α is the angle between the D meson and the Y candidate. They bind φ to the range: $\varphi_{\min} = \alpha - \theta_{BY}$ and $\varphi_{\max} = \alpha + \theta_{BY}$. The product w_Y was computed including the value $\varphi = \frac{\varphi_{\max}+\varphi_{\min}}{2}$ in eq. 5.6.

Diamond-average frame

An even better approximation to the B trajectory is achieved using the fact that the B's are produced preferentially orthogonally to the beam axis. As seen in figure 5.7 the direction of the B must lie on the cone centered on the Y with an opening angle θ_{BY}. The angle φ_{BY}, the azimuthal angle, is not measured so an average over four points is performed: two of them are in the Y plane (the points 0 and π) and the other are out of the plane corresponding to the angles $\pm\pi/2$. Moreover, since the $\Upsilon(4S) \to B\bar{B}$ decay distribution follows a $\sin^2\theta_B$ with respect to the beam axis, where θ_B is the angle between the B direction and the beam axis in the CM-frame, the average is weighted with a $\sin^2\theta_B$ factor at each point.

Figure 5.6: **(a)** The momentum vectors of a signal event are shown. The plane A is the one containing the D and the lepton ℓ, whereas the plane B contains the B and the ν. Since the direction of the B meson is unknown, the angle ξ between the two planes is unknown, too. Assuming $\xi = 0°$ defines φ_{min} and is illustrated in **(b)**. Assuming the other extreme case $\xi = 180°$ defines φ_{max} and is illustrated in **(c)**.

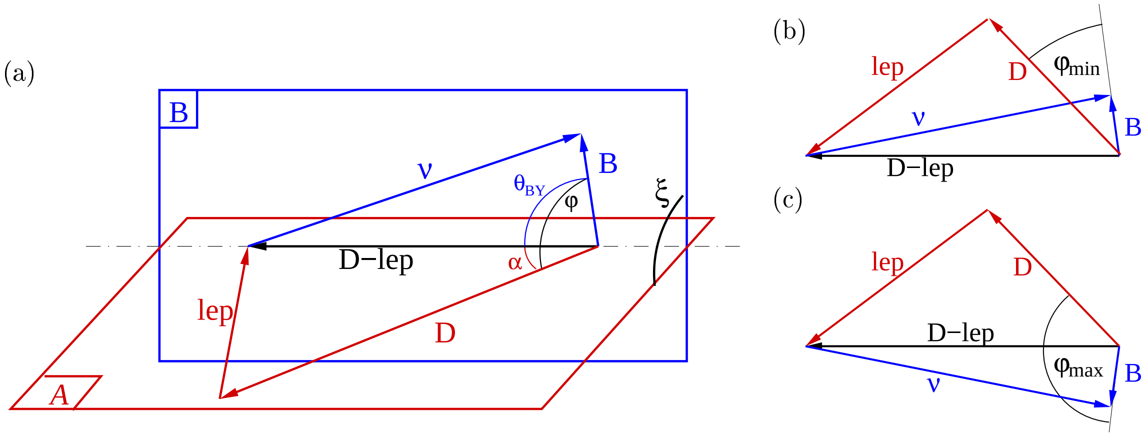

Figure 5.7: In the figure is show how to get the direction of the B meson momentum vector. The direction is needed to calculate w_{Diamond}. True momentum vectors and angles are drawn in red. Reconstructed momentum vectors and angles are drawn in black. For more details see text.

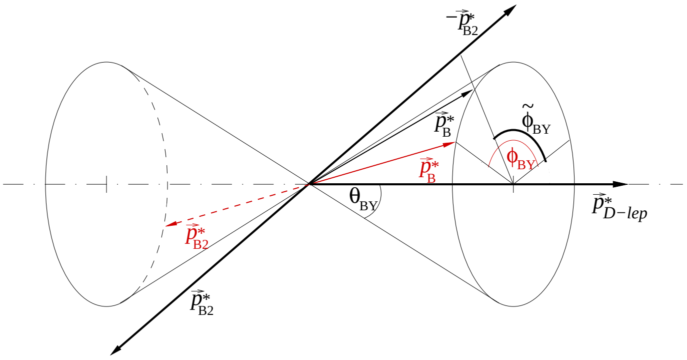

Figure 5.8: Comparison between the four different method studied to reconstruct w (w_{rec}) in the $B^- \to D^0\ell^-\bar{\nu}$(left-hand plot) and $B^0 \to D^-\ell^+\nu$(right-hand plot) reconstructed decay. The distribution plotted is the resolution ($w_{reco} - w_{true}$). Here w_{rough} is the rough estimator, w_ν is the estimator using the neutrino reconstruction, $w_{Y-\mathrm{frame}}$ uses the Y-average frame estimator and w_{Diamond} the diamond-average frame estimator.

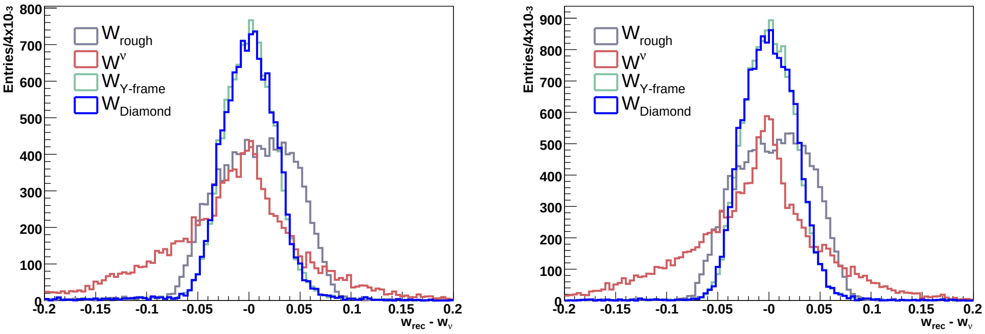

Figure 5.9: The plots show the correlation between the reconstructed w (x-axis) according to the diamond-frame average and the generated w (y-axis) for different signal decay. The decay mode are for the left plot is $B^- \to D^0\ell\nu$, right is $B^- \to D^-\ell\nu$. The plots are done using Signal MC events

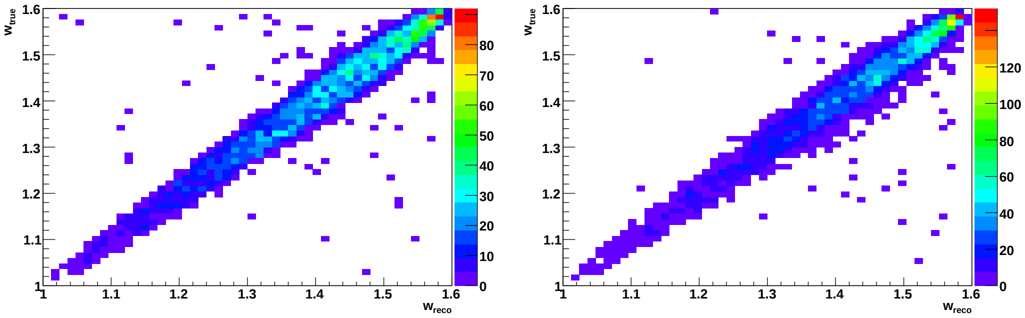

Neutrino Reconstruction

Another approach to get w is from the momenta of the lepton and the neutrino, see equations (5.4) and (5.5). The lepton is fully reconstructed, the neutrino 4-momentum are reconstructed from the missing energy and momentum.

Resolution

The method used in this work to reconstruct w (w_{reco}) is chosen to be the one which gives the best approximation to the true w (w_{true}), the best resolution ($R = w_{reco} - w_{true}$) after all selection criteria (see 5.7) and without introducing any bias. In figure 5.8 the resolution R for all the methods is compared: none of them introduces a bias, the best resolution is given by the Y-frame and the Diamond-frame approximation. Since the Diamond-frame is more precise in the determination of the B direction, this method is used to reconstruct w, providing a resolution better than 0.030. That means that the w distribution can be analyzed in, at least, 10 bins with a bin-width of 0.06 each. The resolution has been studied in each bin of w_{true}, the width is always better than 0.030, and no bias is observed. Figures (5.9) show the correlation between the distribution of the generated value for w (w_{true}) and the reconstructed value w_{rec} for positively identified signal events. From now on when talking about w the diamond-frame approximation is meant unless otherwise stated.

Figure 5.10: The plot shows the ΔE distribution applying all the selection criteria but the ΔE cut, the MC is scaled to have the same amount of events as data. Left hand side for $B^- \to D^0\ell^-\bar{\nu}$ events, on the right hand side for $B^0 \to D^-\ell^+\nu$ events.

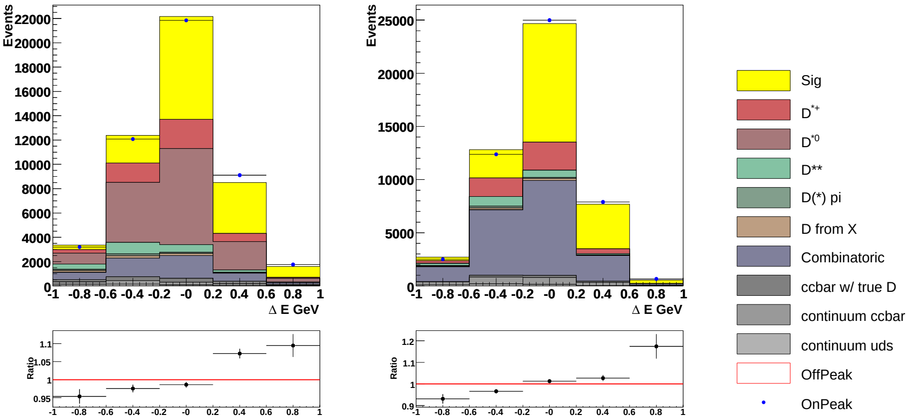

(a) $B^- \to D^0\ell^-\bar{\nu}$ events (b) $B^0 \to D^-\ell^+\nu$ events

5.7 Selection of the $D\ell$ candidate

The selection criteria described in this section aim on one hand to enhance and to identify the contribution of well-reconstructed semileptonic $B \to D\ell\nu$ decay, on the other hand the criteria are designed to reject background events, in particular to suppress the feed down due to the $B \to D^*\ell\nu$ decay. A brief description of the variable employed in the process of selecting is given.

5.7.1 ΔE and m_{ES}

The difference between the reconstructed and the expected energy of the B candidate is defined as ΔE, in the laboratory frame it can be written as:

$$\Delta E = \frac{P_B \cdot P_{beams} - s/2}{\sqrt{s}} \tag{5.8}$$

in this case, taking advantage of the neutrino reconstruction, $P_B = P_Y + P_\nu$, P_{beams} is the 4-vector of the colliding particles and $\sqrt{s}$ is the total energy of the beams in the CMS frame. Only a loose requirement is made on this variable: $(-1.0 < \Delta\mathrm{E} < 1.0)\,\mathrm{GeV}$. A comparison of the ΔE distribution of data with MC can be found on figure 5.10.

The beam energy substituted mass, m_{ES}, is defined in the laboratory frame as:

$$m_{ES} = \sqrt{\frac{(s/2 + \vec{p}_B \cdot \vec{p}_{beams})^2}{E_{beams}} - \vec{p}_B^{\,2}} \tag{5.9}$$

where $\sqrt{s}$ is the total energy of the beams in the CMS frame, $(E_{beams}, \vec{p}_{beams})$ is the 4-momentum vector of the beams, its distribution for data and MC is shown on figure 5.11. All events where $m_{\mathrm{ES}} < 5.15\,\mathrm{GeV}/c^2$ are rejected.

5.7.2 $\cos\Theta_{Thrust}$

The angle between the thrust axis of the $D\ell$ candidate and the thrust axis of the rest of the event is called Θ_{thrust}, where the thrust axis of a collection of particles is defined as the direction along

Figure 5.11: The plot shows the m_{ES} distribution applying all the selection criteria but the m_{ES} cut, the MC is scaled to have the same amount of events as data. Left hand side for $B^- \to D^0\ell^-\bar{\nu}$ events, on the right hand side for $B^0 \to D^-\ell^+\nu$ events.

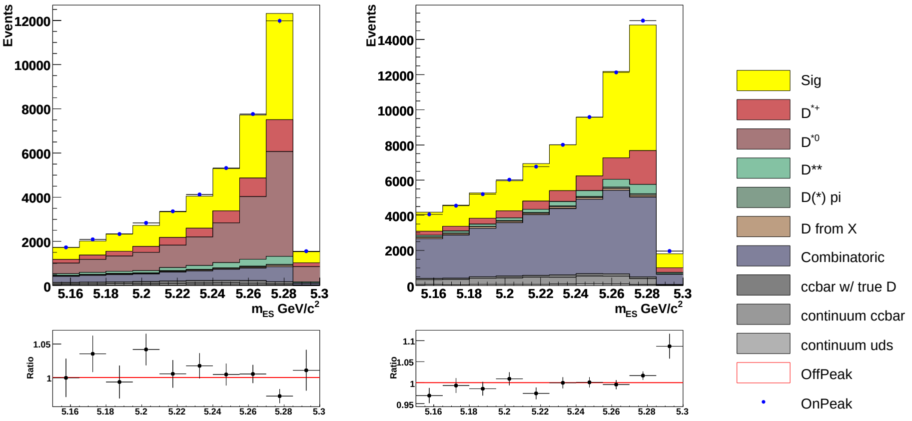

(a) $B^- \to D^0\ell^-\bar{\nu}$ events

(b) $B^0 \to D^-\ell^+\nu$ events

which the sum of the projections of the momenta of the particles is maximized:

$$\text{thrust axis } \hat{n} : max \sum_i |\hat{n} \cdot \vec{p}_i|, \; |\hat{n}| = 1 \tag{5.10}$$

Given the spherical nature of B decays, the thrust axis of a true B candidate is essentially random. For continuum events, however, which are strongly collimated, the above definition ensures that the thrust axis approximates the direction along which the pair of quarks was emitted. This variable has therefore a nearly flat distribution for B candidates while it is sharply peaked at ± 1 for $q\bar{q}$ background events. To reject continuum background events the following restriction is applied: $|\cos\Theta_{Thrust}| < 0.9$ only for the high w region ($w > 1.48$), i.e. where the transferred momentum q^2 is lower and thus the D candidates are faster enhancing the collimation effect, (see figures 5.12 and 5.13).

5.7.3 $\cos\Theta_\ell$

The cosine of the angle between the direction of the lepton boosted into the virtual W rest frame, and the direction of the virtual W in the B^0 rest frame is called $\cos\Theta_\ell$. Its distribution is shown on figures 5.14 and 5.15. The selection depends on the w range: if ($w < 1.36$) then $|\cos\Theta_\ell| < 0.45$ otherwise $\cos\Theta_\ell < 0.6$.

5.7.4 $\cos\Theta_{B-Y}$

The cosine of the angle between the B and the Y system ($\cos\Theta_{B-Y}$). Under the assumption that the Y belongs to a signal decay correctly reconstructed, the 4-momentum conservation in the $\Upsilon(4S)$-frame implies:

$$P_\nu^2 = (P_B - P_Y)^2 = m_B^2 + m_Y^2 - 2E_B E_Y + 2|\vec{p}_B||\vec{p}_Y| cos\Theta_{BY} = 0$$

and thus:

$$cos\Theta_{B-Y} = \frac{2E_B E_Y - m_B^2 - m_Y^2}{2|\vec{p}_B||\vec{p}_Y|}$$

Figure 5.12: The plot shows the $|\cos\Theta_{Thrust}|$ distribution applying all the selection criteria but the $|\cos\Theta_{Thrust}|$ cut, the MC is scaled to have the same amount of events as data. For $B^- \to D^0\ell^-\bar{\nu}$ events. Showing the 1., 6. and 10. w-bin, it can be seen the enhancement of continuum events as events with higher w are selected.

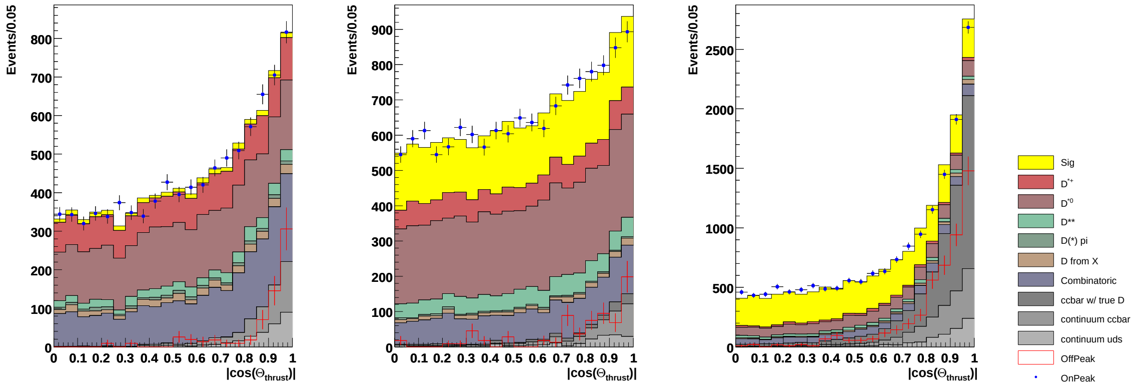

(a) 1. w-bin (b) 6. w-bin (c) 10. w-bin

Figure 5.13: The plot shows the $|\cos\Theta_{Thrust}|$ distribution applying all the selection criteria but the $|\cos\Theta_{Thrust}|$ cut, the MC is scaled to have the same amount of events as data. For $B^0 \to D^-\ell^+\nu$ events. Showing the 1., 6. and 10. w-bin, it can be seen the enhancement of continuum events as events with higher w are selected.

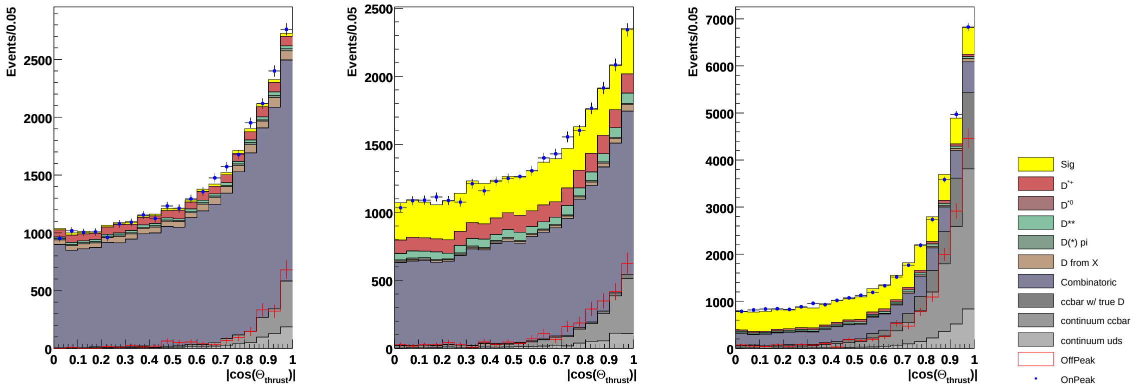

(a) 1. w-bin (b) 6. w-bin (c) 10. w-bin

Figure 5.14: The plot shows the $\cos\Theta_\ell$ distribution applying all the selection criteria but the $\cos\Theta_\ell$ cut, the MC is scaled to have the same amount of events as data. Showing the 1.,6. and 10. w-bin.

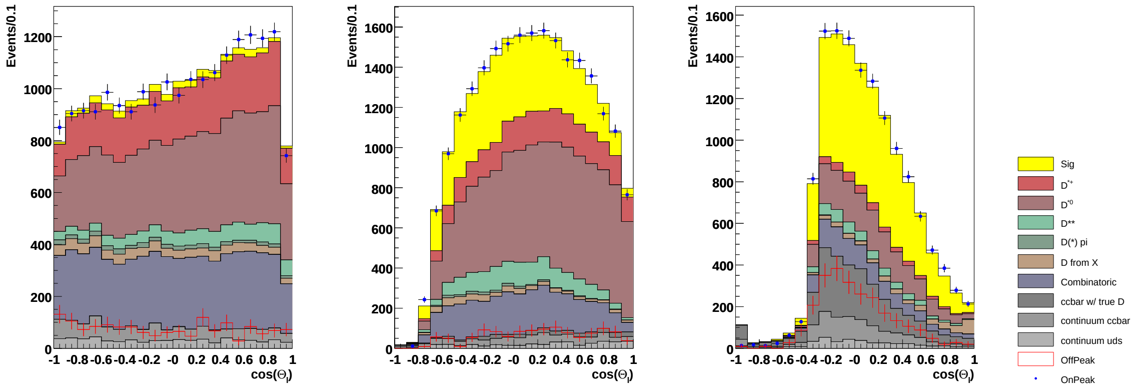

(a) 1. w-bin (b) 6. w-bin (c) 10. w-bin

Figure 5.15: The plot shows the $\cos\Theta_\ell$ distribution applying all the selection criteria but the $\cos\Theta_\ell$ cut, the MC is scaled to have the same amount of events as data. Showing the 1.,6. and 10. w-bin.

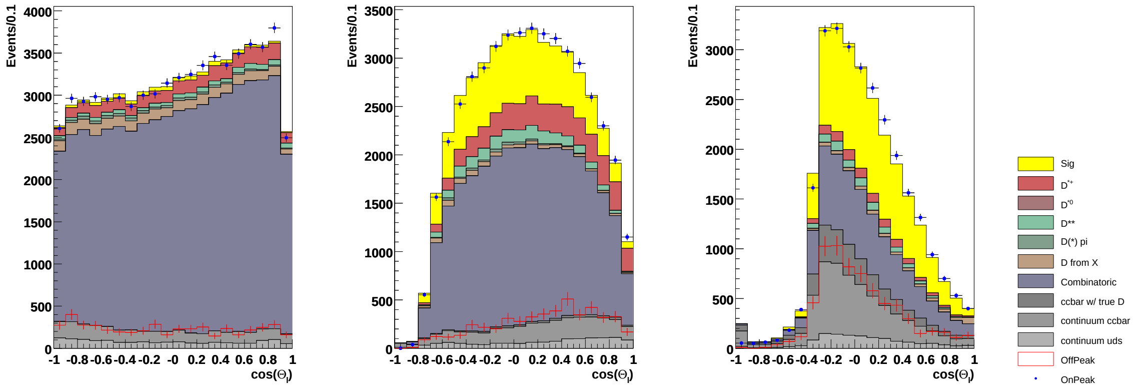

(a) 1. w-bin (b) 6. w-bin (c) 10. w-bin

Figure 5.16: The plot shows the $\cos\Theta_{B-D\ell}$ distribution applying all the selection criteria but the $\cos\Theta_{B-D\ell}$ cut, the MC is scaled to have the same amount of events as data. Left hand side for $B^- \to D^0\ell^-\bar{\nu}$ events, on the right hand side for $B^0 \to D^-\ell^+\nu$ events.

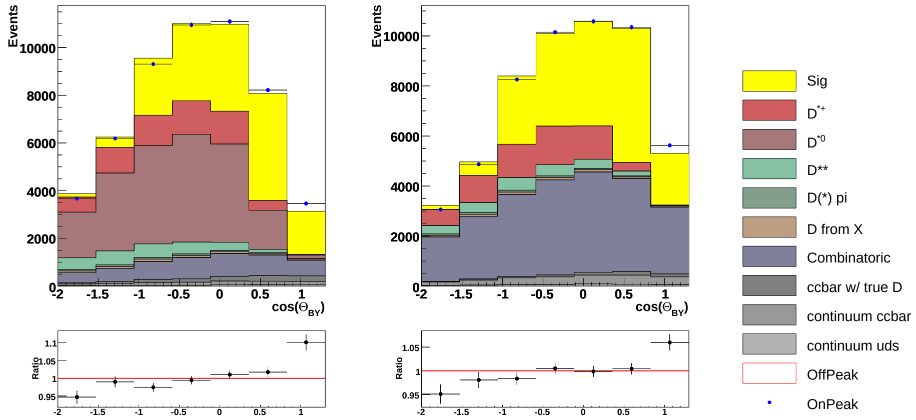

(a) $B^- \to D^0\ell^-\bar{\nu}$ events (b) $B^0 \to D^-\ell^+\nu$ events

where m_B is taken from the PDG[36], $E_B = E^{CMS}_{beams}/2$ and $\vec{p}_B = E_B^2 - m_B^2$. The signal events are distributed mainly in the allowed region between -1 and 1, (see figure 5.16). Poorly reconstructed signal events show tails towards negative values, arising from energy loss of the Y candidates, e.g. due to bremsstrahlung of the electron. A small fraction of signal candidates have $\cos\theta_{\mathrm{BY}} > +1$ due to detector resolution effects. To take this effect into account and since the variable is used to model the background shape in the fit technique explained in the chapter 6 the criteria applied is $-2.0 < \cos\theta_{\mathrm{BY}} < 1.3$.

5.7.5 Momentum restriction

An upper bound on the D and lepton momentum is requested to reject unphysical events, those events beyond the kinematics limit in a signal decay: $p_\ell^{CMS} < 2.4\,\mathrm{GeV}/c$ and $p_D^{CMS} < 2.5\,\mathrm{GeV}/c$.

5.7.6 m_D

A tighter criteria then the one applied in the preselection is asked for m_D: $|m_D - m_D^{PDG}| < 20\,\mathrm{MeV}/c^2$. m_D^{PDG} is taken from [36]. This selected region is conventionally called “signal region”. This restriction is adopted to suppress mis-reconstructed D-candidates. The m_D selection criterion and distribution are shown in figures 5.17, 5.18, 5.19 and 5.20.

5.7.7 D^* veto

One of the biggest sources of background is due to the D^* feed-down. A tight veto on the reconstructed D^* is applied at this stage to suppress the amount. The algorithm combines the selected D candidate with a photon or a pion and rejects the $D\ell$ candidate if the mass difference $\Delta m = m(D^*) - m(D)$ (see figure 5.21) fulfills the requirement $|\Delta m_{PDG} - \Delta m| < 3\,\mathrm{MeV}/c^2$. Δm_{PDG} is taken from [36].

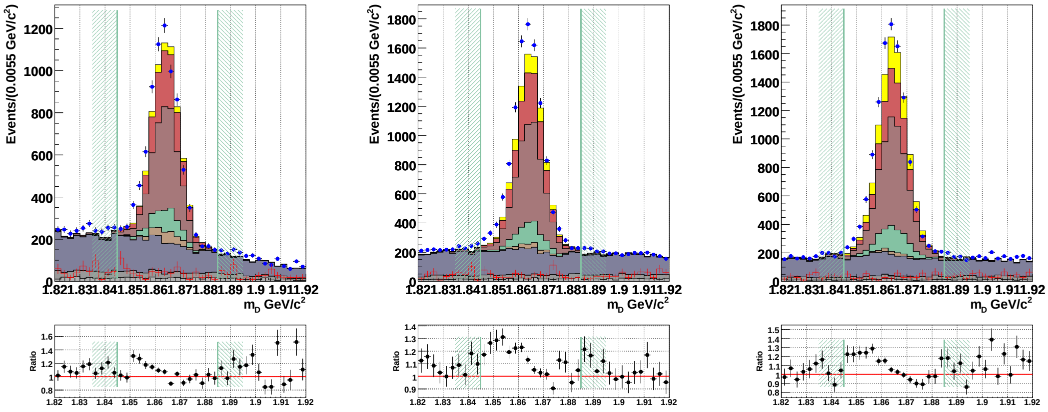

(a) 1. w-bin (b) 2. w-bin (c) 3. w-bin

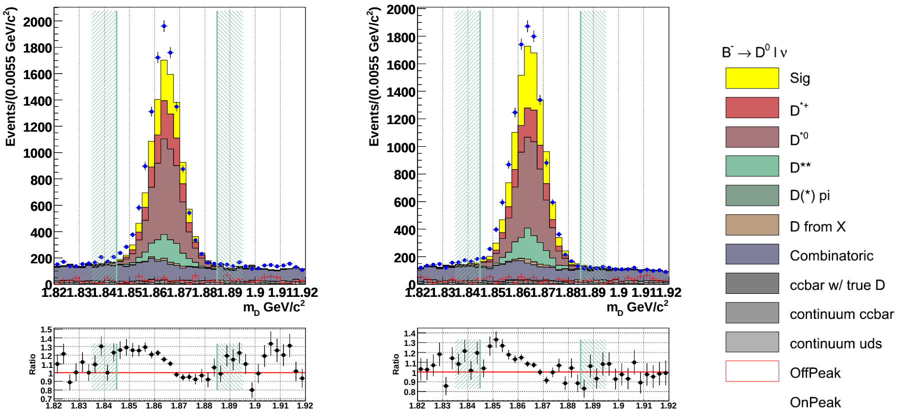

(d) 4. w-bin (e) 5. w-bin

Figure 5.17: The plots show m_D distributions after all the selection criteria were applied, but the m_D cut only for the 1. to 5.w bin , $B^- \to D^0\ell^-\bar{\nu}$ events. The m_D selection criterion is plotted too.

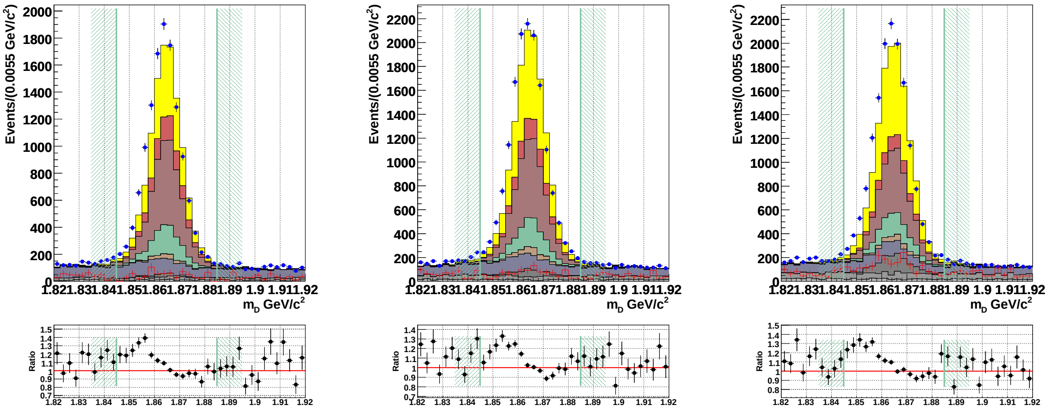

(a) 6. w-bin (b) 7. w-bin (c) 8. w-bin

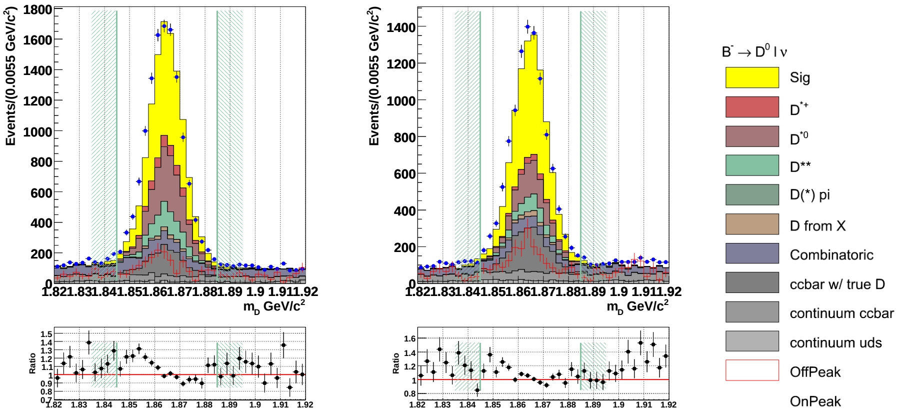

(d) 9. w-bin (e) 10. w-bin

Figure 5.18: The plots show m_D distributions after all the selection criteria were applied, but the m_D cut only for the 6. to 10.w bin , $B^- \to D^0\ell^-\bar{\nu}$ events. The m_D selection criterion is plotted too.

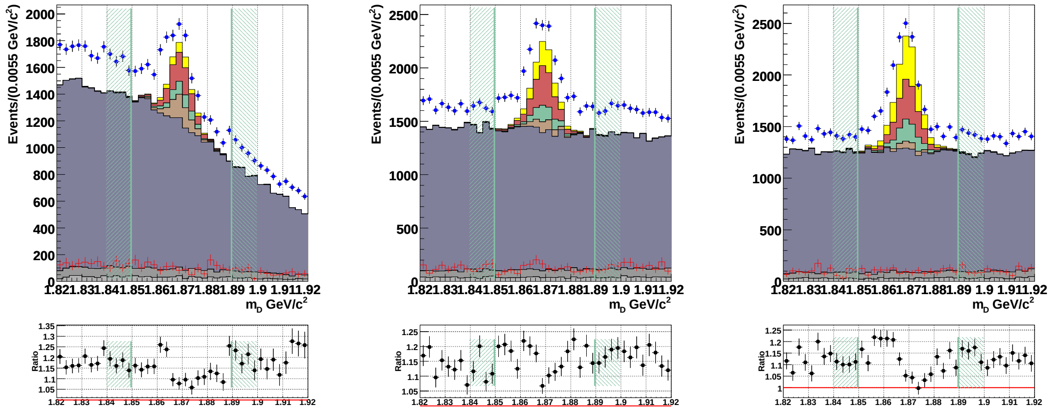

(a) 1. w-bin (b) 2. w-bin (c) 3. w-bin

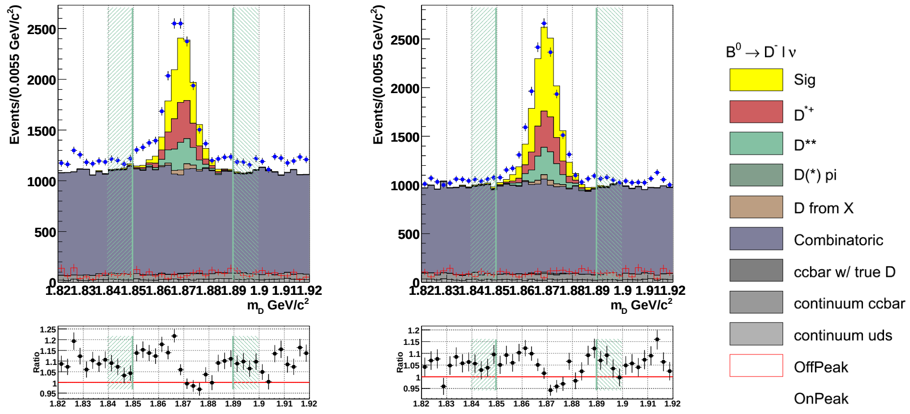

(d) 4. w-bin (e) 5. w-bin

Figure 5.19: The plots show m_D distributions after all the selection criteria were applied, but the m_D cut only for the 1. to 5.w bin , $B^0 \to D^- \ell^+ \nu$ events. The m_D selection criterion is plotted too.

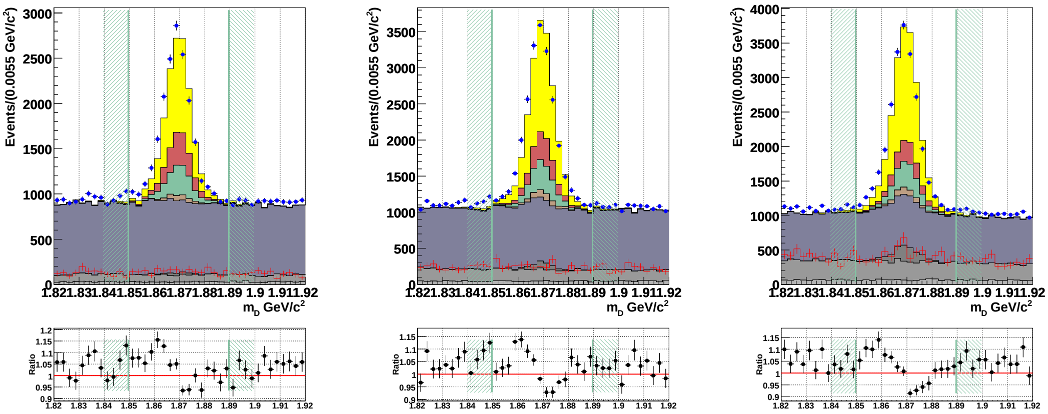

(a) 6. w-bin (b) 7. w-bin (c) 8. w-bin

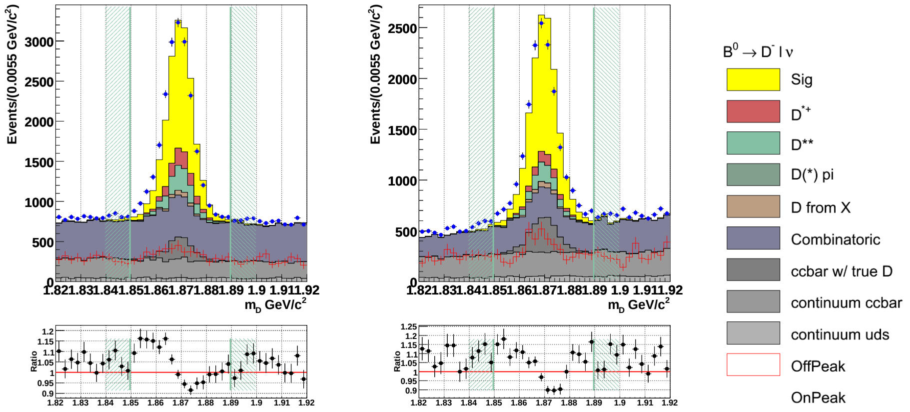

(d) 9. w-bin (e) 10. w-bin

Figure 5.20: The plots show m_D distributions after all the selection criteria, but the m_D cut were applied, only for the 6. to 10.w bin , $B^0 \rightarrow D^- \ell^+ \nu$ events. The m_D selection criterion is plotted too.

Figure 5.21: The plot shows the Δm distribution applying all the selection criteria but the D^*-veto, the MC is scaled to have the same amount of events as data. Left hand side for $B^- \rightarrow D^0 \ell^- \bar{\nu}$ events, on the right hand side for $B^0 \rightarrow D^- \ell^+ \nu$ events.

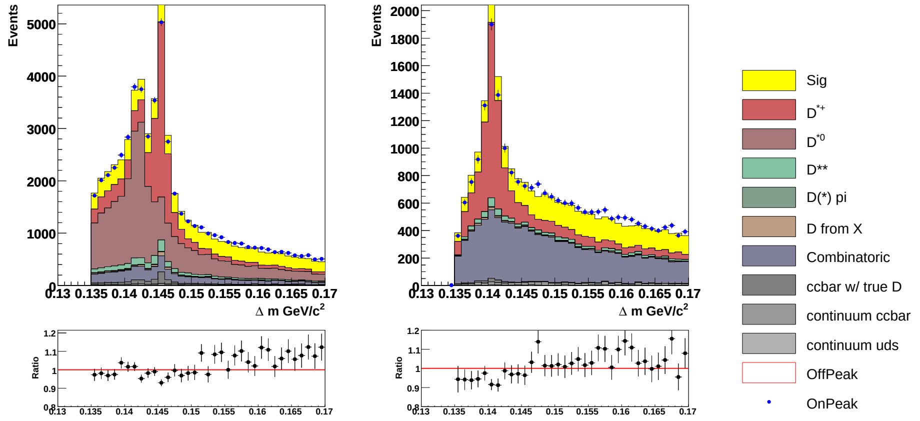

(a) $B^- \rightarrow D^0 \ell^- \bar{\nu}$ events (b) $B^0 \rightarrow D^- \ell^+ \nu$ events

Figure 5.22: The plot shows the number of candidates per event after all the selection criteria are fulfilled. Left hand side for $B^- \to D^0\ell^-\bar{\nu}$ events, on the right hand side for $B^0 \to D^-\ell^+\nu$ events.

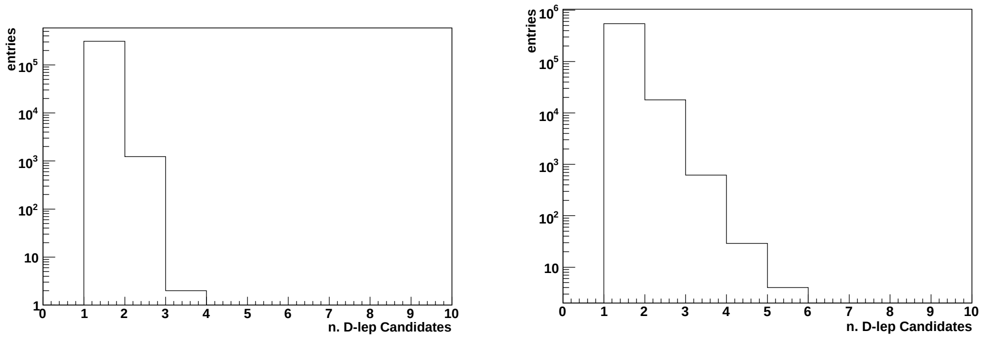

5.7.8 Neutrino Quality Cuts

Some requirements are needed in order to improve the quality of the neutrino reconstruction technique, and to reject background events. The main purpose of this criteria is to reject the events with multiple missing particles: for example other neutrinos, K_L^0 or other neutral particles.

- Q_{event}^{net}: The net charge of an event, if nothing is lost during the reconstruction, should be equal to zero, but, because of the limited geometrical acceptance of the BABAR detector, to maintain a high signal efficiency it is required to be $|Q_{event}^{net}| = 0$ or 1 ,
- N_{event}^{lepton}: removing events, where the total number of good reconstructed leptons $N_{event}^{lepton} > 1$, is useful to remove other possible neutrinos,
- Θ_{miss}: it is the polar angle of the missing momentum P_{miss}. To maintain a high efficiency, the cut is $(0.3 < \Theta_{miss} < 2.9)rad$ due only to detector acceptance. In order to reject events where particles lost in the beam pipe are mistaken as neutrinos.

5.7.9 Multiple Candidates

After applying all the selection criteria, only few events have multiple signal candidates per event (see figure 5.22); on average the ratio of events with multiple candidates over the total number of events is $(0.40 \pm 0.01)\%$ in the reconstruction of the $B^- \to D^0\ell^-\bar{\nu}$ decay and $(3.30 \pm 0.02)\%$ in the reconstruction of the $B^0 \to D^-\ell^+\nu$ decay. In case multiple $D\ell$ candidates are found, the one with the value of m_{ES} closer to m_B^{PDG} is selected. This is motivated by a study done on signal MC. As shown in figure 5.23, the m_{ES} distribution for signal event peaks near m_B, whereas it drops for the background events. As shown in figure (5.24), the algorithm selects the right $B^- \to D^0\ell^-\bar{\nu}$ candidate with a probability of 72.6% and the right $B^0 \to D^-\ell^+\nu$ candidate with a probability of 68.2%.

5.8 Efficiency

Tables 5.3 and 5.4 summarize the efficiency and the background rejection power for the whole selection criteria, and show the signal to background ratio after applying all restrictions. Besides in the tables are also shown the number of events surviving the whole selection criteria.

Figure 5.23: The plots show a comparison of the quantity m_{ES} between signal positively matched and background events done using signal MC events. Left hand side for $B^- \to D^0\ell^-\bar{\nu}$ events, on the right hand side for $B^0 \to D^-\ell^+\nu$ events.

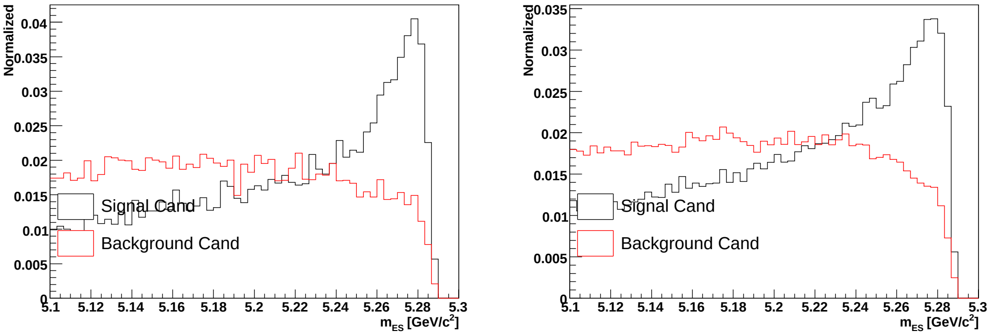

Figure 5.24: In case multiple candidates are found, the difference ($|m_{ES} - m_B^{PDG}|_{\text{other}} - |m_{ES} - m_B^{PDG}|_{\text{sig}}$) can be calculated. The distribution compares the distance of m_{ES} to m_B^{PDG} for candidates of the same event, where the distance defined as "sig" is the one belonging to a positively reconstruct signal decay, whereas the distance defined as "other" belong to a background decay. This tests the quality of the best candidate selection algorithm, if this quantity is positive it means the best candidate selected was a signal candidate. Left hand side for $B^- \to D^0\ell^-\bar{\nu}$ events, on the right hand side for $B^0 \to D^-\ell^+\nu$ events.

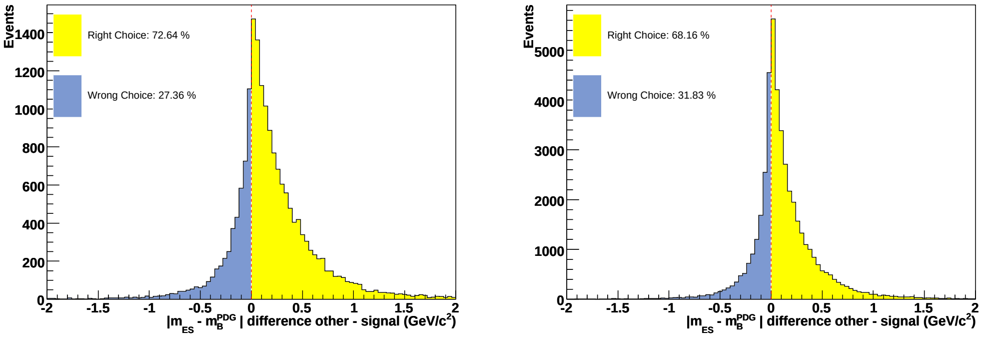

Table 5.3: Summary of the selection efficiency for the $B^0 \to D^- \ell^+ \nu$ events, and background rejection power of the whole selection, values are given in %, splitted for the 10 w-bins. The efficiency are calculated after all selection criteria are applied. The row label S/B shows the total ratio between selected signal and background events after the whole selection. The last row shows the number of events surviving the selection criteria in the different w bins.

$B^0 \to D^- \ell^+ \nu$										
	w bin									
	1.	2.	3.	4.	5.	6.	7.	8.	9.	10.
Signal Eff.	1.55	3.55	4.89	5.79	6.79	7.54	10.16	10.80	10.51	12.32
Background Rejected	99.75	99.71	99.70	99.64	99.56	99.44	99.13	98.88	98.92	98.81
S/B	1.43	3.53	7.5	13.32	21.96	31.32	41.36	50.51	71.01	87.41
Selected Events	24210	30590	28210	26274	24736	24667	30544	31248	26101	20531

Table 5.4: Summary of the selection efficiency for the $B^- \to D^0 \ell^- \bar{\nu}$ events, and the background rejection power of the whole selection, values are given in %, splitted for the 10 w-bins. The efficiency are calculated after all previous selection criteria are applied. The row label S/B shows the total ratio between selected signal and background events after the whole selection. The last row shows the number of events surviving the selection criteria in the different w bins.

$B^- \to D^0 \ell^- \bar{\nu}$										
	w bin									
	1.	2.	3.	4.	5.	6.	7.	8.	9.	10.
Signal Eff.	1.18	2.94	4.54	5.87	7.26	8.16	11.33	12.11	11.80	13.36
Background Rejection	99.47	99.41	99.28	99.15	98.99	98.79	98.22	97.89	97.87	97.73
S/B	2.41	5.49	10.01	16.54	25.60	35.03	47.31	60.88	83.28	108.2
Selected Events	8643	12234	12400	12790	12662	12838	15679	15696	12991	10587

6 Determination of the Signal Yields

The signal yields for the signal decay modes $B^- \to D^0\ell^-\bar{\nu}$ and $B^0 \to D^-\ell^+\nu$ are measured by performing a $(2+1)$-dimensional binned Maximum Likelihood (ML) fit. The fit technique is based on a generalized binned ML first developed by Barlow and Beeston [51]. It fits contributions of various MC samples to the data surviving the selection criteria. It estimates the data composition based on the MC sources taking into account for both data and MC statistical fluctuations.

6.1 The Likelihood

In the following section it is briefly described the functionality of this particular binned ML Fit, more details can be found in [51]. Data and MC distributions are divided into n bins. The numbers of selected events in the data distribution falling into bin i are denoted by d_i, such as $N_D = \sum_i d_i$, where N_D is the total number of events in the data sample. The numbers of selected MC events falling in the same bin i from MC source j is a_{ij}, then $N_j = \sum_i a_{ij}$, where N_j is the total number of events in the j^{th} MC source, assuming m different MC sources, that add up to describe the data. The amount of expected events in the i^{th} bin is denoted by g_i, it can be written as function of the strengths P_j and the number of MC events a_{ij}:

$$g_i = N_D \sum_j P_j w_{ij} \frac{a_{ij}}{N_j} = \sum_j p_j w_{ij} a_{ij}, \tag{6.1}$$

where w_{ij} are weights, they account for MC normalizations and corrections, and $p_j = N_D P_j / N_j$. MC samples are finite, and a_{ij} are subject to statistical fluctuation relative to the value expected for infinite statistics denoted as A_{ij}, and thus the correct way to express the numbers of expected events is:

$$g_i = \sum_j p_j w_{ij} A_{ij}. \tag{6.2}$$

The total likelihood function $\mathcal{L}$ is the product of the probability to find the measured number of data events d_i when g_i events are expected and the likelihood of observing a_{ij} events when A_{ij} are expected, for Poisson distributed events it can be written as:

$$\mathcal{L} = \prod_i \frac{g_i^{d_i}}{d_i!} e^{-g_i} \cdot \prod_i \prod_j \frac{A_{ij}^{a_{ij}}}{a_{ij}!} e^{-A_{ij}}. \tag{6.3}$$

To find the maxima of the likelihood it is usually easier to work with $\ln \mathcal{L}$, since both are maximized for the same parameter values, omitting the terms that don't depend on the fit parameters, since they don't effect the location of the maximum, the log likelihood can be written as:

$$\ln \mathcal{L} = \sum_{i=1}^{n} (d_i \ln g_i - g_i) + \sum_{i=1}^{n} \sum_{j=1}^{m} (a_{ji} \ln A_{ji} - A_{ji}), \tag{6.4}$$

The quantities to be determined are the m normalization factors p_j and the $n \times m$ A_{ij}, but the numbers of unknown parameters can be reduced analytically [51], the A_{ij} can be determined by

Figure 6.1: Plot show the $\cos(\Theta_{BY})$ and ΔE MC distribution corresponding to the $B^- \to D^0\ell^-\bar{\nu}$ decay mode for signal events on the left-hand side, D^* background events in the middle and peaking background events on the right-hand side

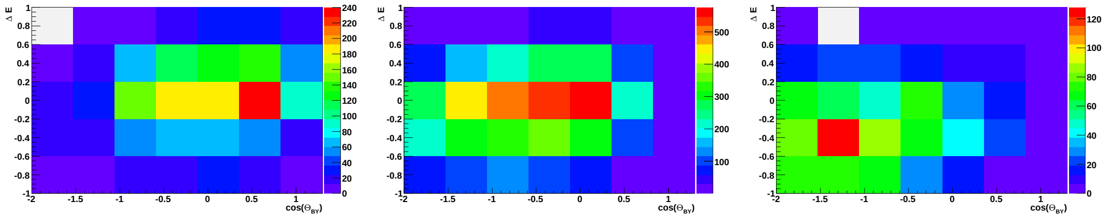

Figure 6.2: Plot show the $\cos(\Theta_{BY})$ and ΔE MC distribution corresponding to the $B^0 \to D^-\ell^+\nu$ decay mode for signal events on the left-hand side, D^* background events in the middle and peaking background events on the right-hand side

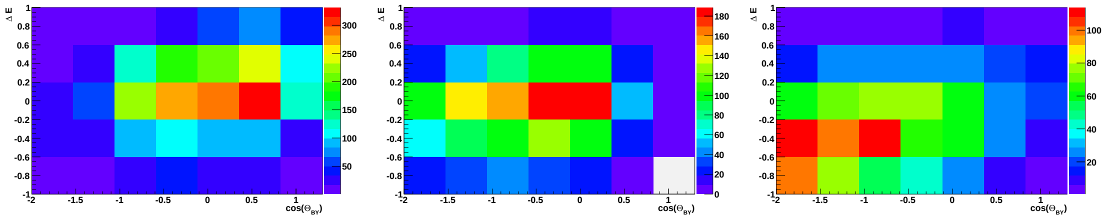

solving the n independent equations:

$$f_i = \sum_{j=1}^{m} p_j w_{ij} A_{ij} = \sum_{j=1}^{m} \frac{p_j w_{ij} a_{ij}}{1 + p_j w_{ij} r_i}, \tag{6.5}$$

where $A_{ij} = a_{ij}/(1 + p_j w_i j r_i)$ and $r_i = 1 - d_i/f_i$. These equations are determined calculating the derivative of the total likelihood with respect to p_j and A_{ij} to find the maxima, and setting the differential to zero. Thus only the m scaling factors p_j have to be determined by maximizing the $\ln \mathcal{L}$ using the `MINUIT` [52] package and solving the equations at each iterations.

6.2 Fit Method and parameters

The fit is performed independently for the decays $B^- \to D^0\ell^-\bar{\nu}$ and $B^0 \to D^-\ell^+\nu$ in each w bin. The distribution used to fit the MC sources to the data are $\cos(\Theta_{BY})$ and ΔE for each bin of w. The two-dimensional distribution (shown on figures 6.1 and 6.2) has been chosen to enhance the signal and background separation, since the two variables are correlated for both signal and background sources. It was not possible to extract a reliable analytic form for these distributions, so it was preferred a binned ML method. The binning has been chosen to optimize signal and background separation while retaining adequate statistics in all bins. The fit plane $(\cos(\Theta_{BY}), \Delta E)$ is divided into 7×5 bins over the region $-2.0 < \cos(\Theta_{BY}) < 1.3$ and $-1.0\,\text{GeV} < \Delta E < 1.0\,\text{GeV}$. The $\cos(\Theta_{BY})$ bin size for the fit is 0.47, for ΔE is $0.4\,\text{GeV}$. The contributions to the fit are: signal events, $B \to D^*\ell\nu$ background events, peaking background events, and combinatoric background events, as introduced in section 3.1. The Monte Carlo simulation provides the shapes for signal events, $B \to D^*\ell\nu$, and peaking background events. The shape of the combinatorial background is taken from events belonging to the data D-mass side-bands. Fit parameters are normalization factors p_j, where j runs over the different fit contributions, free to float in the fit are:

- $p_{B\to D\ell\nu}$: fraction of signal events, $B \to D\ell\nu$ decays.

Table 6.1: Side Band regions used in the analysis

$B^- \to D^0 \ell^- \bar{\nu}$	$B^0 \to D^- \ell^+ \nu$
$1.82 < m_{D^0} < 1.835$ & $1.897 < m_{D^0} < 1.92$	$1.82 < m_{D^+} < 1.835$ & $1.892 < m_{D^+} < 1.92$

Figure 6.3: The plot shows the comparison between the on-peak sidebands data and the combinatoric background MC scaled to the amount of onpeak data for the sixth bin of w in the ΔE distribution, on the left-hand side $B^- \to D^0 \ell^- \bar{\nu}$ selected events, and $B^0 \to D^- \ell^+ \nu$ selected events on the right-hand side.

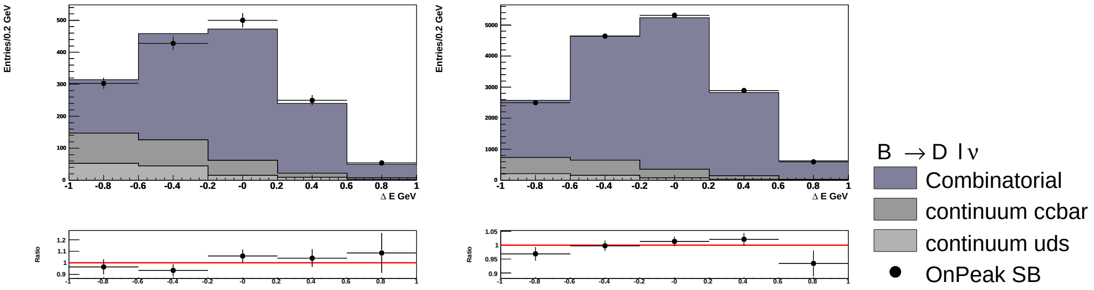

- $p_{B \to D^* \ell \nu}$: fraction of $B \to D^* \ell \nu$ background events, $B \to D^* \ell \nu$ (both D^{*0} and D^{*+}) decays.
- p_{peak}: fraction of peaking background events, $B \to D^{**} \ell \nu$; $B \to D^{(*)} X \ell \nu$; $B \to D_s D$, $D_s \to X \ell \nu$; $B \to D \tau \nu$, $\tau \to \ell \nu_\ell \nu_\tau$; all $B \to DX$ not belonging to signal or D^*-background events, and $c\bar{c} \to D$ background events,

whereas the combinatorial background is fixed.

6.2.1 Side-bands normalization factors

Events in the data D-mass side-band (SB) regions are used to model the combinatoric background in the signal region (defined in section 5.7.6). The SB events well describe the shape of the MC combinatoric background as shown in figure 6.3 and 6.4, where data and MC events are compared. The side band regions are defined in table 6.1. Further tests have been perform to prove the ansatz that SB events well describe combinatoric events in the signal region. In fact sidebands are splitted in four regions (left, right, inner, outer) see table 6.2. Events in the left SB are compared to the one in the right SB and those in the outer SB are compared with those in the inner SB (see Figures 6.5 and 6.6). This proves again that shapes of sidebands are compatibly the same moving towards the signal region.

Figure 6.4: The plot shows the comparison between the MC sidebands and the combinatoric background MC scaled to the amount of onpeak data for the sixth bin of w in the ΔE distribution, on the left-hand side $B^- \to D^0 \ell^- \bar{\nu}$ selected events, and $B^0 \to D^- \ell^+ \nu$ selected events on the right-hand side.

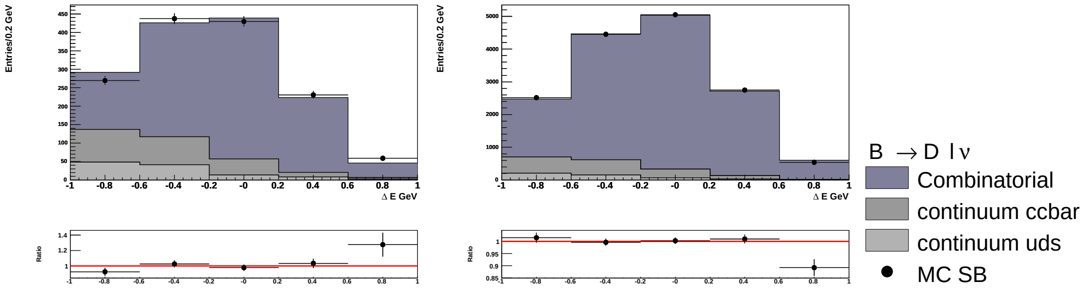

Table 6.2: Side-band regions breakdown used for testing the ansatz that SB events correctly describe combinatoric events in the signal region.

left	right
$1.82 < m_{D^0} < 1.832$	$1.897 < m_{D^0} < 1.92$
$1.82 < m_{D^+} < 1.835$	$1.892 < m_{D^+} < 1.92$
inner	outer
$1.825 < m_{D^0} < 1.832$ & $1.897 < m_{D^0} < 1.9085$	$1.82 < m_{D^0} < 1.825$ & $1.9085 < m_{D^0} < 1.92$
$1.83 < m_{D^+} < 1.835$ & $1.892 < m_{D^+} < 1.907$	$1.82 < m_{D^+} < 1.83$ & $1.907 < m_{D^+} < 1.92$

Figure 6.5: The plot shows the ΔE comparison between inner and outer sidebands on the left-hand side, and comparison between left and right on the right-hand side, done using on-peak data for selected $B^- \to D^0\ell^-\bar{\nu}$ events, for a given w-bin (eighth in this case) .

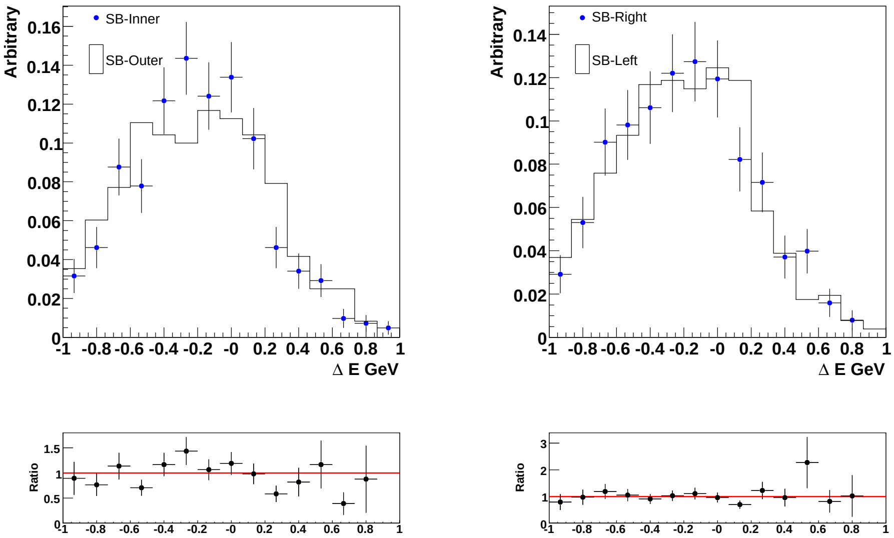

Figure 6.6: The plot shows the ΔE comparison between inner and outer sidebands on the left-hand side, and comparison between left and right on the right-hand side, done using on-peak data for selected $B^0 \to D^-\ell^+\nu$ events, for a given w-bin (eighth in this case).

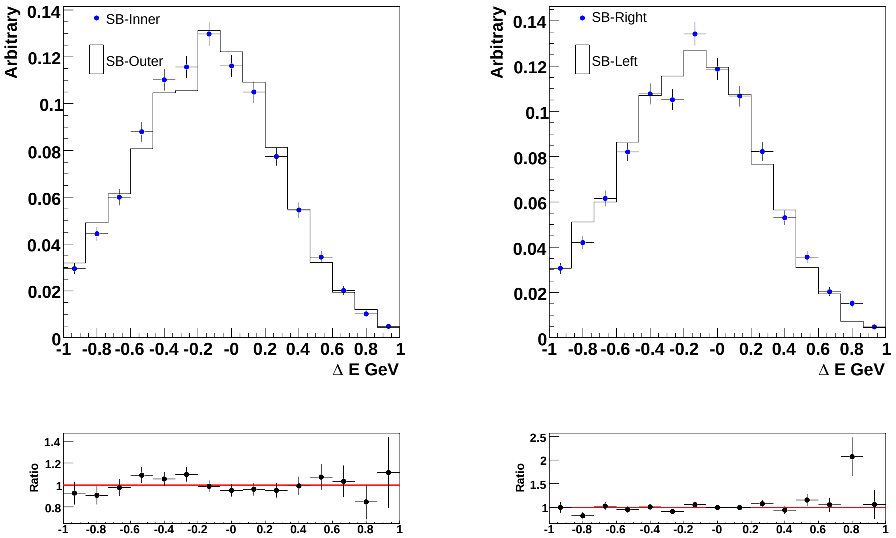

Table 6.3: Scaling factors for the side-band, result of the fit to the D-mass distribution for each w-bin

w bin n.	$B^- \to D^0\ell^-\bar{\nu}$	$B^0 \to D^-\ell^+\nu$
1	1.481 ± 0.028	1.076 ± 0.007
2	1.400 ± 0.028	0.953 ± 0.006
3	1.292 ± 0.028	0.949 ± 0.007
4	1.350 ± 0.043	0.933 ± 0.002
5	1.425 ± 0.035	0.954 ± 0.009
6	1.351 ± 0.034	0.961 ± 0.009
7	1.473 ± 0.036	0.936 ± 2.869
8	1.391 ± 0.035	0.987 ± 0.008
9	1.433 ± 0.038	0.995 ± 0.009
10	1.174 ± 0.038	0.996 ± 0.012

The amount of combinatoric events in the sidebands region is greater than in the signal region, so it has to be normalized to the number of events in the signal region before being used. Normalization factors for the SB is extracted from a fit in the D-mass distribution (see an example on figures 6.8), since the shape of the combinatoric background is not flat, and thus the normalization is not just the ratio between the width of the signal region in the m_D distribution divided by the sum of the width of the s sidebands in the m_D distribution. The fit uses analytic functions, the peak is modeled with a Gauss function, and a second grade polynomial is used for the combinatoric background. Normalization factors are calculated as ratio between the number of fitted background events in the SB and the number of fitted background events in the signal region. They are summarized in the table 6.3.

Figure 6.7: The signal strengths result of the fit in each w-bin is plotted. The red line is at 1.0, the expected value while fitting MC events. Points are also fitted to a zeroth-degree polynomial and the results are compared with the input value in the MC. On plots (a) are shown results using the MC splitted in two equisized samples for $B^- \to D^0\ell^-\bar{\nu}$ events (left-hand side), and for $B^0 \to D^-\ell^+\nu$ events (right-hand side). On plots (b) are shown results using the MC splitted in two samples, one of them having the same amount of events as data, for $B^- \to D^0\ell^-\bar{\nu}$ events (left-hand side), and for $B^0 \to D^-\ell^+\nu$ events (right-hand side).

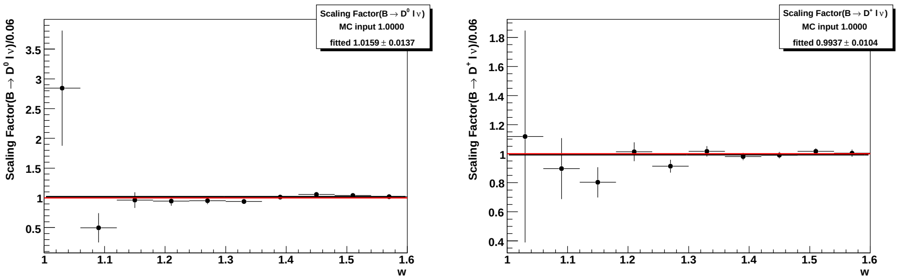

(a) Half MC vs Half MC

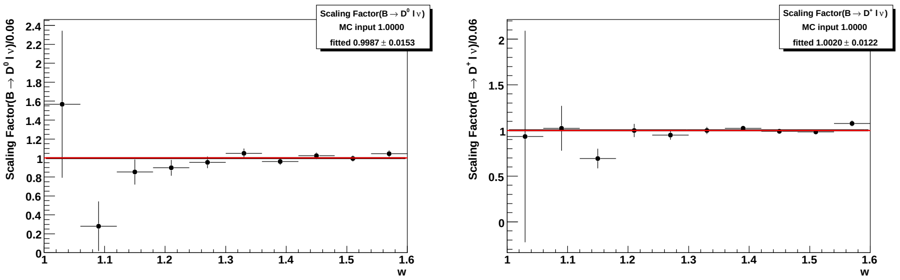

(b) MC Same Lumi as Data

Figure 6.8: The plot shows the results of the fit to the D Mass distribution for a given w-bin (sixth in this case), $B^- \to D^0\ell^-\bar{\nu}$ events on the left-hand side, $B^0 \to D^-\ell^+\nu$ events on the right-hand side. The red curve is the projection of the combinatoric background fitting function, the blue line is the projection of the total fitting function.

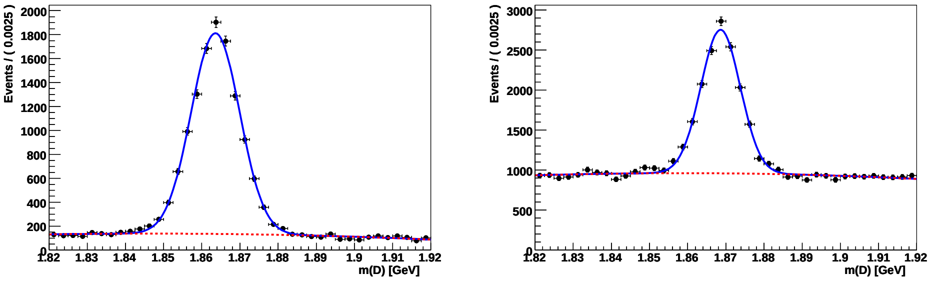

Figure 6.9: Fit validation half MC vs half MC: the MC is splitted in two sample containing the same amount of events. The plot shows the fitted results compared to the true amount of signal events contained in the fitted pseudo-data MC sample. On the right-hand side the results for $B^- \rightarrow D^0\ell^-\bar{\nu}$ events, on the left-hand side for $B^0 \rightarrow D^-\ell^+\nu$ events.

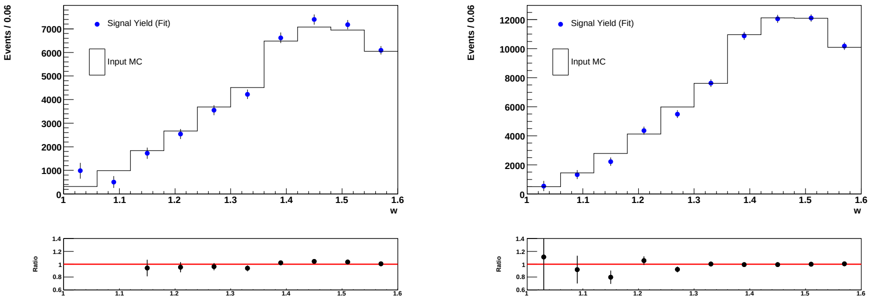

6.3 Fit Validation

A fit validation is performed to verify the stability of the fit method, to look for possible biases and to study the fit statistical error. At first the full MC simulation available is splitted into two independent samples, one of them used as pseudo-data the other to get fit sources, shapes and normalization factors. The fit is successfully performed (see the following section 6.3.1 for more details). Another test performed is a so called Toy Monte Carlo: a simplify method to produce many independent MC samples (toy experiments), by comparing the results of the fit to the independent generated samples, none bias appears in this test.

6.3.1 MC against MC

The full MC is splitted randomly into two independent samples. This is done twice, at first the MC is splitted in two samples containing the same amount of events. One sample is used as pseudo-data the other to get the shape of MC fit sources and the normalization factors. The fit is performed. Figure 6.9 shows the results of the fit (data point) compared to the signal contained in the pseudo-data MC. It turns out that due to the high background in the first w bin is not easy to measure the signal yields for $B^- \rightarrow D^0\ell^-\bar{\nu}$ events, whereas the fit on $B^0 \rightarrow D^-\ell^+\nu$ events reproduces the expected values. Then the MC is splitted in order to get one sample with the amount of events compatible with the on-peak data sample and the other sample contains the complementary events. The figure 6.10 shows the results of the fit (data point) compared to the signal contained in the pseudo-data MC events. The results in this case are slightly better than in the previous case, the first w bin can be fitted. To better understand if the disagreements are real bias arising from the fit technique, the results of the Toy MC have to be studied, since the two test are not statistically independent.

Figure 6.10: Fit validation data-like vs remaining MC. The MC is splitted into two samples, one with the same amount of events as the on-peak data used as pseudo-data, the other with the remaining MC events. The plot shows the fitted results compared to the true amount of signal events contained in the fitted pseudo-data MC sample. On the right-hand side the results for $B^- \to D^0\ell^-\bar{\nu}$ events, on the left-hand side for $B^0 \to D^-\ell^+\nu$ events.

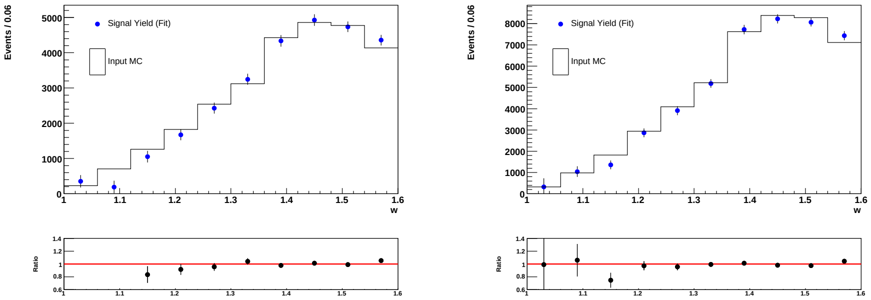

6.3.2 Toy Experiments

The 2D binned maximum likelihood fit has been verified by performing 1000 toy experiments. A toy experiment is made using all the MC events available after the selection for both the pseudo-data and for the fit sources. The bin content and its error of each fit components used are re-generated randomly following the Poisson statistics distribution with mean equal to the unmodified value. Then the fit is performed using the new generated distributions. This procedure has been iterated for thousand times. For a given toy experiment the pull of a fit parameter p_j is defined as:

$$Pull = \frac{p_j^{Fit} - p_j^{True\ value}}{\sigma_{p_j}^{Fit}}. \tag{6.6}$$

The pull is the difference between the generated value of the parameter and the value of the parameter return by the fit divided by the fit error on that given parameter. The pull distribution for a sample of toy experiments should follow a Gauss function with mean value equal to zero and the standard deviation (r.m.s.) equal to one. Discrepancy between those expected values may be hints of biases present in the fit. If the mean is shifted from zero, then this is a sign of bias in the central value of the fitted parameter. If the r.m.s. is different from one, then it is a sign of bias on the error returned from the fit. Figures 6.11 to 6.12 show the pull distribution results of this test for the MC signal strength $p_{B\to D\ell\nu}$. In none case the mean is shifted from zero, but the r.m.s. is slightly different from one in two cases: the fit for the events belonging to the first and last w-bin. On one side (first w-bin) the r.m.s. is bigger than one, i.e. the error is underestimated, on the other side (last w-bin) the r.m.s. is lower the one, i.e. the error is overestimated. To correct for this issue the fit errors are rescaled accordingly.

Figure 6.11: Toy MC: Pull distribution for fit parameter $p_{B \rightarrow D\ell\nu}$, fraction of signal events, for $B^- \rightarrow D^0\ell^-\bar{\nu}$ events.

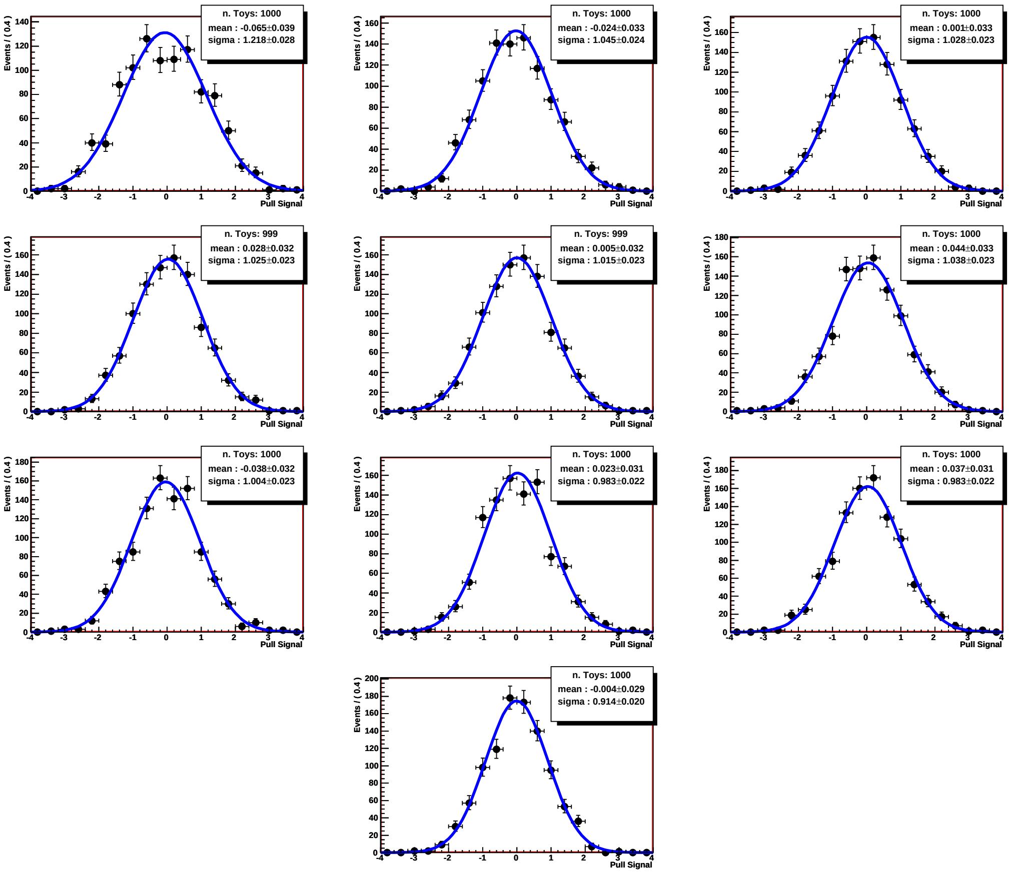

Figure 6.12: Toy MC: Pull distribution for fit parameter $p_{B\rightarrow D\ell\nu}$, fraction of signal events, for $B^0 \rightarrow D^-\ell^+\nu$ events.

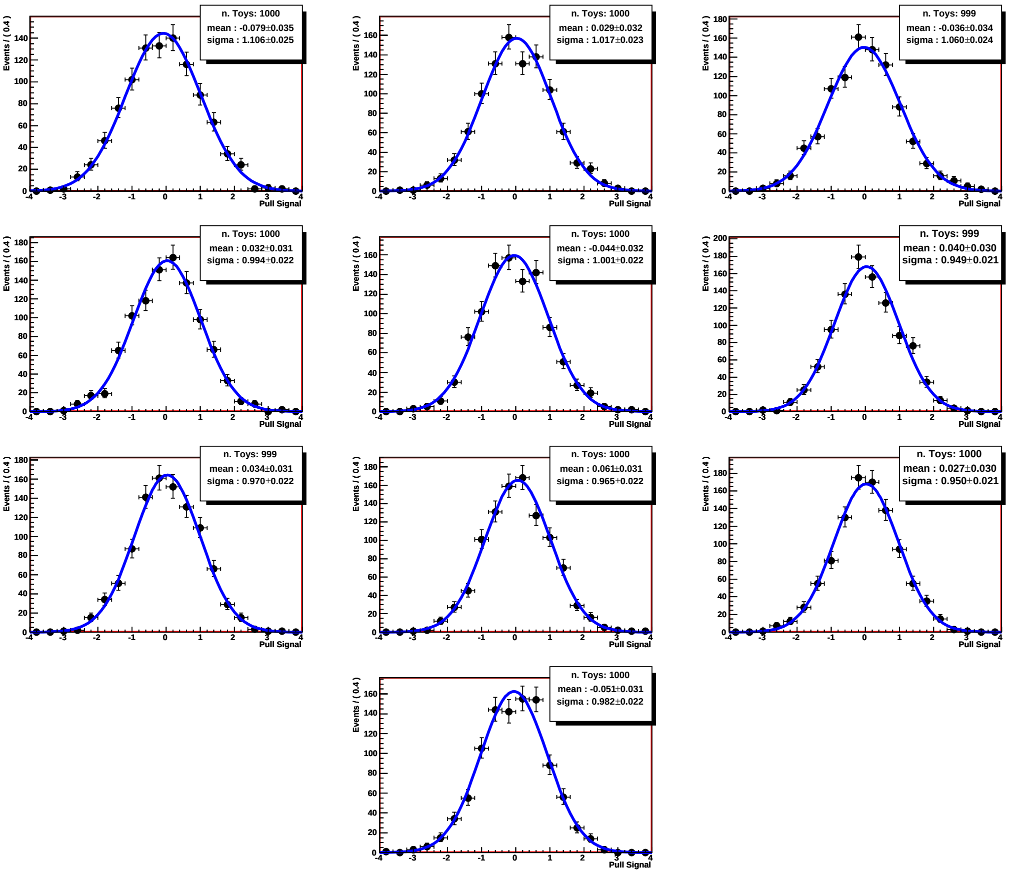

Table 6.4: Scaling factors result of the $2D$ fit, for each bin and the 3 free parameters, $B^- \to D^0\ell^-\bar{\nu}$ events

bin n.	p_{Signal}	p_{D^*}	p_{Peak}	$\chi^2/d.o.f.$	correlation
n.1	-2.06 ± 1.22	1.20 ± 0.07	0.81 ± 0.17	$23.05/31.0$	$\begin{pmatrix} 1 & -0.84 & -0.035 \\ -0.84 & 1 & -0.37 \\ -0.035 & -0.37 & 1 \end{pmatrix}$
n.2	0.52 ± 0.27	1.13 ± 0.05	0.56 ± 0.15	$15.65/31.0$	$\begin{pmatrix} 1 & -0.77 & 0.24 \\ -0.77 & 1 & -0.62 \\ 0.24 & -0.62 & 1 \end{pmatrix}$
n.3	1.10 ± 0.15	1.03 ± 0.05	0.72 ± 0.15	$48.51/31.0$	$\begin{pmatrix} 1 & -0.77 & 0.37 \\ -0.77 & 1 & -0.72 \\ 0.37 & -0.72 & 1 \end{pmatrix}$
n.4	0.90 ± 0.09	1.14 ± 0.05	0.57 ± 0.14	$16.34/31.0$	$\begin{pmatrix} 1 & -0.72 & 0.38 \\ -0.72 & 1 & -0.77 \\ 0.38 & -0.77 & 1 \end{pmatrix}$
n.5	1.03 ± 0.06	1.13 ± 0.05	0.50 ± 0.13	$27.07/31.0$	$\begin{pmatrix} 1 & -0.68 & 0.37 \\ -0.68 & 1 & -0.8 \\ 0.37 & -0.8 & 1 \end{pmatrix}$
n.6	1.06 ± 0.05	1.10 ± 0.06	0.72 ± 0.15	$27.57/31.0$	$\begin{pmatrix} 1 & -0.6 & 0.31 \\ -0.6 & 1 & -0.85 \\ 0.31 & -0.85 & 1 \end{pmatrix}$
n.7	1.10 ± 0.04	1.18 ± 0.06	0.54 ± 0.13	$18.04/31.0$	$\begin{pmatrix} 1 & -0.5 & 0.19 \\ -0.5 & 1 & -0.84 \\ 0.19 & -0.84 & 1 \end{pmatrix}$
n.8	1.18 ± 0.03	1.33 ± 0.07	0.48 ± 0.10	$12.18/31.0$	$\begin{pmatrix} 1 & -0.37 & -0.024 \\ -0.37 & 1 & -0.78 \\ -0.024 & -0.78 & 1 \end{pmatrix}$
n.9	1.20 ± 0.03	1.24 ± 0.08	0.66 ± 0.11	$22.89/31.0$	$\begin{pmatrix} 1 & -0.1 & -0.35 \\ -0.1 & 1 & -0.75 \\ -0.35 & -0.75 & 1 \end{pmatrix}$
n.10	1.35 ± 0.05	0.91 ± 0.11	0.83 ± 0.10	$32.36/31.0$	$\begin{pmatrix} 1 & -0.13 & -0.58 \\ -0.13 & 1 & -0.53 \\ -0.58 & -0.53 & 1 \end{pmatrix}$

6.4 Extraction of signal yields from the fit to data

Table 6.4 and 6.5 report the scale factors p_j (with errors) and the correlation coefficient obtained as results of the binned ML fit to on-peak data in each w bin. Signal yields are then obtained multiplying the fit parameter $p_{B\to D\ell\nu}$ with the total amount of data events selected in a given w bin and they are reported in table 6.6.

Table 6.5: Scaling factors result of the $2D$ fit, for each bin and the 3 free parameters, $B^0 \to D^-\ell^+\nu$ events

bin n.	p_{Signal}	p_{D^*}	p_{Peak}	$\chi^2/d.o.f.$	correlation
n.1	-0.63 ± 0.92	1.07 ± 0.33	1.39 ± 0.27	22.49/31.0	$\begin{pmatrix} 1 & -0.6 & -0.34 \\ -0.6 & 1 & -0.42 \\ -0.34 & -0.42 & 1 \end{pmatrix}$
n.2	0.96 ± 0.31	1.18 ± 0.26	0.83 ± 0.31	12.36/31.0	$\begin{pmatrix} 1 & -0.67 & 0.018 \\ -0.67 & 1 & -0.61 \\ 0.018 & -0.61 & 1 \end{pmatrix}$
n.3	0.89 ± 0.15	1.47 ± 0.25	0.61 ± 0.29	23.98/31.0	$\begin{pmatrix} 1 & -0.68 & 0.22 \\ -0.68 & 1 & -0.74 \\ 0.22 & -0.74 & 1 \end{pmatrix}$
n.4	1.07 ± 0.08	1.14 ± 0.22	0.71 ± 0.21	23.94/31.0	$\begin{pmatrix} 1 & -0.64 & 0.24 \\ -0.64 & 1 & -0.78 \\ 0.24 & -0.78 & 1 \end{pmatrix}$
n.5	1.01 ± 0.06	1.76 ± 0.26	0.14 ± 0.24	14.94/31.0	$\begin{pmatrix} 1 & -0.58 & 0.26 \\ -0.58 & 1 & -0.84 \\ 0.26 & -0.84 & 1 \end{pmatrix}$
n.6	1.07 ± 0.05	1.81 ± 0.27	0.23 ± 0.21	14.36/31.0	$\begin{pmatrix} 1 & -0.49 & 0.16 \\ -0.49 & 1 & -0.86 \\ 0.16 & -0.86 & 1 \end{pmatrix}$
n.7	1.13 ± 0.03	1.08 ± 0.24	0.69 ± 0.15	12.64/31.0	$\begin{pmatrix} 1 & -0.37 & 0.013 \\ -0.37 & 1 & -0.84 \\ 0.013 & -0.84 & 1 \end{pmatrix}$
n.8	1.23 ± 0.03	1.28 ± 0.29	0.45 ± 0.14	17.44/31.0	$\begin{pmatrix} 1 & -0.21 & -0.16 \\ -0.21 & 1 & -0.83 \\ -0.16 & -0.83 & 1 \end{pmatrix}$
n.9	1.27 ± 0.03	1.53 ± 0.31	0.43 ± 0.14	17.53/31.0	$\begin{pmatrix} 1 & 0.022 & -0.43 \\ 0.022 & 1 & -0.78 \\ -0.43 & -0.78 & 1 \end{pmatrix}$
n.10	1.41 ± 0.05	0.77 ± 0.40	0.34 ± 0.14	25.99/31.0	$\begin{pmatrix} 1 & -0.011 & -0.67 \\ -0.011 & 1 & -0.55 \\ -0.67 & -0.55 & 1 \end{pmatrix}$

Table 6.6: Signal yields for each w-bin

w bin n.	$B^- \to D^0\ell^-\bar{\nu}$	$B^0 \to D^-\ell^+\nu$
1.	$-513. \pm 304.$	$-265. \pm 396.$
2.	$416. \pm 217.$	$1077. \pm 347.$
3.	$1527. \pm 205.$	$1770. \pm 304.$
4.	$1928. \pm 182.$	$3523. \pm 279.$
5.	$2934. \pm 175.$	$4163. \pm 255.$
6.	$3656. \pm 168.$	$5609. \pm 249.$
7.	$5288. \pm 178.$	$8962. \pm 262.$
8.	$6004. \pm 173.$	$9842. \pm 257.$
9.	$5755. \pm 166.$	$10065. \pm 250.$
10.	$5537. \pm 188.$	$8820. \pm 293.$

6.4.1 Data MC agreement after Fit

The following figures show the agreement of the data and MC distribution before and after scaling the MC sources according to fit results shown on table 6.4 and 6.5. More comparison plots can be found on appendix D. The figures show data MC comparison after subtracting side-band events, i.e. the components fixed in the fit. The remaining MC events are breakdown into signal events, $B \to D^{*}\ell\nu$ events and peaking background events. Moreover $B \to D^{*}\ell\nu$ events are shown separately the contribution of $B \to D^{*0}\ell\nu$ and $B \to D^{*+}\ell\nu$, and peaking background events are divided into $B \to D^{**}\ell\nu$, $B \to D^{(*)}X\ell\nu$, $B \to DX$ and $c\bar{c} \to DX$.

Figure 6.13: The plots show $\cos\theta_{\mathrm{BY}}$ distributions before and after applying the fit results after all the selection criteria were applied, only for the 1. to 5.w bin , $B^- \to D^0\ell^-\bar{\nu}$ events

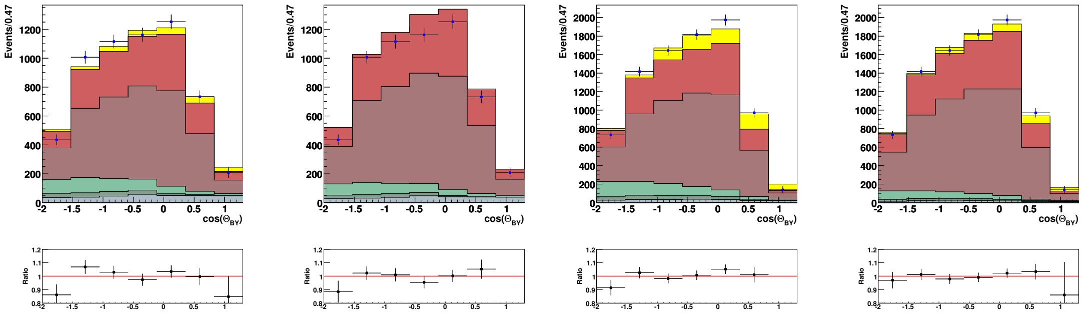

(a) 1. w-bin

(b) 2. w-bin

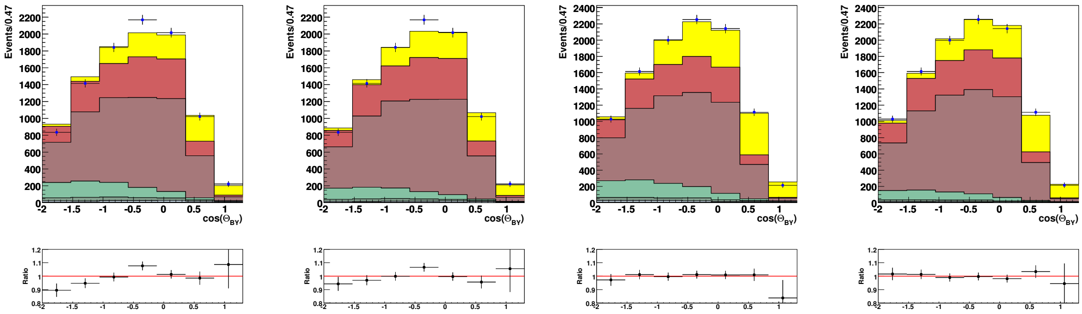

(c) 3. w-bin

(d) 4. w-bin

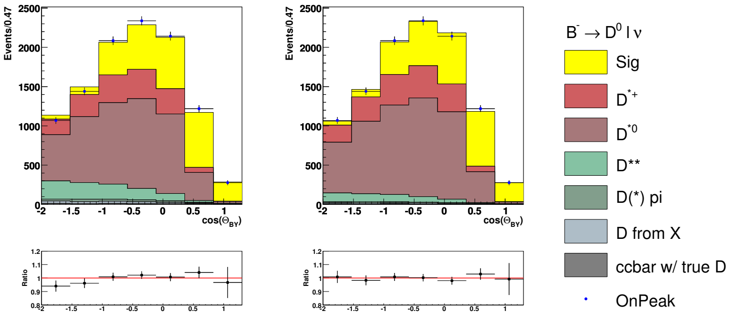

(e) 5. w-bin

Figure 6.14: The plots show $\cos\theta_{\mathrm{BY}}$ distributions before and after applying the fit results after all the selection criteria were applied, only for the 6. to 10.w bin , $B^- \to D^0\ell^-\bar{\nu}$ events

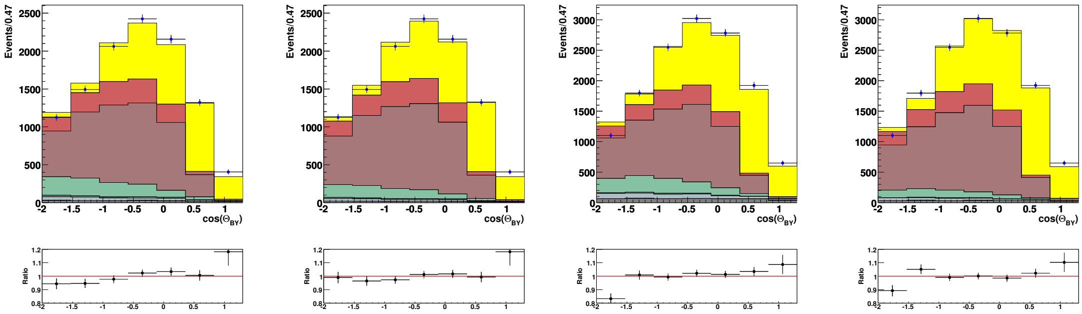

(a) 6. w-bin

(b) 7. w-bin

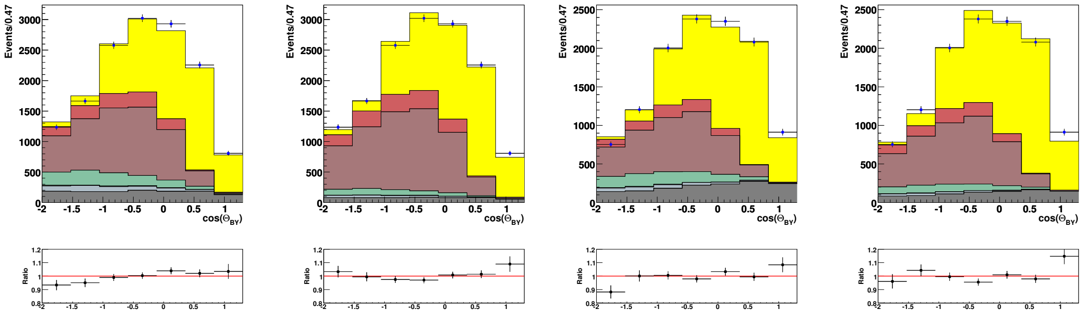

(c) 8. w-bin

(d) 9. w-bin

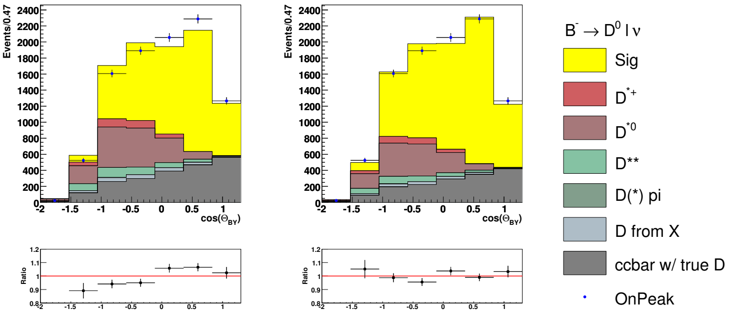

(e) 10. w-bin

Figure 6.15: The plots show $\cos\theta_{\mathrm{BY}}$ distributions before and after applying the fit results after all the selection criteria were applied, only for the 1. to 5.w bin , $B^0 \to D^- \ell^+ \nu$ events

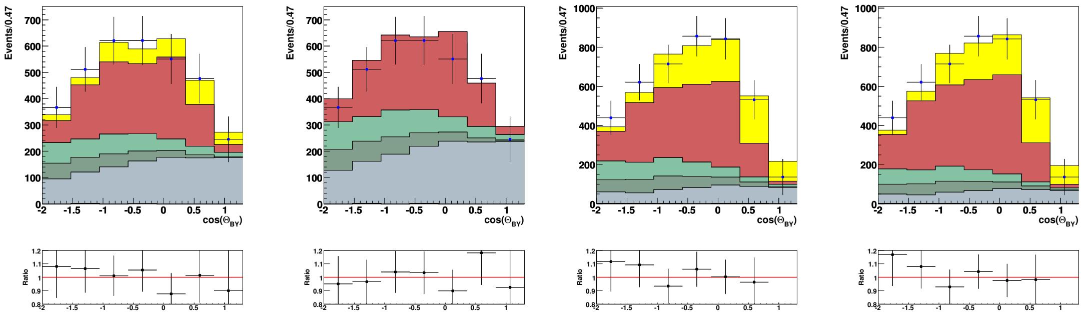

(a) 1. w-bin

(b) 2. w-bin

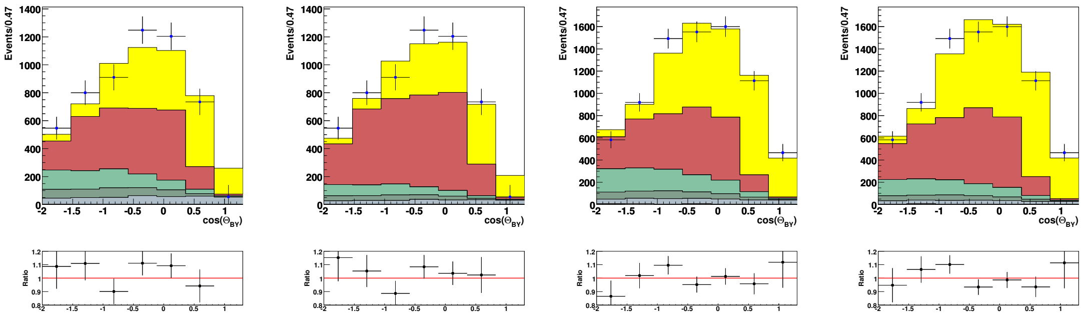

(c) 3. w-bin

(d) 4. w-bin

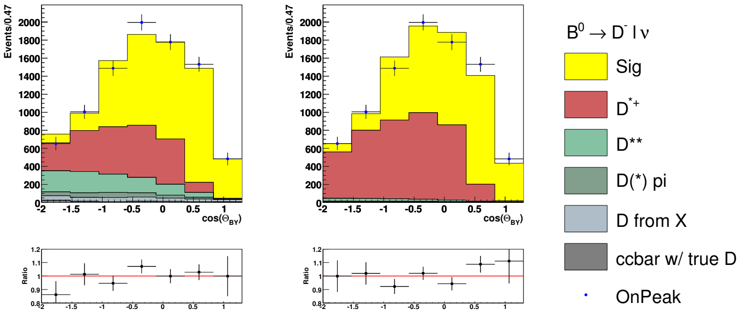

(e) 5. w-bin

Figure 6.16: The plots show $\cos\theta_{\mathrm{BY}}$ distributions before and after applying the fit results after all the selection criteria were applied, only for the 6. to 10.w bin , $B^0 \to D^-\ell^+\nu$ events

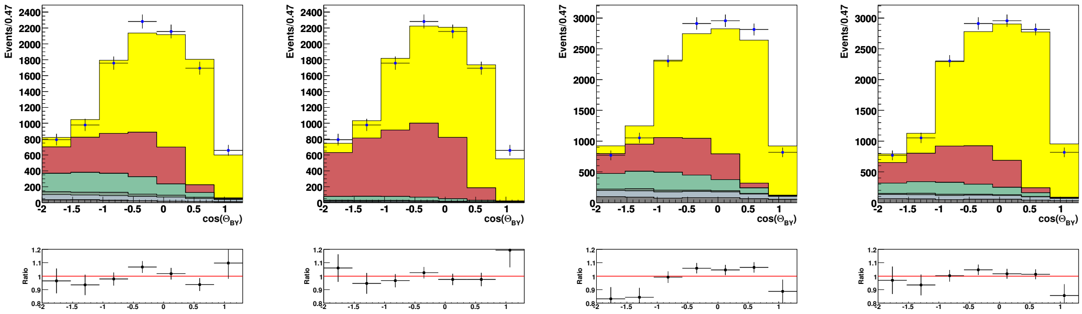

(a) 6. w-bin (b) 7. w-bin

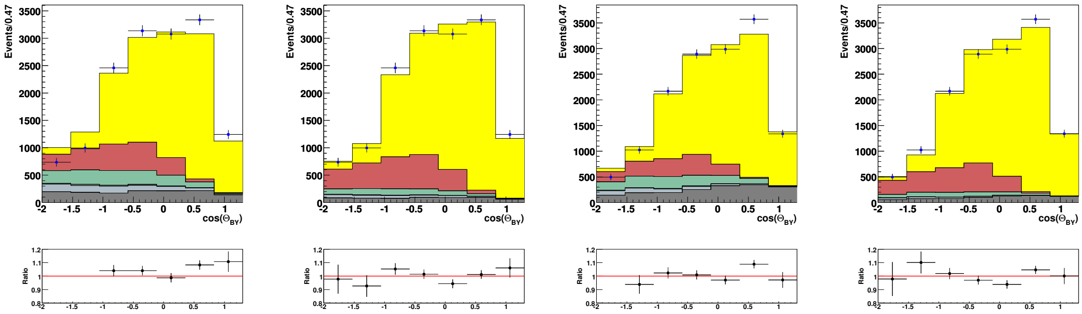

(c) 8. w-bin (d) 9. w-bin

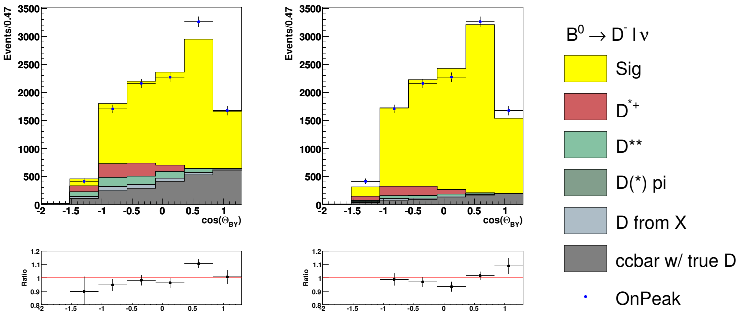

(e) 10. w-bin

7 Extraction of $|V_{cb}|$

In this section it is shown how the resulting signal yields obtained, as described in the previous section, are used to retrieve information about the CKM matrix element $|V_{cb}|$ and the $B \to D$ form factor $\hat{\rho}^2$ using the CLN theoretical framework. Through a minimization of a χ^2 function the parameters: $|V_{cb}|\mathcal{G}(1)$ and $\hat{\rho}^2$ are extracted.

7.1 $|V_{cb}|\mathcal{G}(1)$ Fit

To extract information regarding the CKM matrix element and the form factor, the following χ^2 function is minimized:

$$\chi^2 = \chi^2_{B^- \to D^0 \ell^- \bar{\nu}} + \chi^2_{B^0 \to D^- \ell^+ \nu}. \tag{7.1}$$

which combined the $B^- \to D^0 \ell^- \bar{\nu}$ and $B^0 \to D^- \ell^+ \nu$ fit results.

The $\chi^2_{B^- \to D^0 \ell^- \bar{\nu}}$ and $\chi^2_{B^0 \to D^- \ell^+ \nu}$ can be written as:

$$\chi^2_D = \sum_{i=1}^{N_{bins}} \frac{\left(N_i^{obs} - \sum_{j=1}^{N_{bins}} \epsilon_{i,j} N_j\right)^2}{\sigma^2_{N_i^{obs}} + \sum_{j=1}^{N_{bins}} \sigma^2_{\epsilon_{i,j}} N_j^2}, \tag{7.2}$$

and:

- N_i^{obs} and $\sigma_{N_i^{obs}}$ are the signal yields with their relative error given by the signal yields extraction fit,
- $\epsilon_{i,j}$ and $\sigma_{\epsilon_{i,j}}$ are the matrix and its error-matrix, which takes into account for reconstruction efficiency and smearing in w. It is calculated using Signal MC events,
- N_j is the number of expected events in the j^{th} w-bin, see equations 7.5 and 7.6.
- N_{bins} is the number of w-bins, $N_{bins} = 10$.

7.1.1 The efficiency migration matrix $\epsilon_{i,j}$

The efficiency matrix $\epsilon_{i,j}$ accounts for the smearing due to the detector resolution of w and the reconstruction efficiency. Given

- m_j: number of generated events in the j^{th} w_{true}-bin, without any selection criteria.
- n_j: number of reconstructed events in the j^{th} w_{true}-bin, after all selection criteria.
- $\xi_{i,j}$: this is the matrix, which takes into account the smearing due to the reconstruction, it tells how many events of the j^{th} w_{true}-bin are reconstructed in the i^{th} w_{reco}-bin after all selection criteria. The matrix can be represented as a 2D-plots w_{reco}-vs-w_{true}, as in figure 7.1.

Figure 7.1: Scatter plot of the variable w reconstructed versus the generated. Only in 10 bins. The decay mode are for the upper left plot is $D^0 e\nu$, upper right $D^0\mu\nu$, bottom left plot is $D^+ e\nu$ and bottom right $D^+\mu\nu$.

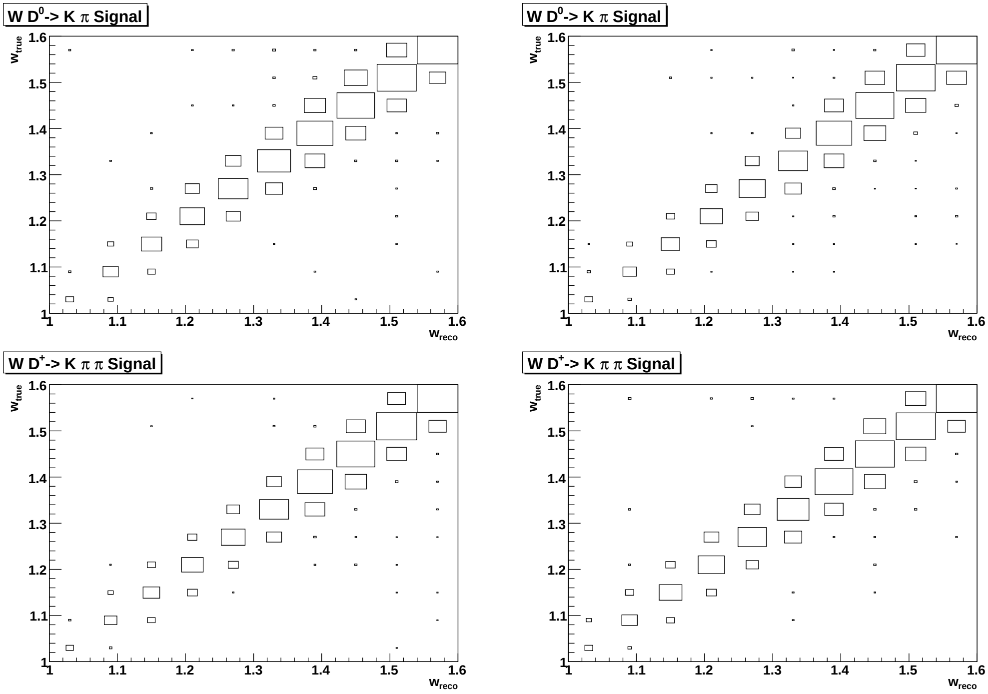

The reconstruction efficiency is simply given by the ratio n_j/m_j. Thus the efficiency migration matrix can be written as:

$$\epsilon_{i,j} = \frac{\xi_{i,j}}{n_j} \cdot \frac{n_j}{m_j} = \frac{\xi_{i,j}}{m_j}. \tag{7.3}$$

and, then, according to the binomial distribution the uncertainties on the matrix elements are:

$$\sigma_{\epsilon_{i,j}} = \sqrt{\frac{\epsilon_{i,j} * (1 - \epsilon_{i,j})}{m_j}}. \tag{7.4}$$

7.1.2 N_j

For the decay $B^- \to D^0 \ell^- \bar{\nu}$ and similarly for the decay $B^0 \to D^- \ell^+ \nu$ the number of expected decay in the j^{th} w bin (N_j) can be written as:

$$N_j^{B^- \to D^0 \ell^- \bar{\nu}} = 4. \cdot f_{+-} N_{\Upsilon(4S)} \cdot \mathcal{B}(D^0) \cdot \tau_{B^-} \int_{w_j} \frac{d\Gamma}{dw} dw, \tag{7.5}$$

$$N_j^{B^0 \to D^- \ell^+ \nu} = 4. \cdot f_{00} N_{\Upsilon(4S)} \cdot \mathcal{B}(D^-) \cdot \tau_{B^0} \int_{w_j} \frac{d\Gamma}{dw} dw. \tag{7.6}$$

where

- f_{+-} is the $\Upsilon(4S) \to B^+B^-$ branching ratio, f_{00} is the $\Upsilon(4S) \to B^0\bar{B}^0$, under the assumption $f_{+-} + f_{00} = 1$, the value is taken from [36].
- τ_{B^-} and τ_{B^0} are the B^- and B^0 lifetime respectively

Table 7.1: Combined fit results using CLN parametrization of the Form Factor

Combined Fit w/ CLN	
$\lvert V_{cb}\rvert \cdot G(1)$	0.0435 ± 0.0011
$\hat{\rho}^2$	1.111 ± 0.055
χ^2/n.d.f.	18.2469 / 18
correlation	$\begin{pmatrix} 1 & 0.9729 \\ 0.9729 & 1 \end{pmatrix}$
BR (%)	2.38 ± 0.03

- $\mathcal{B}(D^0)$ is the $D^0 \to K^-\pi^+$ branching ratio and respectively $\mathcal{B}(D^-)$ is the $D^- \to K^+\pi^-\pi^-$ are the D branching ratio

and

$$\frac{d\Gamma}{dw} = \frac{G_F^2|V_{cb}|^2}{48\pi^3} \cdot (m_{B^+} + m_{D^0})^2 \cdot m_{D^0}^3 \cdot (w^2-1)^{3/2} \cdot |\mathcal{F}_{B\to D}(w)|^2 \tag{7.7}$$

In the framework of the HQET the Form Factor can be written as a Taylor expansion about the point of zero recoil ($w = 1$) in power of $(w-1)$

$$\mathcal{F}_{B\to D}(w) = \mathcal{F}(1)(1 - \hat{\rho}^2(w-1) + \hat{c}(w-1)^2 + O(w-1)^3) \tag{7.8}$$

But the parametrization used in this work is the most up-to-date CLN (see sec. 1.3.2), other parametrizations have been taken into account, the relative results are summarized in appendix A.2.2.

7.2 V_{cb} Fit Results

The fit results using the CLN parametrization are summarized in table 7.1, the figure 7.2 shows the $\mathcal{G}(w)|V_{cb}|$ distribution unfolded for the reconstruction efficiency, but not corrected for smearing in w with the fit results superimposed. The value for Branching Ratio is calculated integrating the differential expression in eq. 7.7. Furthermore an alternative form factor parametrization has been used, it is an extension of the CLN formalism, where the lepton mass is not neglected (see sec. 1.3.2), the results using this extension are in good agreement with the one using the standard CLN. Since most measurements are using the standard CLN model, also in this work the standard CLN has chosen to be the nominal parametrization.

7.2.1 CLN and the lepton mass

In the HQET and CLN model the lepton mass is neglected, as explained in 1.3.2 the lepton mass term can be reintroduced. Results using this ansatz are summarized in table 7.2, figure 7.3 shows the $\mathcal{G}(w)|V_{cb}|$ distribution unfolded for the reconstruction efficiency, but not corrected for smearing in w with the fit results superimposed. The value for Branching Ratio is calculated integrating the differential expression in eq. 7.7. The results are in good agreement with the measurement done using the form factor parametrization where the lepton mass is neglected.

Figure 7.2: $\mathcal{G}(w)|V_{cb}|$ distribution unfolded for the reconstruction efficiency, not corrected for smearing in w with the fit results (line) superimposed the FF parametrization is CLN.

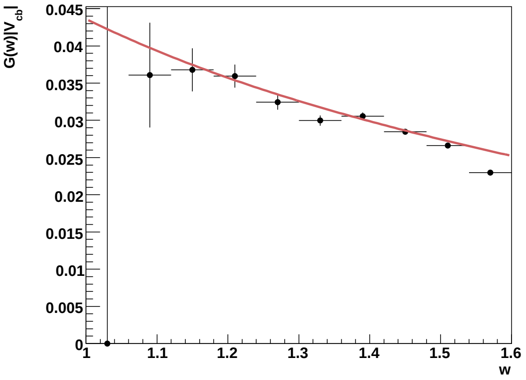

Table 7.2: Combined fit results using CLN parametrization of the Form Factor taking care of the lepton mass

Combined Fit w/ CLN and lep-mass	
$\lvert V_{cb}\rvert \cdot G(1)$	0.0440 ± 0.0011
$\hat{\rho}^2$	1.146 ± 0.053
χ^2/n.d.f.	16.8097 / 18
correlation	$\begin{pmatrix} 1 & 0.9719 \\ 0.9719 & 1 \end{pmatrix}$
BR (%)	2.38 ± 0.03

Figure 7.3: $\mathcal{G}(w)|V_{cb}|$ distribution unfolded for the reconstruction efficiency, not corrected for smearing in w with the fit results (line) superimposed the FF parametrization is CLN with lepton mass.

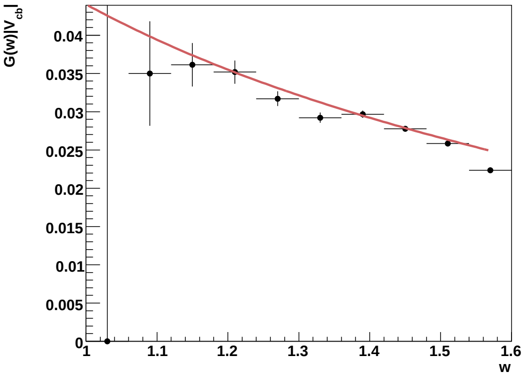

7.2.2 Cross Checks

As cross check fits are performed separately for selected $B \to D e \nu_e$, $B \to D \mu \nu_\mu$, $B \to D^0 \ell \nu$ and $B \to D^+ \ell \nu$ events. Results are shown in table 7.3. Comparing the different fit results with the nominal fit, it is found a good agreement. The same cross check fits are performed using the CLN model with the lepton mass taken into account. Result for selected $B \to D e \nu_e$, $B \to D \mu \nu_\mu$, $B \to D^0 \ell \nu$ and $B \to D^+ \ell \nu$ events are shown in table 7.4. Also in this case a good agreement is found with the nominal fit and between them.

Table 7.3: Combined fit results using CLN parametrization of the Form Factor for the splitted sample

	$B \to D e \nu_e$	$B \to D \mu \nu_\mu$	$B \to D^0 \ell \nu$	$B \to D^+ \ell \nu$
$\lvert V_{cb}\rvert \cdot G(1)$	0.0441 ± 0.0015	0.0426 ± 0.0017	0.0436 ± 0.0016	0.0434 ± 0.0016
$\hat{\rho}^2$	1.116 ± 0.072	1.096 ± 0.086	1.137 ± 0.075	1.087 ± 0.078
χ^2/n.d.f.	6.17818 / 18	19.8555 / 18	10.2689 / 8	6.15291 / 8
correlation	$\begin{pmatrix} 1 & 0.9743 \\ 0.9743 & 1 \end{pmatrix}$	$\begin{pmatrix} 1 & 0.9712 \\ 0.9712 & 1 \end{pmatrix}$	$\begin{pmatrix} 1 & 0.97 \\ 0.97 & 1 \end{pmatrix}$	$\begin{pmatrix} 1 & 0.97 \\ 0.97 & 1 \end{pmatrix}$
BR (%)	2.43 ± 0.04	2.31 ± 0.05	2.51 ± 0.05	2.41 ± 0.04

Table 7.4: Combined fit results using CLN parametrization with lep-mass correction of the Form Factor for the splitted sample

	$B \to D e \nu_e$	$B \to D \mu \nu_\mu$	$B \to D^0 \ell \nu$	$B \to D^+ \ell \nu$
$\lvert V_{cb}\rvert \cdot G(1)$	0.0441 ± 0.0015	0.0439 ± 0.0017	0.0441 ± 0.0016	0.0439 ± 0.0016
$\hat{\rho}^2$	1.116 ± 0.072	1.186 ± 0.078	1.173 ± 0.072	1.123 ± 0.075
χ^2/n.d.f.	6.17799 / 18	18.0328 / 18	9.02567 / 8	5.73115 / 8
correlation	$\begin{pmatrix} 1 & 0.9743 \\ 0.9743 & 1 \end{pmatrix}$	$\begin{pmatrix} 1 & 0.9685 \\ 0.9685 & 1 \end{pmatrix}$	$\begin{pmatrix} 1 & 0.97 \\ 0.97 & 1 \end{pmatrix}$	$\begin{pmatrix} 1 & 0.97 \\ 0.97 & 1 \end{pmatrix}$
BR (%)	2.45 ± 0.04	2.29 ± 0.05	2.52 ± 0.05	2.42 ± 0.04

8 Systematics Uncertainties

The potential sources of systematic uncertainties on the CKM matrix element $|V_{cb}| \cdot \mathcal{G}(1)$ and the form factor parameter $\hat{\rho}^2$ will be studied and determined in the following section. Systematic deviations can arise from uncertainties in the detector simulation, such as uncertainties in the reconstruction efficiency of charged and neutral particles. Systematic uncertainties are also due to non-exact knowledge of the background and its modeling, the fit technique and other sources.

8.1 General evaluation method

The studies and evaluation of the systematic uncertainties on the this measurement are done, if not otherwise stated, as followed: the assumptions on a particular MC quantity, such as background modeling or reconstruction efficiency, are varied within its uncertainties ($\pm 1\sigma$). The full analysis procedure is performed on the modified MC sample, and new values are extracted for $|V_{cb}| \cdot \mathcal{G}(1)$ and $\hat{\rho}^2$. The largest discrepancy respect to the nominal value is taken as systematics, it is calculated as, for ex. $X_{nominal} - X_{sys}$ for a given X measurement.

8.2 Detector effects

In this section are assessed the effect of uncertainties in tracking, photon and other detector uncertainties. Since the normalization and the shape of distribution such ΔE not only depends on the reconstruction of the signal events, namely a lepton and a D meson, but also on the remaining particles in the event, which are used to determined the missing energy and missing momentum for the neutrino reconstruction. It is important to assess correctly the systematics stemming from these effects.

8.2.1 Tracking efficiency

The MC simulation well reproduces tracking efficiencies, as shown on a study using $e^+e^- \rightarrow \tau^+\tau^-$ events[53], where one τ decays leptonically and the other to three charged hadrons (plus an arbitrary number of neutrals). These events are a good control sample for high statistics test since the $e^+e^- \rightarrow \tau^+\tau^-$ cross section is 0.94 nb and the branching fraction to ℓ + 3 hadrons is about 11% [36]. Moreover, the momentum distribution of tracks from τ decays is similar to the one from B decays. Data and Monte Carlo efficiencies are in good agreement within the statistical errors.To assign a systematic uncertainty on the charged particle tracking efficiency, a common prescription [54] within BABAR measurements has been followed. The Monte Carlo has been re-weighted by randomly eliminating tracks with probabilities detailed in Table 8.1, and the difference observed with respect to the default measurements is taken as the systematic uncertainty.

Table 8.1: Uncertainties as function of the Run Cycles for Charged Tracks.

Run	Sys. Uncert. (%)
Run 1	0.44
Run 2	0.32
Run 3	0.18
Run 4	0.54
Run 5	0.57

8.2.2 Neutral Reconstruction

Studies are performed within the *BABAR* collaboration[55] to find disagreement in the photon detection efficiency and production, and energy deposition in the EMC between Data and MC. A good agreement between them has been found, and the ratio is compatible with the unity. One study [56] is performed using the τ hadronic decays that represent an abundant source of neutral pions. This have been studied on samples of $e^+e^- \to \tau^+\tau^-$ events. The $\tau \to e\nu\bar{\nu}$ decay is identified and the recoiling τ decays are studied. The ratio $R = N(\tau \to h^{\pm}\pi^0\nu_\tau)/N(\tau \to h^{\pm}\pi^0\pi^0\nu_\tau)$ is computed both for data and Monte Carlo as a function of the π^0 energy in order to evaluate possible differences in efficiency. The agreement has been found to be good and the ratio is compatible with unity in the full range. A systematic uncertainty of 1.8% per photon (up to 2.5 GeV) is assigned, due to uncertainties in the hadronic interactions in the EMC, to the photon background being not perfectly modeled in the Monte Carlo, and to the uncertainty in the τ branching fractions in $\pi\nu_\tau$ and $\rho\nu_\tau$ final states. In the range $1-7$ GeV the study [57] on $e^+e^- \to \mu^+\mu^-\gamma$ is used and it quotes an uncertainty of 0.7% per photon. To assign a systematic uncertainty on the single photon efficiency, a common prescription[55] within *BABAR* measurements has been followed: no correction has been applied to Monte Carlo for photons up to 1 GeV, whereas for photons from 1 GeV a single photon efficiency correction of 0.993 is applied. The Monte Carlo has been re-weighted by randomly eliminating photons with energy dependent probabilities detailed in Table 8.2, and the difference observed with respect to the default measurements is taken as the systematic uncertainty.

Table 8.2: Uncertainties as function of the photon energy in the laboratory frame.

Energy	Sys. Uncertainty (%)
$E_\gamma < 1GeV$	1.8
$E_\gamma > 1GeV$	0.7

8.2.3 K^0_L Production and Energy

Systematic uncertainties in the simulation of K^0_L interactions have been estimated according to the results shown in [37]. Several corrections are applied on the Monte Carlo in order to reproduce data. The *energy deposition* of calorimeter clusters positive identified as K^0_L are corrected by ad-hoc factors. The systematics uncertainties stemming from this correction are determined by varying the scaling factors within their uncertainties. The K^0_L *detection efficiency* is corrected by rejecting neutral clusters, which are positively identified as K^0_L, with a probability, which is a function of the true K^0_L momentum. To assess the systematics the rejection probability is varied by its uncertainties as given in [37]. A correction due to the differences between the data and the simulation for the K^0_L *production rate* is also applied, based on studies detailed in [38]. To evaluate the systematics the corrections are varied according to their uncertainties as given in[38].

8.2.4 Particle Identification

The systematic uncertainties related to lepton and kaon identification efficiencies and misidentification probabilities are derived from control samples. For electron efficiency, radiative Bhabha events are used. Muons with a momentum spectrum covering the range of interest are extracted from the $e^+e^- \to \mu^+\mu^-\gamma$ and $e^+e^- \to e^+e^-\mu^+\mu^-$ channels. The pions misidentification probabilities are evaluated using samples of $K_S^0 \to \pi^+\pi^-$ and three-prong τ decays. Kaon misidentification probabilities are obtained by using samples selecting $D^{*+} \to D^0\pi^+$, $D^0 \to K\pi$ decays, where only the kinematic information is used to identify the kaon. The systematic uncertainties due to particle identification have been estimated by varying the electron, kaon and muon identification efficiency by its uncertainty namely 2% for electrons and kaon [45, 58], and 3% for the muons [47]. Separately the relative mis-identification probabilities are varied within their uncertainties (15%) and the full analysis is repeated. Then, the difference with respect to the nominal value is taken as systematic uncertainty.

8.2.5 Bremsstrahlung

External bremsstrahlung due to the interaction of electrons with the detector material modifies the measured electron energy and momentum spectra. Studies [59] have been performed to evaluate MC uncertainties in the detector geometry using BhaBha events. A disagreement of 0.14% radiation length has been found. The method suggested in [59] to evaluate this uncertainty is the following: the Monte Carlo electron energy spectrum has been re-weighted in order to match different scenarios of less or additional detector material. Accordingly bremsstrahlung photons have been re-weighted by 1 ± 0.028 to reflect different cases of additional (+) or less (−) detector material.

8.3 Physics modeling

The uncertainties in the physics modeling and simulation of MC samples especially in the main backgrounds introduce further systematic uncertainties into the analysis.

8.3.1 $BR(B \to D^* X \ell\nu)$

Up-to-date measurements of branching ratios for semileptonic decays differ from the values used in the MC simulation. These discrepancies have been corrected by re-weighting each semileptonic decay to match the current values (shown on table 4.4). The estimation of the systematic uncertainties is done following the recipe suggested by the semileptonic working group[42]. The Branching ratio of each semileptonic decay mode is varied separately by its error ($\pm 1\sigma$). To keep the total semileptonic rate $\mathcal{BR}(B \to X_c \ell\nu)$ unchanged, the least known branching ratios are varied accordingly, i.e. $\mathcal{BR}\left(B \to (D^{**}_{\text{broad}}, D^{(*)}\pi)\ell\nu\right)$.

8.3.2 $\mathcal{BR}(D^0 \to K^-\pi^+)$ and $BR(D^+ \to K^-\pi^+\pi^+)$

The values used in the MC to simulate the D-meson branching ratios are in slightly disagreement with the up-to-date measurements. These discrepancies have been corrected by re-weighting to match the current values (shown on table 4.4). To asses a systematic uncertainty $D^0 \to K^-\pi^+$ and $D^+ \to K^-\pi^+\pi^+$ branching ratio are varied within their uncertainties ($\pm 1\sigma$) one at the time, and the full analysis is repeated.

8.3.3 The Form Factor of $B \rightarrow D^{(*,**)}\ell\nu$

The Form Factor parameters for the $B \rightarrow D^{*}\ell\nu$ decays are varied according to their uncertainties [41] taking into account the correlation between them [60]. In the case of $B \rightarrow D^{**}\ell\nu$ events, the systematic uncertainties are computed comparing the sample re-weighted using the LLSW model with the default in the *BABAR* MC, the ISGW2[23] model.

8.4 Other sources

8.4.1 $N_{\Upsilon(4S)}$, B counting

As reported here [31] the uncertainty in the measurement of the number of $\Upsilon(4S)$ is of 1.1%. The $N_{\Upsilon(4S)}$ is varied by its uncertainty only in the $|V_{cb}|$-Fit, and compared with the nominal fit results.

8.4.2 f_{+-}

The value for f_{+-} is taken from the [36] and it is fixed in the $|V_{cb}|$-Fit. To evaluate the uncertainty f_{+-} is varied by its uncertainty and compared with the nominal fit results.

8.4.3 Signal yields Fit

To determine the uncertainties of the fit technique, the binning of the histograms used as input distributions have been changed. Results are compared with the nominal fit results.

8.4.4 Final State Radiation

Final State Radiation (FSR): QED interference and multiple-photon radiation are modeled in the *BABAR* MC using the algorithm `PHOTOS` [35]. To estimate the systematics due to the algorithm the distributions used in the 2D fit to get the partial branching ratio is generated without the full *BABAR* detector response with the `PHOTOS` algorithm switched on and off. The ratio between the distributions with the algorithm on and off is used to re-weight the signal events belonging to the generic MC. Following estimates[35] of uncertainties on the theoretical calculations that went into `PHOTOS`, a 30% uncertainty on this correction is applied.

Table 8.3: Systematic and Statistical uncertainties, the relative uncertainties in % are given for $V_{cb}\mathcal{G}(1)$, whereas the absolute uncertainties are given for ρ^2, the last two line show the absolute values for each measurements.

Syst.	$V_{cb}G(1)(\%)$	ρ^2	$BR(\%)$
$\mathcal{BR}(D^{**}_{broad}\ell\nu)$	0.07	0.003	0.12
$\mathcal{BR}(D^{**}_{narrow}\ell\nu)$	0.01	0.002	0.12
$\mathcal{BR}(D^{*}\ell\nu)$	0.07	0.001	0.07
$\mathcal{BR}(D^{*}\pi\ell\nu)$	−0.00	0.000	0.00
$D^{*}\ell\nu$ FF	1.08	0.018	0.63
$D^{**}\ell\nu$ FF ISGW2	0.38	0.003	0.57
$D^{**}\ell\nu$ FF	0.73	0.012	0.72
tracking	−1.16	−0.002	−2.14
photons	−0.92	−0.012	−0.79
K^0_L Eff	−0.29	−0.005	−0.18
K^0_L Energy	−0.81	−0.015	−0.36
K^0_L Prod	−0.63	−0.009	−0.50
bremsstrahlung	−0.47	−0.007	−0.32
PID elec	1.18	0.008	1.69
PID muon	1.95	0.019	2.34
PID kaon	1.80	0.010	2.80
$N_{\Upsilon(4S)}$	−0.56	−0.000	−1.11
PHOTOS	0.69	0.011	0.45
BR(D)	1.26	0.012	1.85
Fit	−0.27	−0.008	0.11
f_{+-}	0.09	0.000	−0.19
Tot. Syst.	4.12	0.04	5.573
Tot. Stat.	2.64	0.06	1.304
Tot. Syst. (abs.)	0.0018	0.04	0.001
Tot. Stat. (abs.)	0.0011	0.06	0.0003

9 Results

In this chapter the final results of the measurement of the semileptonic $B \to D\ell\nu$ decays are reported, in particular the extraction of $\mathcal{G}(1)|V_{cb}|$ and the $B \to D$ form factor parameter in the CLN model $\hat{\rho}^2$. In table 9.1 the results for the nominal fit to $B \to D\ell\nu$, and for sub samples $B^- \to D^0\ell^-\bar{\nu}$ and $B^0 \to D^-\ell^+\nu$ are shown. All results are in good agreement within uncertainties as also shown on figure 9.1.

Table 9.1: Fit results for the $B^- \to D^0\ell^-\bar{\nu}$, $B^0 \to D^-\ell^+\nu$ and $B \to D\ell\nu$ sample. All values are given with statistical and systematic uncertainties. The branching ratio is also reported and in the $B \to D\ell\nu$ sample refers to $\overline{B}^0$ decays.

	$B \to D^0\ell\nu$	$B \to D^+\ell\nu$	$B \to D\ell\nu$
$\mathcal{G}(1)\lvert V_{cb}\rvert \cdot 10^3$	$43.6 \pm 1.6 \pm 1.5$	$43.4 \pm 1.6 \pm 2.6$	$43.5 \pm 1.1 \pm 1.8$
$\hat{\rho}^2$	$1.14 \pm 0.07 \pm 0.07$	$1.09 \pm 0.08 \pm 0.08$	$1.11 \pm 0.05 \pm 0.04$
correlation	0.97	0.97	0.97
BR (%)	$2.51 \pm 0.05 \pm 0.10$	$2.41 \pm 0.04 \pm 0.20$	$2.38 \pm 0.03 \pm 0.10$

Figure 9.1: $\Delta\chi^2 = 1$ ellipses in the plane $\mathcal{G}(1)|V_{cb}|$ and $\hat{\rho}^2$, taking into account for both statistical and systematics uncertainties. For $B^- \to D^0\ell^-\bar{\nu}$ in blue, $B^0 \to D^-\ell^+\nu$ in red (see table 9.1 for numerical values) and the combined results in black.

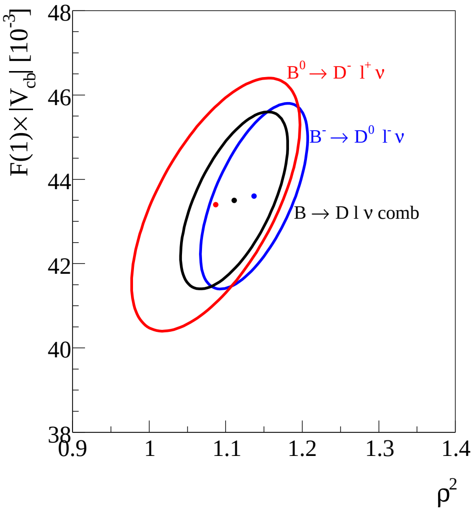

As shown on figure 9.2 the nominal results have also been compared, with a *BABAR* analysis studying the same final states [10], on the recoil of a fully reconstructed B meson from an $\Upsilon(4S)$ decay, a tagged analysis. The major advantage of the tagged techniques over the untagged is a relatively high purity and signal over background ratio. The major disadvantage is the relatively poor efficiency.

Besides the final results are also compared with past measurements by ALEPH[7], CLEO[8] and BELLE[9], and two recent *BABAR* independent measurements, one is based on tagged events [10],

Figure 9.2: $\mathcal{G}(w)|V_{cb}|$ distribution unfolded for the reconstruction efficiency, not corrected for smearing in w with the fit results (line) superimposed the FF parametrization is CLN. The comparison is made between the *BABAR* tagged[10] analysis results and this analysis (untagged).

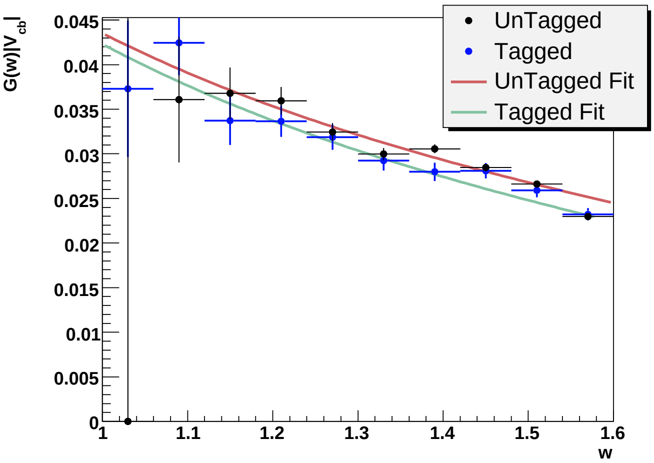

the other on a semi-inclusive reconstruction of $B \to DX\ell\nu$ decays [11], where the D-meson and the lepton are identified and a global fit to them allows to measure simultaneously both the $B \to D\ell\nu$ and $B \to D^*\ell\nu$ decays. The agreement with past measurement is good as shown on figure 9.3.

Figure 9.3: Summary of the existing results for the $\mathcal{G}(1)|V_{cb}|$ on the left-hand plot, and $\hat{\rho}^2$ on the right-hand plot, compared with results of this work. The other measurements shown are from ALEPH[7], CLEO[8] and BELLE[9], *BABAR* and *BABAR* Tagged [10], and *BABAR* Global Fit [11].

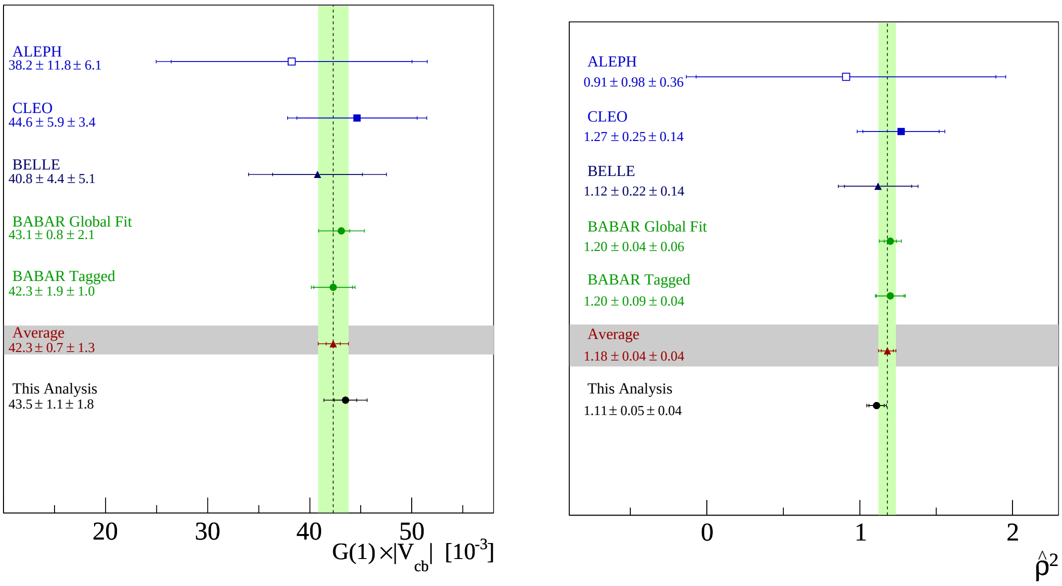

Conclusions

In this thesis the study of the exclusive semileptonic decays $B^- \to D^0\ell^-\bar{\nu}$ and $B^0 \to D^-\ell^+\nu$ ($\ell = e, \mu$) has been presented. These decays provide a clean environment to study $b \to c$ transitions and to determine the $|V_{cb}|$ parameter of the CKM matrix. In particular exclusive $B \to D\ell\nu$ semileptonic decays have been used to measure $\mathcal{G}(1)|V_{cb}|$ and the $B \to D$ form factor parameter $\hat{\rho}^2$ using the CLN parametrization [24]. The analysis uses a sample of $(383.6 \pm 4.2) \times 10^6$ events where $\Upsilon(4S) \to B\overline{B}$ collected at the BABAR experiment. Semileptonic $B \to D\ell\nu$ decays has been exclusively reconstructed both as $B^- \to D^0\ell^-\bar{\nu}$ and $B^0 \to D^-\ell^+\nu$, both identified electrons and muons have been used and the presence of the neutrino is inferred from the missing momentum and energy in the whole event. The D^0 mesons are reconstructed in the $D^0 \to K^-\pi^+$ decay and the D^+ mesons in the $D^+ \to K^-\pi^+\pi^+$ decay. The results of this study are:

$$\mathcal{G}(1)|V_{cb}| = (43.5 \pm 1.1 \pm 1.8) \times 10^{-3}, \tag{9.1}$$

$$\hat{\rho}^2 = 1.11 \pm 0.05 \pm 0.04, \tag{9.2}$$

where the first uncertainties are statistical and the second systematic. The current measurements of $\mathcal{G}(1)|V_{cb}|$ from $B \to D\ell\nu$ decays have reached an experimental precision of about 5%, and a good agreement with previous measurements have been found. Furthermore this work leads to the most precise measurement for both $\mathcal{G}(1)|V_{cb}|$ and $\hat{\rho}^2$, even if it is dominated by systematics. The main systematic uncertainties are due to particle identification and background description, namely the form factor parametrization.

The results have been used to determine the branching fraction $\mathcal{B}(B \to D\ell\nu)$, integrating the differential decay rate $d\Gamma/dw$ over the allowed values of w, and it results as:

$$\mathcal{B}(B \to D\ell\nu) = (2.38 \pm 0.03 \pm 0.10), \tag{9.3}$$

From the measurement of $\mathcal{G}(1)|V_{cb}|$ the CKM matrix element $|V_{cb}|$ can be extract using results of the unquenched lattice calculation [2] ($\mathcal{G}(1) = 1.074 \pm 0.018 \pm 0.016$) corrected by QED effects (namely by multiplying the results by a factor of 1.007),

$$|V_{cb}| = (40.2 \pm 1.0 \pm 1.7 \pm 0.9) \times 10^{-3}, \tag{9.4}$$

the third uncertainty is due to the theoretical uncertainties on $\mathcal{G}(1)$. The value extracted for $|V_{cb}|$ is in good agreement with other measurements [36], obtained using $B \to D\ell\nu$ decays $|V_{cb}| = (39.8 \pm 2.9) \times 10^{-3}$, from exclusive $B \to D^*\ell\nu$ decay $|V_{cb}| = (38.6 \pm 1.3) \times 10^{-3}$ or inclusive semileptonic $b \to c$ measurements $|V_{cb}| = (41.6 \pm 0.6) \times 10^{-3}$.

Bibliography

[1] N. Uraltsev, "A BPS expansion for B and D mesons," *Phys. Lett.* **B585** (2004) 253–262, `arXiv:hep-ph/0312001`.

[2] M. Okamoto *et al.*, "Semileptonic $D \to \pi/K$ and $B \to \pi/D$ decays in $2+1$ flavor lattice QCD," *Nucl. Phys. Proc. Suppl.* **140** (2005) 461–463, `arXiv:hep-lat/0409116`.

[3] **Fermilab Lattice and MILC** Collaboration, J. Laiho, "$B \to D^* \ell \nu$ with $2+1$ flavors," *PoS* **LAT2007** (2007) 358, `arXiv:0710.1111 [hep-lat]`.

[4] **The Heavy Flavor Averaging Group** Collaboration, E. Barberio *et al.*, "Updates of Semileptonic Results for ICHEP08 2008,". `http://www.slac.stanford.edu/xorg/hfag/semi/ichep08/home.shtml`.

[5] G. M. de Divitiis, E. Molinaro, R. Petronzio, and N. Tantalo, "Quenched lattice calculation of the $B \to D\ell\nu$ decay rate," *Phys. Lett.* **B655** (2007) 45–49, `arXiv:0707.0582 [hep-lat]`.

[6] G. M. de Divitiis, R. Petronzio, and N. Tantalo, "Quenched lattice calculation of the vector channel $B \to D^*\ell\nu$ decay rate," *Nucl. Phys.* **B807** (2009) 373–395, `arXiv:0807.2944 [hep-lat]`.

[7] **ALEPH** Collaboration, D. Buskulic *et al.*, "Measurements of $|V_{cb}|$, form factors and branching fractions in the decays $\overline{B}^0 \to D^{*+}\ell^-\overline{\nu}_\ell$ and $\overline{B}^0 \to D^+\ell^-\overline{\nu}_\ell$," *Phys. Lett.* **B395** (1997) 373–387.

[8] **CLEO** Collaboration, J. E. Bartelt *et al.*, "Measurement of the $B \to D\ell\nu$ branching fractions and form factor," *Phys. Rev. Lett.* **82** (1999) 3746, `arXiv:hep-ex/9811042`.

[9] **Belle** Collaboration, K. Abe *et al.*, "Measurement of $\mathcal{B}(\overline{B}^0 \to D^+\ell^-\overline{\nu}_\ell)$ and determination of $|V_{cb}|$," *Phys. Lett.* **B526** (2002) 258–268, `arXiv:hep-ex/0111082`.

[10] **BABAR** Collaboration, B. Aubert *et al.*, "Measurement of $|V_{cb}|$ and the form-factor slope for $\overline{B} \to D\ell\overline{\nu}$ decays on the recoil of fully reconstructed B mesons," `arXiv:0807.4978 [hep-ex]`.

[11] **BABAR** Collaboration, B. Aubert *et al.*, "Measurements of the Semileptonic Decays $\overline{B} \to D\ell\overline{\nu}$ and $\overline{B} \to D^*\ell\overline{\nu}$ Using a Global Fit to $DX\ell\overline{\nu}$ Final States," `arXiv:0809.0828 [hep-ex]`.

[12] M. Kobayashi and T. Maskawa, "CP Violation in the Renormalizable Theory of Weak Interaction," *Prog. Theor. Phys.* **49** (1973) 652–657.

[13] L. L. Chan and W. L. Keung *Phys. Rev. Lett.* **53** (1984) 1802.

[14] L.-L. Chau and W.-Y. Keung, "Comments on the Parametrization of the Kobayashi-Maskawa Matrix," *Phys. Rev. Lett.* **53** (1984) 1802.

[15] L. Wolfenstein, "Parametrization of the Kobayashi-Maskawa Matrix," *Phys. Rev. Lett.* **51** (1983) 1945.

[16] A. J. Buras, M. E. Lautenbacher, and G. Ostermaier, "Waiting for the top quark mass, $K^+ \to \pi^+\nu\overline{\nu}$, B_s^0 - $\overline{B}_s^0$ mixing and CP asymmetries in B decays," *Phys. Rev.* **D50** (1994) 3433–3446, `arXiv:hep-ph/9403384`.

[17] M. Neubert, “Heavy quark symmetry,” *Phys. Rept.* **245** (1994) 259–396, `arXiv:hep-ph/9306320`.

[18] N. Isgur, D. Scora, B. Grinstein, and M. B. Wise, “Semileptonic B and D Decays in the Quark Model,” *Phys. Rev.* **D39** (1989) 799.

[19] M. Wirbel, B. Stech, and M. Bauer, “Exclusive Semileptonic Decays of Heavy Mesons,” *Z. Phys.* **C29** (1985) 637.

[20] J. G. Korner and G. A. Schuler, “Exclusive Semileptonic Heavy Meson Decays Including Lepton Mass Effects,” *Z. Phys.* **C46** (1990) 93.

[21] M. Neubert and V. Rieckert, “New approach to the universal form-factors in decays of heavy mesons,” *Nucl. Phys.* **B382** (1992) 97–122.

[22] N. Isgur and M. B. Wise, “Weak Decays of Heavy Mesons in the Static Quark Approximation,” *Phys. Lett.* **B232** (1989) 113.

[23] N. Isgur and M. B. Wise, “Weak transition form-factors between Heavy Mesons,” *Phys. Lett.* **B237** (1990) 527.

[24] I. Caprini, L. Lellouch, and M. Neubert, “Dispersive bounds on the shape of $\overline{B} \to D^{(*)}\ell\overline{\nu}$ form factors,” *Nucl. Phys.* **B530** (1998) 153–181, `arXiv:hep-ph/9712417`.

[25] J. C. Dingfelder, E. Feltresi, and A. Snyder, “On biases due to neglecting the muon mass in the determination of the form factors and $|V_{cb}|$ using exclusive $B \to D^{(*)}\mu\nu$ decays,” *BABAR Analysis Document* **2099** (2008) .

[26] **BABAR** Collaboration, B. Aubert *et al.*, “The BABAR detector,” *Nucl. Instrum. Meth.* **A479** (2002) 1–116, `arXiv:hep-ex/0105044`.

[27] “PEP-II: An Asymmetric B Factory. Conceptual Design Report. June 1993,”. SLAC-418.

[28] **BABAR** Collaboration, e. Harrison, P. F. and e. Quinn, Helen R., “The BABAR physics book: Physics at an asymmetric B factory,”. Papers from Workshop on Physics at an Asymmetric B Factory (BABAR Collaboration Meeting), Rome, Italy, 11-14 Nov 1996, Princeton, NJ, 17-20 Mar 1997, Orsay, France, 16-19 Jun 1997 and Pasadena, CA, 22-24 Sep 1997.

[29] **BABAR** Collaboration, M. H. Kelsey, “Performance and aging of the BABAR drift chamber,” *Nucl. Instrum. Meth.* **A535** (2004) 206–211.

[30] F. Anulli *et al.*, “The muon and neutral hadron detector for BABAR,” *Nucl. Instrum. Meth.* **A409** (1998) 542–546.

[31] **BABAR** Collaboration, C. Hearty, “Measurement of the Number of $\Upsilon(4S)$ Mesons Produced in Run 1 (B Counting),” *BABAR Analysis Document* **134** (2001) .

[32] D. J. Lange, “The EvtGen particle decay simulation package,” *Nucl. Instrum. Meth.* **A462** (2001) 152–155.

[33] T. Sjostrand, “High-energy physics event generation with PYTHIA 5.7 and JETSET 7.4,” *Comput. Phys. Commun.* **82** (1994) 74–90.

[34] **GEANT4** Collaboration, S. Agostinelli *et al.*, “GEANT4: A simulation toolkit,” *Nucl. Instrum. Meth.* **A506** (2003) 250–303.

[35] E. Barberio and Z. Was, “PHOTOS: A Universal Monte Carlo for QED radiative corrections. Version 2.0,” *Comput. Phys. Commun.* **79** (1994) 291–308.

[36] **Particle Data Group** Collaboration, C. Amsler *et al.*, “Review of particle physics,” *Phys. Lett.* **B667** (2008) 1.

[37] **BABAR** Collaboration, M. Bona, G. Cavoto, D. Cote, E. D. Marco, and M. Pelliccioni, “A study of K_L^0 identification and efficiencies ,” *BABAR Analysis Document* **1191** (2006) .

[38] **BABAR** Collaboration, W. H. Wulsin, J. C. Dingfelder, and V. Luth, "K_S^0 Production Spectra," *BABAR Analysis Document* **1642** (2006) .

[39] A. K. Leibovich, Z. Ligeti, I. W. Stewart, and M. B. Wise, "Semileptonic B decays to excited charmed mesons," *Phys. Rev.* **D57** (1998) 308–330, `arXiv:hep-ph/9705467`.

[40] D. Cote, S. Brunet, P. Taras, and B. Viaud, "Re-weighting of the form factors in exclusive $B \to X\ell\nu$ decays," *European Physical Journal C* **38** (2004) 105, `arXiv:0409046v1 [hep-ex]`.

[41] **BABAR** Collaboration, B. Aubert *et al.*, "Determination of the Form Factors for the Decay $B^0 \to D^{*-}\ell^+\nu_\ell$ and of the CKM Matrix Element $|V_{cb}|$," *Phys. Rev.* **D77** (2008) 032002, `arXiv:0705.4008 [hep-ex]`.

[42] **BABAR** Collaboration, V. Lüth and D. L. Pegna, "Semileptonic AWG : $B \to X_c\ell\nu$ Re-weighting 28th July 2009,". `https://www.slac.stanford.edu/BFROOT/www/doc/BbrMeetingOrganizer/vol02/pro/mtg001505/itm0004679/SL_BF_slides_new.pdf`.

[43] P. Billoir, R. Fruhwirth, and M. Regler, "Track element merging strategy and vertex fitting in complex modular Detectors," *Nucl. Instrum. Meth.* **A241** (1985) 115–131.

[44] **BABAR** Collaboration, M. A. Mazur, "Measurement of the exclusive branching fractions $B \to D^{(*)}\tau\nu$," *BABAR Analysis Document* **1111** (2007) .

[45] **BABAR** Collaboration, T. Brandt, "Likelihood-based Electron Identification," *BABAR Analysis Document* **396** (2002) .

[46] **BABAR** Collaboration, R. Faccini *et al.*, "Bremsstrahlung recovery for J/ψ decays," *BABAR Analysis Document* **12** (2000) Appendix B.

[47] **BABAR** Collaboration, H. Band, J. Hollar, and A. Mohapatra, "Studies of A Neural Net Based Muon Selector for the BABAR Experiment," *BABAR Analysis Document* **474** (2004) .

[48] **BABAR** Collaboration, M. Carpinelli and F. Martinez-Vidal, "The BABAR Vertexing," *BABAR Analysis Document* **102** (2005) .

[49] **BABAR** Collaboration, P. Jackson and R. Kowalewski, "Tagging using $B \to D\ell\nu X$ decays," *BABAR Analysis Document* **537** (2003) .

[50] G. C. Fox and S. Wolfram, "Event Shapes in e^+e^- Annihilation," *Nucl. Phys.* **B149** (1979) 413.

[51] R. J. Barlow and C. Beeston, "Fitting using finite Monte Carlo samples," *Comput. Phys. Commun.* **77** (1993) 219–228.

[52] F. James and M. Roos, "Minuit: A System for Function Minimization and Analysis of the Parameter Errors and Correlations," *Comput. Phys. Commun.* **10** (1975) 343–367.

[53] **BABAR** Collaboration, I. Nugent, "Tau31 Tracking Efficiency Study For 2004," *BABAR Analysis Document* **931** (2006) .

[54] **BABAR** Collaboration, "Tracking Efficiency Task Force on R18,". `http://www.slac.stanford.edu/BFROOT/www/Physics/TrackEfficTaskForce/TrackingTaskForce-2006.html`.

[55] **BABAR** Collaboration, "Recipe for Neutral Corrections,". `http://www.slac.stanford.edu/BFROOT/www/Physics/Analysis/AWG/Neutrals/validation/recipie18.html`.

[56] **BABAR** Collaboration, M. T. Allen, M. T. Naisbit, and A. Roodman, "A Study of π^0 Efficiency," *BABAR Analysis Document* **870** (2004) .

[57] **BABAR** Collaboration, D. J. Payne, "High Energy Single Photon Efficiency Using $e^+e^- \to \mu^+\mu^-\gamma$ events," *BABAR Analysis Document* **1110** (2005) .

[58] **BABAR** Collaboration, G. Mancinelli and S. M. Spanier, “Kaon Selection at BABAR,” *BABAR Analysis Document* **116** (2001) .

[59] **BABAR** Collaboration, F. Bernlochner, H. Lacker, A. Volk, *et al.*, “On the effect of additional Bremsstrahlung due Detector geometry on MC simulated electrons energy spectra,” *BABAR Analysis Document* **1911** (2008) .

[60] **BABAR** Collaboration, S. Menke, “Treatment of correlated systematic errors,” *BABAR Analysis Document* **387** (2002) .

Acknowledgments

I would like to take the opportunity to express my sincere gratitude to the people: faculty, colleagues, friends and family who made it possible to achieve this dissertation.

Zu aller erst ist hier Herr Prof. Dr. Bernhard Spaan zu nennen, der meine wissenschaftliche Ausbildung geprägt hat. Ich möchte Ihnen für die freundliche Überlassung des hochinteressanten Themas herzlich danken. Besonders bedanken will ich mich auch für die Freiheit, die Sie mir während des gesamten Forschungsprojektes gewährt haben, für das große Vertrauen und die Förderung, die ich von Ihnen immer erfahren habe, sowie für viele anregende Diskussionen und jede erdenkliche, hilfreiche Unterstützung, was maßgeblich zum Gelingen dieser Arbeit beitrug.

I am strongly indebted to Dr. Jochen Dingfelder, for his fruitful supervision and his enormous patience. Within these years, I shared his rich ideas of science, his great friendship, his wonderful flat in San Francisco, and a few dirty martini in the best alternative place in the City. I was benefited significantly from his deep knowledge and many critical discussions as well as constant assistance in all possible ways.

I want to thank all members and colleagues that I met at the Institutes für Kern- und Teilchenphysik at the TU Dresden: Denis, Verena, Thomas, Jan Erik, Andreas for the friendly, helpful, and frequent discussions, the help they provided me in many ways as well as they introduce me to the marvelous Saxon dialect.

Many thanks go to the *BaBarians*: Alessia, Neus, Justine, Nicola, Antonio, Diego, Andreas, Mario, David, Silvano, Florian, Maurizio, Elisa, Riccardo, and many many others with which I shared short and long periods at SLAC working on *BABAR* , but also having fun.

I cannot avoid to mention and to thank my friends and colleagues in Dortmund: Mirco, Magnus, Matthias, Klaus, and in particular Heiko for his invaluable help in the fight against the bureaucracy jungle (e.g. das Ausfüllen der Steuererklärung, das Konto zu schliesen). Moritz and Jesko for the great moments we spent together around the world, for your help in the proof reading of this work, for cooking and drinking, for "Kicker spielen".

I would like to remember also my numerous flat-mates I had during my stay around the world: Dennis, Jesko, Alessia, Jochen, Devis, Davis, Riccardo, Moritz, Stephan. I have always felt very welcome, like at home, thank you!

I am also grateful to my best Italians friend, those who are spread in the world, and those who don't: Gianni, Michele, Michele, Devis, Alessandro, Monica, Massimo, Marco, Stefano. Questi anni via dall'Italia sono stati ricchi da un punto di vista umano e professionale. Sono peró felice che i legami con la mia terra e con gli amici siano rimasti saldi e forti.

Grazie alla mia famiglia per il sostegno e la comprensione, e per avermi dato gli strumenti per arrivare fin qui.

Last but not least, grazie Laura, senza di te tutto questo non avrebbe un senso.

A Cross-Check

A.1 Partial ($\mathcal{BR}$) Fit

A.1.1 Merging first two w bins

Since the first bins of w are difficult to fit, due to the very high background and the physical reason, in order to avoid this issue, merging the first two bins of w has been tested. The results are reported on tablesA.1 and A.2.

The $|V_{cb}|$ results are given on table A.3 and A.4.

A.1.2 Fixing the Backgrounds on the first w bin

In the first w bin the background is very high, it leads to a negative scaling factors and negative signal yields. One method to get physical results is to fix the background in the fit to the MC value only for the first w bin. In the fit to $B^- \to D^0\ell^-\bar{\nu}$ events, only the $B \to D^*\ell\nu$ background is fixed, while in the fit to $B^0 \to D^-\ell^+\nu$ events all the background parameters are fixed.

The results are reported on tablesA.6 and A.6.

$B^- \to D^0\ell^-\bar{\nu}$ **events**					
bin n.	f_{Signal}	f_{D^*}	f_{Peak}	$\chi^2/d.o.f.$	correlation
n.1+2	0.10 ± 0.30	1.15 ± 0.04	0.64 ± 0.11	23.53/31.0	$\begin{pmatrix} 1 & -0.78 & 0.18 \\ -0.78 & 1 & -0.59 \\ 0.18 & -0.59 & 1 \end{pmatrix}$
n.3	1.10 ± 0.15	1.03 ± 0.05	0.72 ± 0.15	48.51/31.0	$\begin{pmatrix} 1 & -0.77 & 0.37 \\ -0.77 & 1 & -0.72 \\ 0.37 & -0.72 & 1 \end{pmatrix}$
n.4	0.90 ± 0.09	1.14 ± 0.05	0.57 ± 0.14	16.35/31.0	$\begin{pmatrix} 1 & -0.72 & 0.38 \\ -0.72 & 1 & -0.77 \\ 0.38 & -0.77 & 1 \end{pmatrix}$
n.5	1.03 ± 0.06	1.13 ± 0.05	0.50 ± 0.13	27.07/31.0	$\begin{pmatrix} 1 & -0.68 & 0.37 \\ -0.68 & 1 & -0.8 \\ 0.37 & -0.8 & 1 \end{pmatrix}$
n.6	1.06 ± 0.05	1.10 ± 0.06	0.72 ± 0.15	27.57/31.0	$\begin{pmatrix} 1 & -0.6 & 0.31 \\ -0.6 & 1 & -0.85 \\ 0.31 & -0.85 & 1 \end{pmatrix}$
n.7	1.10 ± 0.04	1.18 ± 0.06	0.54 ± 0.13	18.04/31.0	$\begin{pmatrix} 1 & -0.5 & 0.19 \\ -0.5 & 1 & -0.84 \\ 0.19 & -0.84 & 1 \end{pmatrix}$
n.8	1.18 ± 0.03	1.33 ± 0.07	0.48 ± 0.10	12.18/31.0	$\begin{pmatrix} 1 & -0.37 & -0.024 \\ -0.37 & 1 & -0.78 \\ -0.024 & -0.78 & 1 \end{pmatrix}$
n.9	1.20 ± 0.03	1.24 ± 0.08	0.66 ± 0.11	22.89/31.0	$\begin{pmatrix} 1 & -0.1 & -0.35 \\ -0.1 & 1 & -0.75 \\ -0.35 & -0.75 & 1 \end{pmatrix}$
n.10	1.33 ± 0.05	0.89 ± 0.11	0.87 ± 0.09	33.11/31.0	$\begin{pmatrix} 1 & -0.13 & -0.57 \\ -0.13 & 1 & -0.53 \\ -0.57 & -0.53 & 1 \end{pmatrix}$

Table A.1: Scaling factors result of the $2D$ fit, for each bin and the 3 free parameters, $B^- \to D^0\ell^-\bar{\nu}$ events

$B^0 \to D^-\ell^+\nu$ **events**					
bin n.	f_{Signal}	f_{D^*}	f_{Peak}	$\chi^2/d.o.f.$	correlation
n.1+2	0.80 ± 0.33	1.05 ± 0.21	1.08 ± 0.21	15.32/31.0	$\begin{pmatrix} 1 & -0.64 & -0.1 \\ -0.64 & 1 & -0.55 \\ -0.1 & -0.55 & 1 \end{pmatrix}$
n.3	0.88 ± 0.15	1.48 ± 0.25	0.60 ± 0.29	24.03/31.0	$\begin{pmatrix} 1 & -0.68 & 0.22 \\ -0.68 & 1 & -0.74 \\ 0.22 & -0.74 & 1 \end{pmatrix}$
n.4	1.07 ± 0.08	1.11 ± 0.21	0.75 ± 0.21	23.86/31.0	$\begin{pmatrix} 1 & -0.64 & 0.24 \\ -0.64 & 1 & -0.78 \\ 0.24 & -0.78 & 1 \end{pmatrix}$
n.5	1.00 ± 0.06	1.61 ± 0.25	0.31 ± 0.22	15.78/31.0	$\begin{pmatrix} 1 & -0.58 & 0.26 \\ -0.58 & 1 & -0.84 \\ 0.26 & -0.84 & 1 \end{pmatrix}$
n.6	1.07 ± 0.05	1.81 ± 0.27	0.23 ± 0.21	14.36/31.0	$\begin{pmatrix} 1 & -0.49 & 0.16 \\ -0.49 & 1 & -0.86 \\ 0.16 & -0.86 & 1 \end{pmatrix}$
n.7	1.13 ± 0.03	1.09 ± 0.24	0.69 ± 0.15	12.66/31.0	$\begin{pmatrix} 1 & -0.37 & 0.013 \\ -0.37 & 1 & -0.84 \\ 0.013 & -0.84 & 1 \end{pmatrix}$
n.8	1.22 ± 0.03	1.28 ± 0.29	0.46 ± 0.14	17.46/31.0	$\begin{pmatrix} 1 & -0.21 & -0.16 \\ -0.21 & 1 & -0.83 \\ -0.16 & -0.83 & 1 \end{pmatrix}$
n.9	1.27 ± 0.03	1.53 ± 0.31	0.43 ± 0.14	17.53/31.0	$\begin{pmatrix} 1 & 0.022 & -0.43 \\ 0.022 & 1 & -0.78 \\ -0.43 & -0.78 & 1 \end{pmatrix}$
n.10	1.30 ± 0.04	0.53 ± 0.36	0.64 ± 0.12	27.65/31.0	$\begin{pmatrix} 1 & -0.017 & -0.66 \\ -0.017 & 1 & -0.55 \\ -0.66 & -0.55 & 1 \end{pmatrix}$

Table A.2: Scaling factors result of the $2D$ fit, for each bin and the 3 free parameters, $B^- \to D^0\ell^-\bar{\nu}$ events

Combined Fit w/ CLN	
$\lvert V_{cb}\rvert \cdot G(1)$	0.0438 ± 0.0012
$\hat{\rho}^2$	1.120 ± 0.055
chi^2/n.d.f.	21.7626 / 18
correlation	$\begin{pmatrix} 1 & 0.9729 \\ 0.9729 & 1 \end{pmatrix}$
BR (%)	2.39 ± 0.03

Table A.3: Combined fit results using CLN parametrization of the Form Factor, merging the first two bins of w

Combined Fit w/ CLN and lep-mass	
$\lvert V_{cb}\rvert \cdot G(1)$	0.0443 ± 0.0011
$\hat{\rho}^2$	1.155 ± 0.053
chi^2/n.d.f.	20.0084 / 18
correlation	$\begin{pmatrix} 1 & 0.9719 \\ 0.9719 & 1 \end{pmatrix}$
BR (%)	2.39 ± 0.03

Table A.4: Combined fit results using CLN and lep mass parametrization of the Form Factor, merging the first two bins of w

$B^- \to D^0 \ell^- \bar{\nu}$ **events**					
bin n.	f_{Signal}	f_{D^*}	f_{Peak}	$\chi^2/d.o.f.$	correlation
n.1	0.72 ± 0.68	1.00 ± 0.00	1.03 ± 0.15	29.52/31.0	$\begin{pmatrix} 1 & -0.69 \\ -0.69 & 1 \end{pmatrix}$
n.2	0.58 ± 0.30	1.25 ± 0.05	0.62 ± 0.17	15.65/31.0	$\begin{pmatrix} 1 & -0.77 & 0.24 \\ -0.77 & 1 & -0.62 \\ 0.24 & -0.62 & 1 \end{pmatrix}$
n.3	1.17 ± 0.16	1.10 ± 0.05	0.77 ± 0.15	48.51/31.0	$\begin{pmatrix} 1 & -0.77 & 0.37 \\ -0.77 & 1 & -0.72 \\ 0.37 & -0.72 & 1 \end{pmatrix}$
n.4	1.00 ± 0.09	1.26 ± 0.05	0.63 ± 0.15	16.34/31.0	$\begin{pmatrix} 1 & -0.72 & 0.38 \\ -0.72 & 1 & -0.77 \\ 0.38 & -0.77 & 1 \end{pmatrix}$
n.5	1.10 ± 0.07	1.21 ± 0.06	0.54 ± 0.14	27.07/31.0	$\begin{pmatrix} 1 & -0.68 & 0.37 \\ -0.68 & 1 & -0.8 \\ 0.37 & -0.8 & 1 \end{pmatrix}$
n.6	1.12 ± 0.05	1.16 ± 0.07	0.76 ± 0.15	27.57/31.0	$\begin{pmatrix} 1 & -0.6 & 0.31 \\ -0.6 & 1 & -0.85 \\ 0.31 & -0.85 & 1 \end{pmatrix}$
n.7	1.11 ± 0.04	1.20 ± 0.06	0.55 ± 0.13	18.04/31.0	$\begin{pmatrix} 1 & -0.5 & 0.19 \\ -0.5 & 1 & -0.84 \\ 0.19 & -0.84 & 1 \end{pmatrix}$
n.8	1.17 ± 0.03	1.32 ± 0.07	0.47 ± 0.10	12.18/31.0	$\begin{pmatrix} 1 & -0.37 & -0.024 \\ -0.37 & 1 & -0.78 \\ -0.024 & -0.78 & 1 \end{pmatrix}$
n.9	1.14 ± 0.03	1.18 ± 0.08	0.62 ± 0.10	22.88/31.0	$\begin{pmatrix} 1 & -0.1 & -0.35 \\ -0.1 & 1 & -0.75 \\ -0.35 & -0.75 & 1 \end{pmatrix}$
n.10	1.26 ± 0.04	0.85 ± 0.10	0.78 ± 0.09	32.38/31.0	$\begin{pmatrix} 1 & -0.13 & -0.58 \\ -0.13 & 1 & -0.53 \\ -0.58 & -0.53 & 1 \end{pmatrix}$

Table A.5: Scaling factors result of the $2D$ fit, for each bin and the 3 free parameters, $B^- \to D^0 \ell^- \bar{\nu}$ events

$B^0 \to D^-\ell^+\nu$ **events**					
bin n.	f_{Signal}	f_{D^*}	f_{Peak}	$\chi^2/d.o.f.$	correlation
n.1	0.59 ± 0.52	1.00 ± 0.00	1.00 ± 0.00	23.72/31.0	$\begin{pmatrix} 1 \end{pmatrix}$
n.2	1.02 ± 0.33	1.24 ± 0.27	0.89 ± 0.33	12.33/31.0	$\begin{pmatrix} 1 & -0.67 & 0.018 \\ -0.67 & 1 & -0.61 \\ 0.018 & -0.61 & 1 \end{pmatrix}$
n.3	0.87 ± 0.15	1.45 ± 0.25	0.60 ± 0.29	23.98/31.0	$\begin{pmatrix} 1 & -0.68 & 0.22 \\ -0.68 & 1 & -0.74 \\ 0.22 & -0.74 & 1 \end{pmatrix}$
n.4	1.14 ± 0.09	1.22 ± 0.23	0.75 ± 0.23	23.96/31.0	$\begin{pmatrix} 1 & -0.64 & 0.24 \\ -0.64 & 1 & -0.78 \\ 0.24 & -0.78 & 1 \end{pmatrix}$
n.5	0.95 ± 0.06	1.66 ± 0.25	0.13 ± 0.22	14.94/31.0	$\begin{pmatrix} 1 & -0.58 & 0.26 \\ -0.58 & 1 & -0.84 \\ 0.26 & -0.84 & 1 \end{pmatrix}$
n.6	1.01 ± 0.04	1.72 ± 0.26	0.22 ± 0.20	14.39/31.0	$\begin{pmatrix} 1 & -0.49 & 0.17 \\ -0.49 & 1 & -0.86 \\ 0.17 & -0.86 & 1 \end{pmatrix}$
n.7	1.11 ± 0.03	1.07 ± 0.24	0.68 ± 0.15	12.66/31.0	$\begin{pmatrix} 1 & -0.37 & 0.013 \\ -0.37 & 1 & -0.84 \\ 0.013 & -0.84 & 1 \end{pmatrix}$
n.8	1.11 ± 0.03	1.16 ± 0.26	0.41 ± 0.13	17.46/31.0	$\begin{pmatrix} 1 & -0.21 & -0.16 \\ -0.21 & 1 & -0.83 \\ -0.16 & -0.83 & 1 \end{pmatrix}$
n.9	1.15 ± 0.03	1.38 ± 0.28	0.39 ± 0.12	17.53/31.0	$\begin{pmatrix} 1 & 0.022 & -0.43 \\ 0.022 & 1 & -0.78 \\ -0.43 & -0.78 & 1 \end{pmatrix}$
n.10	1.19 ± 0.04	0.65 ± 0.34	0.29 ± 0.12	25.99/31.0	$\begin{pmatrix} 1 & -0.011 & -0.67 \\ -0.011 & 1 & -0.55 \\ -0.67 & -0.55 & 1 \end{pmatrix}$

Table A.6: Scaling factors result of the $2D$ fit, for each bin and the 3 free parameters, $B^- \to D^0\ell^-\bar{\nu}$ events

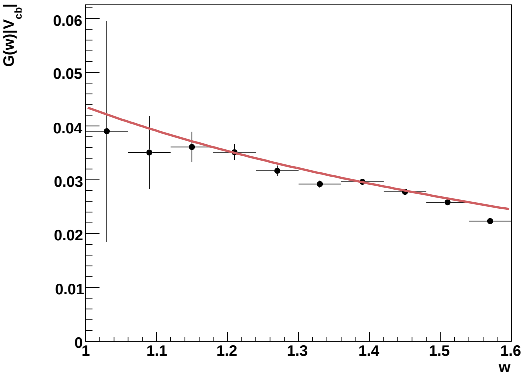

Figure A.1: $G(w)|V_{cb}|$ distribution unfolded for the reconstruction efficiency, not corrected for smearing in w with the fit results (line) superimposed. The parametrization is CLN. The results are extracted from the fit where the first w bin background components have been fixed.

The $|V_{cb}|$ results are given on table A.7 and A.8 and on figureA.1.

Combined Fit w/ CLN	
$\lvert V_{cb}\rvert \cdot G(1)$	0.0436 ± 0.0011
$\hat{\rho}^2$	1.113 ± 0.055
χ^2/n.d.f.	13.3482 / 18
correlation	$\begin{pmatrix} 1 & 0.9727 \\ 0.9727 & 1 \end{pmatrix}$
BR (%)	2.38 ± 0.03

Table A.7: Combined fit results using CLN parametrization of the Form Factor. The results are extracted from the fit where the first w bin background components have been fixed.

Combined Fit w/ CLN and lep-mass	
$\lvert V_{cb}\rvert \cdot G(1)$	0.0441 ± 0.0011
$\hat{\rho}^2$	1.149 ± 0.053
χ^2/n.d.f.	11.8515 / 18
correlation	$\begin{pmatrix} 1 & 0.9717 \\ 0.9717 & 1 \end{pmatrix}$
BR (%)	2.38 ± 0.03

Table A.8: Combined fit results using CLN and lep mass parametrization of the Form Factor. The results are extracted from the fit where the first w bin background components have been fixed.

$B^- \to D^0 e^- \bar{\nu}$ **events**					
bin n.	f_{Signal}	f_{D^*}	f_{Peak}	$\chi^2/d.o.f.$	correlation
n.1	0.53 ± 1.41	1.09 ± 0.09	0.69 ± 0.25	$20.85/31.0$	$\begin{pmatrix} 1 & -0.8 & -0.012 \\ -0.8 & 1 & -0.45 \\ -0.012 & -0.45 & 1 \end{pmatrix}$
n.2	0.53 ± 0.42	1.13 ± 0.07	0.54 ± 0.22	$18.15/31.0$	$\begin{pmatrix} 1 & -0.81 & 0.29 \\ -0.81 & 1 & -0.65 \\ 0.29 & -0.65 & 1 \end{pmatrix}$
n.3	1.15 ± 0.20	0.98 ± 0.07	0.92 ± 0.22	$51.52/31.0$	$\begin{pmatrix} 1 & -0.78 & 0.39 \\ -0.78 & 1 & -0.74 \\ 0.39 & -0.74 & 1 \end{pmatrix}$
n.4	0.95 ± 0.11	1.10 ± 0.06	0.63 ± 0.19	$18.88/31.0$	$\begin{pmatrix} 1 & -0.7 & 0.36 \\ -0.7 & 1 & -0.78 \\ 0.36 & -0.78 & 1 \end{pmatrix}$
n.5	1.02 ± 0.09	1.19 ± 0.07	0.26 ± 0.19	$19.56/31.0$	$\begin{pmatrix} 1 & -0.69 & 0.37 \\ -0.69 & 1 & -0.8 \\ 0.37 & -0.8 & 1 \end{pmatrix}$
n.6	1.02 ± 0.06	1.08 ± 0.08	0.84 ± 0.19	$44.72/31.0$	$\begin{pmatrix} 1 & -0.6 & 0.28 \\ -0.6 & 1 & -0.83 \\ 0.28 & -0.83 & 1 \end{pmatrix}$
n.7	1.09 ± 0.05	1.19 ± 0.09	0.47 ± 0.18	$24.59/31.0$	$\begin{pmatrix} 1 & -0.52 & 0.23 \\ -0.52 & 1 & -0.86 \\ 0.23 & -0.86 & 1 \end{pmatrix}$
n.8	1.20 ± 0.04	1.29 ± 0.09	0.42 ± 0.13	$15.92/31.0$	$\begin{pmatrix} 1 & -0.35 & -0.031 \\ -0.35 & 1 & -0.79 \\ -0.031 & -0.79 & 1 \end{pmatrix}$
n.9	1.23 ± 0.04	1.14 ± 0.10	0.70 ± 0.14	$27.28/31.0$	$\begin{pmatrix} 1 & -0.15 & -0.28 \\ -0.15 & 1 & -0.77 \\ -0.28 & -0.77 & 1 \end{pmatrix}$
n.10	1.35 ± 0.06	0.89 ± 0.13	0.83 ± 0.13	$17.45/31.0$	$\begin{pmatrix} 1 & -0.13 & -0.59 \\ -0.13 & 1 & -0.53 \\ -0.59 & -0.53 & 1 \end{pmatrix}$

Table A.9: Scaling factors result of the $2D$ fit, for each bin and the 3 free parameters, $B^- \to D^0 \ell^- \bar{\nu}$ events, where ℓ is an electron

A.1.3 Splitted samples

On the following tables are reported the scale factors (with errors) and the correlation coefficient obtained from the fit to on-peak data in each w bin, separately for $B^- \to D^0 e^- \bar{\nu}$A.9, $B^- \to D^0 \mu^- \bar{\nu}$A.10, $B^0 \to D^- e^+ \nu$A.11, $B^0 \to D^- \mu^+ \nu$A.12.

.

A.2 V_{cb} Fit

Several tests are performed to check the stability of the Fit algorithm.

A.2.1 $|V_{cb}|$ Fit with $f_{+/-}$ floated with Gaussian constrain

An additional term $\chi^2_{f_{+-}}$ in the eq.7.1 has been added is added to constrain the parameter f_{+-}, the branching fraction of the decay $\Upsilon(4S) \to B^+ B^-$.

$$\chi^2_{f_{+-}} = \frac{(f_{+-} - f_{+-}^{PDG})^2}{\sigma^2_{f_{+-}^{PDG}}}, \tag{A.1}$$

Here the results on tablesA.13 andA.14.

$B^- \to D^0\mu^-\bar{\nu}$ **events**					
bin n.	f_{Signal}	f_{D^*}	f_{Peak}	$\chi^2/d.o.f.$	correlation
n.1	-3.64 ± 1.93	1.25 ± 0.11	0.94 ± 0.23	$14.86/31.0$	$\begin{pmatrix} 1 & -0.85 & -0.035 \\ -0.85 & 1 & -0.34 \\ -0.035 & -0.34 & 1 \end{pmatrix}$
n.2	0.37 ± 0.36	1.17 ± 0.06	0.43 ± 0.22	$19.50/31.0$	$\begin{pmatrix} 1 & -0.73 & 0.2 \\ -0.73 & 1 & -0.61 \\ 0.2 & -0.61 & 1 \end{pmatrix}$
n.3	1.02 ± 0.21	1.09 ± 0.07	0.54 ± 0.19	$18.94/31.0$	$\begin{pmatrix} 1 & -0.76 & 0.35 \\ -0.76 & 1 & -0.71 \\ 0.35 & -0.71 & 1 \end{pmatrix}$
n.4	0.80 ± 0.13	1.19 ± 0.07	0.48 ± 0.20	$13.51/31.0$	$\begin{pmatrix} 1 & -0.74 & 0.4 \\ -0.74 & 1 & -0.75 \\ 0.4 & -0.75 & 1 \end{pmatrix}$
n.5	1.04 ± 0.09	1.08 ± 0.08	0.74 ± 0.19	$22.43/31.0$	$\begin{pmatrix} 1 & -0.67 & 0.37 \\ -0.67 & 1 & -0.8 \\ 0.37 & -0.8 & 1 \end{pmatrix}$
n.6	1.13 ± 0.08	1.09 ± 0.10	0.63 ± 0.21	$20.60/31.0$	$\begin{pmatrix} 1 & -0.6 & 0.33 \\ -0.6 & 1 & -0.86 \\ 0.33 & -0.86 & 1 \end{pmatrix}$
n.7	1.13 ± 0.06	1.16 ± 0.10	0.64 ± 0.17	$9.17/31.0$	$\begin{pmatrix} 1 & -0.48 & 0.14 \\ -0.48 & 1 & -0.81 \\ 0.14 & -0.81 & 1 \end{pmatrix}$
n.8	1.15 ± 0.06	1.44 ± 0.11	0.52 ± 0.14	$13.83/31.0$	$\begin{pmatrix} 1 & -0.38 & -0.017 \\ -0.38 & 1 & -0.75 \\ -0.017 & -0.75 & 1 \end{pmatrix}$
n.9	1.20 ± 0.06	1.43 ± 0.13	0.56 ± 0.16	$12.21/31.0$	$\begin{pmatrix} 1 & -0.089 & -0.38 \\ -0.089 & 1 & -0.71 \\ -0.38 & -0.71 & 1 \end{pmatrix}$
n.10	1.40 ± 0.07	1.02 ± 0.19	0.78 ± 0.14	$29.26/31.0$	$\begin{pmatrix} 1 & -0.13 & -0.53 \\ -0.13 & 1 & -0.56 \\ -0.53 & -0.56 & 1 \end{pmatrix}$

Table A.10: Scaling factors result of the $2D$ fit, for each bin and the 3 free parameters, $B^- \to D^0\ell^-\bar{\nu}$ events, where ℓ is a muon

$B^0 \to D^- e^+ \nu$ **events**					
bin n.	f_{Signal}	f_{D^*}	f_{Peak}	$\chi^2/d.o.f.$	correlation
n.1	0.18 ± 1.32	0.34 ± 0.48	1.72 ± 0.40	$33.72/31.0$	$\begin{pmatrix} 1 & -0.58 & -0.31 \\ -0.58 & 1 & -0.48 \\ -0.31 & -0.48 & 1 \end{pmatrix}$
n.2	1.03 ± 0.43	0.89 ± 0.36	1.24 ± 0.42	$12.00/31.0$	$\begin{pmatrix} 1 & -0.69 & 0.035 \\ -0.69 & 1 & -0.6 \\ 0.035 & -0.6 & 1 \end{pmatrix}$
n.3	1.03 ± 0.21	1.17 ± 0.35	0.80 ± 0.42	$17.40/31.0$	$\begin{pmatrix} 1 & -0.67 & 0.2 \\ -0.67 & 1 & -0.75 \\ 0.2 & -0.75 & 1 \end{pmatrix}$
n.4	1.15 ± 0.12	0.96 ± 0.31	0.82 ± 0.29	$23.14/31.0$	$\begin{pmatrix} 1 & -0.68 & 0.28 \\ -0.68 & 1 & -0.78 \\ 0.28 & -0.78 & 1 \end{pmatrix}$
n.5	1.00 ± 0.08	1.60 ± 0.36	0.35 ± 0.34	$14.43/31.0$	$\begin{pmatrix} 1 & -0.57 & 0.24 \\ -0.57 & 1 & -0.85 \\ 0.24 & -0.85 & 1 \end{pmatrix}$
n.6	1.11 ± 0.07	1.75 ± 0.45	0.07 ± 0.37	$24.80/31.0$	$\begin{pmatrix} 1 & -0.58 & 0.32 \\ -0.58 & 1 & -0.9 \\ 0.32 & -0.9 & 1 \end{pmatrix}$
n.7	1.11 ± 0.04	0.84 ± 0.31	0.88 ± 0.20	$16.21/31.0$	$\begin{pmatrix} 1 & -0.37 & 0.015 \\ -0.37 & 1 & -0.84 \\ 0.015 & -0.84 & 1 \end{pmatrix}$
n.8	1.22 ± 0.04	1.22 ± 0.37	0.47 ± 0.18	$14.02/31.0$	$\begin{pmatrix} 1 & -0.22 & -0.16 \\ -0.22 & 1 & -0.83 \\ -0.16 & -0.83 & 1 \end{pmatrix}$
n.9	1.30 ± 0.04	1.53 ± 0.40	0.34 ± 0.19	$20.89/31.0$	$\begin{pmatrix} 1 & 0.037 & -0.45 \\ 0.037 & 1 & -0.79 \\ -0.45 & -0.79 & 1 \end{pmatrix}$
n.10	1.36 ± 0.06	0.96 ± 0.50	0.36 ± 0.19	$24.81/31.0$	$\begin{pmatrix} 1 & 0.066 & -0.69 \\ 0.066 & 1 & -0.6 \\ -0.69 & -0.6 & 1 \end{pmatrix}$

Table A.11: Scaling factors result of the $2D$ fit, for each bin and the 3 free parameters, $B^0 \to D^- \ell^+ \nu$ events, where ℓ is an electron

$B^0 \to D^-\mu^+\nu$ **events**					
bin n.	f_{Signal}	f_{D^*}	f_{Peak}	$\chi^2/d.o.f.$	correlation
n.1	-1.12 ± 1.30	1.56 ± 0.50	1.19 ± 0.39	13.34/31.0	$\begin{pmatrix} 1 & -0.64 & -0.25 \\ -0.64 & 1 & -0.44 \\ -0.25 & -0.44 & 1 \end{pmatrix}$
n.2	1.01 ± 0.46	1.49 ± 0.38	0.23 ± 0.45	12.58/31.0	$\begin{pmatrix} 1 & -0.65 & 0.0045 \\ -0.65 & 1 & -0.62 \\ 0.0045 & -0.62 & 1 \end{pmatrix}$
n.3	0.74 ± 0.22	1.71 ± 0.35	0.56 ± 0.40	20.37/31.0	$\begin{pmatrix} 1 & -0.68 & 0.21 \\ -0.68 & 1 & -0.7 \\ 0.21 & -0.7 & 1 \end{pmatrix}$
n.4	1.00 ± 0.12	1.32 ± 0.31	0.57 ± 0.31	20.81/31.0	$\begin{pmatrix} 1 & -0.61 & 0.21 \\ -0.61 & 1 & -0.78 \\ 0.21 & -0.78 & 1 \end{pmatrix}$
n.5	1.02 ± 0.09	1.88 ± 0.37	-0.01 ± 0.32	19.93/31.0	$\begin{pmatrix} 1 & -0.59 & 0.27 \\ -0.59 & 1 & -0.83 \\ 0.27 & -0.83 & 1 \end{pmatrix}$
n.6	1.01 ± 0.07	1.93 ± 0.35	0.37 ± 0.26	13.45/31.0	$\begin{pmatrix} 1 & -0.41 & 0.027 \\ -0.41 & 1 & -0.81 \\ 0.027 & -0.81 & 1 \end{pmatrix}$
n.7	1.17 ± 0.05	1.58 ± 0.37	0.34 ± 0.23	16.51/31.0	$\begin{pmatrix} 1 & -0.36 & -0.0018 \\ -0.36 & 1 & -0.82 \\ -0.0018 & -0.82 & 1 \end{pmatrix}$
n.8	1.25 ± 0.05	1.45 ± 0.44	0.40 ± 0.20	16.62/31.0	$\begin{pmatrix} 1 & -0.22 & -0.14 \\ -0.22 & 1 & -0.82 \\ -0.14 & -0.82 & 1 \end{pmatrix}$
n.9	1.26 ± 0.05	1.60 ± 0.48	0.51 ± 0.20	20.03/31.0	$\begin{pmatrix} 1 & 0.0044 & -0.39 \\ 0.0044 & 1 & -0.78 \\ -0.39 & -0.78 & 1 \end{pmatrix}$
n.10	1.54 ± 0.08	0.48 ± 0.69	0.26 ± 0.20	12.69/31.0	$\begin{pmatrix} 1 & -0.11 & -0.61 \\ -0.11 & 1 & -0.51 \\ -0.61 & -0.51 & 1 \end{pmatrix}$

Table A.12: Scaling factors result of the $2D$ fit, for each bin and the 3 free parameters, $B^0 \to D^-\ell^+\nu$ events, where ℓ is a muon

Combined Fit w/ CLN and lep-mass with $f_{+/-}$ floated	
$\lvert V_{cb}\rvert \cdot G(1)$	0.0440 ± 0.0011
$\hat{\rho}^2$	1.146 ± 0.053
$f_{+/-}$	0.5114 ± 0.0044
chi^2/n.d.f.	15.7754 / 18
correlation	$\begin{pmatrix} 1 & 0.9716 & 0.02612 \\ 0.9716 & 1 & 0.0006619 \\ 0.02612 & 0.0006619 & 1 \end{pmatrix}$
BR (%)	2.38 ± 0.03

Table A.13: Combined fit results using CLN and lep-mass parametrization of the Form Factor, floating the parameter $f_{\pm}$

Combined Fit w/ CLN with $f_{+/-}$ floated	
$\lvert V_{cb}\rvert \cdot G(1)$	0.0435 ± 0.0011
$\hat{\rho}^2$	1.111 ± 0.055
$f_{+/-}$	0.5114 ± 0.0044
chi^2/n.d.f.	17.2394 / 18
correlation	$\begin{pmatrix} 1 & 0.9726 & 0.026 \\ 0.9726 & 1 & 0.001039 \\ 0.026 & 0.001039 & 1 \end{pmatrix}$
BR (%)	2.37 ± 0.03

Table A.14: Combined fit results using CLN parametrization of the Form Factor, floating the parameter $f_{+/-}$

A.2.2 Alternative parametrization for the FF

Alternative parametrization other than the standard CLN are used to extract $\lvert V_{cb}\rvert$:

- Linear ($\mathcal{F}_{B\to D}(w) = \mathcal{F}(1)(1 - \hat{\rho}^2(w-1))$), results are shown in table A.15 and on figureA.2.
- Parabolic ($\mathcal{F}_{B\to D}(w) = \mathcal{F}(1)(1 - \hat{\rho}^2(w-1) + \hat{c}(w-1)^2)$, results are shown in table A.16 and on figureA.3.
- the model ISGW2[23] results are shown in table A.17 and on figureA.4.

Combined Fit w/ linear	
$\lvert V_{cb}\rvert \cdot G(1)$	0.0401 ± 0.0009
$\hat{\rho}^2$	0.660 ± 0.034
χ^2/n.d.f.	20.419 / 18
correlation	$\begin{pmatrix} 1 & 0.9619 \\ 0.9619 & 1 \end{pmatrix}$
BR (%)	2.36 ± 0.03

Table A.15: Combined fit results using linear parametrization of the Form Factor

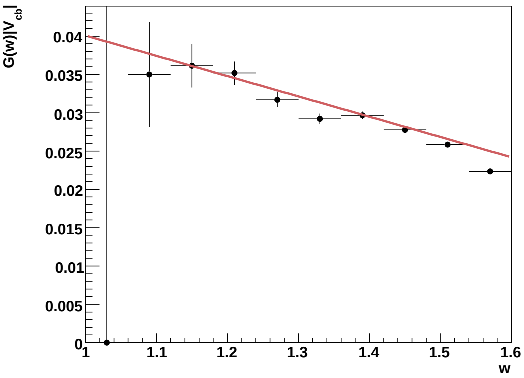

Figure A.2: $G(w)|V_{cb}|$ distribution unfolded for the reconstruction efficiency, not corrected for smearing in w with the fit results (line) superimposed. The parametrization is a linear function.

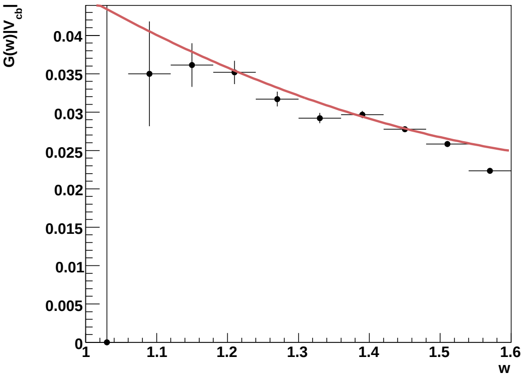

Figure A.3: $G(w)|V_{cb}|$ distribution unfolded for the reconstruction efficiency, not corrected for smearing in w with the fit results (line) superimposed. The parametrization is a quadratic function (1).

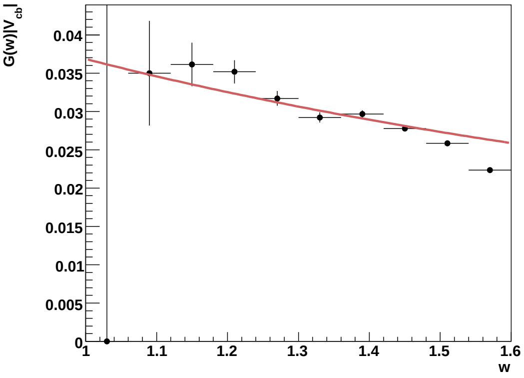

Figure A.4: $G(w)|V_{cb}|$ distribution unfolded for the reconstruction efficiency, not corrected for smearing in w with the fit results (line) superimposed. The parametrization is done using ISGW2[23].

Combined Fit w/ Parabolic param.	
$\lvert V_{cb}\rvert \cdot G(1)$	0.0449 ± 0.0028
$\hat{\rho}^2$	1.152 ± 0.244
$f_{+/-}$	0.5160 ± 0.0000
$\hat{c}$	0.68 ± 0.34
χ^2/n.d.f.	17.2244 / 18
correlation	$\begin{pmatrix} 1 & 0.9708 & 0.9363 \\ 0.9708 & 1 & 0.9923 \\ 0.9363 & 0.9923 & 1 \\ nan & nan & nan \end{pmatrix}$
BR (%)	1.57 ± 0.36

Table A.16: Combined fit results using Parabolic parametrization of the Form Factor

Combined Fit w/ ISGW2 param.	
$\lvert V_{cb}\rvert \cdot G(1)$	0.0369 ± 0.0002
χ^2/n.d.f.	45.9733 / 18
correlation	$\begin{pmatrix} 1 \\ inf \end{pmatrix}$
BR (%)	$4.50 \pm nan$

Table A.17: Combined fit results using ISGW2 parametrization of the Form Factor

B More on Systematics

B.1 Systematics splitted sample

The systematics are also calculated for the fit to the $B^- \to D^0\ell^-\bar{\nu}$ B.1 and $B^0 \to D^-\ell^+\nu$ B.2 sample separately.

Syst and Stat uncertainties

Syst.	$V_{cb}G(1)(\%)$	ρ^2	$BR(\%)$
Sys $\mathcal{BR}(D^{**}_{broad}\ell\nu)$	0.10	0.002	0.01
Sys $\mathcal{BR}(D^{**}_{narrow}\ell\nu)$	0.03	0.001	0.06
Sys $\mathcal{BR}(D^{*}\ell\nu)$	0.04	0.000	0.08
Sys $\mathcal{BR}(D^{*}\pi\ell\nu)$	0.00	0.000	0.00
Sys $D^{*}\ell\nu$ FF	0.64	0.016	0.48
Sys $D^{**}\ell\nu$ FF ISGW2	0.75	0.019	0.51
Sys $D^{**}\ell\nu$ FF	1.03	0.022	0.65
Sys tracking	-0.76	0.007	-2.09
Sys photons	-0.33	-0.001	-0.62
Sys K^0_L Eff	0.25	0.006	-0.04
Sys K^0_L Energy	-0.26	-0.003	-0.27
Sys K^0_L Prod	0.00	0.003	-0.24
Sys bremsstrahlung	-0.48	-0.007	-0.37
Sys PID elec	0.63	0.007	1.23
Sys PID muon	1.57	0.010	2.26
Sys PID kaon	1.29	0.008	2.84
Sys $c\bar{c}$ Scaling	0.00	0.000	0.00
Sys $N_{\Upsilon(4S)}$	-0.55	0.000	-1.11
Sys PHOTOS	0.76	0.012	0.52
BR(D)	1.31	0.010	1.73
Sys Fit	-0.22	-0.010	0.42
Sys f_{+-}	-0.59	0.000	-1.18
Tot. Syst.	3.34	0.04	5.506
Tot. Stat.	3.64	0.07	1.819
Tot. Syst. (abs.)	0.0015	0.04	0.001
Tot. Stat. (abs.)	0.0016	0.07	0.0005

Table B.1: Systematic and Statistical uncertainties for $B^- \to D^0\ell^-\bar{\nu}$ events, the relative uncertainties in % are given for f_{+-} and $V_{cb}G(1)$, whereas the absolute uncertainties are given for ρ^2, the last two line show the absolute values for each measurements.

Syst and Stat uncertainties			
Syst.	$V_{cb}G(1)(\%)$	ρ^2	$BR(\%)$
Sys $\mathcal{BR}(D^{**}_{broad}\ell\nu)$	0.02	0.003	0.20
Sys $\mathcal{BR}(D^{**}_{narrow}\ell\nu)$	0.04	0.001	0.16
Sys $\mathcal{BR}(D^{*}\ell\nu)$	0.10	0.002	0.07
Sys $\mathcal{BR}(D^{*}\pi\ell\nu)$	-0.00	-0.000	0.00
Sys $D^{*}\ell\nu$ FF	1.61	0.029	0.82
Sys $D^{**}\ell\nu$ FF ISGW2	0.89	0.014	0.69
Sys $D^{**}\ell\nu$ FF	1.76	0.033	0.92
Sys tracking	-1.50	-0.010	-2.17
Sys photons	-1.40	-0.022	-0.91
Sys K^0_L Eff	-0.79	-0.015	-0.29
Sys K^0_L Energy	-1.46	-0.029	-0.43
Sys K^0_L Prod	-1.21	-0.020	-0.70
Sys bremsstrahlung	-0.62	-0.011	-0.35
Sys PID elec	1.73	0.017	2.03
Sys PID muon	2.36	0.029	2.40
Sys PID kaon	2.23	0.020	2.75
Sys $c\bar{c}$ Scaling	-0.00	-0.000	-0.00
Sys $N_{\Upsilon(4S)}$	-0.56	-0.000	-1.12
Sys PHOTOS	0.63	0.010	0.40
BR(D)	1.92	0.013	2.98
Sys Fit	-0.31	-0.006	-0.12
Sys f_{+-}	-0.63	-0.000	-1.26
Tot. Syst.	5.91	0.08	6.781
Tot. Stat.	3.69	0.08	1.795
Tot. Syst. (abs.)	0.0026	0.08	0.002
Tot. Stat. (abs.)	0.0016	0.08	0.0004

Table B.2: Systematic and Statistical uncertainties for $B^0 \to D^-\ell^+\nu$ events, the relative uncertainties in % are given for f_{+-} and $V_{cb}G(1)$, whereas the absolute uncertainties are given for ρ^2,the last two line show the absolute values for each measurements.

B.2 Systematics as function of w

In this section the relative systematics uncertainties are calculated as the difference of the results of the signal yields fit.

Syst and Stat uncertainties $B^0 \to D^- \ell^+ \nu$ events

Mode/w-bin	1.	2.	3.	4.	5.	6.	7.	8.	9.	10.
Nominal Fit	-147.06	32.24	17.16	7.92	6.13	4.44	2.92	2.61	2.49	3.32
$\mathcal{BR}(D^{**}_{broad}\ell\nu)\uparrow$	-11.66	-0.43	0.39	-0.13	0.20	0.00	-0.36	-0.34	-0.33	-0.03
$\mathcal{BR}(D^{**}_{broad}\ell\nu)\downarrow$	10.59	0.48	-0.25	0.22	-0.22	-0.04	0.38	0.35	0.32	0.03
$\mathcal{BR}(D^{**}_{narrow}\ell\nu)\uparrow$	5.65	0.69	-0.10	0.21	-0.14	-0.01	0.31	0.26	0.23	0.03
$\mathcal{BR}(D^{**}_{narrow}\ell\nu)\downarrow$	-5.68	-0.63	0.17	-0.16	0.13	-0.01	-0.29	-0.26	-0.24	-0.04
D^* FF $Par_1\uparrow$	58.95	-0.54	-3.59	-0.19	-0.25	-0.33	-0.45	-0.01	-0.01	-0.16
D^* FF $Par_1\downarrow$	91.87	-1.89	-2.35	0.23	0.12	-0.21	-0.52	-0.09	0.06	-0.05
D^* FF $Par_2\uparrow$	90.98	-3.14	-1.94	0.97	-0.62	0.27	-0.43	-0.05	-0.03	0.18
D^* FF $Par_2\downarrow$	71.63	-2.70	-0.47	0.98	-0.67	0.19	-0.48	-0.21	-0.13	0.11
D^* FF $Par_3\uparrow$	46.03	-2.74	-2.38	-0.65	-0.19	-0.16	-0.34	-0.01	0.08	-0.20
D^* FF $Par_3\downarrow$	37.92	-0.90	-0.68	0.13	-0.44	-0.63	-0.16	-0.27	0.14	0.19
$\mathcal{BR}(D^*\ell\nu)\uparrow$	-11.82	1.54	0.31	0.15	0.00	-0.00	0.11	0.06	0.03	0.03
$\mathcal{BR}(D^*\ell\nu)\downarrow$	12.08	-1.49	-0.28	-0.14	-0.00	0.00	-0.10	-0.06	-0.03	-0.03
K^0_L Eff	17.09	-6.29	-1.87	0.57	-0.24	-0.01	-0.13	0.01	0.11	0.26
photons	68.10	0.55	-0.38	0.85	-0.43	-0.50	-0.42	-0.06	0.14	0.05
tracking	-6.09	-5.80	-5.21	0.29	0.07	-0.58	-0.13	-0.10	0.31	0.23
PID elec eff	49.26	-5.04	-3.16	0.55	-0.30	-0.15	-0.24	0.14	0.06	0.40
PID muon eff	55.44	-2.66	-4.38	0.59	-0.04	-0.88	-0.36	0.05	-0.23	0.17
PID elec mis-Id	63.27	-3.24	-1.84	0.48	-0.70	-0.35	-0.14	-0.17	0.05	0.46
PID muon mis-Id	69.50	-3.19	-0.76	-0.35	-0.47	-0.18	-0.23	-0.06	-0.02	0.41
$c\bar{c}$ Scaling $\uparrow$	0.46	0.00	0.00	-0.00	-0.00	-0.00	-0.00	0.00	-0.00	0.00
$c\bar{c}$ Scaling $\downarrow$	-0.00	0.01	0.01	0.00	0.00	-0.00	-0.00	-0.00	-0.00	0.00
D^{*1} FF B2	39.19	-3.57	-1.24	0.03	0.43	-0.40	-0.13	-0.06	-0.00	0.20
D^{*1} FF tau $\downarrow$	44.27	-0.91	-1.22	0.34	0.06	-0.39	-0.07	0.09	0.06	0.19
D^{*1} FF tau $\uparrow$	62.51	-1.87	0.37	0.28	0.14	-0.25	-0.36	-0.02	-0.03	0.19
D^{*2} FF B2	70.91	-2.32	-0.63	0.21	0.22	0.04	-0.11	0.04	0.15	0.48
D^{*2} FF tau $\downarrow$	25.17	-0.42	-0.95	-0.08	0.54	0.06	-0.36	-0.05	-0.18	0.20
D^{*2} FF tau $\uparrow$	23.67	-2.23	-1.73	-0.18	0.34	-0.12	-0.28	0.23	0.36	-0.00
D^{*0} FF B2	28.40	-1.45	-1.03	0.27	-0.13	0.11	-0.17	0.29	0.16	0.35
D^{*0} FF tau $\downarrow$	29.72	-2.90	0.25	0.76	0.35	-0.32	-0.40	0.10	0.01	0.11
D^{*0} FF tau $\uparrow$	27.26	-3.48	-1.06	0.41	0.05	-0.19	-0.72	-0.19	-0.14	-0.11
$D^{*1'}$ FF B2	55.83	-1.98	-1.19	0.23	0.04	-0.23	-0.40	-0.00	0.00	0.23
$D^{*1'}$ FF tau $\downarrow$	44.50	-2.23	-0.65	0.05	0.17	-0.28	0.09	0.08	0.12	0.08
$D^{*1'}$ FF tau $\uparrow$	33.40	-2.30	1.48	0.54	0.04	0.20	-0.26	-0.03	-0.06	0.14
PHOTOS	-1.55	0.94	0.93	0.75	0.60	0.54	0.44	0.41	0.19	-0.10
BR(D^0) $\downarrow$	54.48	-3.94	-1.62	0.01	-0.02	-0.07	-0.43	-0.14	0.02	0.30

Continued on Next Page…

Syst and Stat uncertainties $B^0 \to D^-\ell^+\nu$ events – Continued									
BR(D^0) ↑	48.56	-4.37	-0.65	0.12	-0.03	0.11	-0.32	0.07	0.07	0.39
BR(D^+) ↓	75.14	-2.70	-1.64	-0.00	-0.17	-0.39	-0.21	-0.02	-0.23	0.29
BR(D^+) ↑	38.93	-3.73	-0.99	0.55	-0.72	-0.03	-0.48	-0.21	-0.13	-0.20
D^{*1} FF isgw2	14.88	-0.92	0.40	0.51	-0.08	-0.44	-0.47	0.10	0.09	0.20
D^{*2} FF isgw2	52.85	0.81	-0.56	-0.45	0.43	0.05	-0.49	-0.11	-0.10	0.06
D^{*0} FF isgw2	58.97	-0.50	-3.47	1.09	-0.82	-0.29	-0.48	-0.07	-0.07	-0.20
$D^{*1'}$ FF isgw2	43.87	-6.17	-2.66	0.13	-0.38	0.22	-0.47	-0.07	0.10	0.20
PID kaon eff	77.84	0.51	-1.68	0.55	0.14	-0.13	-0.26	0.20	-0.15	0.28
PID kaon mis-Id	41.82	-0.13	-1.55	0.21	-0.70	-0.02	-0.42	-0.01	-0.06	0.01
bremsstrahlung ↓	62.49	-1.35	-2.93	0.72	-0.19	-0.09	-0.24	-0.29	-0.06	0.06
bremsstrahlung ↑	76.76	-2.60	-1.24	-0.59	-0.57	-0.23	-0.53	-0.15	-0.04	-0.11
K_L^0 Prod ↑	72.65	-4.90	-0.92	-0.12	-0.18	0.17	-0.56	-0.17	0.04	0.24
K_L^0 Prod ↓	51.36	-2.51	-1.85	-0.87	-0.07	0.01	-0.28	-0.09	0.00	0.14
K_L^0 Energy ↑	65.98	-2.34	-1.22	0.56	-0.33	-0.51	-0.43	0.15	0.13	0.40
K_L^0 Energy ↓	41.18	-4.79	-2.91	0.28	-0.20	0.05	-0.21	0.09	-0.14	0.17
Fit	-3.85	-1.64	-2.16	6.29	-2.96	0.66	-1.47	-0.44	0.33	0.93

Table B.3: Systematic and Statistical relative uncertainties stemming from the signal yields extraction fit for $B^0 \to D^-\ell^+\nu$ events. Relative uncertainties are given in %. The ↑(↓) means a variation of $+(-)\sigma$ of the quantity involved in the study of the given systematics

Syst and Stat uncertainties $B^- \to D^0\ell^-\bar{\nu}$ events

Mode/w-bin	1.	2.	3.	4.	5.	6.	7.	8.	9.	10.
Nominal Fit	-59.19	52.16	13.40	9.45	5.97	4.61	3.36	2.88	2.88	3.40
$\mathcal{BR}(D^{**}_{broad}\ell\nu) \uparrow$	-3.98	3.58	-0.15	0.50	0.20	-0.31	0.13	-0.17	-0.06	0.03
$\mathcal{BR}(D^{**}_{broad}\ell\nu) \downarrow$	3.95	-3.20	0.19	-0.40	-0.15	0.31	-0.10	0.15	0.04	-0.05
$\mathcal{BR}(D^{**}_{narrow}\ell\nu) \uparrow$	2.42	-2.10	0.19	-0.17	-0.05	0.26	-0.00	0.14	0.09	0.03
$\mathcal{BR}(D^{**}_{narrow}\ell\nu) \downarrow$	-2.36	2.24	-0.18	0.22	0.08	-0.26	0.02	-0.15	-0.11	-0.04
D^* FF $Par_1 \uparrow$	-1.76	-17.41	-2.13	-1.79	0.03	-0.62	-0.04	0.15	-0.72	0.05
D^* FF $Par_1 \downarrow$	-2.20	-16.21	-2.23	2.15	1.17	-0.67	-0.03	-0.14	-0.71	-0.78
D^* FF $Par_2 \uparrow$	-23.35	-14.51	-2.39	-0.08	0.23	-0.10	-0.07	-0.09	-0.41	-0.20
D^* FF $Par_2 \downarrow$	-22.92	-20.54	-3.48	0.28	0.26	-0.36	-0.14	-0.09	-0.60	-0.52
D^* FF $Par_3 \uparrow$	-5.27	-5.24	-2.27	0.90	0.43	-0.96	0.39	-0.03	-0.95	-0.43
D^* FF $Par_3 \downarrow$	-19.44	-8.96	-1.99	0.24	0.74	-0.49	0.06	0.24	-0.59	-0.16
$\mathcal{BR}(D^*\ell\nu) \uparrow$	-2.29	0.23	0.29	0.10	0.04	0.08	0.06	0.07	0.10	0.08
$\mathcal{BR}(D^*\ell\nu) \downarrow$	2.18	-0.19	-0.27	-0.10	-0.03	-0.07	-0.06	-0.07	-0.10	-0.08
K^0_L Eff	7.82	-3.02	0.61	-0.56	0.95	-0.11	-0.05	0.24	-0.31	-0.38
photons	-7.10	-23.61	-3.38	-0.15	1.09	-0.88	0.28	0.20	-0.59	-0.17
tracking	42.78	-8.59	-0.45	-0.25	-0.18	-0.03	-0.06	0.37	-0.76	-0.45
PID elec eff	-5.50	-10.04	-2.62	1.12	0.75	-0.55	0.60	0.19	-0.31	-0.30
PID muon eff	14.88	-21.21	-1.06	-1.73	0.34	-0.86	-0.59	-0.20	-0.49	-0.09
PID elec mis-Id	-26.60	-9.74	-1.53	0.71	-0.43	-0.35	0.18	0.15	-0.27	0.15
PID muon mis-Id	2.89	-21.09	-1.40	1.04	0.94	-0.63	-0.37	0.01	-0.41	0.30
$c\bar{c}$ Scaling $\uparrow$	0.03	-0.00	-0.01	0.00	0.00	0.00	-0.00	0.00	-0.00	-0.00
$c\bar{c}$ Scaling $\downarrow$	-0.00	0.00	0.00	-0.00	0.00	-0.00	-0.00	0.00	-0.00	-0.00
D^{*1} FF B2	18.15	-16.33	-1.79	0.04	-0.02	-0.28	0.15	0.09	-0.73	-0.17
D^{*1} FF tau $\downarrow$	1.78	-16.20	-0.36	0.41	1.12	-0.12	0.59	0.36	-0.04	0.47
D^{*1} FF tau $\uparrow$	15.13	-13.95	-1.31	0.52	0.42	-0.44	-0.13	-0.33	-1.14	-0.91
D^{*2} FF B2	0.03	-10.72	0.28	-0.51	0.90	0.07	0.37	0.26	-0.73	-0.30
D^{*2} FF tau $\downarrow$	-0.96	-17.75	-1.24	-0.03	-0.24	-0.11	0.23	-0.10	-0.56	-0.61
D^{*2} FF tau $\uparrow$	-6.67	-19.26	-0.96	-0.01	0.56	0.02	0.04	0.34	-0.75	0.24
D^{*0} FF B2	-0.78	-13.35	-0.77	0.39	0.46	0.35	0.46	0.23	-0.36	0.11
D^{*0} FF tau $\downarrow$	-9.28	-18.70	-2.86	1.07	0.54	-0.07	0.31	0.24	-0.38	-0.59
D^{*0} FF tau $\uparrow$	9.19	-8.31	-1.61	0.67	-0.29	0.17	-0.21	-0.14	-0.97	-0.59
$D^{*1'}$ FF B2	1.66	-10.99	-3.83	-0.14	0.22	-0.66	0.39	-0.15	-0.86	-0.41
$D^{*1'}$ FF tau $\downarrow$	-2.03	-9.37	-1.96	0.27	0.73	-0.10	0.36	0.26	-0.34	0.02
$D^{*1'}$ FF tau $\uparrow$	-13.41	-12.34	-1.73	0.06	0.68	-0.91	0.02	-0.03	-0.88	-0.14
PHOTOS	2.80	1.20	1.32	0.90	0.79	0.61	0.67	0.43	0.24	0.03
BR(D^0) $\downarrow$	31.99	-18.90	-4.30	-0.16	-0.07	-1.15	0.28	0.10	-0.68	-0.39

Continued on Next Page…

Syst and Stat uncertainties $B^- \to D^0\ell^-\bar{\nu}$ events – Continued										
BR(D^0) ↑	13.23	-11.94	-0.73	-0.30	1.17	-0.60	-0.09	-0.09	-0.39	-0.03
BR(D^+) ↓	-5.01	-9.38	-1.59	0.78	1.59	-0.62	0.08	0.37	-0.40	-0.10
BR(D^+) ↑	-24.84	-18.86	-1.46	-0.74	0.75	-0.81	-0.03	0.23	-0.47	0.02
D^{*1} FF isgw2	-26.37	-12.74	-1.68	0.10	1.29	-0.33	-0.13	-0.15	-1.01	-0.59
D^{*2} FF isgw2	19.49	-12.27	-2.10	-0.06	0.78	-1.19	0.03	0.08	-0.61	-0.24
D^{*0} FF isgw2	-26.54	-17.01	-2.30	-0.10	1.17	-0.11	0.28	-0.42	-0.74	-0.12
$D^{*1'}$ FF isgw2	9.75	-16.68	-1.81	0.44	0.77	-0.52	0.25	-0.36	-1.02	-0.37
PID kaon eff	-2.95	-18.58	-2.70	0.49	0.87	-0.85	0.13	-0.19	-0.37	-0.43
PID kaon mis-Id	-8.81	-15.43	-1.06	-0.71	-0.36	0.27	0.27	0.51	-0.46	-0.23
bremsstrahlung ↓	5.84	-14.86	-2.88	-0.20	0.05	-0.75	0.03	0.03	-0.73	-0.13
bremsstrahlung ↑	50.58	-14.20	-0.71	1.04	-0.87	-0.63	0.16	-0.02	-0.23	-0.49
K_L^0 Prod ↑	-5.89	-13.89	-2.91	0.55	0.93	-0.40	-0.11	0.16	-0.71	-0.46
K_L^0 Prod ↓	7.21	-13.05	-1.34	0.10	0.65	-0.58	-0.21	0.06	-0.98	-0.75
K_L^0 Energy ↑	2.73	-17.61	-0.96	0.89	0.41	-1.21	-0.14	0.10	-0.48	-0.18
K_L^0 Energy ↓	16.45	-20.64	-2.01	0.55	0.19	0.13	-0.28	-0.13	-0.31	-0.22
Fit	10.49	-16.00	7.45	-3.95	-1.96	1.84	1.84	-0.07	0.80	0.65

Table B.4: Systematic and Statistical relative uncertainties stemming from the signal yields extraction fit for $B^- \to D^0\ell^-\bar{\nu}$ events. Relative uncertainties are given in %. The ↑(↓) means a variation of $+(-)\sigma$ of the quantity involved in the study of the given systematics

C Charged Tracks and Neutral Clusters Selection Criteria

In this appendix are described the selection criteria used in this work to reconstruct and to select charged tracks and photons.

C.1 Charged particles reconstruction

Charged track candidates are reconstructed according to different quality selection criteria, and they are store in dedicated lists. Charged track lists used in this analysis and their requirements are described in the following section.

C.1.1 Charged Tracks (CT)

The list of track candidates satisfying CT selection criteria contains all charged track objects reconstructed in the tracking system, the Kalman [43] fit algorithm assigns by default the $\pi^{\pm}$ mass hypothesis to each track candidates.

C.1.2 Good Track Very Loose (GTVL)

The GTVL list contains all the CT track candidates satisfying the following criteria:

- *Distance of closest approach to the beam spot* measured in the x - y plane ($|d_0|$) and along the z axis ($|z_0|$). A cut on those variables rejects fake tracks and background tracks not originating near the beam-beam interaction point. It is required: $|d_0| < 1.5$ cm and $|z_0| < 10$ cm.
- *Maximum momentum.* To remove tracks not compatible with the beam energy we require $p_{lab} < 10\,\mathrm{GeV}/c$, where p_{lab} refers to the laboratory momentum of the track, this restriction discriminates against misreconstructed tracks.

C.2 Neutral particles reconstruction

Neutral candidates, such as photons, are reconstructed according to different quality selection criteria similarly to charged candidates. In this section the criteria used to select them are summarized.

C.2.1 Calor Neutral (CN)

In the CN list of neutral candidates are stored all energy deposit clusters reconstructed in the EMC. If the cluster has more than one energy minimum, the cluster is splitted into two objects, called bumps. To all neutral candidates have been assign the photon mass hypothesis.

C.2.2 Good Photon Loose (GPL)

The GPL list contains all CN candidates satisfying:

- $E_{tot} > 0.03\,\mathrm{GeV}$, where $E_{tot} = \sum_i^n E_i$ the sum of energy deposits in each crystals belonging to a given bump.
- Lateral momentum (see definition in section 5.1) $LAT < 0.8$

D Comparison Plots before and after fit

All quantities employed in the analysis are plotted before and after applying the fit results.

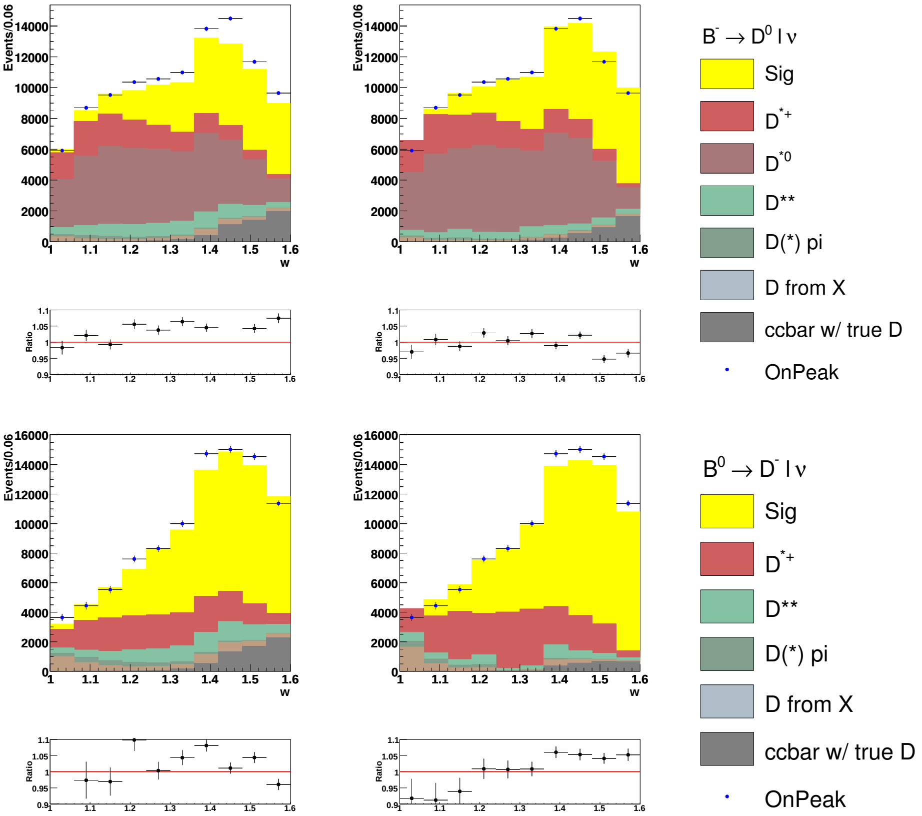

Figure D.1: The plot shows the w distribution before and after applying the fit results, once all the selection criteria were applied

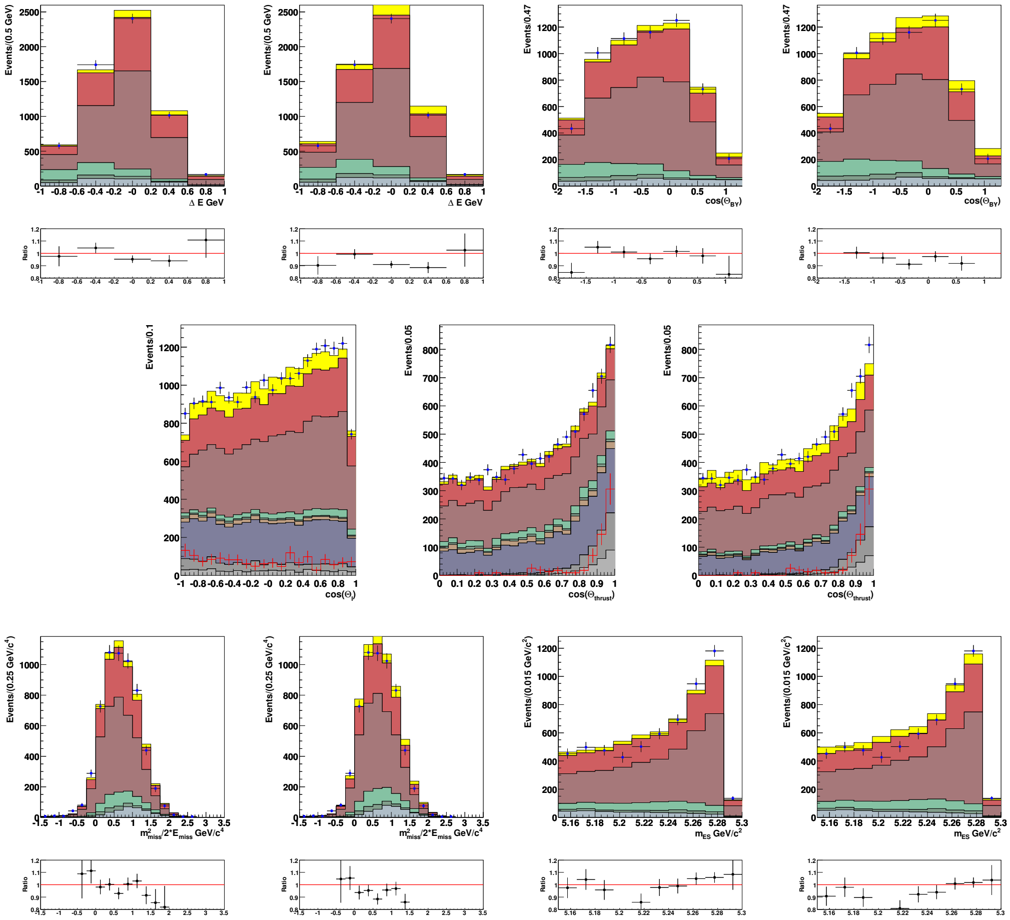

Figure D.2: The plots show several distribution before and after applying the fit results after all the selection criteria were applied, only for the $1.w$ bin , D^0 -channel

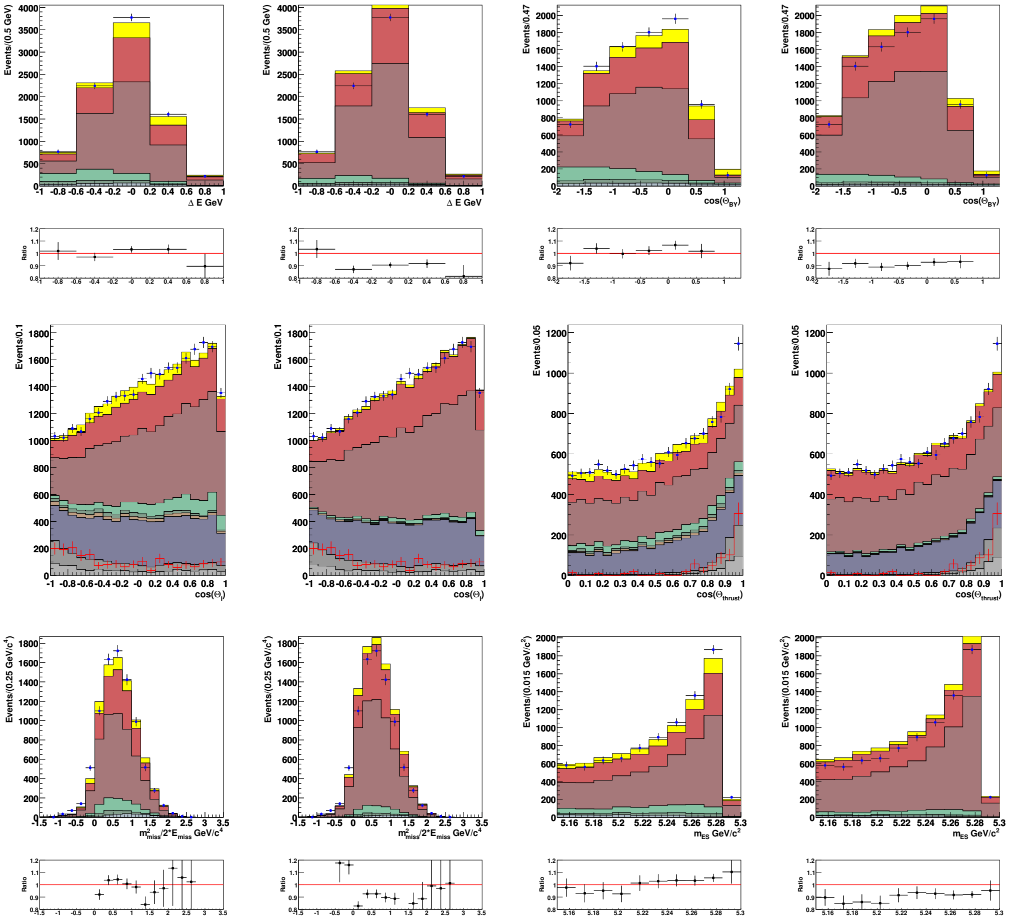

Figure D.3: The plot shows the w distribution applying before and after applying the fit results after all the selection criteria were applied, only for the $2.w$ bin, D^0 -channel

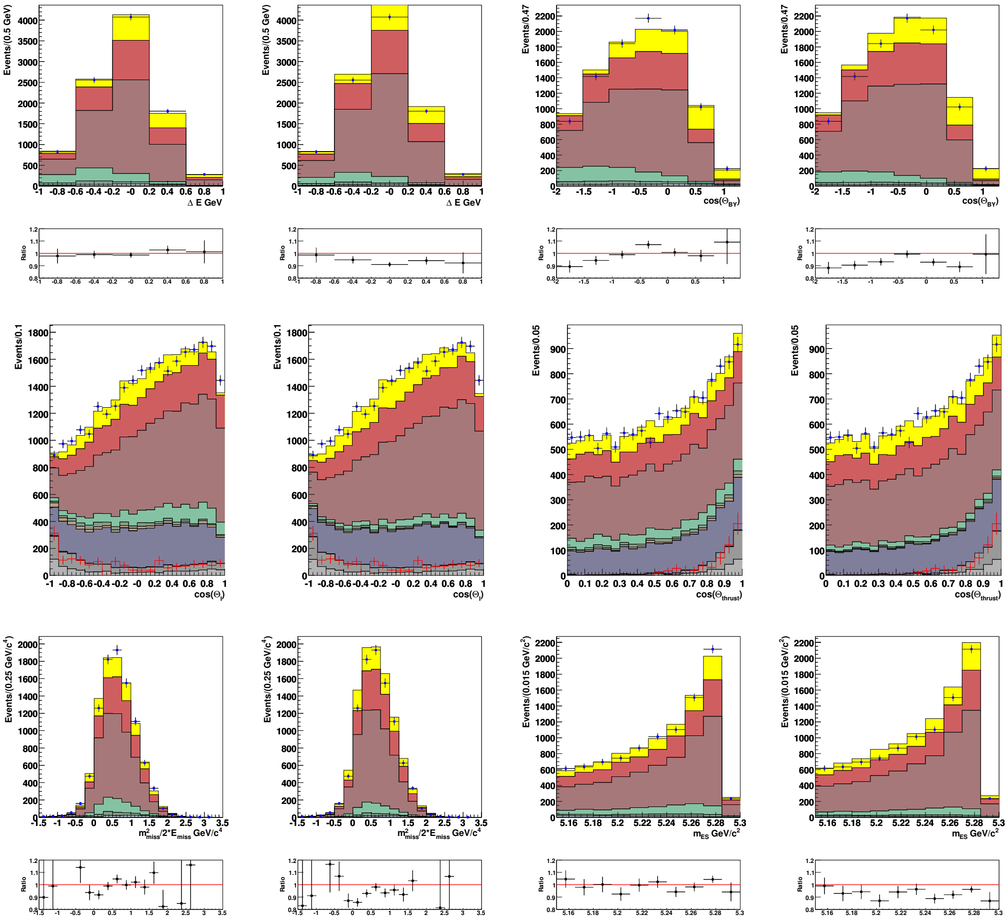

Figure D.4: The plot shows the w distribution applying before and after applying the fit results after all the selection criteria were applied, only for the $3.w$ bin , D^0 -channel

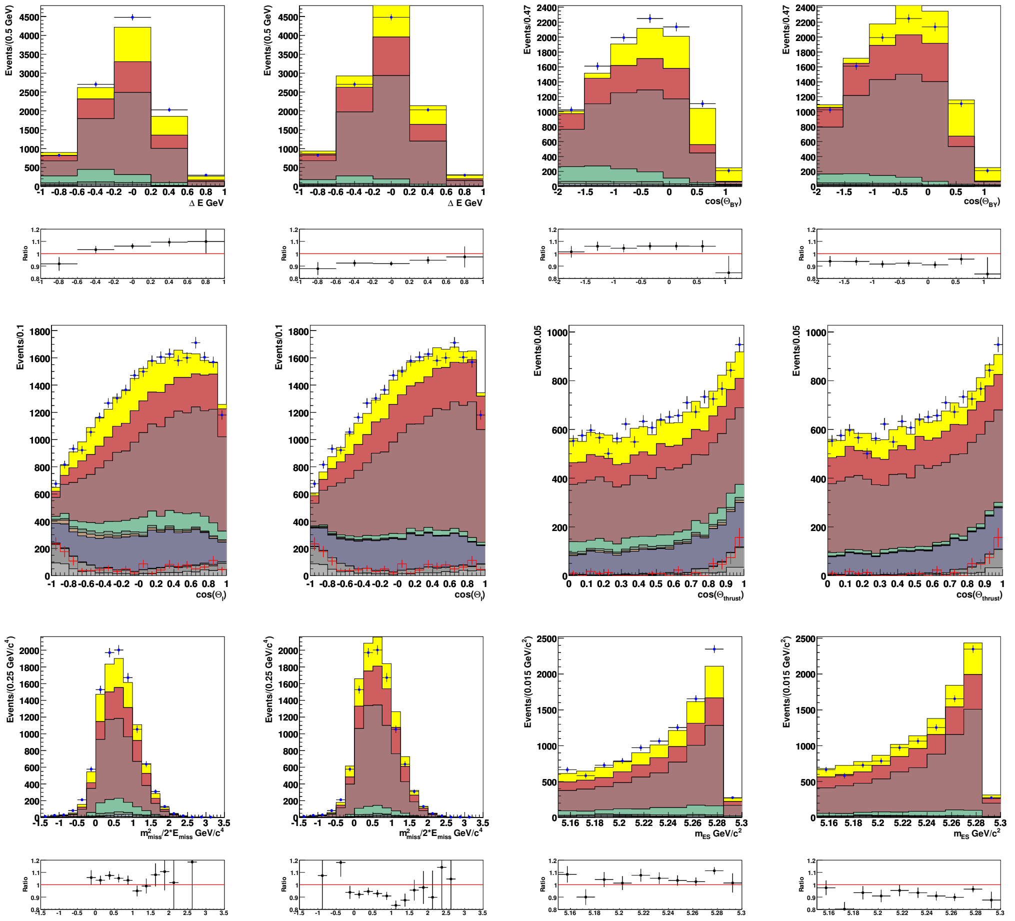

Figure D.5: The plot shows the w distribution applying before and after applying the fit results after all the selection criteria were applied , only for the $4.w$ bin, D^0 -channel

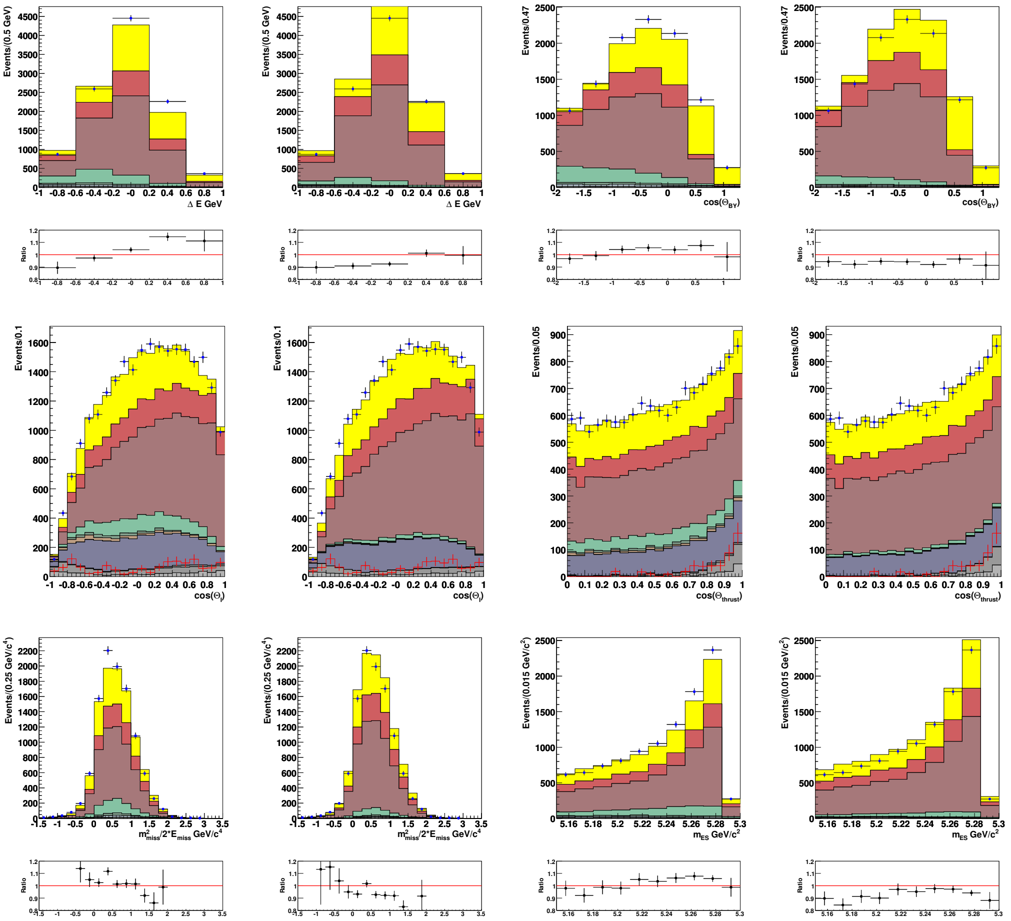

Figure D.6: The plot shows the w distribution applying before and after applying the fit results after all the selection criteria were applied, only for the 5.w bin , D^0 -channel

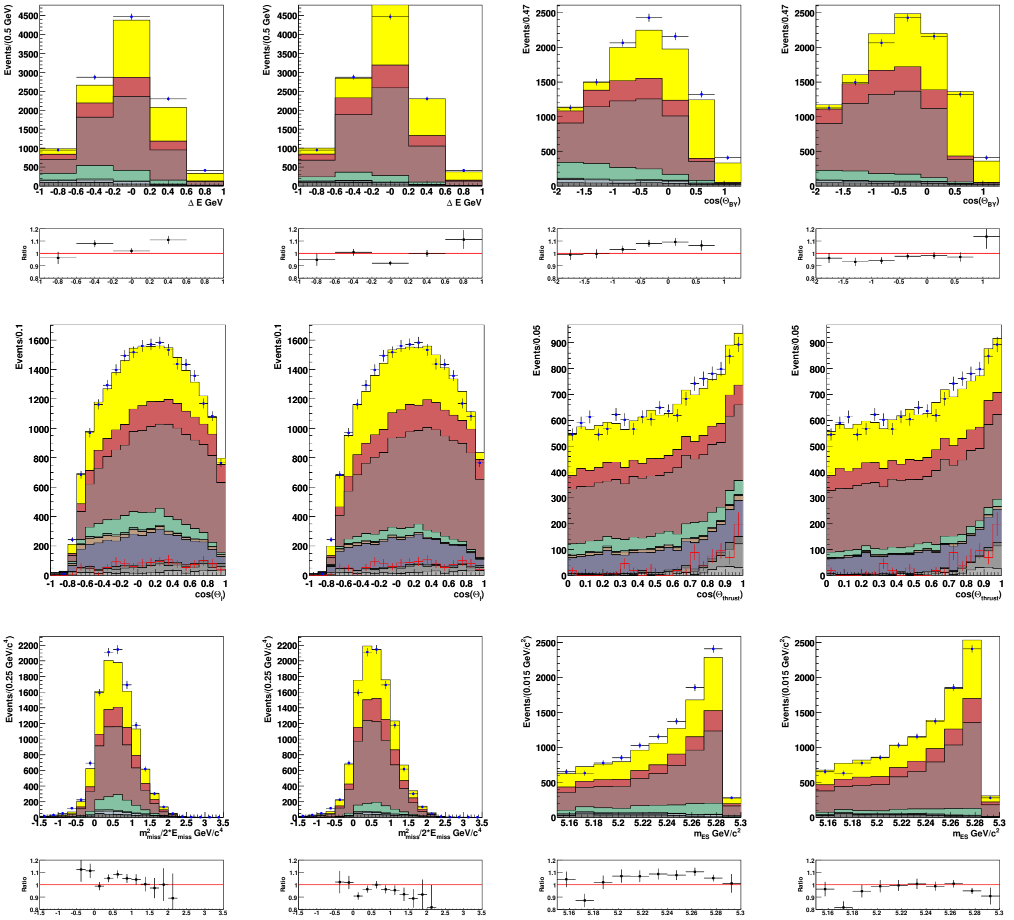

Figure D.7: The plot shows the w distribution applying before and after applying the fit results after all the selection criteria were applied, only for the $6.w$ bin , D^0 -channel

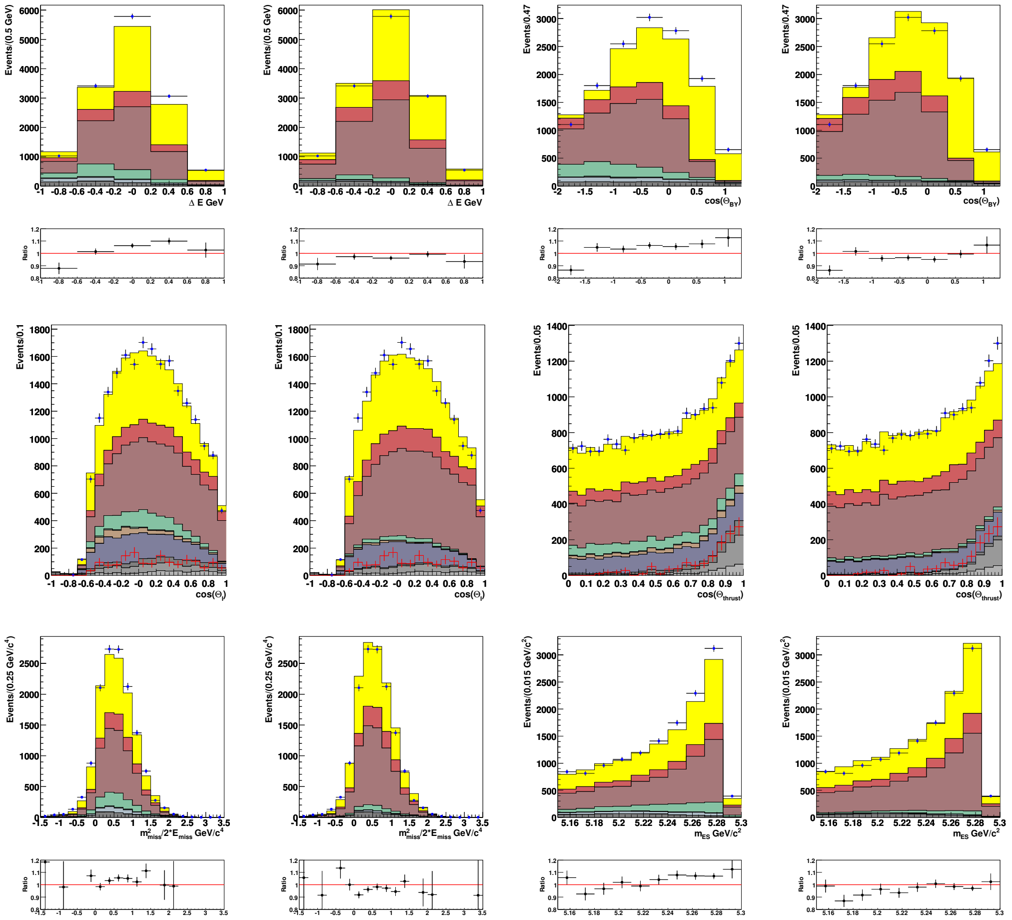

Figure D.8: The plot shows the w distribution applying before and after applying the fit results after all the selection criteria were applied, only for the $7.w$ bin , D^0 -channel

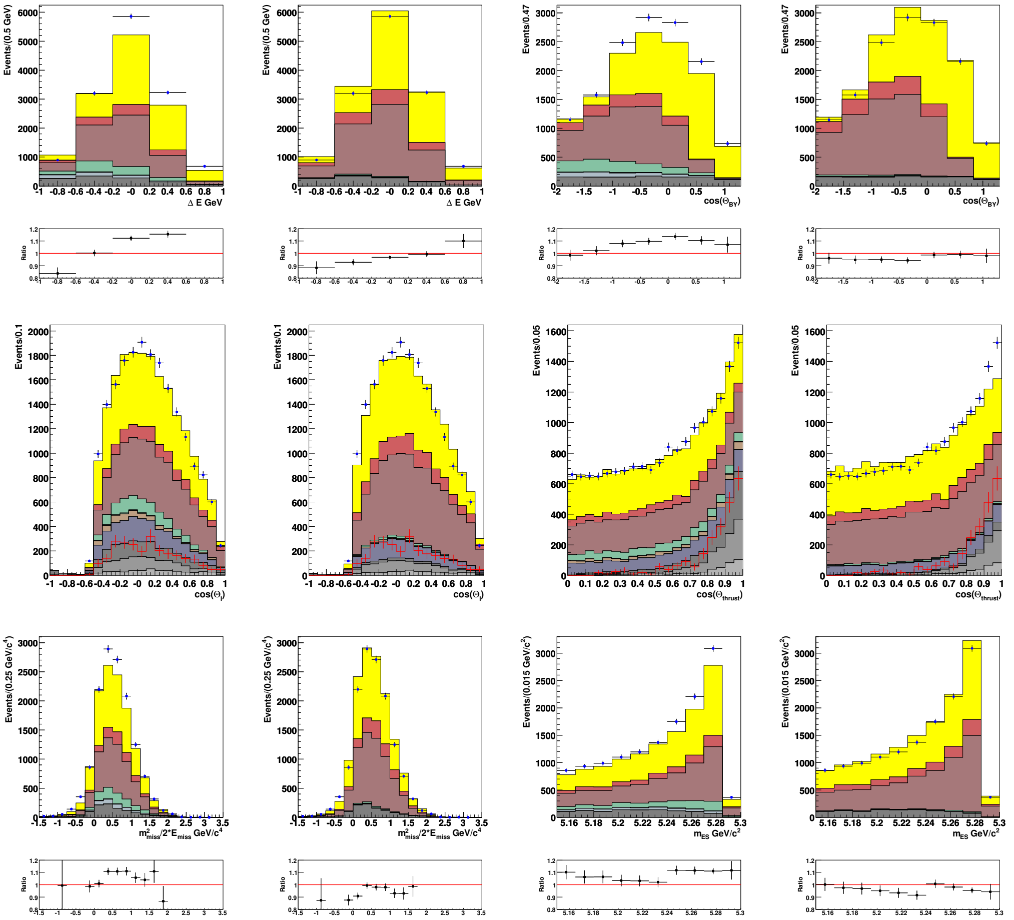

Figure D.9: The plot shows the w distribution applying before and after applying the fit results after all the selection criteria were applied, only for the 8.w bin , D^0 -channel

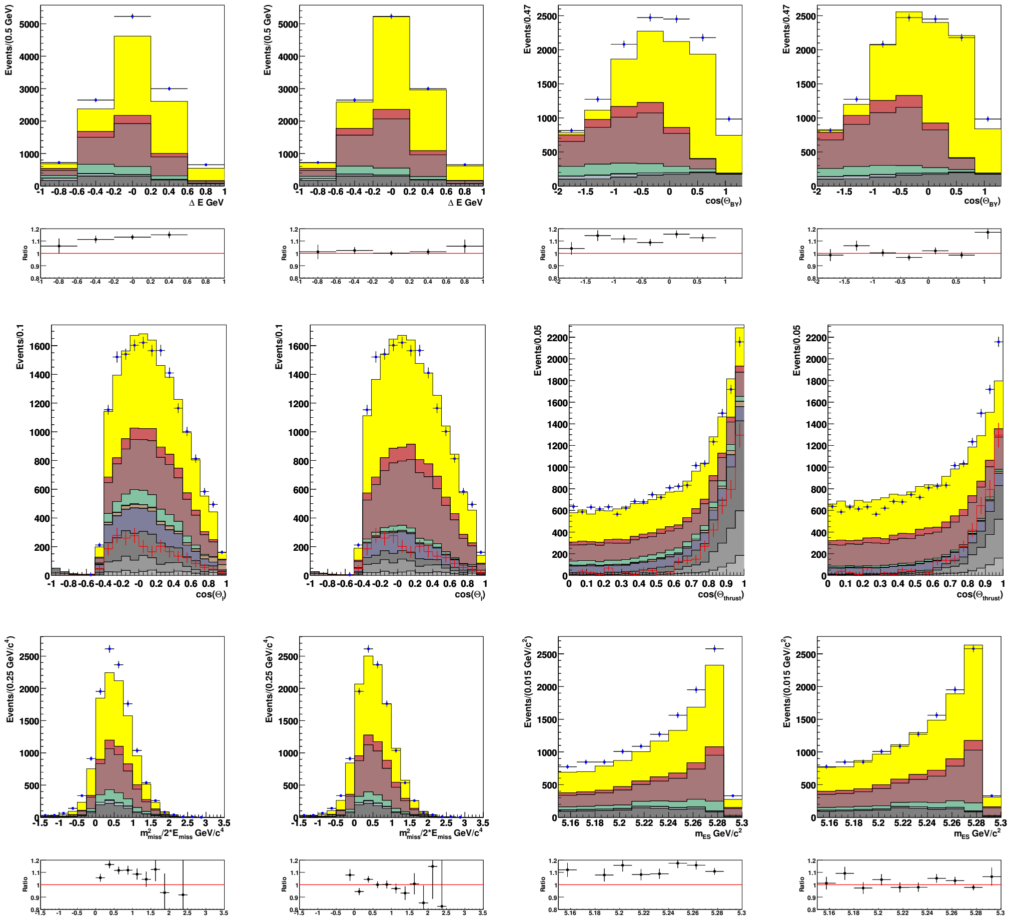

Figure D.10: The plot shows the w distribution applying before and after applying the fit results after all the selection criteria were applied, only for the 9.w bin , D^0 -channel

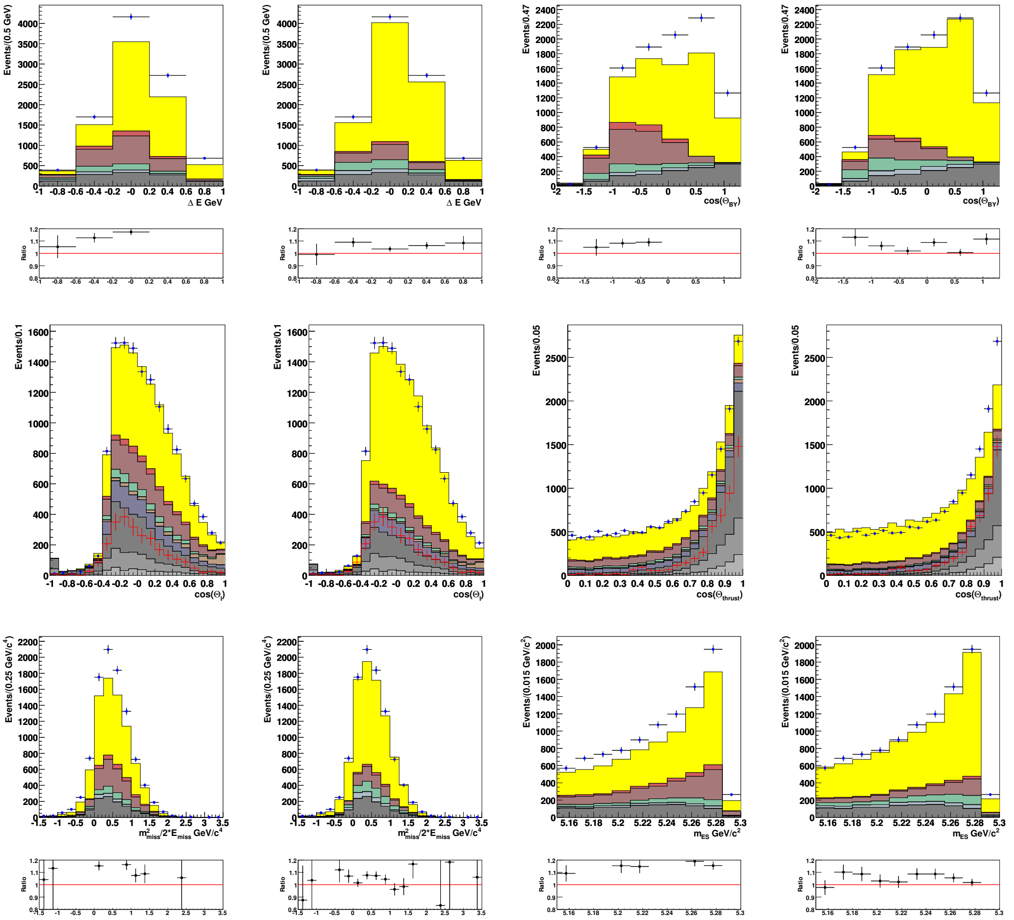

Figure D.11: The plot shows the w distribution applying before and after applying the fit results after all the selection criteria were applied, only for the 10.w bin , D^0 -channel

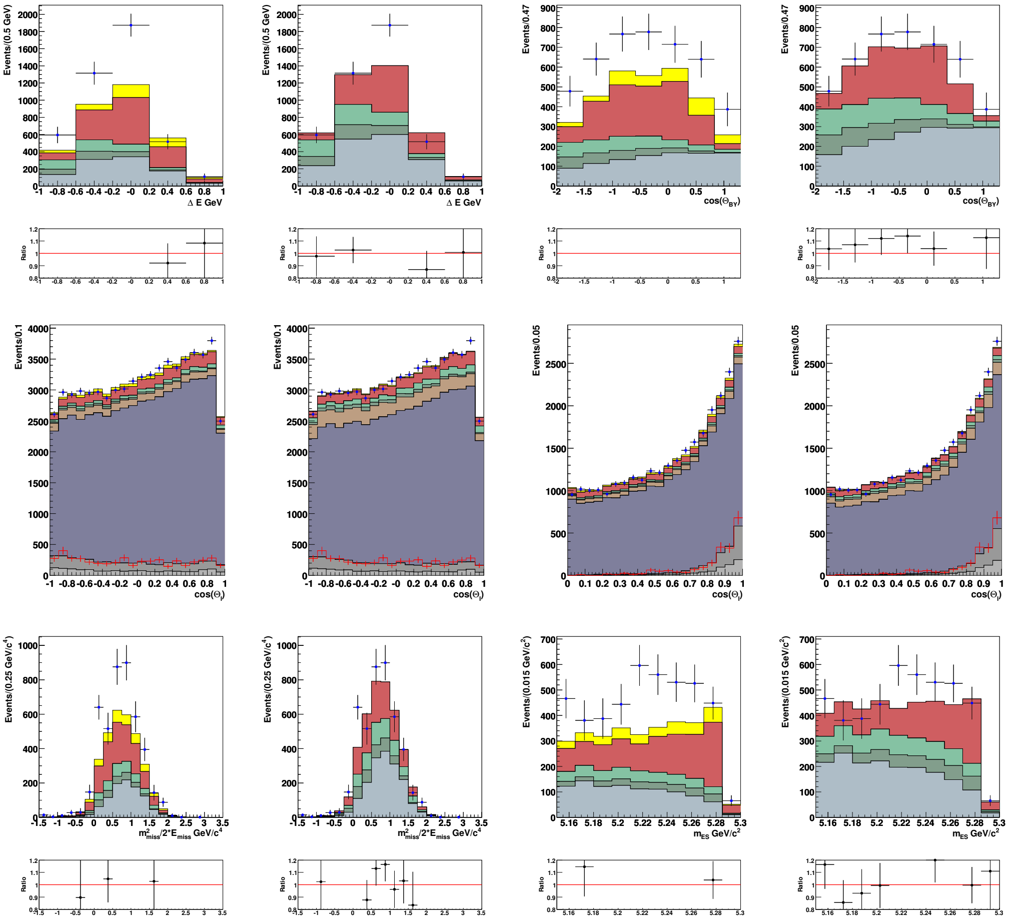

Figure D.12: The plot shows the w distribution applying before and after applying the fit results after all the selection criteria were applied, only for the $1.w$ bin, D^+ -channel

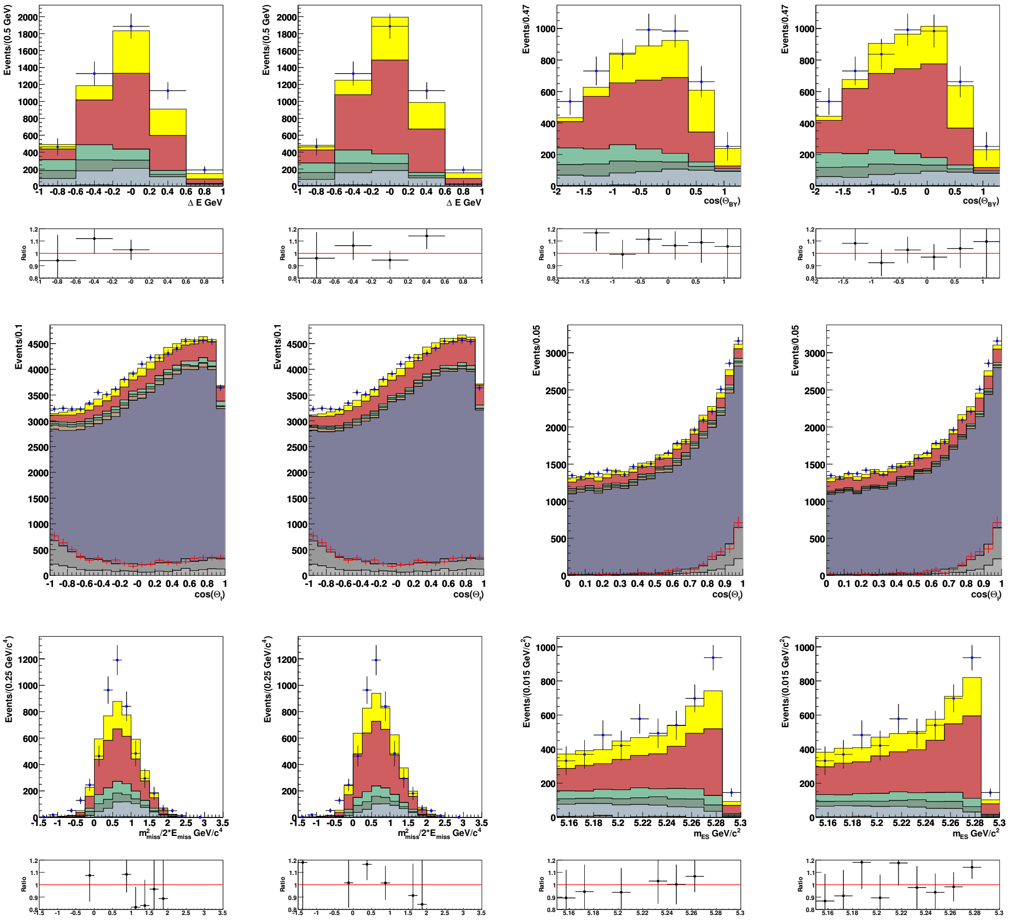

Figure D.13: The plot shows the w distribution applying before and after applying the fit results after all the selection criteria were applied, only for the $2.w$ bin, D^+ -channel

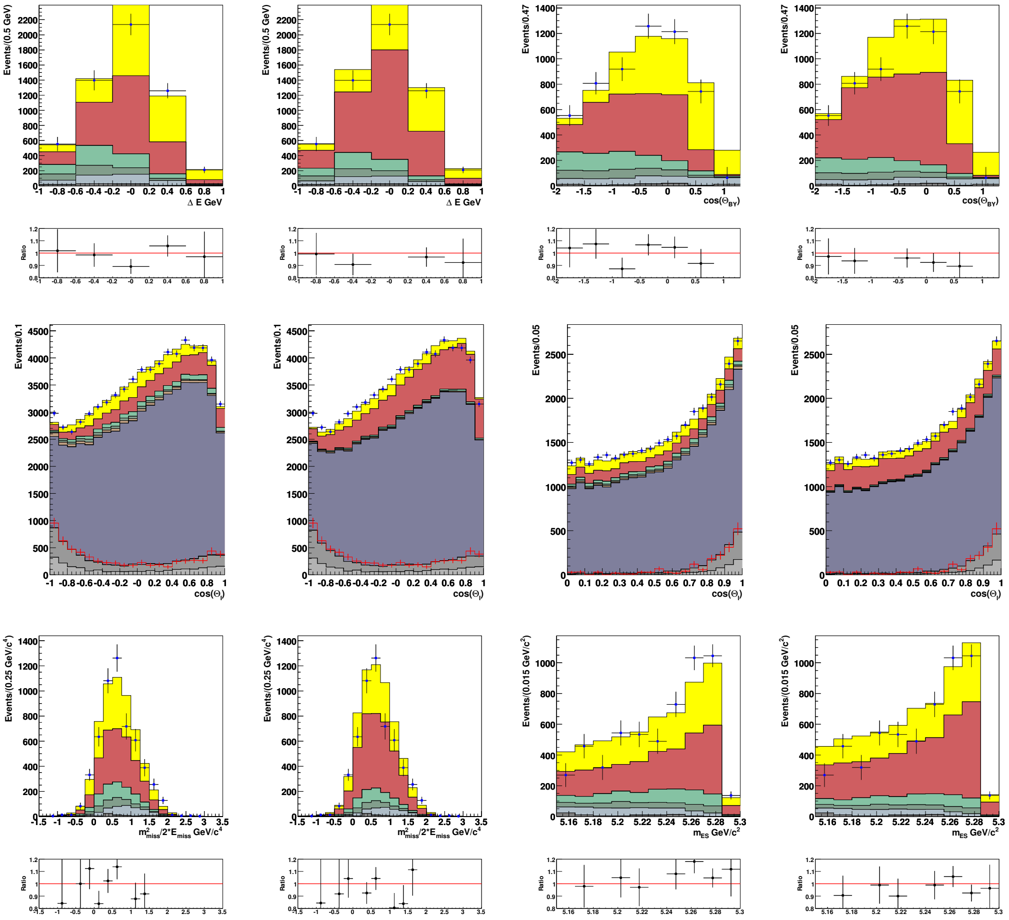

Figure D.14: The plot shows the w distribution applying before and after applying the fit results after all the selection criteria were applied, only for the $3.w$ bin, D^+ -channel

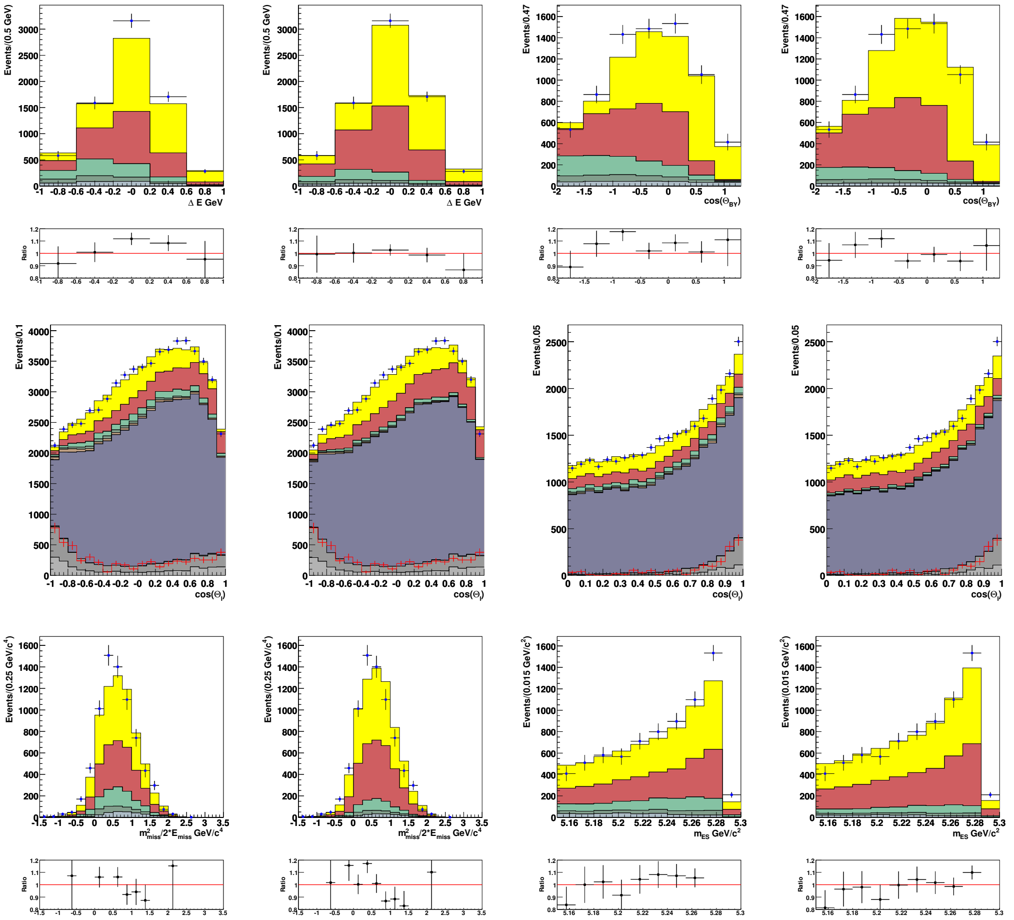

Figure D.15: The plot shows the w distribution applying before and after applying the fit results after all the selection criteria were applied, only for the 4.w bin, D^+ -channel

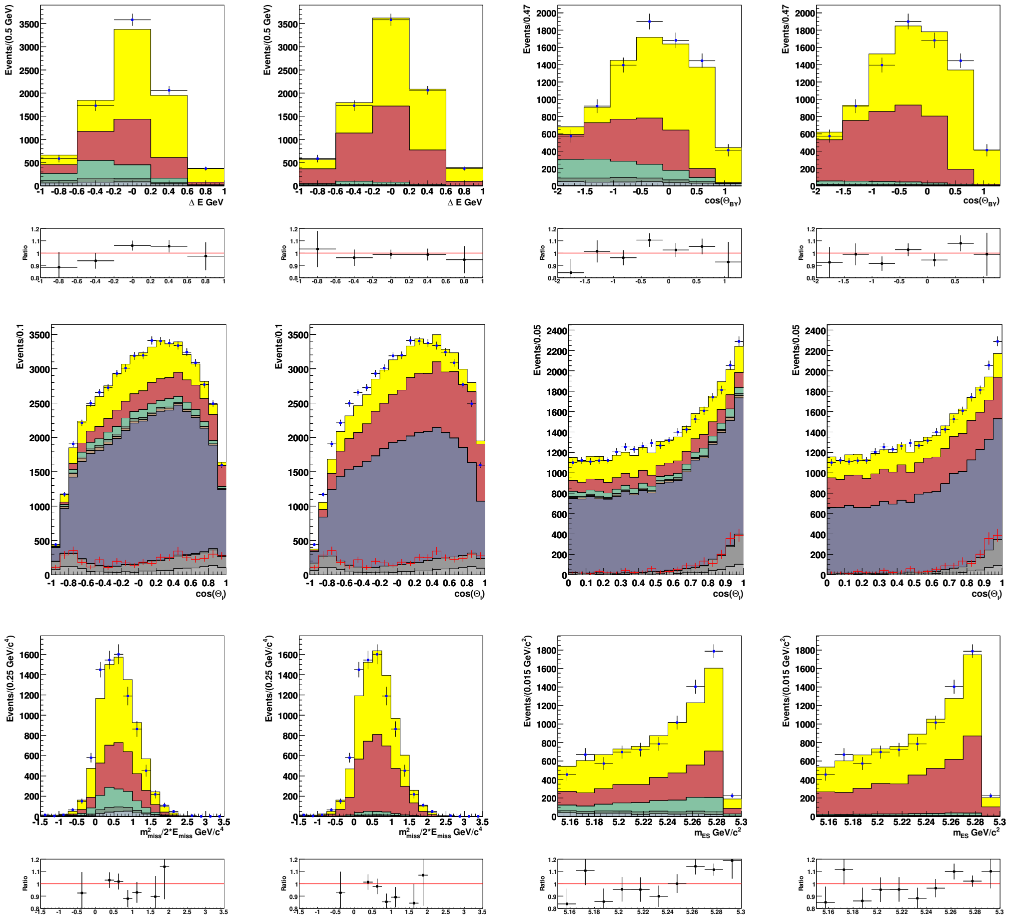

Figure D.16: The plot shows the w distribution applying before and after applying the fit results after all the selection criteria were applied, only for the $5.w$ bin, D^+ -channel

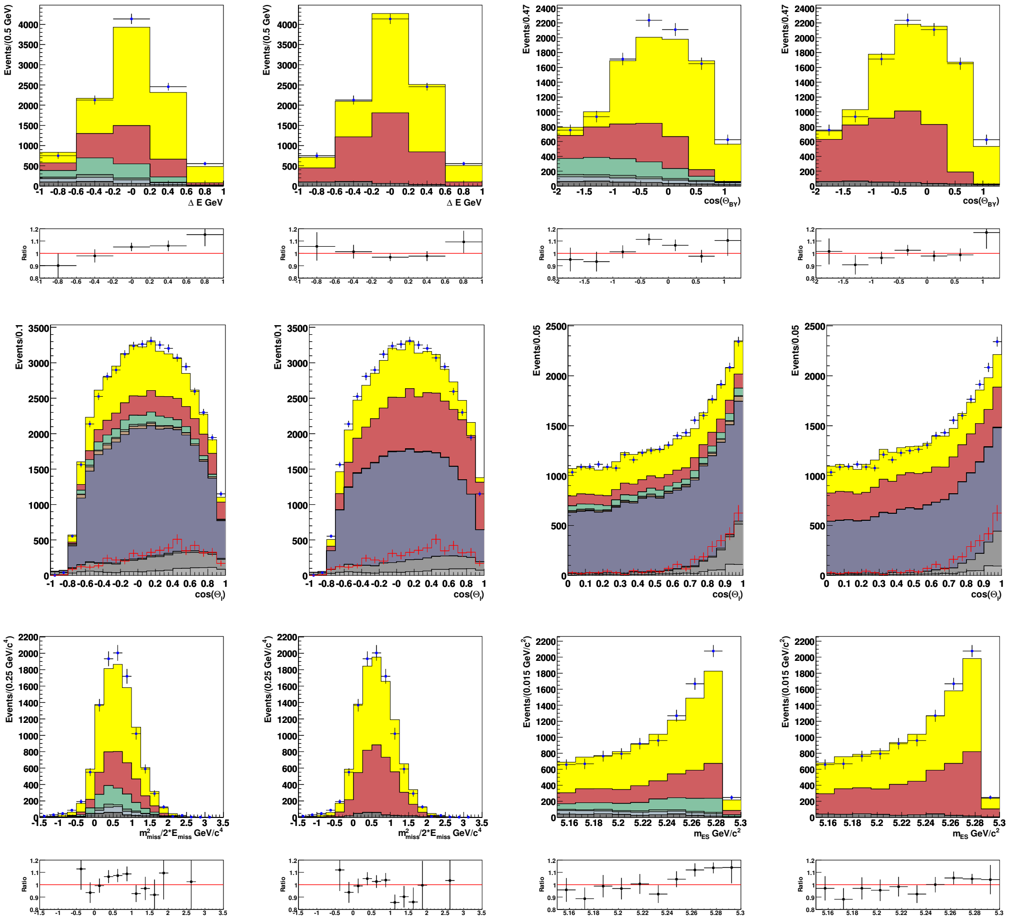

Figure D.17: The plot shows the w distribution applying before and after applying the fit results after all the selection criteria were applied, only for the 6.w bin, D^+ -channel

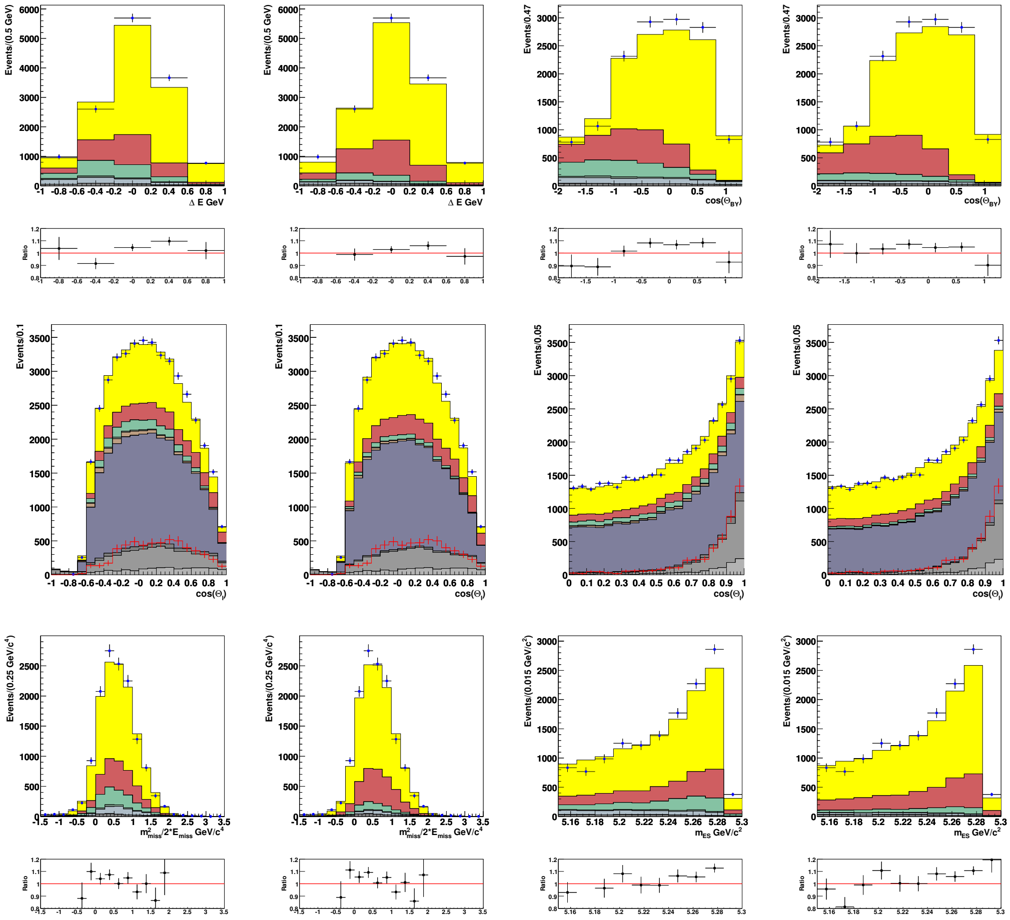

Figure D.18: The plot shows the w distribution applying before and after applying the fit results after all the selection criteria were applied, only for the $7.w$ bin, D^+ -channel

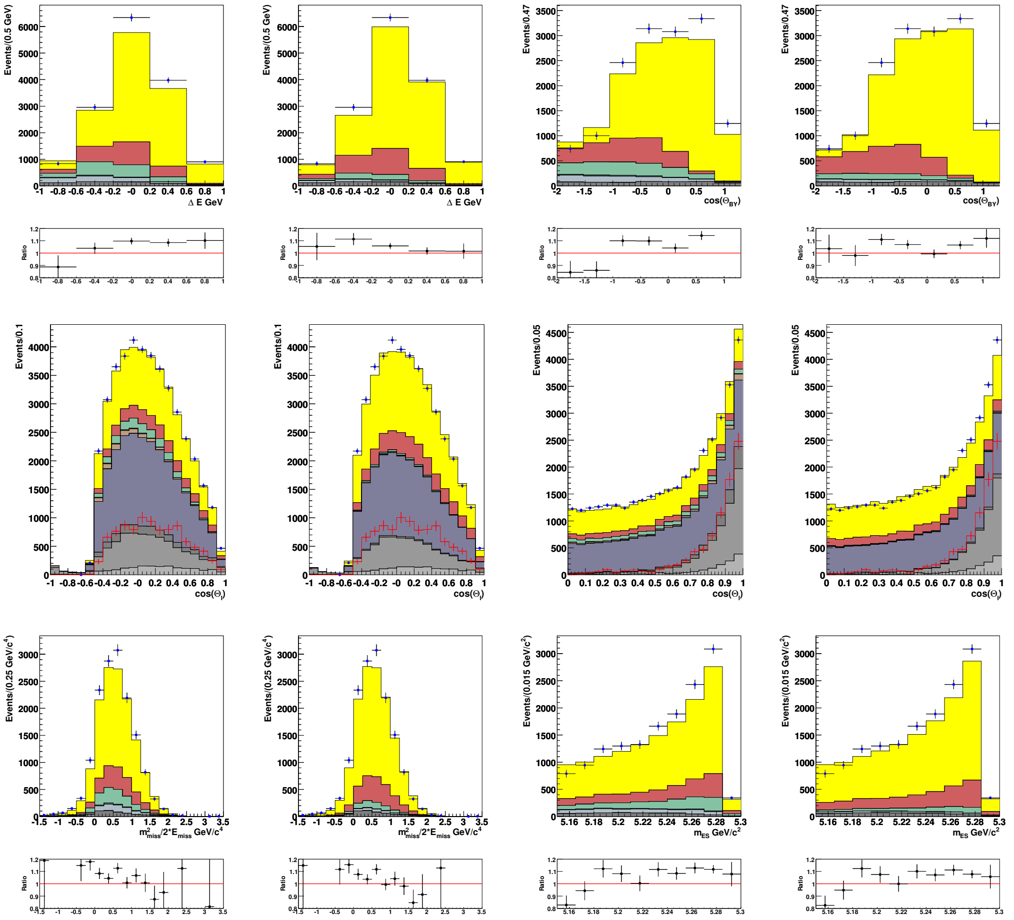

Figure D.19: The plot shows the w distribution applying before and after applying the fit results after all the selection criteria were applied, only for the 8.w bin, D^{+} -channel

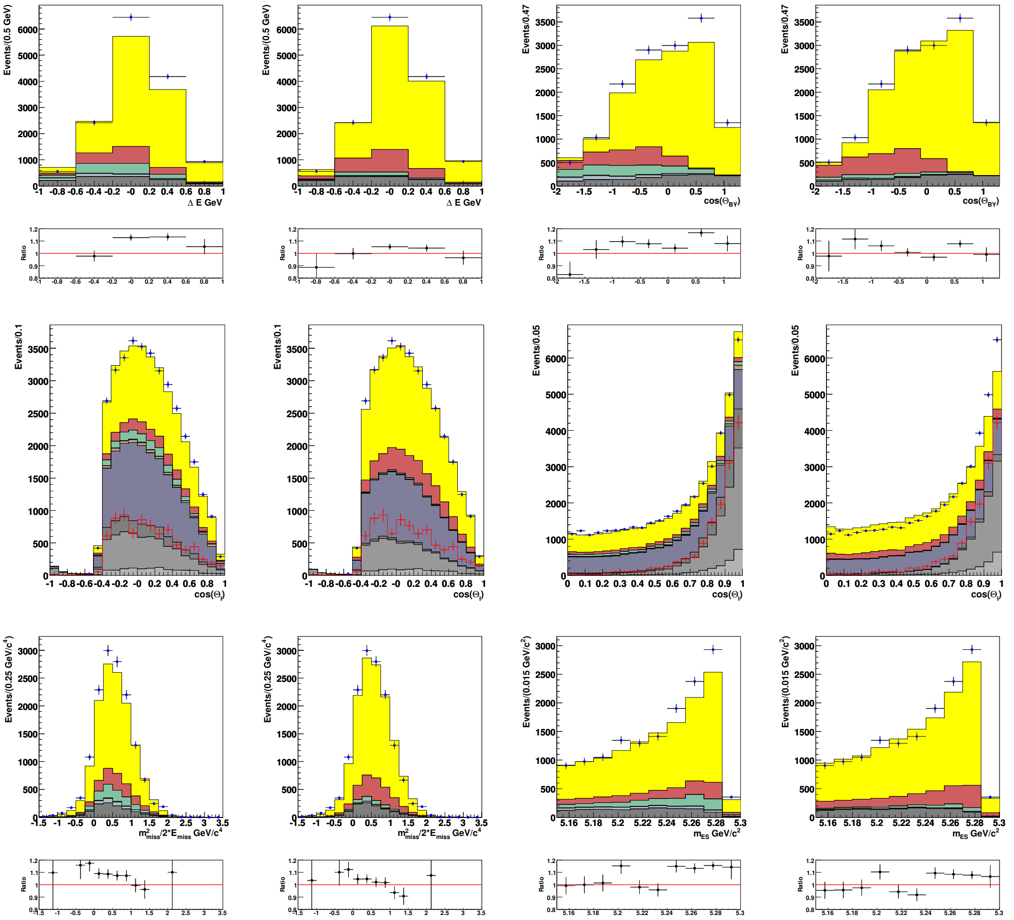

Figure D.20: The plot shows the w distribution applying before and after applying the fit results after all the selection criteria were applied, only for the 9.w bin, D^+ -channel

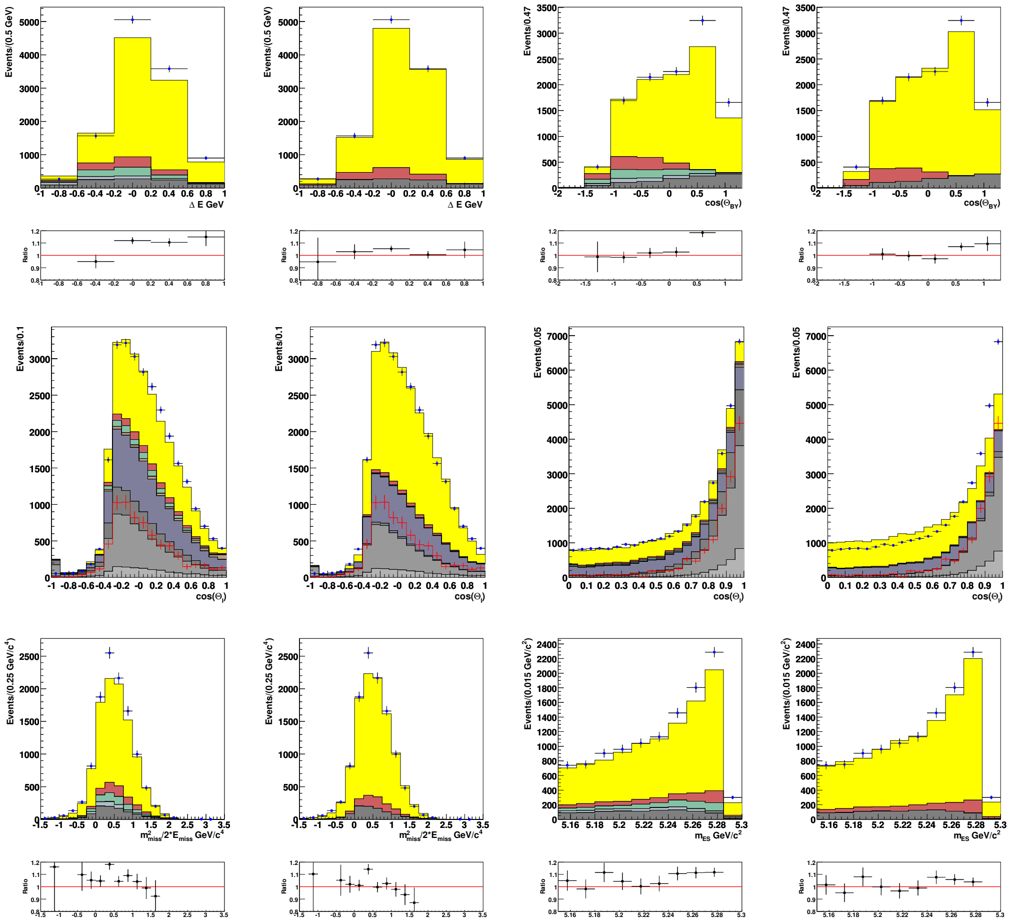

Figure D.21: The plot shows the w distribution applying before and after applying the fit results after all the selection criteria were applied, only for the $10.w$ bin, D^+ -channel

E Side-Band studies

In this appendix are shown the results of studies done to see the prove the ansatz: m_D side-band events can be used to describe combinatoric background in the mass region. At first E.1 this study is done using only MC events, MC side band events have been compared to MC combinatoric background events in the mass region. Then E.2 on-peak data side-band events have been compared to MC combinatoric background events in the mass region. These studies show a good agreement between side-band events and combinatoric background events.

E.1 Side-Band MC vs Combinatoric and $q\bar{q}$ MC

Comparison are made using only MC events both side-band events and combinatoric background. The figures show for $B^- \to D^0\ell^-\bar{\nu}$ and $B^0 \to D^-\ell^+\nu$ the distribution $\cos\theta_{BY}$ E.1 E.2, ΔE E.3 E.4 and m_{ES} E.5 E.6

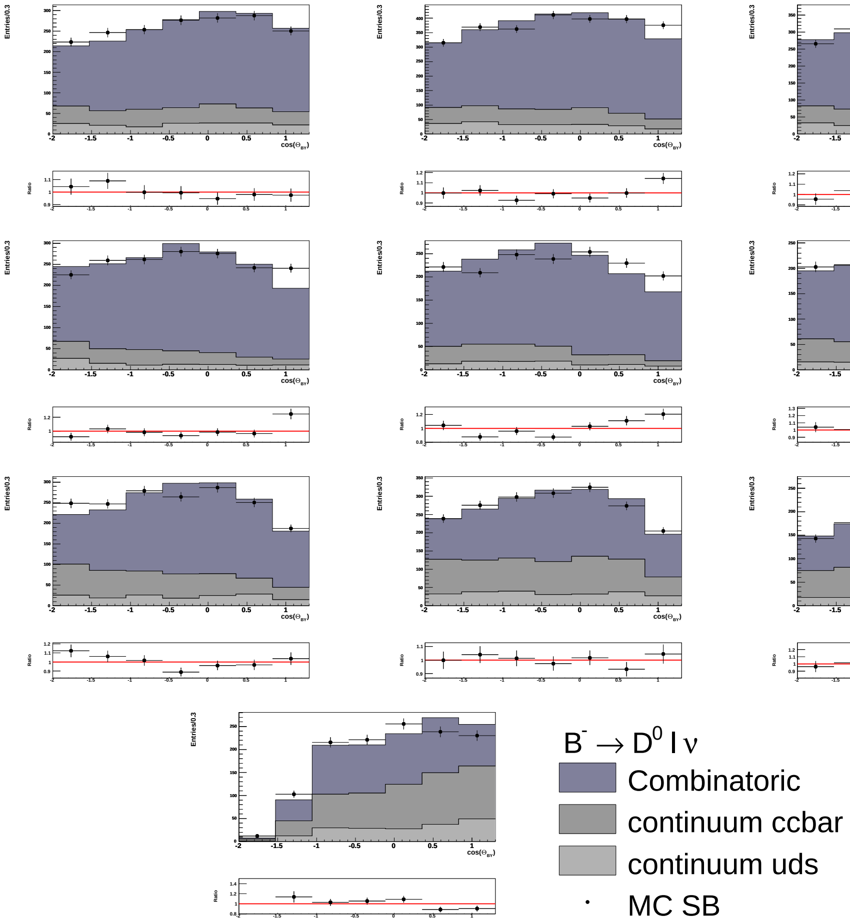

Figure E.1: The plot shows the $\cos\theta_{BY}$ comparison between the sideband distribution and the combinatoric background for MC events w-bin separately

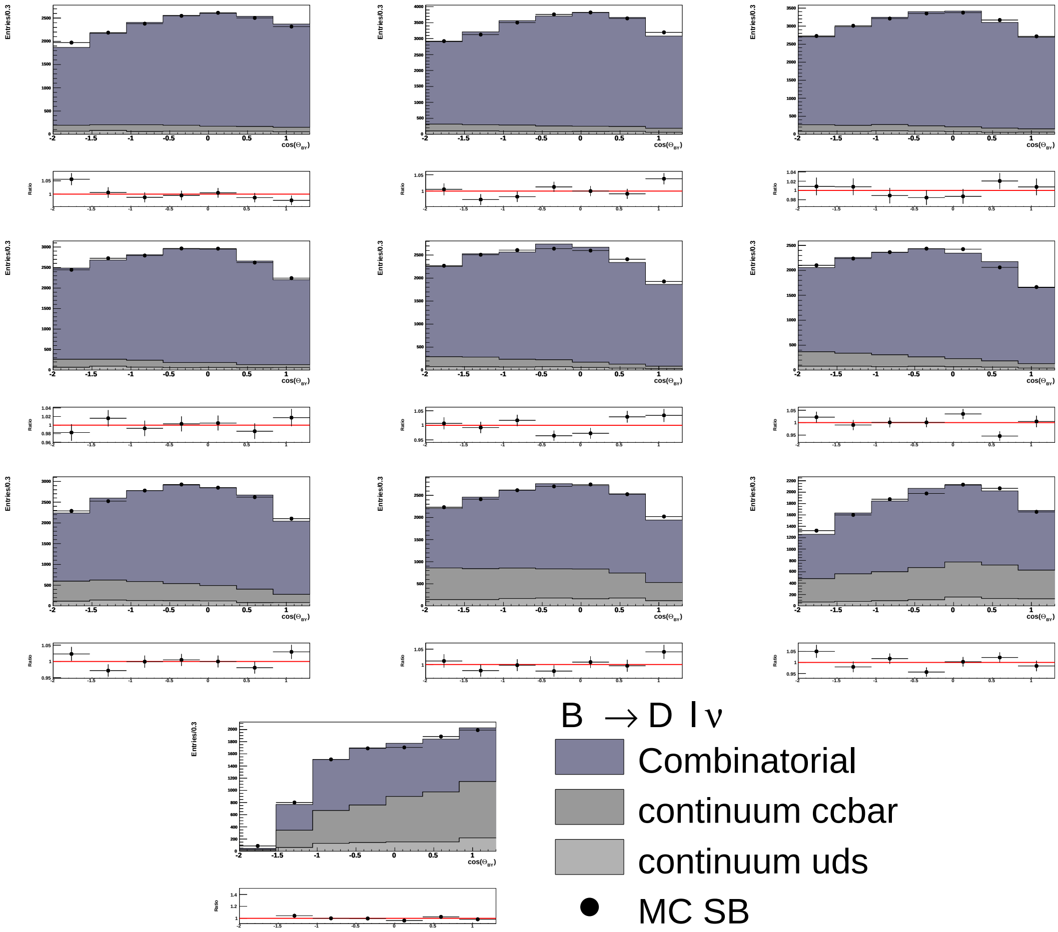

Figure E.2: The plot shows the $\cos\theta_{BY}$ comparison between the sideband distribution and the combinatoric background for MC events w-bin separately

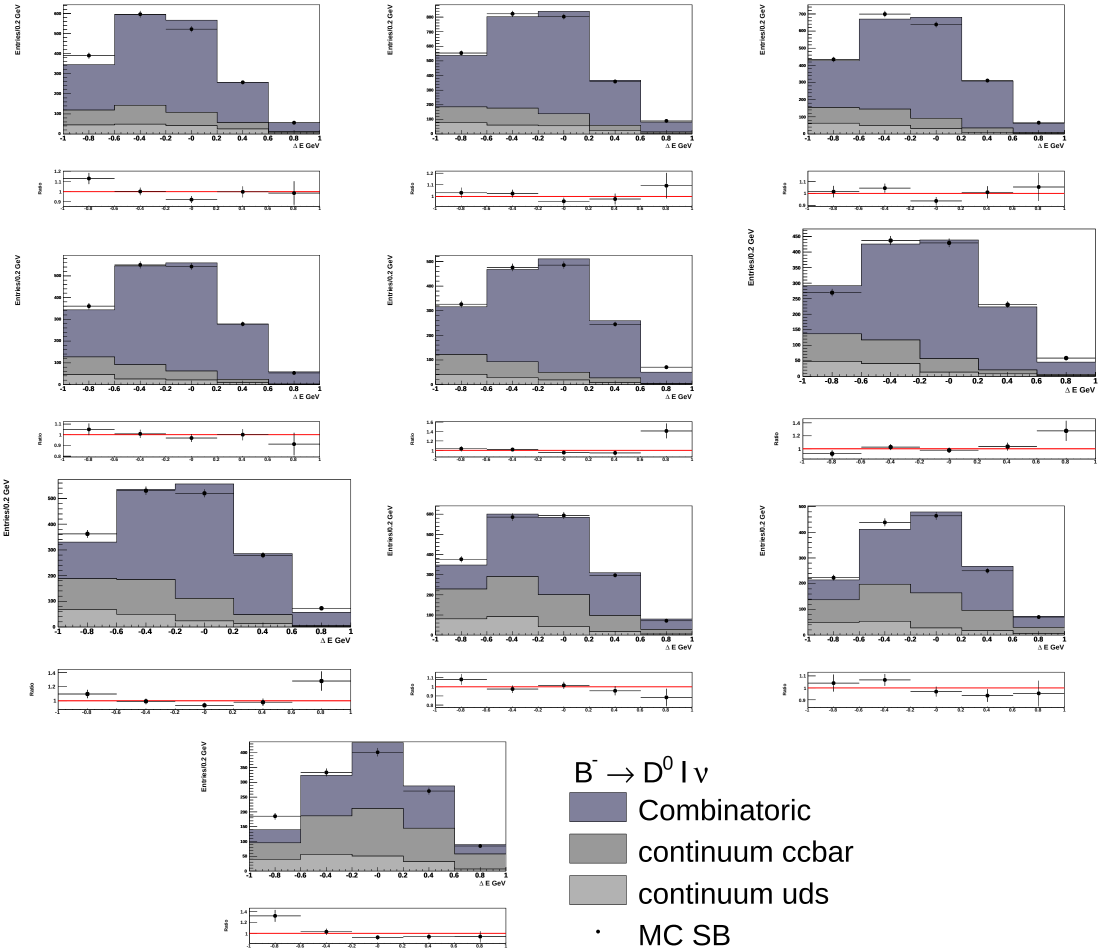

Figure E.3: The plot shows the ΔE comparison between the sideband distribution and the combinatoric background for MC events w-bin separately

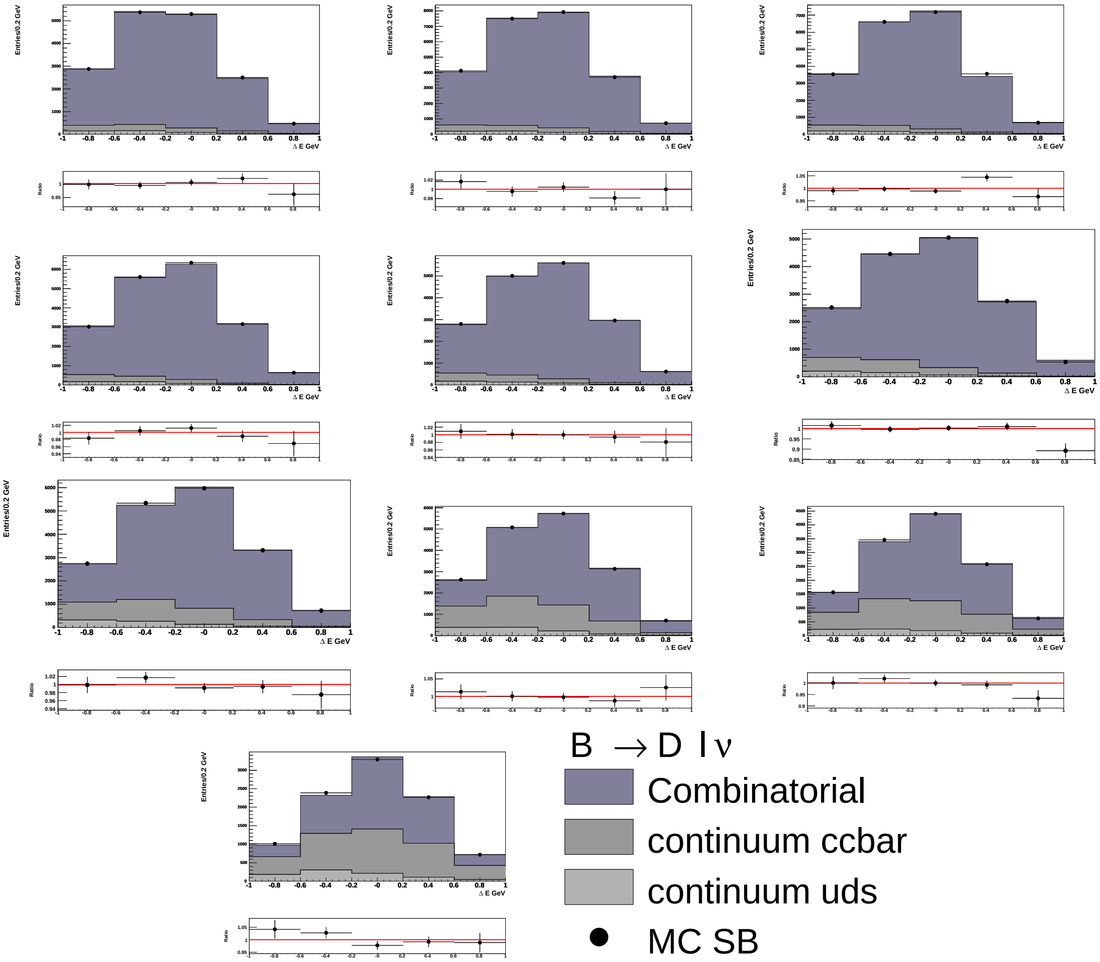

Figure E.4: The plot shows the ΔE comparison between the sideband distribution and the combinatoric background for MC events w-bin separately

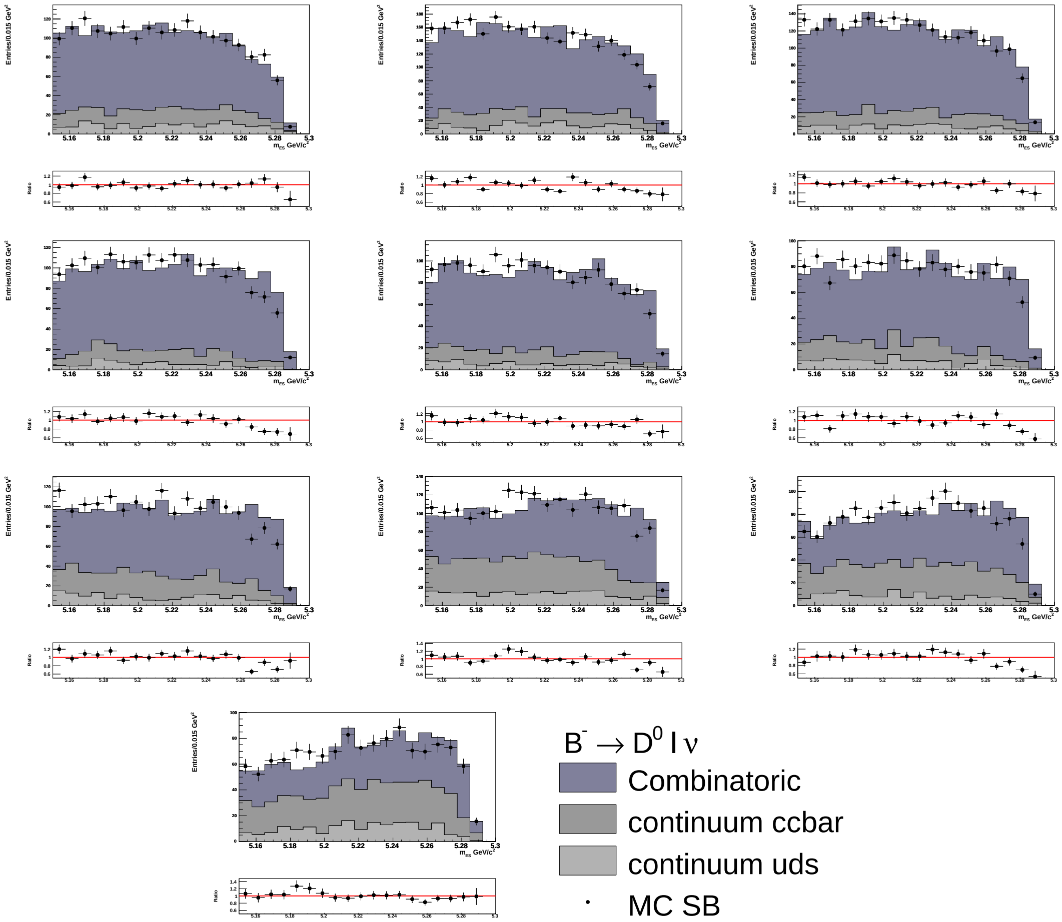

Figure E.5: The plot shows the m_{ES} comparison between the sideband distribution and the combinatoric background for MC events w-bin separately

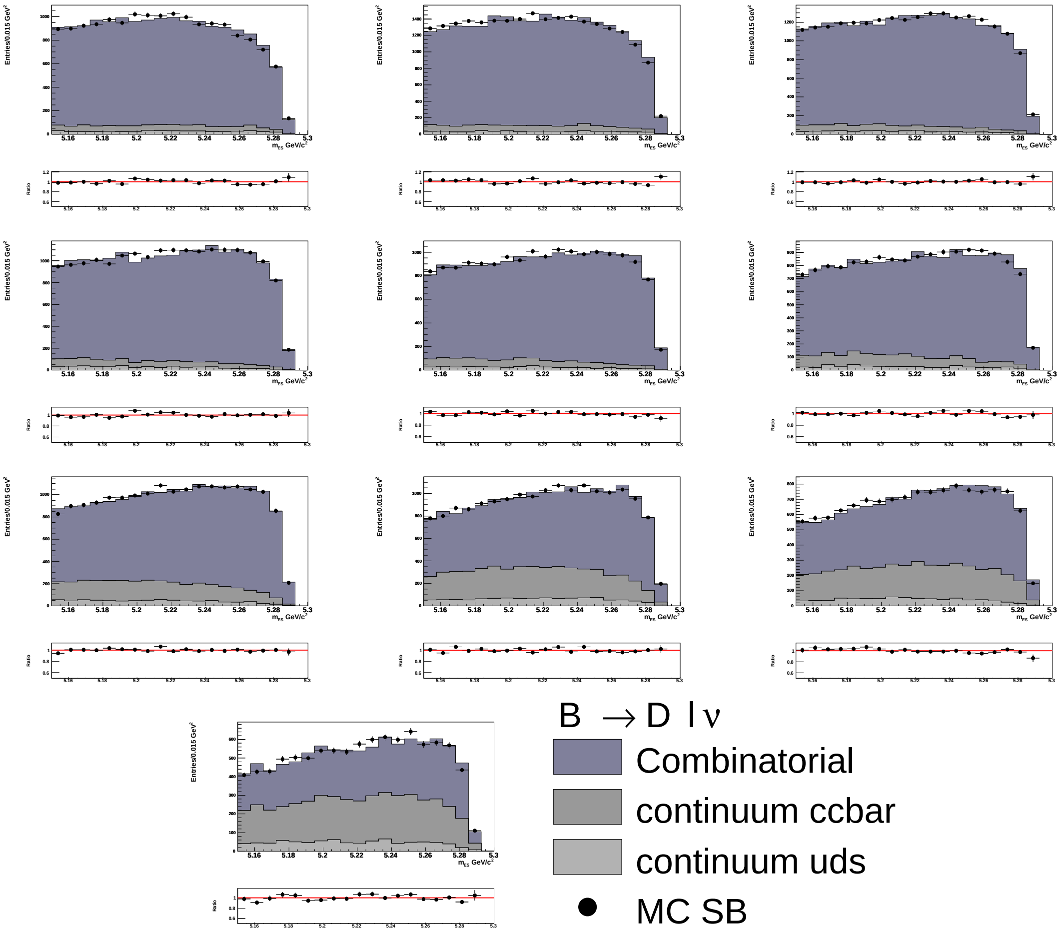

Figure E.6: The plot shows the m_{ES} comparison between the sideband distribution and the combinatoric background for MC events w-bin separately

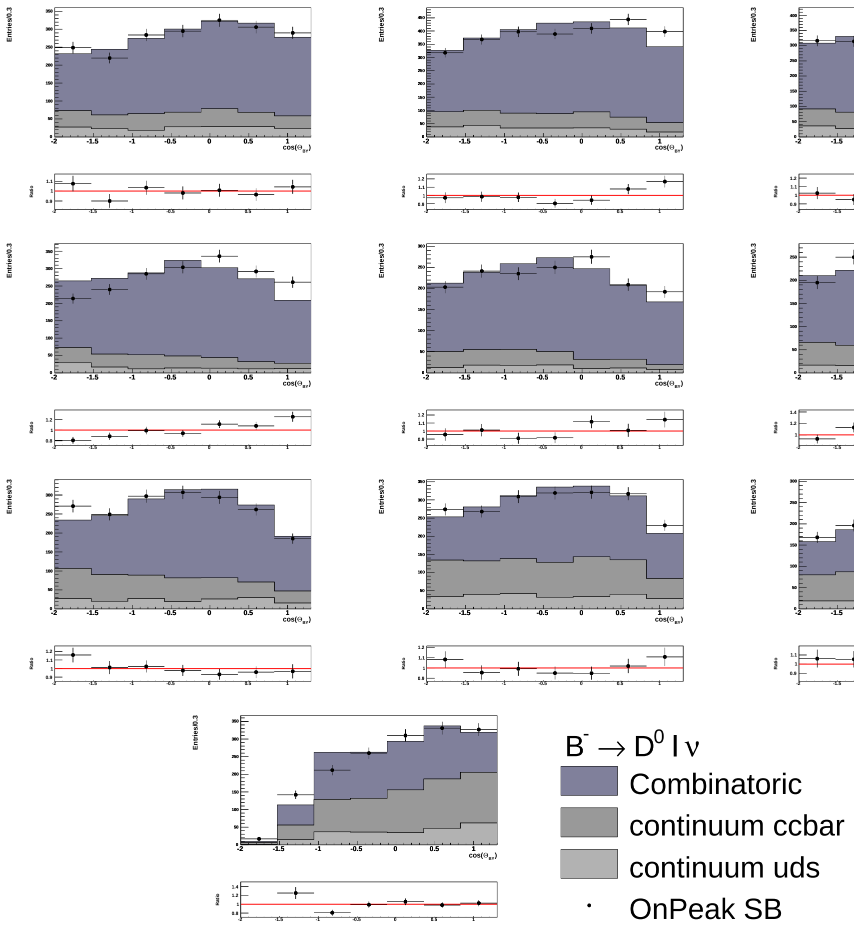

Figure E.7: The plot shows the $\cos\theta_{BY}$ comparison between the on-peak sideband data distribution vs the combinatoric background MC w-bin separately, scaled to on-peak luminosity

E.2 Side-Band On-Peak-Data vs Combinatoric and $q\bar{q}$ MC

In this section on-peak data side-band events are compared to MC combinatoric background events. The figures show for $B^- \to D^0\ell^-\bar{\nu}$ and $B^0 \to D^-\ell^+\nu$ the distribution $\cos\theta_{BY}$ E.7 E.8, ΔE E.9 E.10 and m_{ES} E.11 E.12

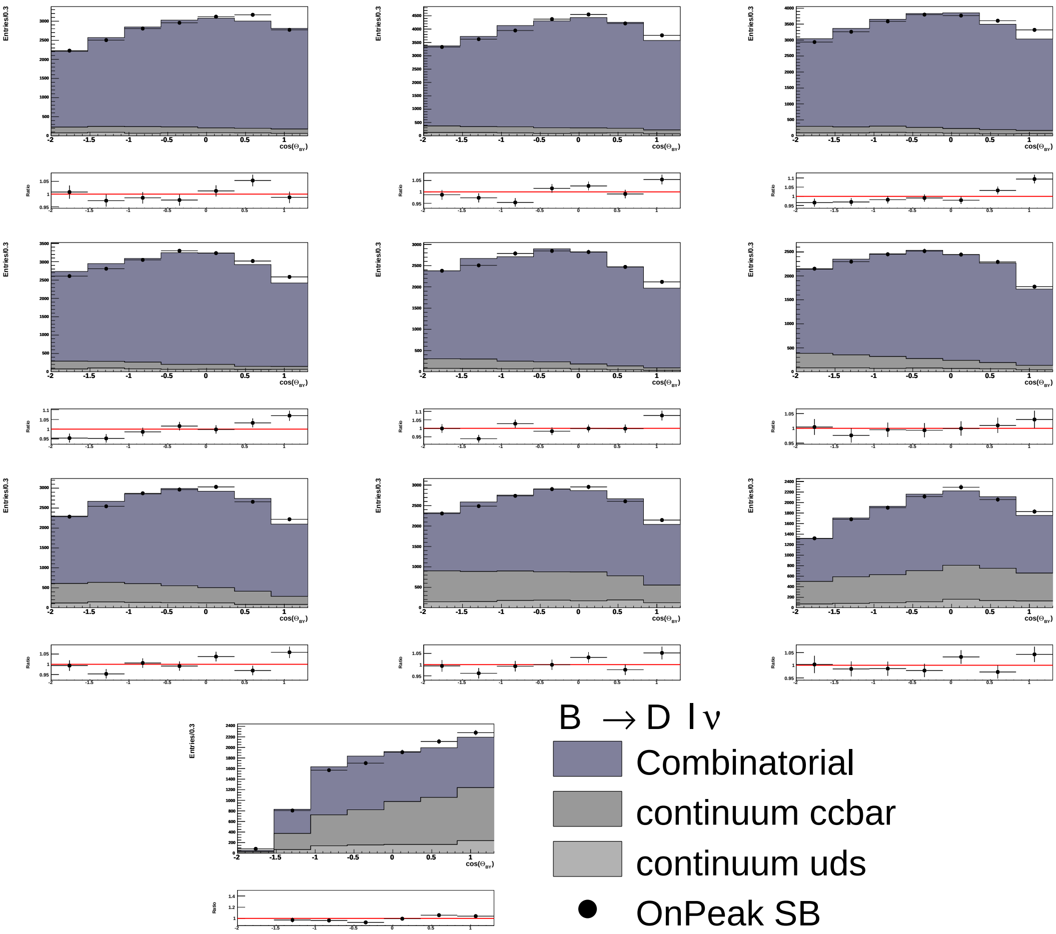

Figure E.8: The plot shows the $\cos\theta_{BY}$ comparison between the on-peak sideband data distribution vs the combinatoric background MC w-bin separately, scaled to on-peak luminosity

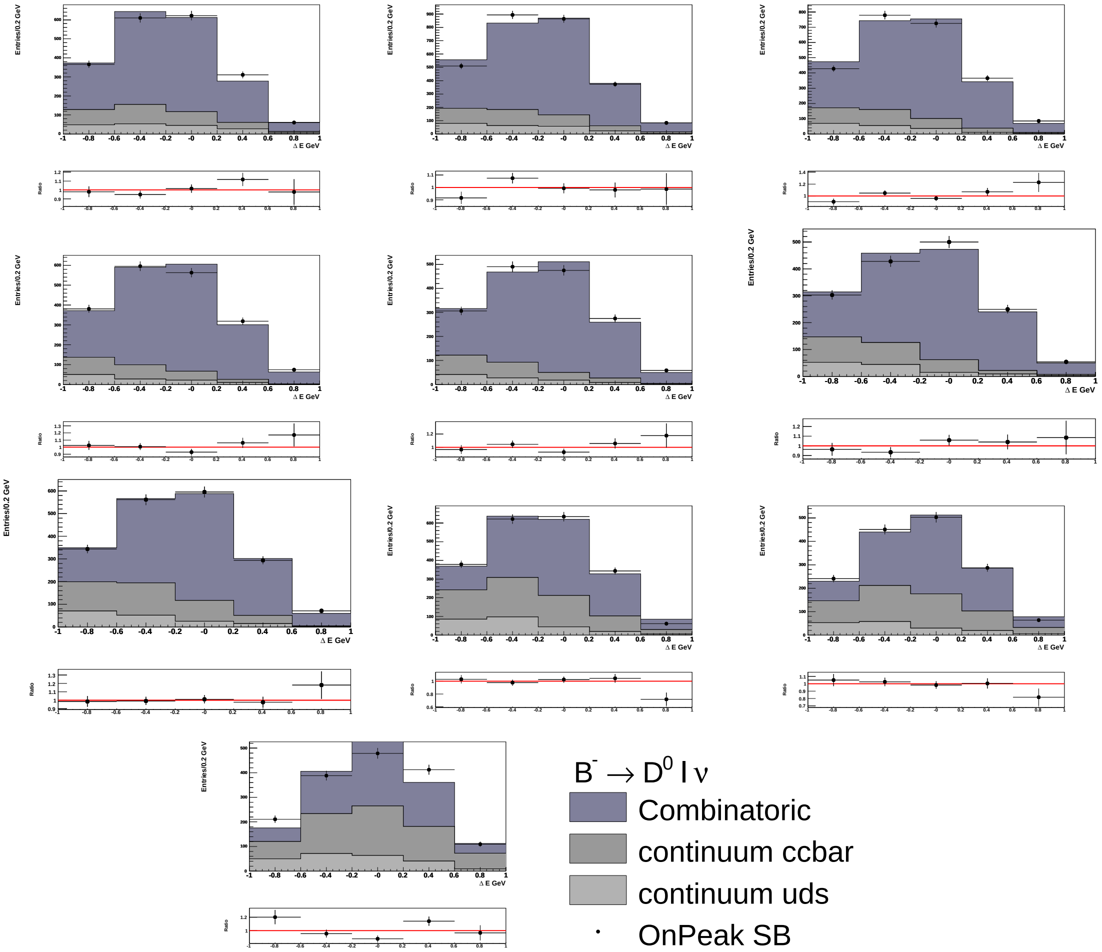

Figure E.9: The plot shows the ΔE comparison between the on-peak sideband data distribution vs the combinatoric background MC w-bin separately, scaled to on-peak luminosity

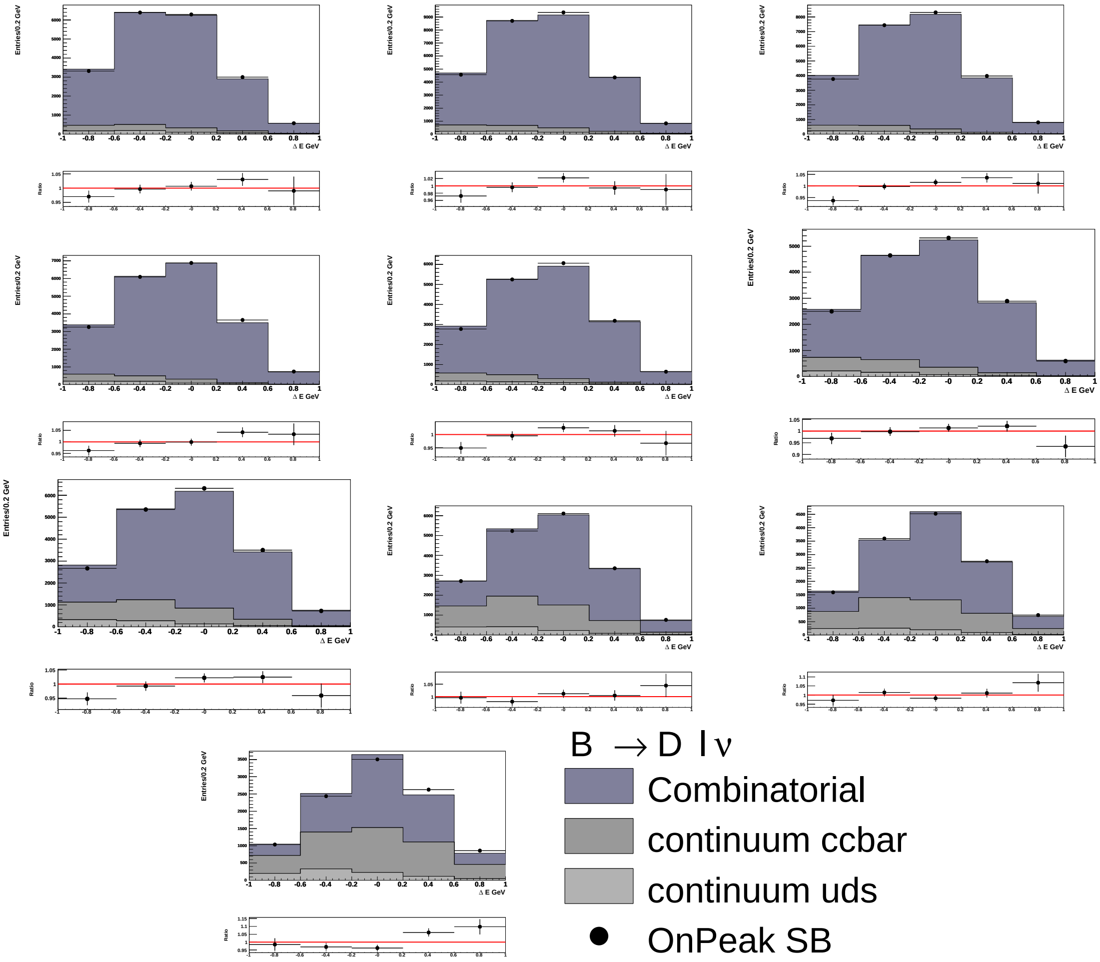

Figure E.10: The plot shows the ΔE comparison between the on-peak sideband data distribution vs the combinatoric background MC w-bin separately, scaled to on-peak luminosity

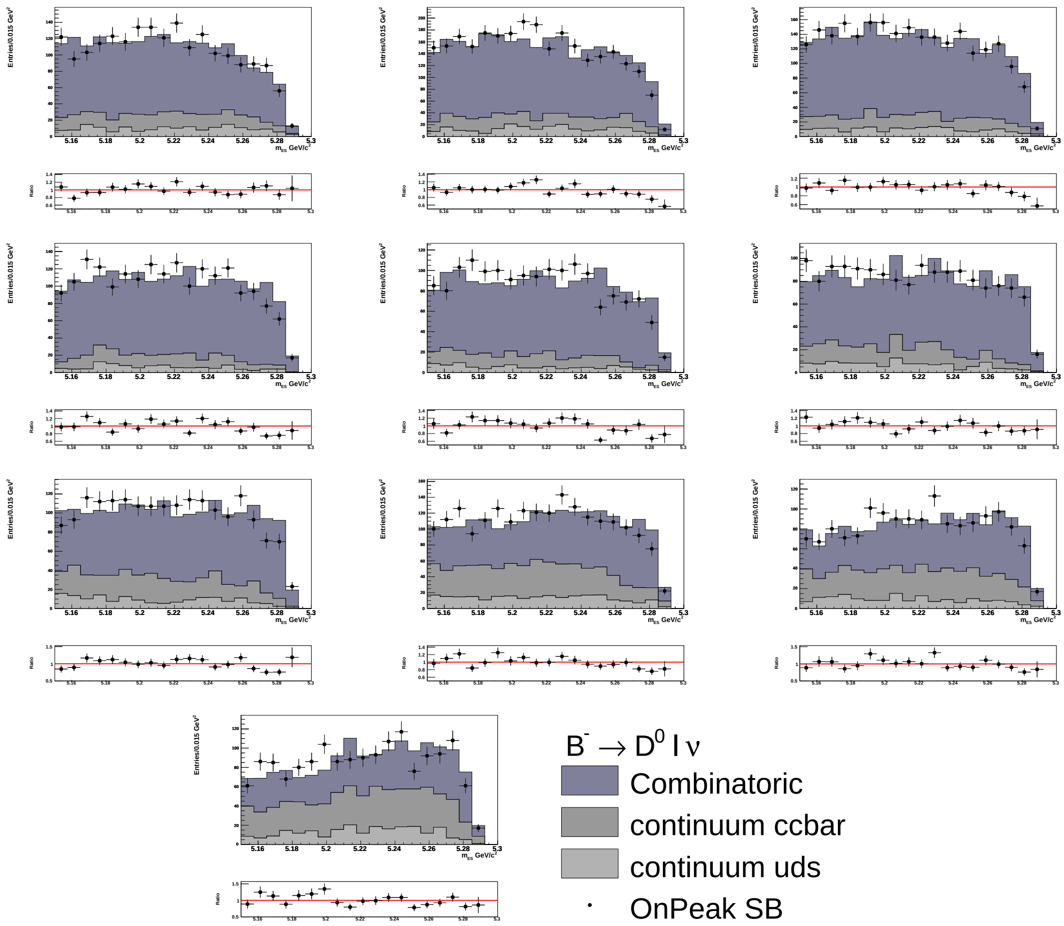

Figure E.11: The plot shows the m_{ES} comparison between the on-peak sideband data distribution vs the combinatoric background MC w-bin separately, scaled to on-peak luminosity

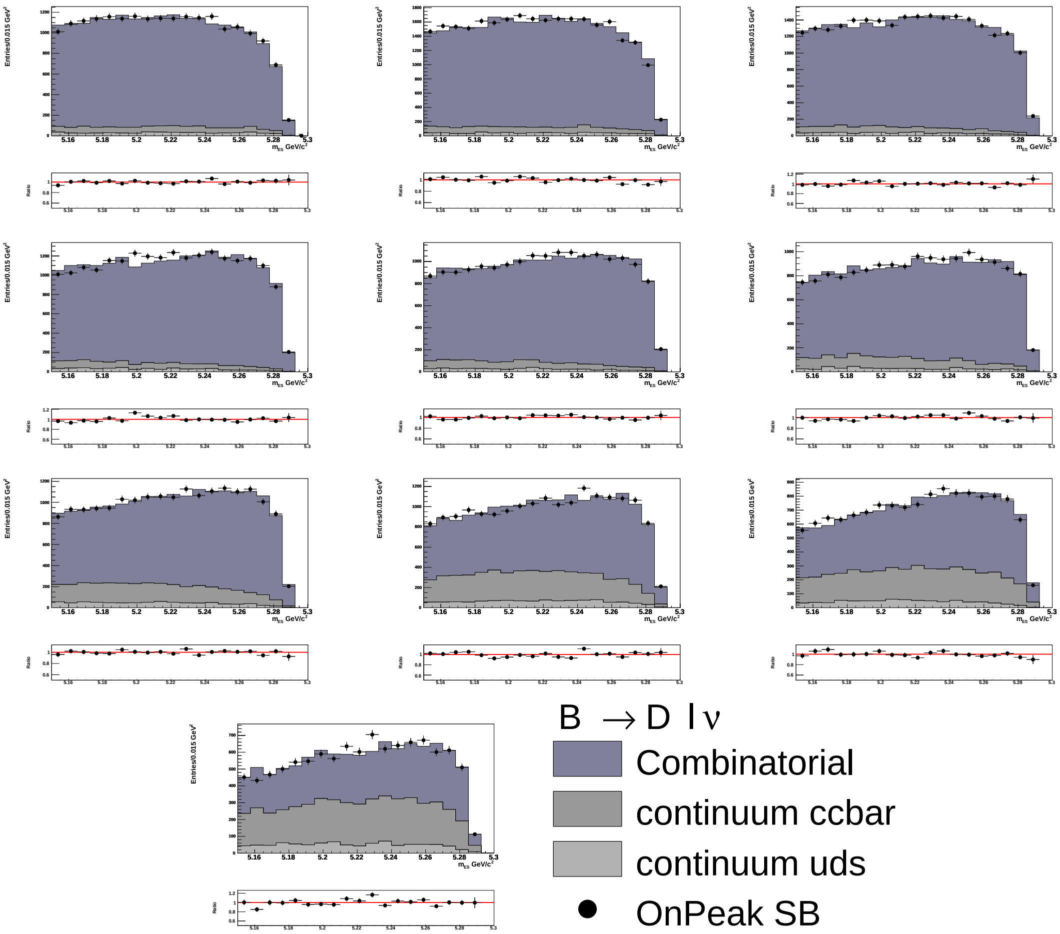

Figure E.12: The plot shows the m_{ES} comparison between the on-peak sideband data distribution vs the combinatoric background MC w-bin separately, scaled to on-peak luminosity